Defects in silicon: revisiting theoretical frameworks to guide ab initio characterization

Gabriela Herrero-Saboya

Université Fédérale
Toulouse Midi-Pyrénées

THÈSE

En vue de l'obtention du
DOCTORAT DE L'UNIVERSITÉ DE TOULOUSE

Délivré par l'Université Toulouse 3 - Paul Sabatier

Présentée et soutenue par

Gabriela HERRERO SABOYA

Le 19 novembre 2020

Les défauts dans le silicium : revisiter les modèles théoriques pour guider les calculs ab initio

---

Ecole doctorale : **GEET - Génie Electrique Electronique et Télécommunications : du système au nanosystème**

Spécialité : **MicroNano Systèmes**

Unité de recherche :
LAAS - Laboratoire d'Analyse et d'Architecture des Systèmes

Thèse dirigée par
Anne HEMERYCK et Nicolas Richard

Jury

M. Jorge José KOHANOFF, Rapporteur
M. Jean-François ROCH, Rapporteur
M. Vincent GOIFFON, Examinateur
M. Christophe DELERUE, Examinateur
Mme Layla MARTIN-SAMOS COLOMER, Examinatrice
M. Xavier BLASE, Examinateur
Mme Anne HEMERYCK, Directrice de thèse
M. Nicolas RICHARD, Co-directeur de thèse

A mi madre, a mi abuela y a A. Rhys,
por abrir el camino

Abstract

In this thesis, we describe the effect of localized defects on the electronic properties of silicon. After 60 years of silicon devices production, one might expect all details of this material to be fully understood, especially considering that the manufacture of nowadays nanometer-sized transistors requires quasi-atomic accuracy. However, as a direct result of such extreme miniaturization, the accidental creation of even one single trapping center can be sufficient to alter the desired electronic properties of the sample, becoming one of the most feared phenomena in the industry. Since the early years, the identification of these centers has been possible through the development of characterization techniques, capable of targeting specific defect properties, related to the position of the center-induced states within the semiconductor gap (infrared optical absorption, DLTS spectroscopy) or to the atomic distortions triggered by the form of the localized electronic density (EPR spectroscopy). Such collection of experimental data motivated the development of simple symmetry-based models, qualitatively reproducing the basic features of defects. The later exponential increase in computational power made *ab initio* calculations the perfect candidate to give a quantitative theoretical model of point defects in semiconductors. Atomistic numerical simulations in silicon, based on the Density Functional Theory, do however typically target specific defect-properties, not giving a complete theoretical picture of the system, often overlooking previous models and experimental evidence. In the present thesis, we provide new insight into iconic defects in silicon through the quantification of long-established atomistic models, making an explicit link with the characterization techniques. Our detailed exploration of the DFT energy surface of the silicon E-center, guided by a simple Jahn-Teller model, confirmed the observed defect-dynamics at different temperature regimes, allowing us to link the presence of such point- like defect to a burst noise in image sensors. Moreover, we investigate the hypothesis of enhancing photon-absorption in titanium-doped silicon solar cells by describing many-body effects in the form of the GW approximation, assigning the charged electronic excitations to transitions between Ti- related states, previously depicted by a phenomenological model for transition metals in silicon. We also propose a generalization of the preexisting toy-models to tackle complex centers, for which a notorious controversy within the *ab initio* community still exists, showing explicitly the limitations of mean-field approaches when targeting highly localized electronic densities. We conclude with a brief critical review of the theoretical characterization of the defects electronic activity, and in particular the capture cross section of non-radiative transitions.

Contents

Acknowledgments

When one is facing her third (and last) year as a PhD student, innocently believing to be in front of the most crucial moment in her research career (*i.e.* writing and defending her PhD work), a global pandemic can definitely seem like the end of the world. This is the reason I feel particularly driven to write the present section, since acknowledgments feel especially needed in such critic circumstances.

First, I would like to thank my thesis supervisors, A. Hémeryck and N. Richard, for giving me the opportunity to develop this research project and for always letting me feel welcome in a foreign country. I would also like to thank L. Martín-Samos, for facing my stubbornness, helping me become a better researcher.

I am grateful to J. Kohanoff and J-F. Roch for the care they put in reviewing this thesis manuscript and for their valuable comments. I am equally grateful to V. Goiffon, C. Delerue and X. Blase for kindly agreeing to be part of my thesis jury, giving me useful perspectives on my work.

I am also indebted to the Multiscale and Multi-Model Approach for Materials in Applied Science consortium, for their constant scientific and moral support. In particular, I would like to thank M. Gunde, T. Jarrin, R. Lot, N. Salles, A. Jay, S. de Gironcoli, and especially F. Pellegrini, who reminded me about the beauty of simple models. Thank you very much.

Regarding my daily life as a PhD student, it will be hard to forget the endless French lectures during coffee breaks and for that I am thankful to Claude, Mélanie, Dudu, Sébastien, Damien, Thierry, Philippe. Merci beaucoup.

Beyond office hours, I found an unconditional support in the community (should I say family?) brought together at Colegio de España de París and so I am thankful to (notice the long, but necessary list) Ari, Manuel, Luis, Alba, Julia, Marta, Sonia, Nico, Aída, Andrés, Carlos, César, Xisco, Jan, Manuel, Maria, Sergio, Isa. Last, but definitely not least, I outline the essential guidance I found in Paula, Manel and Paula. Muchísimas gracias.

Finally, I am thankful to my friends and my family spread around the globe, from whom I felt the strongest support despite the kilometers. I especially acknowledge my cousins Carmen and Teresa for their early role-modeling, this thesis has traces of your constant influence. For their infinite care, I am grateful to my *abuela*, my aunts and my oldest friends, Ato y Elena. Lastly, I thank my parents and my brother, for whom a detailed list of acknowledgments would be too long.

Acronyms

BCB Bottom of Conduction Band.

BG Band Gap.

BO Born-Oppenheimer.

CB Conduction Band.

CI-NEB Climbing Image-Nudged Elastic Band.

CMOS Complementary Metal-Oxide-Semiconductor.

CTL Charge Transition Level.

DFT Density Functional Theory.

DLTS Deep Level Transient Spectroscopy.

DOS Density Of States.

EA Electronic Affinity.

EPR Electronic Paramagnetic Resonance.

HF Hartree-Fock.

HOMO Highest Occupied Molecular Orbital.

HR Huang-Rhys.

IP Ionization Potential.

JT Jahn-Teller.

KS Kohn-Sham.

LC Level-Crossing.

LCAO Linear Combination of Atomic Orbitals.

LDA Localized Density Approximation.

LUMO Lowest Unoccupied Molecular Orbital.

LW Ludwig-Woodbury.

MBPT Many-Body Perturbation Theory.

MEP Minimum Energy Path.

MO Molecular Orbital.

NEB Nudged Elastic Band.

OA Optical Absorption.

PBC Periodic Boundary Conditions.

PBE Perdew-Burke-Ernzehorf.

PES Potential Energy Surface.

QP Quasi-Particle.

RTS Random Telegraph Signal.

SP Saddle Point.

SRH Shockley-Red-Hall.

TM Transition Metal.

TVB Top of the Valence Band.

VB Valence Band.

XC eXchange-Correlation.

Introduction

One should not keep busy with semiconductors, they are dirt effects - Who knows whether they really exist.

W. Pauli (1931)

In the present era of silicon microelectronics, in which semiconductor properties are tuned at will, Pauli's advice seems certainly incredible. One should however grant him the critique to the ideal concept of semiconductors as materials with a native insulator character, since their electronic properties are often governed and modified by these so-called *dirt effects*. At the very basis of our nowadays technology, the intentional inclusion of certain foreign elements or *impurities* in the material crystalline structure promotes the generation of free carriers across the band gap, circumventing the native absence of charge mobility in semiconductors. Opposite to the *doping* character of these impurities, the accidental creation of *lattice imperfections* or defects capable of *trapping* free charges, decreasing the extrinsic concentration of carriers, might alter the desired and targeted properties of the semiconductor. We might therefore conclude that one should keep busy with semiconductors, whose intrinsic properties are dominated by dirt effects, constituting the complex and rich field of defects in semiconductors.

In the case of silicon, after more than 60 years of Si-based devices production, one might expect all details of this material to be fully understood, especially considering that the manufacture of nowadays nanometer-sized transistors requires quasi-atomic accuracy. However, as a direct result of such extreme miniaturization, the accidental creation of even one single trapping center can be sufficient to alter the desired electronic properties of the sample, becoming one of the most feared phenomena in the industry. Regardless of the improved accuracy in the manufacturing process, embedded systems can be subject to radiative environments, where highly energetic particles might interact with the device, altering the material underlying atomic structure.

As a consequence of such irradiation damage, uncontrollable output signals (*i.e.* dark current, burst random noises, etc.) are measured in electronic components, decreasing their reliability during utilization. It is the case, for example, of devices sent to aerospace expeditions, during which they might face solar flares, events characterized by the projection of particles through the Sun corona into outer space. With an even more specific scope, the success of future Mars missions could be compromised by the degradation of the image sensors employed to guide the observation of the planet (Figure 1). One is then said to be concerned by the"hardening of the electronic components", guaranteeing the well-functioning of any embedded system. In such context, characterizing defects in semiconductors at the atomic scale might be regarded as the first step in mitigation strategies. The investigation of the electronic properties of defects in silicon at such scale might be achieved through *ab initio* computational approaches, describing the center embedded in the material quantum-mechanically (Figure 1).

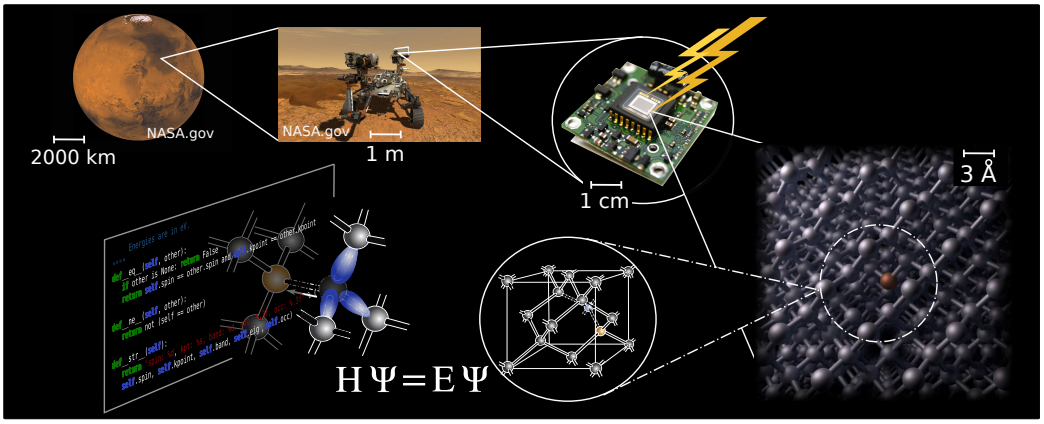

Figure 1: Atomistic scale calculations as mitigations strategies of irradiation damage in silicon-based electronic devices used in aerospace applications.

Historically, the electronic properties or the electronic activity of defects in semiconductors have been understood in terms of their ability to capture or release carriers from the bulk bands within a certain region of the lattice, corresponding to the defect-induced wavefunction. As it is then commonly and simply depicted, the *trapping mechanism* consists on transferring a free carrier from the valence band (VB) or the conduction band (CB) to the trap level, T, whose energy lies within the band gap (Figure 2). In the case of for example a silicon-based photodiode, the radiative transitions (I and II in Figure 2) have then to compete with trapping mechanisms or the so-called non-radiative transitions (III-VI in Figure 2), resulting in a decrease in the di-

ode efficiency. The electronic occupation of such trap level or the occurrence of such transitions were first estimated in the seminal work of Shockley-Red-Hall (SRH), *Statistics of electrons and holes*, in which four thermal transitions were considered: the electron capture (III), the electron emission (IV), the hole capture (V) and the hole emission (VI). By simply imposing charge balance or conservation, the concentration of free carriers was determined upon three single parameters: the position of the trap level (E_T), the electronic capture cross section (σ_n) and the hole capture cross section (σ_p). One can therefore conclude that within such simple model, the electronic activity of the defect is fully characterized once the positions of the defect levels and their capture cross sections are determined in a certain theoretical framework or computational approach. In the present work, we are precisely interested in modeling the electronic activity of defects in semiconductors due to its immediate interest for the microelectronic industry. More concretely, we focus on the characterization of selected defects in silicon, aiming to generalize the individual theoretical pictures to general trends or models by revisiting the established methodology or computational approaches.

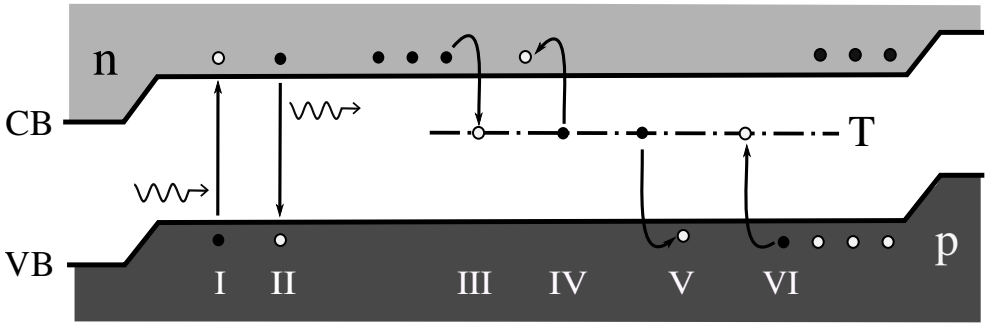

Figure 2: Radiative (I, II) *versus* non-radiative transitions (III-VI) across the silicon pn-junction. Defects in the crystal structure of the material introduce the trap level T within the band gap, defined by the valence band (VB) and conduction band (CB). Filled and empty dots represent negative and positive carriers (electrons and holes) in semiconductors respectively.

Characterization techniques, such as optical absorption (OA) measurements, electronic paramagnetic resonance (EPR) or the deep level transient spectroscopy (DLTS) have however revealed the complexity of describing electronic transitions involving trap levels, since defects might be regarded as molecule-like entities subject to the crystal field of the host material. A single defect, similarly to a molecule in vacuum, might induce several molecular orbitals or localized defect states, whose form and eigenvalues are to

be determined within the crystal band structure. Moreover, it has been observed that changes in the electronic occupation of such orbitals can trigger atomic distortions in nearby nuclei, presenting different geometries or configurations depending on the electronic excitation (*i.e.* the Jahn-Teller effect). Experimental evidence has therefore proved that localized-defect electronic densities are strongly coupled to the lattice and it has been postulated that such electron-lattice coupling is precisely responsible for the non-radiative or thermal transitions in the early work of Huang and Rhys and Lang. The simple diagram in Figure 2 or the simple model of SRH has therefore to be re-conceived, including the description of the trap levels dependence on the electronic excitation and local atomic rearrangements.

An accurate estimation of the defect electronic activity, taking into consideration experimental evidence, can be sought thorough a complete theoretical model of the point-like defect and its surrounding lattice. The description of such systems quantum mechanically has been previously performed through *ab initio* computational approaches, where the electronic structure of defect and lattice is given in terms of a one-particle picture in the clamped nuclei approximation. In particular, trap levels induced by defects in silicon have been characterized by methods based on the Density Functional Theory (DFT) for the last three decades. In the case of the computation of capture cross sections, only recently DFT-based models for defects in ZnO, GaAs or GaN have been proposed. These theoretical approaches did however target specific quantities (E_T and σ_n), without giving a complete and understanding picture of the studied center, often overlooking basic fundamental symmetry considerations and/or experimental evidence.

With nowadays computational resources and sophisticated theories to solve the Coulomb electronic repulsion, one might be surprised that previous first-principles models for defects in silicon were not capable of capturing the observed complexity of the systems. In the present work, we aim at building full and comprehensive models (Figure 3), taking one step back and starting from simple molecular orbital approaches, before including more general treatments of the electron-electron interaction, *i.e* DFT or Many-Body Perturbation Theory (MBPT). Through this approach we would like to refute the idea that advanced computational methods need to be blind, as opposed to simple symmetry-based theories qualitatively reproducing the experience. Advancing one of the main conclusion of the present work, toy-models might be the first interpretation of defects in semiconductors, guiding the characterization at higher levels of theory.

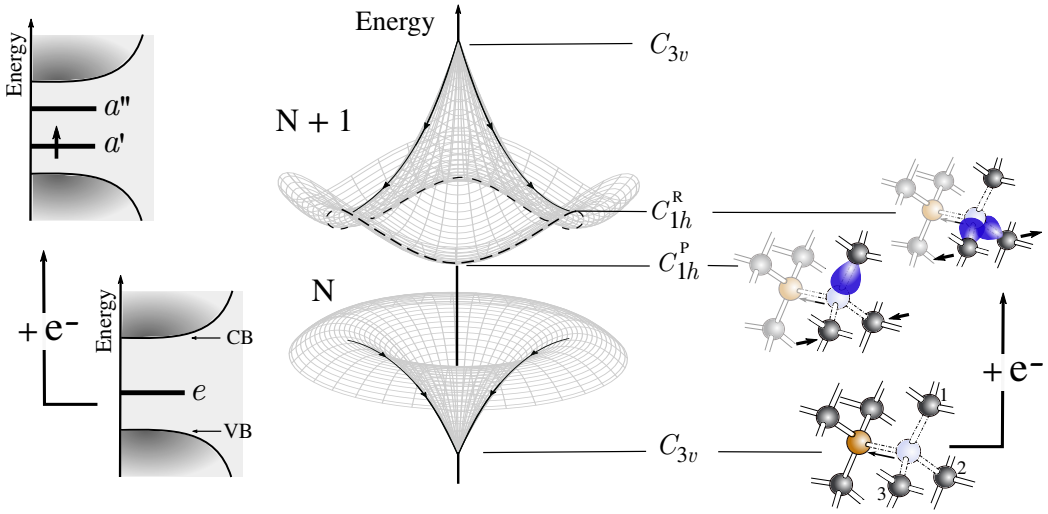

Figure 3: Theoretical model of an electron capture by a point-defect in silicon: from single-particle band structures to atomic distortions.

The present thesis begins with an introduction to the field of point defects in semiconductors (Chapter 1), where preliminary ideas such as the difference between shallow and deep centers, the formation of defects at equilibrium, the concept of charge transitions levels, etc. are reviewed. Special attention is then given to silicon as the most used semiconductor in electronic devices, for which relevant defect-inducing processes and the resulting realistic catalog of defects are discussed. The Chapter ends with an extensive description of the characterization techniques of defects in semiconductors, with a special emphasis on measures performed in silicon.

In Chapter 2, we review the computational approaches employed throughout this thesis, starting from the simplest treatment of the electronic interaction in the form of a Linear Combination of Atomic Orbitals (LCAO), moving into more accurate levels of theory with the DFT and MBPT. We conclude the Chapter by discussing the limitations of applying the introduced numerical methods to the description of isolated or diluted defects in a host lattice.

In Chapter 3, we revisit the characterization of iconic centers in silicon, for which previous computational approaches overlooked or misinterpreted the existence of atomic distortions or Jahn-Teller distortions when the charge state of the defect is modified. In the case of the titanium impurity, we reconsider the interaction of the 3d orbitals with tetra and octa-hedral crystal fields to guide our investigation of the Ti-related states in silicon. Such ana-

lysis together with an accurate description of many-body effects allow us to support the idea that this degrading impurity could be used to enhance the efficiency of solar cells by inducing an intermediate band in the interacting defect-defect regime. The second part of the Chapter is dedicated to the understanding of the finite-temperature dynamics of the silicon E-center, one of the most common centers in Si wafers, since it consists of a vacancy adjacent to a dopant impurity (phosphorous, arsenic or antimony). By guiding our first-principles exploration of the energy landscape with a Jahn-Teller model, we are able to link specific defect mechanisms to technologically relevant processes.

The numerical analysis of the Jahn-Teller effect is then generalized to a symmetry-based theory in Chapter 4, where the seminal and original Watkins model is revisited. Our simple toy-model for the E-center reproduces the underlying and basic features of the centers in line with higher levels of theory and experimental evidence. The model is then employed to study more complex defects such as the divacancy or heavy transition metals like platinum or gold, for which a long-established controversy still exists in the *ab initio* community. The later quantification of the simple models allows us to have a better understanding of the centers and hence, we are capable of farther comparing our numerical estimations with experimental data, revealing the limitations of the employed approach to accurately treat highly localized electronic densities.

Before concluding, the perspectives or natural continuation of the present work on the characterization of the electronic activity of defects (*i.e.* position of the trap levels and respective capture cross sections) are collected in Chapter 5. We discuss the accuracy of the state-of-the-art computed deep levels of selected centers in silicon, in the general context of the reproducibility of *ab initio* calculations. We later revisit the long-established *multi-phonon* theories to determine the non-radiative transition probability, before discussing recent *ab initio* approaches.

Chapter 1

Point defects in semiconductors

Many scientists have fortunately not heeded Pauli's advice. Had they done so, not only would the world have missed a revolutionary and nowadays ubiquitous technology, but basic physical science would have lost some of the most fruitul, beautiful and sucessful applications of quantum mechanics.

M. Cardona (2007)

Giving an exact date to the first mention of point defects in semiconductors as entities capable of altering the intrinsic properties of the host material is probably an impossible task. We can however trace the first ideas on the ability of structural imperfections to alter material properties to the work of R. W. Pohl in the thirties on alkali halides. He realized that the absorption of visible light by electrons localized within the anion vacant site in an ionic crystal was responsible for the color of samples containing crystallographic defects, being transparent for an otherwise *perfect* solid. In the mid-1930s, R. Ohl measured a considerable jump in the electrical current of a silicon slab exposed to a bright light. Such sample was then determined to be marked by the separation of two regions containing different types of impurities, yielding a slight excess of electrons and holes respectively. The union of semiconductors containing opposite signs of free carriers allowed W. Shockley, W. Brattain and J. Bardeen to build the first transistor and to be rewarded by the Nobel Prize in Physics in 1956. Short after the explosion in the manufacturing of silicon-based devices, evidence of a second type of

impurities, capable of trapping or localizing free carriers within a certain region of the silicon crystal was reported. The ability of these *trapping centers* to alter the electronic properties of the material triggered the interest of the community to characterize these systems over a few decades ago.

Having established the age of the field, we have justified the need to briefly settle some preliminary ideas as they are going to be employed throughout the thesis (section 1.1). Basic features of the centers at equilibrium (local-induced lattice distortions, relative concentration depending on the formation regime, finite-temperature dynamics) are introduced at the atomic scale, at which the electronic activity of these centers is explained by the inclusion of defects-related energy levels in the semiconductor gap. From a more applied perspective, far from equilibrium conditions, the large catalog of point defects in silicon devices is sustained by the examination of actual defect-inducing process, justifying the need to characterize these centers at the atomic scale as the first step in mitigation strategies (section 1.2). The big effort already made by the experimental community to identify such trapping centers is reflected in the large number of experimental evidence retrieved through a series of characterization techniques (section 1.3).

1.1 Preliminary ideas

Starting from their simplest definition as structural perturbations breaking the translational symmetry of a crystalline material (section 1.1.1), we dedicate the present section to reviewing basic ideas regarding point defects in semiconductors. Properties such as their electronic activity, linked to the position of their eigenvalues within the semiconductor gap and to their ability to generate free carriers in the host bands, allow us to differentiate between shallow *vs.* deep centers (section 1.1.2) and the host material between intrinsinc *vs.* extrinsinc semiconductors (section 1.1.3). At equilibrium conditions, their relative occurrence or concentration depending on the presence of a chemical and/or electronic reservoir is also considered (section 1.1.4). The creation of charged defects upon the variation of the Fermi energy (or concentration of free carriers) lets us reexamine the electronic properties of deep centers in terms of their charge transition levels (section 1.1.5). We finally consider point defects as dynamic structural distortions in an infinite medium, introducing thermal mechanisms such as migration, diffusion, clustering and metastable-switching processes (section 1.1.6).

1.1.1 The notion of crystallographic defects

An ideal crystalline material can be defined as a periodic arrangement of atoms infinitely extended. The set of primitive vectors, $\{\mathbf{a_i}\}$, defines the unit cell of the crystal, which determines the translational symmetry of the atomic lattice. Electrons in a crystal are therefore subject to a periodic potential of the form $V(\mathbf{r}) = V(\mathbf{r} + \mathbf{R})$, with $\mathbf{R} = n_1\mathbf{a_1} + n_2\mathbf{a_2} + n_3\mathbf{a_3}$ a vector of the so-called Bravais lattice (n_i integer). The electronic wavefunction, $\psi(\mathbf{r})$, of the one-electron Hamiltonian defined by $V(\mathbf{r})$ was demonstrated to have the form of a Bloch state (see [1, 2]),

$$\psi_{\mathbf{k}}(\mathbf{r}) = e^{i\,\mathbf{k}\cdot\mathbf{r}}u(\mathbf{r}) \tag{1.1}$$

where $u(\mathbf{r})$ has the same periodicity as the atomic structure of the solid and the plane wave, $e^{i\mathbf{k}\cdot\mathbf{r}}$, is characterized by a *crystal* wave vector, $\mathbf{k}$. The eigenvalues of the Schrödinger equation, $\epsilon_{n\mathbf{k}}$, are therefore characterized by a discrete quantum number n and the continuous crystal momentum, $\mathbf{k}$. The single-electron energies plotted against the wave vector constitute the so-called electronic band structure of the solid material. Due to the translational symmetry of the crystal, the definition of the electronic wave function is not unique, since any k-vector of the form $\mathbf{k} + (2\mathrm{m}\pi\mathbf{R})$ fulfills equation 1.1, m being any integer. Any crystal wave vector of the lattice is thus, $\mathbf{k}' = \mathbf{k} - \mathbf{G}$, where $\mathbf{G}$ is a vector of the reciprocal lattice, defined by the relation $\mathrm{e}^{i\,\mathbf{R}\cdot\mathbf{G}} = 1$. The band structure of the solid is then typically represented within the unit cell of the reciprocal lattice or the first Brillouin zone.

In such context of crystalline materials, a structural defect is simply defined as any local perturbation of the solid periodicity. As a common example of point-like defect, we can picture a missing atom or a *vacancy* at a certain position in the lattice, $\mathbf{r}_\mathrm{T}$, disrupting the already mentioned translational invariance of the solid, since $V(\mathbf{r}_\mathrm{T}) \neq V(\mathbf{r}_\mathrm{T} + \mathbf{R})$. An electronic wavefunction *trapped* within such perturbation of the potential, ψ^T, is therefore not a Bloch state, being completely delocalized in reciprocal space. In other words, the defect-induced states are confined within a certain region of the Bravais lattice, in contrast with the bulk states. The one-electron eigenvalues of such localized wavefunctions, ϵ_T, are represented as constant energy levels in the host band structure as shown in Figure 1.1. To conclude, point-like defects are crystalline imperfections of the order of one to a few atoms, introducing constant energy levels due to the localization of the induced states.

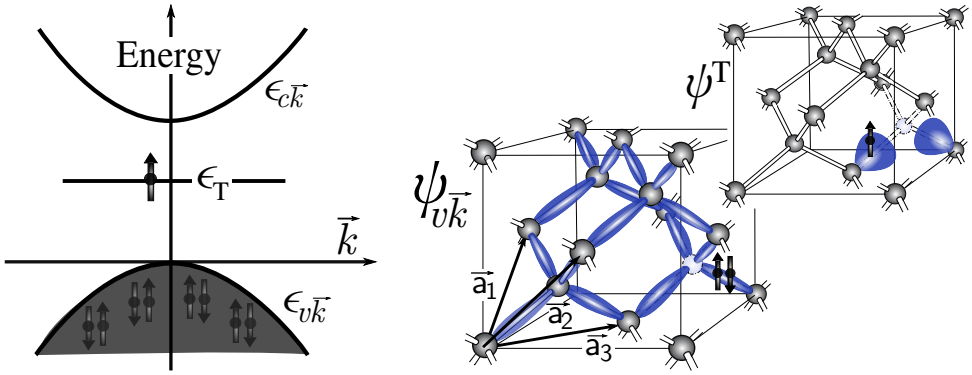

Figure 1.1: Diamond structure of a IV-type semiconductor containing a point-like defect. The periodicity of the crystal is indicated by the primitive lattice vectors, $\{\mathbf{a}_i\}$, and the imperfection, a mono-vacancy, is represented in light blue. The host band structure, $\epsilon_{n\mathbf{k}}$, is depicted on the left, where bulk states are denoted by v if the belong to the valence band and c for conduction states. A hypothetical defect eigenvalue is plotted within the semiconductor band gap: ϵ_{T}. The electronic density corresponding to the bulk wavefunction, $\psi_{v\mathbf{k}}$, and the defect-induced state, ψ^{T}, is represented in blue.

1.1.2 Shallow *vs.* Deep centers

Historically, point defects in semiconductors have been classified as *shallow* and *deep* centers depending on the position of their defect levels (ϵ_{T} in Figure 1.1) within the semiconductor gap. In the literature, the definition of a deep level as one located in the *middle* of the band gap and a shallow level as one *close* to the band gap edges is often found. There are however defect levels with the same properties of a *deep level* whose energies are far from the middle of the gap. We therefore employ the *qualitative* definition used in [3]: a shallow or hydrogenic center is one that can be described by a simple Hydrogen model and a deep center is one that can not. To exemplify the Hydrogen model, we consider the case of foreign elements from the V- and III-columns in the periodic table introduced at substitutional positions in IV-type semiconductors (e.g. at a given $\mathbf{r}$ belonging to the Bravais lattice represented in Figure 1.1). These foreign atoms therefore contribute to the tetra-folded covalent bonds of the crystal, having one extra (V-elements) or one *missing* (III-elements) electron with respect to the host element. The extra negative or positive charge (missing electron in the case of III-elements) is located at the so-called shallow states centered at the impurity atom, whose properties are induced from the analogy with the hydrogen atom. In the

common example of a phosphorus atom embedded in silicon, the extra electron is subject to the spherical potential of the impurity, screened by the dielectric constant of the material. Within the Hydrogen model, the extra charge is then said to be weakly bound to the foreign element, localized at defect states with rather extended effective radius. In the ongoing example of silicon, the extended radius is estimated to be [2],

$$a^* = a_0 \frac{\epsilon_\infty}{m^*} \tag{1.2}$$

where $m^* = 0.3$, $\epsilon_\infty = 12$ and a_0 are the effective mass, the dielectric constant and the Bohr radius respectively, giving an effective radius, a^*= 18 Å (as a reference magnitude, the nearest neighbor distance in the silicon crystal is 2.35 Å). Defect wavefunctions are therefore said to be shallow states if their effective radius is significantly larger than the distance to the first and second neighbours of the point-like defect, introducing energy levels close to the top or the bottom of the valence or conduction bands.

In Figure 1.2 the band structures of shallow and deep centers are represented along with a shallow wavefunction, ψ_{p}, and a deep state, $\psi_{\mathrm{d_1}}$. In the shallow domain, two energy levels, ϵ_{n} and ϵ_{p}, located at $\sim k_{\mathrm{B}}T_{\mathrm{RT}}$ from the bottom of conduction band and the top of the valence band are introduced in the band gap. The ϵ_{n} level represents the binding energy of the *extra* electron to the V-element impurity in the above-introduced example of IV-type semiconductors. Such electron is easily thermalized into the conduction band, contributing with a negative carrier to the host, and the impurity is said to be a *donor* center. The impurity embedded in the semiconductor goes from being at neutral *charge state*, for the configuration $\epsilon_{\mathrm{n}}^{\uparrow}$, to a positive charge state, $\epsilon_{\mathrm{n}}^{0}$, describing the *charge transition* $0 \rightarrow +1$. The energy level ϵ_{p}, introduced by the III-element impurity, can capture electrons from valence band or contribute with one positive charge (hole) to the bulk states. These centers are therefore typically referred to as *acceptors*, since they are responsible for the charge transition $0 \rightarrow$ -1, corresponding to the change in the electronic configuration $\epsilon_{\mathrm{p}}^{\uparrow} \rightarrow \epsilon_{\mathrm{p}}^{\uparrow\downarrow}$. Point defects in semiconductors are therefore expected to be present at different charge states if they are capable of capturing/releasing electrons from/to bulk bands.

Deep centers in semiconductors, in contrast with shallow impurities, induce highly localized states (state ψ^T in Figure 1.1), with effective radius varying from 2.5 to 4 Å. Furthermore, one single center might introduce several states within the band gap, whose energies can not be estimated by simple theoretical models. In Figure 1.2 a deep center with two energy states,

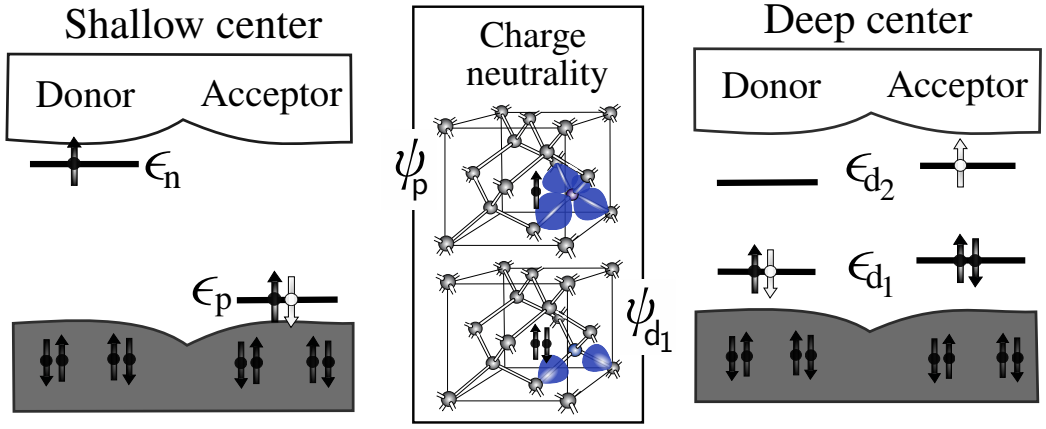

Figure 1.2: Band structures of hypothetical shallow and deep centers embedded in a IV-type semiconductor. Besides the valence and conduction bands, defect-related eigenvalues are denoted by ϵ. Two different shallow defects are considered, the so-called donor and acceptor centers, with one extra negative and positive charge respectively. Two different electronic occupations or charge states of a single deep centers are also represented. The electronic density corresponding to a shallow state, ψ_{p}, and a deep state, $\psi_{\mathrm{d_1}}$, are also depicted.

$\epsilon_{\mathrm{d_1}}$ and $\epsilon_{\mathrm{d_2}}$, located in the gap is considered. Assuming such defect is *neutrally charged* for an electronic occupation equal 2 (a singlet of electrons in energy level $\epsilon_{\mathrm{d_1}}$; $\mathrm{d}_1^{\uparrow\downarrow}$), the electronic configuration $\mathrm{d}_1^{\uparrow}$ corresponds to a *charge defect state* equal +1 and $\mathrm{d}_1^{\uparrow\downarrow}\mathrm{d}_2^{\uparrow}$ for a singly negative state, -1. If the defect at neutral charge state releases one electron, $\mathrm{d}_1^{\uparrow\downarrow} \rightarrow \mathrm{d}_1^{\uparrow}$, the charge transition $0 \rightarrow +1$ occurs and the deep center is said to act as a *donor*, by analogy with the transition between the shallow state of the V-element impurity and the conduction band. The change in electronic occupation $\mathrm{d}_1^{\uparrow\downarrow}\mathrm{d}_2^{0} \rightarrow \mathrm{d}_1^{\uparrow\downarrow}\mathrm{d}_2^{\uparrow}$ leads to a second charge transition $0 \rightarrow$ -1, and the center is now behaving as an *acceptor*. Deep centers introducing several states ϵ_{T} in the semiconductor band gap, being capable of capturing and releasing electrons can therefore act both as donors and acceptors. To conclude, deep centers capable of *trapping* free carriers *deep* into the semiconductor band gap are said to be *electronically active*, since they modify the electronic properties of the material.

1.1.3 Intrinsinc *vs.* Extrinsinc semiconductors

Probably the most important quantity of any semiconductor is the concentration of free carriers, *i.e.* the number of electrons in conduction band, n_c, and

the number of holes in the valence band, p_v, at a given temperature T. Assuming that no accessible levels are available within the band gap (definition of native or intrinsinc semiconductor), the relation $n_c = p_v$ is satisfied and the Fermi energy lies close to the middle of the band gap [1]. When shallow impurities are however introduced in the crystal, donor and acceptor centers contribute with negative and positive carriers to the host bands respectively, altering the intrinsic condition. Increasing the concentration of shallow impurities therefore increases the number of free carriers, often receiving the name of *dopant* impurities and the host material a *doped* or extrinsinc semiconductor. Crystals intentionally doped with donor centers (typically P, As and Sb in the case of silicon) are referred to as n-type doped semiconductors, whereas p-type semiconductors present a majority of positive carriers, arising from acceptor centers (e.g. B in silicon). If the concentration of shallow impurities is large enough (10^{13}-10^{18} cm^{-3} for doped-silicon), the position of the Fermi energy is shifted towards the conduction band for n-type doping, whereas it is positioned close to the valence band for p-type doping (position of ϵ_n and ϵ_p in band structures of Figure 1.2).

Deep centers, such as native defects like vacancies and interstitials, can be found in both intrinsinc and doped semiconductors and will therefore be in contact with an electronic reservoir given by n_c. In other words, deep centers can be found at different charge states if they trap/release free carriers generated by the shallow impurities. These structural imperfections are therefore responsible for decreasing the desired concentration of free carriers, and so their electronic activity is said to degrade the well-functioning of electronic devices. Certain metallic elements (*e.g.* titanium and gold in silicon) are thus *accidentally* introduced in semiconductors, since they might affect the doping concentration in the sample even at concentrations of a few percent of the desired free carrier concentration [4], being *unwanted* impurities. To conclude, impurities are intentionally introduced in the material if they induce shallow states and they are referred to as dopants, whereas metallic, chalcogen, halogen, etc. contamination of the sample introduces deep levels in the band gap for both intrinsinc and extrinsinc semiconductors.

1.1.4 Formation of defects at equilibrium

The *accidental* formation of point defects in semiconductors strongly depends on the specific defect-inducing process to which the sample is subject such as dopant implantation, irradiation, exposition to an oxide surface (section 1.2.2). At equilibrium, it is however possible to generalize the formation probability of different defects for a given material, *i.e.* to estimate the re-

lative probability of finding a specific center from the catalog of common "imperfections". Such probability of occurrence or concentration of a given defect, d, can be written in terms of the Gibbs formation energy, G_f,

$$c^d = e^{-G_f^d / k\mathrm{T}} \tag{1.3}$$

where k is the Boltzmann constant and T the temperature. Since most computational approaches are limited to the description of zero-temperature regime, the Gibbs formation energy is often substituted by the formation enthalpy, H_f^d,

$$G_f^d = E_f^d + \Omega_f^d \mathrm{P} - S^d \mathrm{T} = H_f^d - S^d \mathrm{T} \tag{1.4}$$

where E_f^d is the formation energy and Ω_f^d is the change in volume due to the inclusion of the defect in the infinite crystal. Assuming the limit of diluted defects or non-interacting defects, local atomic expansion/compression are minimal, and so the formation enthalpy is often simply identified with the formation energy. In such temperature-pressure conditions, the creation of defects is mainly determined by the the chemical environment of the sample or the presence of chemical reservoirs. We must therefore distinguish between a homogeneous and heterogeneous regime of formation, depending whether the stoichiometry of the sample remains invariant or not. In the former case, for which there is no exchange with an external chemical phase, native defects such as vacancies and interstitials are typically studied for an intrinsic semiconductor. For an extrinsinc semiconductor, a given concentration or stoichiometry of dopant impurities characterizes the sample and so, dopant-related defects must also be accounted for in the homogeneous regime. In the test case of a mono-vacancy in the silicon crystal, the formation reaction is simply,

$$\mathrm{Si}_{\,[\mathrm{bulk}]} \rightleftharpoons \mathrm{Si}^{\,\mathrm{V}}_{\,[\mathrm{bulk}]} + \mathrm{Si}. \tag{1.5}$$

The formation energy of the vacancy can be estimated by imposing the conservation of energy in the above reaction and so,

$$E_f^{\mathrm{V}} = E_{[\mathrm{Si},\,N-1]} + \mu_{\mathrm{Si}} - E_{[\mathrm{Si},\,N]} = E_{[\mathrm{Si},\,N-1]} - \frac{N-1}{N} E_{[\mathrm{Si},\,N]}, \tag{1.6}$$

where $E_{[\mathrm{Si},\,N]}$ is the energy of N units of silicon crystal, $E_{[\mathrm{Si},\,N-1]}$ is the energy of N units of silicon crystal containing one vacancy, and μ_{Si} is the chemical potential of silicon for the missing atom, which is defined from the silicon bulk energy cohesion, $\frac{E_{[\mathrm{Si},\,N]}}{N}$. In the more complex scenario for which the sample is in contact with an external reservoir, the chemical potential of different species must be determined in order to fulfill the conservation of mass. Due to the large variety of chemical environments of silicon wafers

(section 1.2), the estimation of chemical potentials becomes a challenging task and beyond the interest of the present work. On the other hand, the relative stability of an external species at different sites in the lattice might be easily computed since the dependency with μ is canceled out. In the case of metallic impurities in silicon, the relative formation energy of the species at substitutional or interstitial positions in the lattice is simply,

$$E_f^{\mathrm{TM_I}} - E_f^{\mathrm{TM_S}} = E_{[\mathrm{Si},\, N;\, \mathrm{TM_I}]} - E_{[\mathrm{Si},\, N-1;\, \mathrm{TM_S}]} - \frac{1}{N} E_{[\mathrm{Si},\, N]} \tag{1.7}$$

where TM stands for Transition Metal and the subscripts S and I indicate a substitutional or interstitial lattice sites. Such energy difference therefore reveals which of the two defects is energetically more favorable or stable regardless of the chemical environment.

So far we have considered the creation of defects for which the quantities p_v and n_v remain constant during the formation reaction. In other words, in equation 1.5 the created defect is imposed to be neutrally charged, without trapping/releasing free carriers from the crystal bands. It is however possible that a given defect is prominently found at a different electronic occupation, and so, the formation energy of *charged* centers becomes the key quantity to analyze the relative stability of a given center at different charge states. The reaction process for the charged vacancy is, for example,

$$\mathrm{Si}_{\,[\mathrm{bulk}]} \rightleftharpoons \mathrm{Si}^{\mathrm{V}^q}_{\,[\mathrm{bulk}]} + \mathrm{Si} - qe \tag{1.8}$$

where q symbolizes the charge of the defect or the number of electrons released by the center to the crystal. The notation d^q for charged defects is the one employed throughout the present manuscript. Since at equilibrium the electronic exchange is determined by the Fermi energy position, the energy of q electrons transferred to an electronic reservoir is given by $q\mu_e$,

$$E_f^{\mathrm{V}^q} = E^{\,q}_{[\mathrm{Si},\, N-1]} - \frac{N-1}{N} E_{[\mathrm{Si},\, N]} + q\mu_{\mathrm{e}} \tag{1.9}$$

The most thermodynamic stable charge state can therefore differ depending on the position of the Fermi energy, which is typically represented with respect the top of the valence band (TVB), $\mu_{\mathrm{e}} = \epsilon_{\mathrm{TVB}} + \mathcal{E}_{\mathrm{F}}$. In the case of extrinsinc semiconductors, for example, the center might be stable at positive charge state for a p-doped sample, whereas it is found in its negative charge state in the n-type doped semiconductor. Identifying the energetically most preferable charge state for a given center and $\mathcal{E}_{\mathrm{F}}$ is typically achieved by analyzing the so-called charge transition levels (CTLs), as described in the following.

1.1.5 The notion of charge transition levels

The charge transitions levels (CTLs) of a deep center delimit energy regions within the semiconductor band gap in which the defect is energetically more favorable in a certain charge state. The Fermi level for which the charge transition $(q/q \pm 1)$ occurs is therefore referred to as charge transition level and it is denoted as $\mathcal{E}(q/q \pm 1)$. In Figure 1.3a, the positions of the charge transition levels $\mathcal{E}^{+/0}$ and $\mathcal{E}^{0/-}$ corresponding to the hypothetical deep center in Figure 1.2 are represented with respect to the host band edges (top of the valence band, TVB, and bottom of conduction band, BCB). Such defect is therefore *stable* at three charge states (+1, 0, -1), with transitions occurring at different energy intervals through the band gap: $\epsilon_{\mathrm{TVB}} \rightarrow \mathcal{E}^{+/0}$, $\mathcal{E}^{+/0} \rightarrow \mathcal{E}^{0/-}$, $\mathcal{E}^{0/-} \rightarrow \epsilon_{\mathrm{BCB}}$ respectively. We remark that even if CTLs are commonly called *defect levels*, they correspond to transitions between different electronic occupations of the *defect-induced states*. If we reconsider the example given in Figure 1.2, the donor level $(0/+1)$ corresponds to a change in occupation of the *orbital* ψ_{d_1} from one to two electrons and *viceversa*, $\mathrm{d}_1^{\uparrow} \leftrightharpoons \mathrm{d}_1^{\uparrow\downarrow}$ (where charge neutrality was assumed for the configuration $\mathrm{d}_1^{\uparrow\downarrow}$). In other naive words, an optical absorption band can be identified with an electronic excitation involving two *defect-states* ($\mathrm{d}_1^{\uparrow} \rightarrow \mathrm{d}_2^{\uparrow}$ in the ongoing example), but never between two CTLs. For this reason, the charge transition levels are also named as *thermodynamic levels*, to differentiate them from the *optical levels*, equal to the absorbed or emitted photon energies [5].

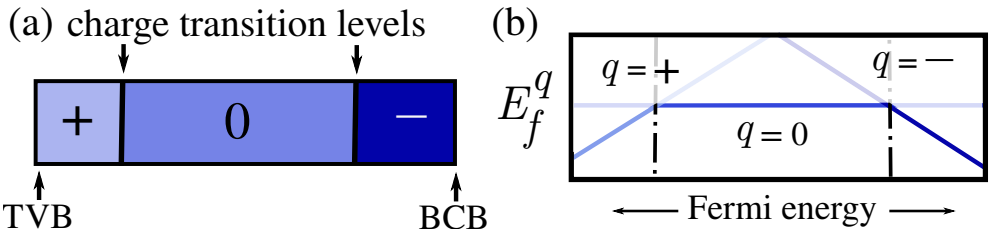

Figure 1.3: (a) Charge transition levels $\mathcal{E}^{+/0}$ and $\mathcal{E}^{0/-}$ with respect to the top of the valence band (TVB) and the bottom of conduction band (BCB) for a hypothetical deep center. (b) Stability diagram for the same center: formation energy for $q = 0, \pm 1$ versus the Fermi energy, $\mathcal{E}_{\mathrm{F}} \in [\epsilon_{\mathrm{TVB}}, \epsilon_{\mathrm{BCM}}]$.

In terms of the formation energy of charge defects (equation 1.9), the transition level $\mathcal{E}(q/q')$ is defined as the Fermi energy for which $E_f^q = E_f^{q'}$,

$$\mathcal{E}(q/q') = \frac{E^{\,q}_{[\mathrm{Si},\,d]} - E^{\,q'}_{[\mathrm{Si},\,d]}}{q' - q} \tag{1.10}$$

CTLs are often represented in stability diagrams, like the one in Figure 1.3b, since they represent the *thermodynamic* most stable charge state of the defect at a given Fermi energy. The ordinate axis corresponds to the formation energy at a given charge state and the abscissa, the Fermi energy varying from the top of the valence band and the bottom of conduction band, $\mathcal{E}_{\mathrm{F}} \in [\epsilon_{\mathrm{TVB}}, \epsilon_{\mathrm{BCM}}]$. The intersection of two curves, E_f^q and $E_f^{q'}$, represents the CTL corresponding to the transition $q \leftrightarrow q'$.

1.1.6 Finite-temperature defect dynamics

Besides altering the electronic properties of semiconductors, point-like imperfections are also responsible for matter-transport thorough the crystal at small length-scale (metastable-switching phenomena) and at larger length-scales, with the diffusion of dopants and metallic impurities, the clustering of native defects, etc. These mechanisms are only visible for certain temperature regimes since they are originated by the lattice dynamics or vibrations. In Figure 1.4, we have represented different defect lattice-related mechanisms within an energy surface corresponding to the formation free enthalpy for a given atomic configuration, involving the center (a silicon vacancy) and its first neighbors. As depicted, the minima of the energy surface (points designated by m_1, m_2 and m_3) correspond to local atomic rearrangements or elastic distortions in the surroundings of the center, induced by the form and orientation of the defect-related states. Such structural reorganization might be in the form of an isotropic expansion, or more complex symmetry-breaking mechanisms (like the two-against-two paired distortion represented for the vacancy in Figure 1.4). If a given center presents two or more structural patterns with different symmetry as global and local minima of the surface, it is said to be metastable. The mechanism for which the defect modifies its geometry between local/global minima (at constant lattice site) is referred to as the metastable-switching process. In the example given in Figure 1.4, the defect presents two equivalent minima due to the equivalent symmetry of both configurations m_2 and m_3, but different orientation in the lattice. The vacancy can therefore reorient through the transition $\mathrm{m}_2 \rightarrow \mathrm{m}_3$. If, on the other hand, the defect migrates to a different position in the lattice, the defect is diffusing through the crystal (process $\mathrm{m}_1 \rightarrow \mathrm{m}_2$). In the case of native defects, such as the mono-vacancy in the ongoing example, the diffusion mechanism (*e.g.* intermediate structural conformations between minima) is relatively easy to conceive. Vacancies and self-interstitials are however known for gathering in nearby lattice sites, constituting large clusters of defects. Metallic impurities might migrate from interstitial lattice sites to a substitutional position by a kick-out mechanism, creating one self-interstitial

in the process.

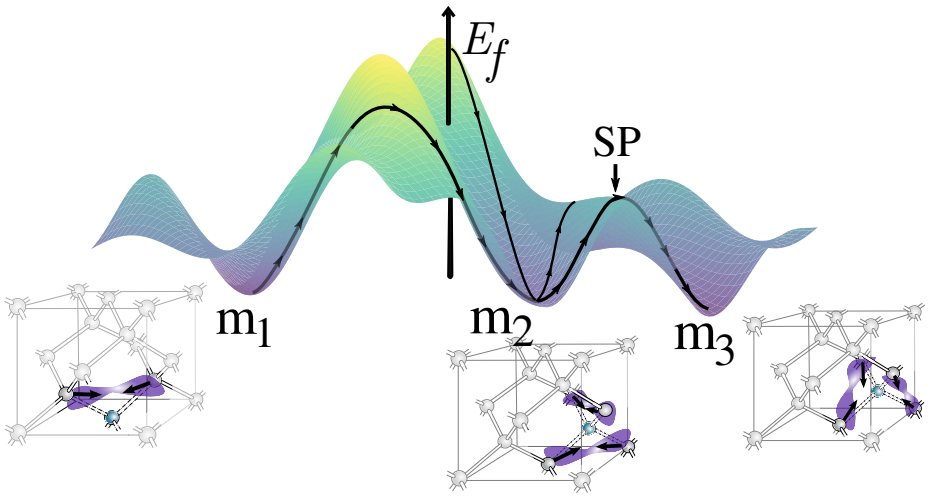

Figure 1.4: Schematic energy surface constructed by assigning a formation energy value to a certain atomic configuration of the mono-vacancy in silicon. The three minima of the surface, denoted as m_1, m_2 and m_3, are represented. Transition paths between different geometries are also depicted, only the one between m_2 and m_3 being a minimum energy path. The saddle point (SP) of the MEP is also marked. Electronic densities at different atomic configurations are represented in purple.

So far we have merely described the matter-transport mechanisms without determining the probability of each event to occur. Given I and F, two stable configurations of the energy surface, the simple transition-state theory establishes that the reaction I $\rightarrow$ F passes through an intermediate state, referred to as the transition state. Such transition state determines the reaction constant, R, since it allows to define the Gibbs activation energy, ΔG_{a}, as the energy required to go from the initial point I to the active-state,

$$\mathrm{R} \propto e^{-\Delta G_{\mathrm{a}} \,/\, k\mathrm{T}} \tag{1.11}$$

The description of ΔG_{a} in terms of the variation of enthalpy allows to disentangle a temperature-independent prefactor, from the Arrhenius law, $e^{-\Delta H_{\mathrm{a}} \,/\, k\mathrm{T}}$. As however commented above, within the employed theoretical models, the formation enthalpy is often substituted by the formation energy, E_f (Figure 1.4). In general terms, among all the existent transition paths between states I and F in the energy-configuration space, the saddle point of the Minimum Energy Path (MEP) corresponds to the active-state of the

reaction. In Figure 1.4, the active state or saddle point of the transitions $m_2 \rightarrow m_3$ is marked by SP, and so the MEP is represented. From the form of the energy surface, the activation energy for the second mechanism $m_1 \rightarrow m_2$ is larger than the former one, even if the depicted path does not correspond to the MEP. Comparing activation energies between different processes allows to have a first insight of the relative occurrence of each lattice-related mechanism at a given temperature. If however the estimated reaction constant wants to be compared to measured transition rates, the prefactor in equation 1.11, or more generally, the diffusion coefficient is to be determined.

1.2 The case of silicon

From an applied point of view, the idea of modifying the characteristic Fermi level of semiconductors by introducing shallow centers or dopants in the crystalline structure is at the fundamental basis of silicon-based technology. More specifically, these electronic devices are based on the well-known pn-junction, presented in section 1.2.1, constituted by the union of n-type doped silicon and p-type doped silicon. In the context of microelectronic technology, both donor and acceptor shallow centers are intentionally introduced in the crystal during the device manufacturing process. Deep centers, on the other hand, are typically undesirable side effects of the doping process that might strongly affect the performance of microelectronic devices. An overview of the most common defect-inducing processes in silicon diodes is presented in section 1.2.2, whose resulting damage constitutes a large catalog of imperfections in the diamond structure. A representative part of such catalog is introduced in section 1.2.3, where both shallow and deep centers, intrinsic versus extrinsic defects are classified.

1.2.1 Introduction to the pn-junction

This section aims to give a few basic ideas behind the operation of the junction so that the fundamentals behind the experimental technique Deep Level Transient Spectroscopy (DLTS) are later more easily introduced. The pn-junction is built by the union of n-type doped silicon, for which a certain concentration of shallow donor impurities has been introduced in the crystal, and p-type doped silicon, with a given concentration of shallow acceptor centers. As has been previously discussed, shallow defects modify the Fermi level of the semiconductor, being close to the conduction band in the case of n-type silicon, and around the valence band for the p-type silicon. Free

electrons are therefore thermally generated for n-doped silicon, while an increment of the hole concentration can be expected for p-doped silicon. When both types of doped silicon are joined, a free carrier concentration as the one showed in Figure 1.5A is then to be expected. Within the proximity of the junction interface, bound electrons might *leave* their respective donor impurity and be trapped by the acceptor levels. The result of this electronic exchange is a *charge space region*, characterized by positively charged donors and negatively charged acceptors (*i.e.* P^+ and B^-, in the case of phosphours and boron doped silicon). The confronted opposite charged regions (blue *vs.* green regions in Figure 1.5B) induce an electric field which acts against the charge exchange between impurities, defining the charge space region. The width of the charge space region (denote by W in Figure 1.5) is therefore balanced by the *drift* of electrons, $P + B \rightarrow P^+ + B^-$, and the induced electric field, $\vec{E}$, opposite to the drift. We note that within the region where shallow impurities are charged, there is no mobile carrier concentration, and so such region is also known as *depletion region*. Profiles of charge distribution and the absolute electric field along the junction, and especially thorough the depletion region are shown in Figure 1.5B. Finally, the potential difference across the junction or the energy needed for free carriers to go from one doped side to the other is represented in Figure 1.5C as eV_0.

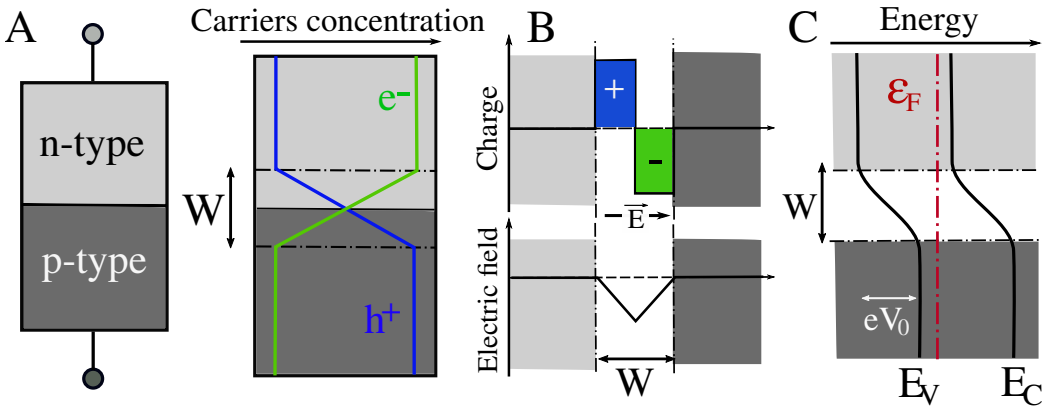

Figure 1.5: The pn-junction and the free carriers concentration along the union (A); the charge distribution and the induced electric field, **E**, are represented in (B); and the band diagram is drawn in (C), where the position of the Fermi energy is indicated, $\mathcal{E}_F$. The so-called depletion region or charge space region (W) is also shown.

To conclude, if an external potential is applied to the equilibrium junction, two operating regimes of the diode can be distinguished: the forward

bias and the reverse bias regimes. In the case of the forward bias regime, the n-side and the p-side of the junction are respectively connected to the anode and cathode of the external battery. Free carrier on each side are therefore repelled towards the junction interface, narrowing the depletion region. For a certain applied potential, the depletion region narrows sufficiently so free carriers can cross the junction, and a current can be measured in the circuit. If, on the contrary, the cathode and anode connections to the junction are inverted, the depletion region is expanded, leading to a high resistivity to the flow of current (reverse bias regime).

1.2.2 Defect-inducing processes

Within the vast catalog of silicon-based devices, let us give the example of the image sensors based on the Complementary Metal Oxide Semiconductor (CMOS) photodiodes, for which the photon absorption mechanism occurs in the depletion region of the junction (Figure 1.6a). After growing the silicon wafer, the first step in the fabrication process of any device is to introduce the shallow impurities in the perfect crystal. Among the most common *doping* techniques, we cite the *diffusion* of the dopants into the semiconductors by putting it in contact with a gas containing the desired impurities; and the *ion implantation process* to accurately target positions of the doped region. During the ion implantation process, silicon is bombarded by III- and V-elements ions at low temperature. The crystal structure is often damaged since the incident ion triggers the so-called *energetic collision cascades* or *displacement cascades*. These cascades can be defined as consecutive collisions of atoms, leading to their displacement from their original lattice positions, creating traces of vacancies and self-interstitials, amorphizing the material. In Figure 1.6b the displacement cascade of an energetic ion accelerated into silicon is shown. A second process, known as the *dopant activation* mechanism, is then started by heating the sample, allowing vacancies and interstitials to become mobile, finding and annealing each other, recrystallizing the material. Once the underlying pn-junction of the photodiode is constituted, the passivation of the silicon surface is often achieved by *thermal oxidation*, creating an insulating SiO_2 layer (Figure 1.6a), allowing the electronic current to flow through the device overcoming surface states. Finally, the realization of an integrated circuit is possible if electronic devices can be interconnected through the metallic electrodes. This last process is typically referred to as *metallization* of the silicon substrate, since the metal-semiconductor junction is manufactured. To conclude, during the described manufacturing process, other impurities besides the implanted ions might be *accidentally*

introduced in the material; it is the case of hydrogen-rich environment, oxidation of surfaces or even the presence of small metallic particles coming from the degradation of the chamber components. Purification techniques and recrystallization of the semiconductor are often not sufficient to ensure optimal samples, thus motivating the study and characterization of deep centers as a fundamental step for defining mitigation strategies.

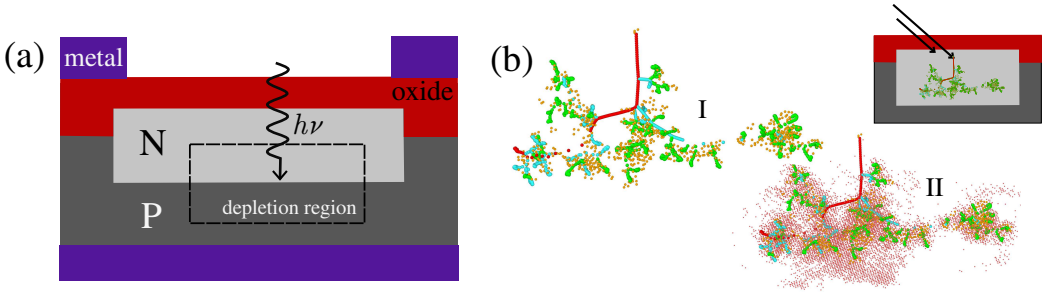

Figure 1.6: CMOS conventional photodiode (a) and the displacement damage due to incident energetic particles into the silicon wafer (b). Displacement cascades I and II show the trace of the *Primary Knock-On atom* (PKA) in red, and the ones corresponding to the *Secondary Knock-On atoms* (SKA) in blue. Atoms kicked by the SKAs are also shown in green, whereas the resulting interstitials are represented in orange. The *thermal wave* in cascade II is constituted by atoms kicked out from their original positions, rapidly taking back their corresponding lattice sites. Simulated cascades are courtesy of T. Jarrin.

Besides the manufacturing-induced damage, electronic devices might be subject to highly energetic irradiation if, for example, they are used in extreme conditions, such as aerospace applications. Environmental incident energetic particles generate a displacement damage similar to the one described in the manufacturing process, characterized by displacement cascades as the one shown in Figure 1.6b. In this context, silicon doped wafers subjected to incident energetic particles, like electrons, protons or neutrons are referred to as *irradiated* silicon in the present manuscript. According to the size of the incident particle, different displacement effects can be expected. Protons and neutrons are known to generate *clusters of defects*, whereas point-like defects are mostly found in electron-damaged silicon. Experimental measures to characterize point defects in silicon are therefore often performed on electron-irradiated doped silicon (section 1.3).

1.2.3 A catalog of common defects

As a result of the above described defect-inducing processes, a large catalog of point defects can be commonly encountered in silicon-based devices. Among such variety, a relatively small, but representative, selection of defects in crystalline silicon is represented in Figure 1.7. Within the given catalog, native defects such as monovacancies (Fig.1.7 a) and self-interstitals (Fig.1.7 b) are small imperfections of the lattice, capable of easily diffusing through the bulk, often finding another point defect to form a bigger complex. The vacancy-self-interstitial pair, for example, known as the Frenkel pair, is a common defect in all types of semiconductors. In irradiated silicon, small clusters or aggregation of intrinsic defects have been observed, such as, for example, the silicon divacancy (Fig.1.7 c), constituted by two adjacent vacancies. The subset of defects involving small elements like H, C and O are present in a large variety of forms, from being isolated impurities to complex stoichiometric compounds: O_i, VO (the vacancy-oxygen complex or the A-center, Fig.1.7 d), VOH, V_2O, C_i, C_sC_i, C_iO_i, etc; where the subscripts s and i stand for substitutional and interstitial positions respectively. As mentioned above, to increase the number of free carriers in the semiconductor, impurity dopants are intentionally implanted in the bulk; in n-type doped silicon, phosphorus, arsenic and antimony atoms can therefore be found at substitutional positions (Fig.1.7 e). Even if such donor elements introduce *harmless* shallow levels in the band gap, their interaction with other intrinsic defects modifies the nature of the defect states, becoming deep centers. This is the case of the silicon E-center, constituted by a vacancy trapped next to a donor element (Fig.1.7 f). During the mentioned manufacturing process, certain unwanted metallic contamination might occur. Transitions metals might therefore be present in both substitutional and/or interstitial positions of the lattice (Fig.1.7 g-h).

From the above given catalog, only the (e) centers, elements from the V-column of the periodic table, introduce shallow states in the silicon band gap. The rest of the pictured defects are *deep* centers, most of them acting both as donors and acceptors of carriers upon the position of the Fermi energy (or the concentration of free carriers). The A-center (d) is known to only capture electrons, being exclusively an acceptor center. Interstitial Ti gives up to two electrons, receiving the name of a *double donor*, in p-type doped silicon, and it traps one electron in n-type doped silicon, acting as a *single acceptor*. Substitutional Ti, on the contrary, does not capture or release electrons, since it is not *electronically active*. As stated before, there is no simple model capable of predicting the charge states of a deep center at different

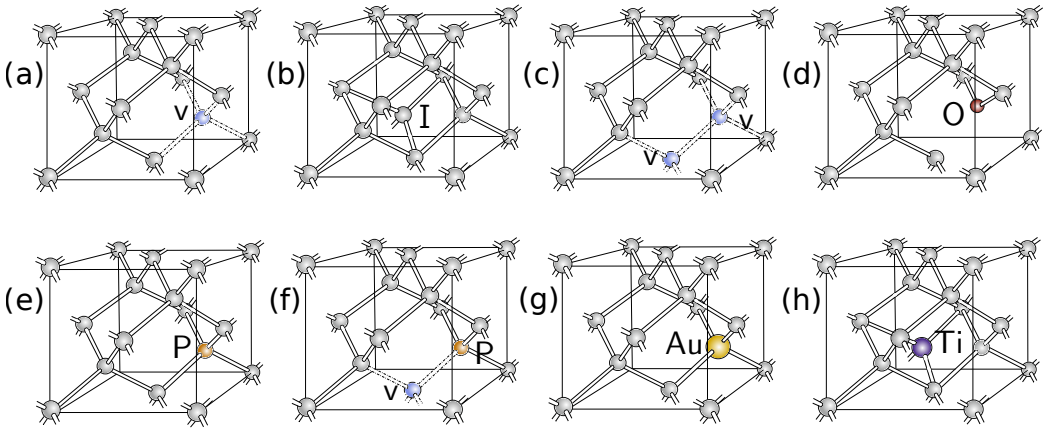

Figure 1.7: Non-exhaustive catalog of point defects in silicon: the monovacancy (a), the self-interstitial (b), the divacancy (c), the A-center (d), the V-element dopant impurity (e), the E-center (f) and the substituional (g) and the interstitial (h) metallic impurities. In structures (a), (c) and (f), vacancies, v, are represented as light blue missing atoms; whereas the absent silicon is not explicitly depicted for the oxygen-vacancy complex (d).

$\mathcal{E}_{\mathrm{F}}$, or whether it acts as a donor or as an acceptor center. The DLTS experimental technique, described in section 1.3.3, and the theoretical formulation of the CTLs, section 1.1.5, represent the effort made by the community to characterize the electronic activity of deep centers in semiconductors.

1.3 Characterization techniques

Since silicon is the most used semiconductor in the microelectronic industry, point defects in silicon have been extensively characterized both experimentally and theoretically. The physical fundamentals of the most common experimental techniques, Optical Absorption, Luminescence, and Photoconductivity, the Electronic Paramagnetic Resonance (EPR), and Deep Level Transient Spectroscopy (DLTS), are reviewed in this section, as well as some of the most relevant references in silicon. As it will be evident shortly, these techniques *complement* each other, since they respectively provide information regarding light-induced electronic transitions within the center, the local defect geometry, and the electronic activity of deep centers.

1.3.1 Optical Absorption, Luminescence and Photoconductivity

Optical absorption is probably the most ancient technique employed to characterize defects in solids, since in the thirties R. W. Pohl named as *Farbzentren* the F-centers in alkali halide solids [6]. The absorption of visible light by electrons localized within the anion vacant site in the ionic lattice were said to be responsible for the color of the samples containing crystallographic defects, being transparent for an otherwise *perfect* solid. In the context of point defects in semiconductors (Figure 1.8A), one or several trap-induced states are introduced in the band gap, allowing electronic excitations (triggered by light absorption) or deexcitations (e.g. spontaneous emission of photons or luminescence) within the forbidden gap. The absorption of light might lead to a measurable *photocurrent* if the electronic transition involves a localized defect state and one of the host bands. Optical absorption and photoconductivity measures are therefore of great interest to characterize optical and electronic properties of point defects embedded in a semiconductor.

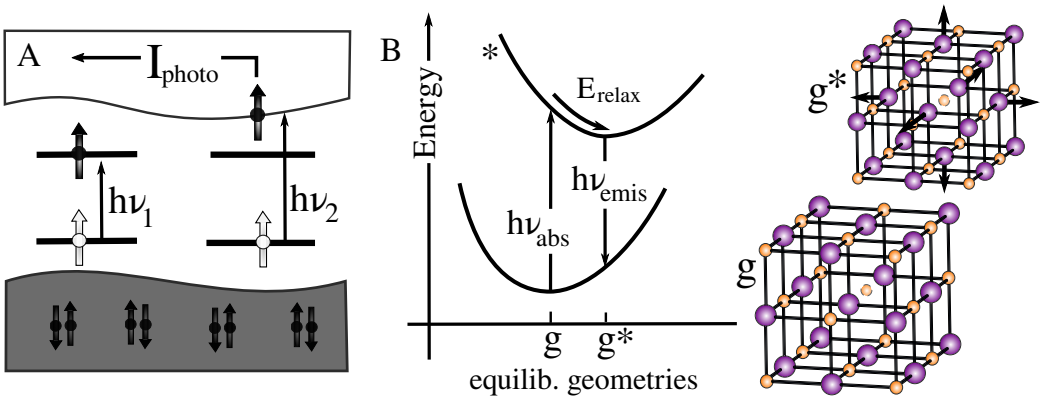

Figure 1.8: (A) Photon absorptions, $h\nu_1$ and $h\nu_2$, and photoconductivity in semiconductors. (B) Coordination diagram of the photon absorption and emission cycle for an electron trapped in the anion vacant side of an alkali halide solid. Equilibrium geometries corresponding to the ground state (prior to light absorption, $h\nu_{\text{abs}}$), g; and to the excited state after lattice relaxation (prior to photon emission, $h\nu_{\text{emis}}$), g* are also shown.

One of the main conclusions extracted from the pioneer work of R. W. Pohl is that point defects might trigger a local rearrangement of nearby atoms after the electronic occupation of its localized states is modified. In other words, the equilibrium geometry of the defect might differ between its

ground state (prior to light absorption) and its excited state (once the exciton or electron-hole pair is created). Evidence of this atomic rearrangement was the measure of two different photon frequencies in the absorption and the emission spectra, $h\nu_{\text{abs}} \neq h\nu_{\text{emis}}$. The energy loss was said to be given to the lattice, stored as a local atomic rearrangement or lattice relaxation, E_{relax}. The energy exchange during the cycle of photon absorption and emission is represented in the so-called coordination diagram (Figure 1.8B). Coordination diagrams are widely used to discuss defect-related processes in solids [7] and they will be reviewed in detail in Chapter 5. Recovering the interest of the present section, we emphasize the experimental evidence that point defects with different electronic occupations might induce different local atomic geometries (equilibrium geometries g and g^* in Figure 1.8). In the case of silicon, characterized by an indirect optical band gap equal 1.1 eV, the characterization of the photon absorption and emission cycle by point defects is very limited. However, by using complementary experimental techniques (like the EPR spectroscopy) the equilibrium geometry of point defects in silicon at different charge states might be determined. A second conclusion naturally raised by the coordination diagram in Figure 1.8B is that in the limit case of $\text{T} \rightarrow 0$ one can in principle assume that the number of absorbed and emitted photons is equal. In the however common finite temperature conditions, far from the limit case, the phenomenon known as *quenched* luminescence typically occurs. In other words, different deexcitation processes besides the one of spontaneous emission compete, being ranked by their respective capture cross sections. In this context, we cite the pioneer work of Huang and Rhys [8] on the evaluation of capture cross section of luminescense versus thermal deexcitations, referred to as non-radiative transitions.

Infrared-absorption in silicon

We now introduce some optical measures performed in irradiated silicon. Even if such experimental evidence was collected over a few decades ago, certain absorption bands have not yet been assigned to a particular defect or, when they have, to a specific electronic transition within the defect electronic configuration. There is therefore an actual need and/or motivation to theoretically investigate the point-defect band structure, estimating the electronic excitations, predicting the optical signature of centers. Early work on infrared absorption and photoconductivity in silicon was collected in [9]; they reported up to eight bands at wavelenghts 1.8, 3.3, 3.9, 5.5, 6.0, 20.5, 27.0 and 30.1 μ (microns). Even if complementary information regarding the electronic transitions was reported, such as measurable photocurrent, none of the bands were assigned to a particular defect. Later EPR and infrared

absorption joined studies [10, 11] succeded in assigning the 12 μ band to the silicon A-center, motivating the work on infrared absorption in silicon. A great effort was later made by Watkins and Corbett [12] to unequivocally assign the 1.8, 3.3 and 3.9 μ bands to a single defect: the silicon divacancy. We note that even if the defect was identified, the assignment of each band to a specific electronic transition for a certain charge state remains uncertain. Figure 1.9 represents an optical signature of irradiated n-type and p-type silicon and their yet unassigned charged centers. Covering the vast literature of optical characterization of silicon defects is beyond the scope of the present work; relatively recent collections of optical-related measures can be found in [13, 4].

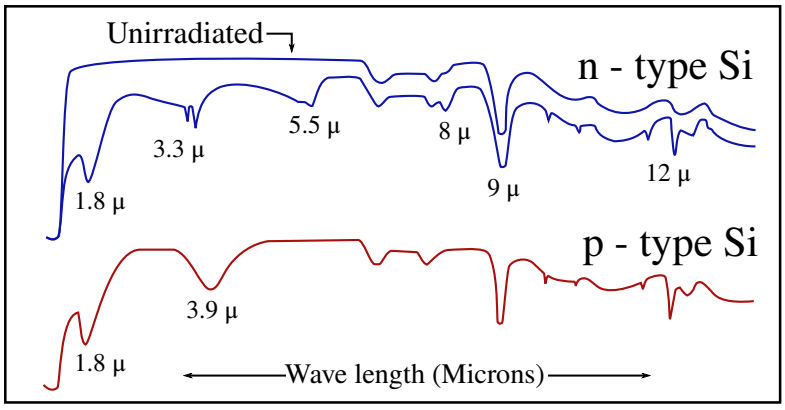

Figure 1.9: Schematic diagram of radiation-induced defect infrared absorption bands in both n- and p-type silicon in the wavelenght region 1-13 μ, based on [12].

1.3.2 Electronic Paramagnetic Resonance (EPR)

The present section is dedicated to review the fundamental physical concepts behind the Electronic Paramagnetic Resonance (EPR) technique. The reader should expect a short introduction to the topic, with emphasis on characterizing point defects in semiconductors; for a more advance reading, we recommend [14]. EPR spectroscopy is a powerful technique which targets paramagnetic centers (or point defects with an unpaired electron) in a perfect diamagnetic crystal. It reveals information about the local environment of such unpaired localized electron, by analyzing the *relativistic interaction* between the unpaired electron, an external applied magnetic field and the surrounding nuclei.

As in any confined system, paramagnetism arises from the magnetic dipole moment, μ, induced by the electronic *total* angular momentum, $\mathbf{J}$. Besides its intrinsic angular momentum or Spin, $\mathbf{S}$, a bound electron presents the so-called *orbital* momentum associated to its interaction with a central potential, $\mathbf{L}$, giving $\mathbf{J} = \mathbf{S} + \mathbf{L}$. Now, for simplicity and in order to focus on the fundamental magnetic interaction, we consider the case of a free electron, with $\mathbf{L} = 0$. The magnetic dipole moment can then be written as,

$$\mu_{\mathbf{S}} = -\mathrm{g}\beta\mathbf{S}. \tag{1.12}$$

Where β is the Bohr magneton and g is the Landé factor (being g = 2.0023 for a free electron). If the system is perturbed by an external magnetic field along the z-axis, $\mathbf{H}$, an energy shift of the electronic states in the form of the Zeeman Hamiltonian is expected,

$$\mathcal{H}_{\mathrm{Z}} = -\mu_{\mathbf{S}} \cdot \mathbf{H} = \mathrm{g}\beta\mathrm{H}\mathrm{S}_z, \tag{1.13}$$

where the projected spin values, S_z, are given by the Pauli matrix operator $\mathrm{S}_z = \frac{\hbar}{2}\sigma_z$, with eigenvectors $|\mathrm{S}_z, \mathrm{M}\rangle$ and eigenvalues $\mathrm{M} = \pm\frac{1}{2}$. The perturbative Hamiltonain in equation 1.13 therefore gives a total energy splitting equal gβH (Figure 1.10A). The energy splitting due to unpaired electrons subject to a static magnetic field can then be measured by photon absorption if $\mathrm{h}\nu = \mathrm{g}\beta\mathrm{H}$. In a more realistic picture, the orbital angular momentum is not quenched, $\langle\mathbf{L}\rangle \neq 0$, and the total momentum J_z has $2\mathrm{J}_z + 1$ eigenstates, $|\mathrm{J}_z, \mathrm{M}\rangle$. Similarly to the previous example, the applied magnetic field breaks the degeneracy of the angular momentum eigenstates by shifting their energy levels by gβHM respectively. For a J_z relatively large, the multiplicity of the levels in principle allows multiple optical transitions to occur ($|\mathrm{J}_z, \mathrm{M} = -\mathrm{J}_z\rangle \rightarrow |\mathrm{J}_z, \mathrm{M} = -\mathrm{J}_z + 1\rangle$, ... $|\mathrm{J}_z, \mathrm{M} = -\mathrm{J}_z\rangle \rightarrow |\mathrm{J}_z, \mathrm{M} = \mathrm{J}_z\rangle$). However, if we impose the conservation of the total angular momentum, only transitions with $\Delta\mathrm{M} = \pm 1$ can actually be observed, characterized by a photon frequency equal gβH. The *resonant condition* or the photon frequency for which an EPR peak will be observed is therefore $\mathrm{h}\nu_0 = \mathrm{g}\beta\mathrm{H}$, independently of J_z. The EPR spectra can be generated by varying the microwave frequency of the incident photon, keeping the applied magnetic field constant or *viceversa*.

For an even more realistic model, the inclusion of hyperfine terms arising from a nearby nucleus should be included in equation 1.13. In other words, the resonant condition or energy shifts might be modified by the presence of a nucleus with a non-zero nuclear magnetic moment dipole, $\mu_{\mathbf{I}} = \mathrm{g}_n\beta_n\mathbf{I}$ (Figure 1.10B). Similarly to the electronic angular momentum, the nuclear spin

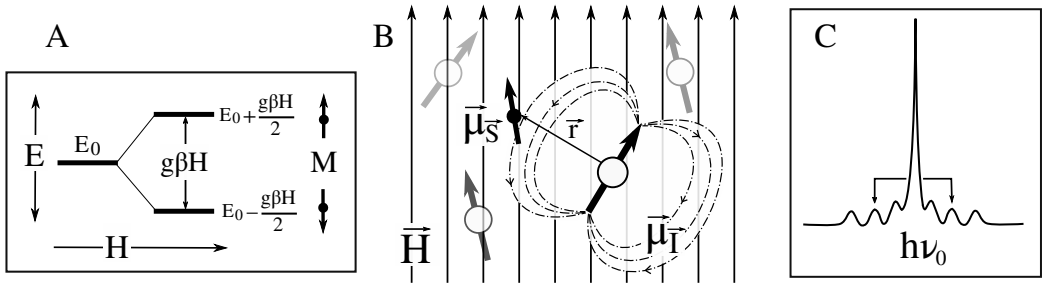

Figure 1.10: (A) Energy splitting for a $\mathbf{J} = \frac{1}{2}$ system due to the external field H_z. (B) Electronic and nuclear magnetic dipoles, $\mu_{\mathbf{S}}$ and $\mu_{\mathbf{I}}$, subject to an applied magnetic field, $\mathbf{H}$. (C) Schematic EPR spectra for interstitial Al^{+2} in silicon after [14].

projected along the z-axis, I_z, presents $2I_z + 1$ degenerate eigenstates, $|I_z, m\rangle$. The interaction of such nuclear magnetic dipole with an applied magnetic field is at the base of the Nuclear Magnetic Resonance spectroscopy, which reveals information regarding the energy shifts for a given momentum eigenvalue, m. In the case of EPR spectroscopy, the interest is to determine how the electronic and nuclear magnetic dipole interaction shifts the unperturbed electronic states or the resonant frequencies, $h\nu_0$. The effective magnetic field *seen* by the unpaired electron depends on the distance between dipoles and the relative orientation of the nuclear spin (Figure 1.10B). In its more general form, the energy correction can be written in terms of the *hyperfine tensor* [14], $\mathcal{H}_I = \mathbf{A} \cdot \mathbf{I}/g\beta$, giving new resonant frequencies at,

$$h\nu_0 \simeq g\beta \left(H + \frac{Am}{g\beta} \right). \tag{1.14}$$

We note the presence of the nuclear magnetic eigenvalue in the above resonant condition, indicating that for each azimuth-projected quanta an EPR peak is observed. In the case of irradiated silicon, the EPR spectrum of interstitial Al at charge state +2 reveals several *satellites* arising from the hyperfine interaction with nearby Si nucleus (Figure 1.10C). These weak signals are typically assigned to the interaction with non-equivalent silicon neighbors sites. We also remark the equivalent peaks due to opposite projections of the nuclear spin, $\pm m$ (marked with arrows in Figure 1.10C).

To this moment, we have merely considered the simplest case of a free electron subject to an applied magnetic field and one nuclear magnetic dipole. If we now considered a localized unpaired electron within a crystal, interactions with several nearby nuclei can be expected, with corresponding nuclear

spins $\mathbf{I}_j$, and whose interactions with the electronic dipole are described by the hyperfine tensors $\mathbf{A}_j$. We also note that the orbital angular momentum contribution to the electronic magnetic dipole might be introduced by the so-called g-tensor, $\mathbf{g}$. In a few words, the g-tensor, typically expressed as $\mathbf{g} = \mathrm{g}_0\mathbf{1} + \Delta\mathbf{g}$ (being $\mathrm{g}_0 = 2.0023$), *measures* the angular momentum deviation of the *real* unpaired electron in the crystal from a free electron. The isotropic or anisotropic contribution $\Delta\mathbf{g}$ therefore reveals information regarding the form and extension of the defect induced state, giving an idea of the defect local environment or the defect local symmetry. EPR spectroscopy is capable of measuring the magnitude of $\Delta\mathbf{g}$ through the interaction of the *effective* electronic magnetic dipole, defined as $\mu_{\mathrm{effec}} = \beta\mathbf{S}\cdot\mathbf{g}$, with the applied magnetic field,

$$\mathcal{H}_{\mathrm{Z}} = \beta\mathbf{S}\cdot\mathbf{g}\cdot\mathbf{H} + \sum_j \mathbf{S}\cdot\mathbf{A}_j\cdot\mathbf{I}_j. \tag{1.15}$$

To conclude, the main axis and eigenvalues of the g-tensor enclose information regarding the form, location and environment of the defect electronic state responsible for the paramagnetism.

EPR spectra of silicon

Since the present manuscript is not conceived as a *complete* review of EPR spectroscopy in silicon, only the work of G. D. Watkins & J. W. Corbett on point defects in irradiated silicon [15, 10, 11, 16, 17, 18, 19] is here introduced. Watkins and Corbett performed an extensive analysis of point defects created in silicon upon irradiation. In particular, they used an electronic beam as incident energetic particles, since they create *simpler damage* with respect to protons or neutrons, allowing the investigation of primary defects (isolated vacancies, interstitials, etc.). Examples of these primary defects in n-type silicon are, for example, the silicon monovacancy, the A-center, the divacancy, the E-center (a-d,f in Figure 1.7). The main axis and main values of the g-tensor for the A-center (vacancy-oxygen complex in Figure 1.11A) were determined to be [10],

$$\mathrm{g}_1\,[0\bar{1}1] = 2.0093, \quad \mathrm{g}_2\,[011] = 2.0025, \quad \mathrm{g}_3\,[\bar{1}00] = 2.0031. \tag{1.16}$$

The tensor axis, given in the form of axis of the crystal, reveals the relative orientation of the defects, whereas the main values show the anisotropy of such directions. As shown in Figure 1.11, the unpaired electron for the negatively charged center was deduced to be located within an *extended orbital* between silicon atoms 1 and 2. Auxiliary techniques to the EPR spectroscopy were typically used to supplement the study of deep centers. It is the case

of the optical illumination *in situ* and uniaxial stress application. Optical illumination of defects with frequencies larger than the silicon band gap allows the exchange of free carriers between valence and conduction bands. If the original diamagnetic center captures or releases an electron, EPR signals corresponding to its paramagnetic charge states will appear. It is the case, for example, of the diamagnetic A-center at neutral charge state. Defects presenting multiple equivalent orientations in the lattice are equally probable, given equivalent EPR signals. Continuing with the A-center example, we note that it presents up to six equivalent orientations, depending on the position of the interstitial oxygen and therefore of the extended orbital. Such equivalency can be broken by applying an unixial stress, forcing the defect to have a preferred relative orientation. The dynamics of the center can be studied by measuring the recovery or relaxation time to populate again all possible configurations. The applications of these techniques to irradiated silicon is discussed in detail in Chapters 4 and 5 for the E-center and the divacancy.

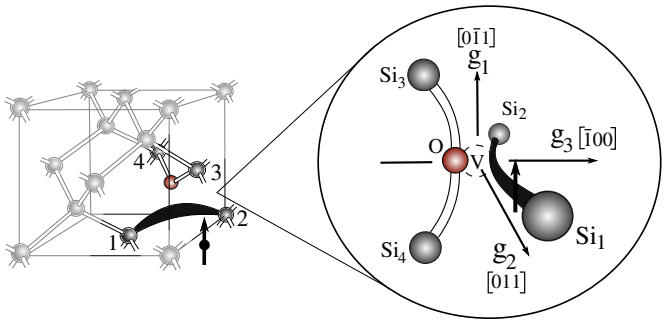

Figure 1.11: The main axis of the g-tensor for the silicon A-center or the vacancy-oxygen complex after [10]. The extended defect orbital is represented in black.

1.3.3 Deep Level Transient Spectroscopy (DLTS)

The Deep Level Transient Spectroscopy (DLTS) technique to characterize deep levels in semiconductors was first proposed by D. V. Lang in 1974 [20]. In a few words, DLTS allows to estimate the relative position of a *trap level* with respect to the bulk bands, by monitoring its capacity for emitting electrons at a given temperature. DLTS therefore aims at a full characterization of the electronic activity of a given center by measuring the activation energy required for a trap to release an electron (equivalent to the binding energy of

the extra electron to a shallow donor impurity) and the probability of such thermal process to occur.

Before describing how a DLTS measurement is performed, let us quickly review the pioneer work of Shockley and Read from 1952 regarding the *statistics of the recombinations of holes and electrons* in a semiconductor, for which the recombination process occurs thourgh a trapping mechanism [21]. According to such early work, four *trapping mechanisms* should be distinguished: electron capture (I), electron emission (II), hole capture (III) and hole emission (IV); such processes I-IV induced by the defect, T, are represented in Figure 1.12A. Within the principle of detailed balance, the capture and emission rates of free carriers by the trap were estimated, by establishing that at thermal equilibrium the same number of carriers were emitted and captured by the defect. If n_{T} denotes the density of electrons in the trap and N_t the concentration of traps in the semiconductor, the electronic emission and capture rates, e_n and c_n, can be balanced as,

$$\mathrm{e}_n n_{\mathrm{T}} = \mathrm{c}_n (N_{\mathrm{T}} - n_{\mathrm{T}}) \tag{1.17}$$

The capture rate of an electron in conduction by a trap, was written as $\mathrm{c}_n = \sigma_n \langle v_n \rangle n$, being σ_n the so-said *intrinsic* capture cross section of the defect, n the concentration of free electrons and $\langle v_n \rangle$ the thermal velocity of electrons. The probability of the trap being occupied, $f = n_{\mathrm{T}}/N_{\mathrm{T}}$ was determined by imposing the Fermi-Dirac distribution, $f = \left[1 + e^{(\mathrm{E_T} - \mathcal{E}_{\mathrm{F}})\,\beta}\right]^{-1}$. The emission rate from equation 1.17 was then written as,

$$\mathrm{e}_n = \sigma_n \langle v_n \rangle N_{\mathrm{c}}\, e^{-(\mathrm{E_C} - \mathrm{E_T})\,\beta} \tag{1.18}$$

where N_{c} was defined as the effective density of levels for conduction band, with energy $\mathrm{E_C}$. The importance of reviewing this model in the context of DLTS is that these equations served as guidance in the post-processing of the output signal. As a first idea, the *activation energy*, $\mathrm{E_C} - \mathrm{E_T}$ in Figure 1.12A, and the capture cross section of the trap, σ_n, are the quantities aimed *to be determined* by DLTS.

The experimental set up of DLTS is based on the fundamental operation of the pn-junction (section 1.2.1), since it monitors the release of carriers from trap levels located within its depletion region, by measuring the variation of the so-called pn-junction capacitance at a given temperature (Figure 1.12B). Acknowledging the definition of the charge space region for a pn-junction under reverse bias, the reader might agree that a depletion capacitance might be naturally defined as a function of the total charged ions

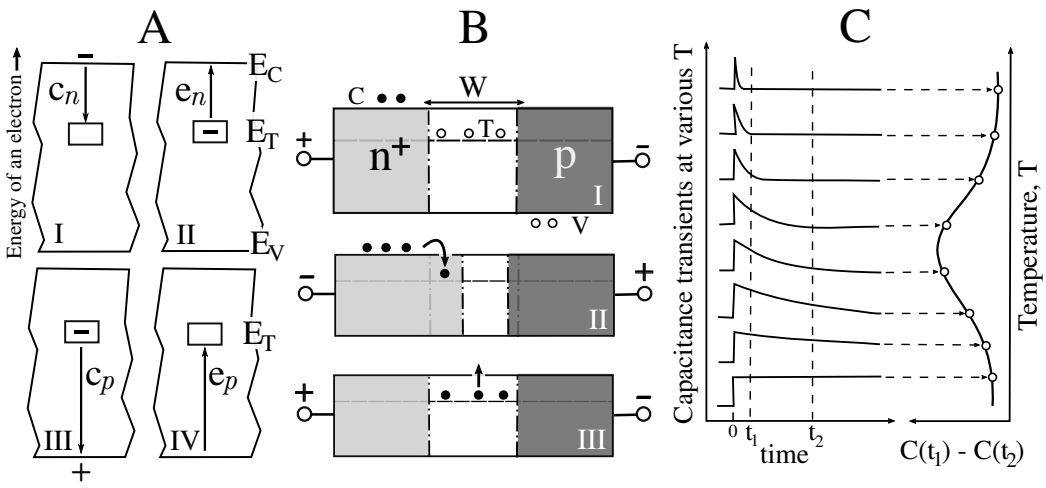

Figure 1.12: (A) Shockley and Read theory of recombination of electrons and holes in a semiconductor through trapping mechanisms, I-IV, based on [21]. (B) Fundamental operation behind a DLTS measure, from [20]. The pn-junction at reverse bias with no trapped electrons (I), the *filling pulse* at forward bias (II), and the emission of trapped electrons at reverse bias (III). (C) A DLTS characteristic peak, S(T), defined as the depletion capacitance transient in the time interval, $t \in [t_1, t_2]$, at various temperatures.

within W might be naturally defined. If however, traps in the depletion region are to be charged/discharged (to capture/release electrons from the host bands), they can also contribute to modify such capacitance. In order to measure the capacitance transient in the junction due to the presence of traps, the occupation of such levels needs to be ensured. The filling of the traps is achieved by applying an *injection pulse* to the junction or switching from reverse bias to forward bias regimes. As shown in Figure 1.12B, during the injecting pulse the depletion region is compressed, allowing free carriers to be captured by defects. Once the junction is again at reverse bias, traps start to emit carriers to bulk bands. Since the re-emission of carriers modifies the charge in the depletion region, the capacitance changes accordingly. One DLTS signal (Figure 1.12C) is *constructed* by several consecutive injection pulses at different temperatures. The capacitance variation or *transient*, C(t_1) - C(t_2), at different temperatures for a given time interval, $t \in [t_1, t_2]$, constitutes the DLTS peak. Now, before concluding with the experimental procedure, we remark that the pn-junction in Figure 1.12B actually corresponds to a pn^+-junction; *i.e.* the n-side of the junction presents a heavier impurity doping level than the p-side, presenting a majority carrier concentration of electrons. The injection pulse would therefore mainly inject electrons,

almost exclusively filling traps located in the upper side of the band gap. Similarly, measures performed on a p^+n-junction reveal information about traps located within the lower side of the gap, electrons being the minority carrier concentration.

A DLTS peak, like the one showed in Figure 1.12C, already gives an idea of the temperature regime for which a given defect is electronically active; *i.e.* the regime for which the center is most probably going to emit its trapped electrons. Ultimately, the question to be addressed now is how the capacitance transient can be related to the emission rate of the defect. After a few manipulations of equations given the dependency of the capacitance transient, $\Delta C = C(t_1)$ - $C(t_2)$, upon the depletion region width, W, the trap and donor concentrations and the saturated capacitance, the normalized DLTS signal, S, was related to the emission rate as [20],

$$S(T) = \frac{C(t_1) - C(t_2)}{\Delta C\,(0)} = \exp\left(-e_n(T)\,\Delta t\right), \tag{1.19}$$

where $\Delta C\,(0)$ is the capacitance change due to the pulse at $t = 0$ and $\Delta t = t_2 - t_1$. Even beyond this first exponential dependency, D. V. Lang *approximated* the thermal velocity as the mean square speed of the Maxwell-Boltzman distribution, $v_n = (3kT/m^*)^{1/2}$, and the density of states in conduction as the one of a non-degenerate semiconductor, $N_c = \frac{1}{4}(2m^*kT/h^2)^{3/2}$, showing from equation 1.18 the follow tendency,

$$e_n(T) = \gamma T^2 \sigma_n \exp\left(-\frac{E_C - E_T}{kT}\right), \tag{1.20}$$

where γ includes all the non-temperature dependent factors, included in the definition of v_n, N_c. A linear dependence can therefore be expected from the natural logarithm of the above expression, $\ln\left(e_n/T^2\right) \sim -E_a/kT$, where the plotted slope corresponds to the trap energy level with respect to conduction, $E_a = E_C - E_T$ (*i.e. an Arrhenius plot*). One year after the technique was proposed, deviations from the expected linear dependence were reported [22] and said to be caused by a lattice relaxation mechanism triggered by the electronic emission. C. H. Henry and D. V. Lang then proposed their *nonradiative carriers capture and emission by multiphonon emission* theory [23], approximating the capture cross section as,

$$\sigma_n = \sigma_\infty \exp\left(-\frac{E_\infty}{kT}\right), \tag{1.21}$$

by equivalency with the capture cross section of spontaneous emission or luminescence. More details regarding the above approximation are given in

Chapter 5, where these multiphonon theories are carefully reviewed. From an applied point of view (to which this experimental section is dedicated), the DLTS technique allows to measure the activation energy, defined as $E_a + E_\infty$, required by the trap to emit an electron and the capture cross section, σ_∞, of such process. Now, in order to give a practical idea of how these magnitudes can be exploited to give meaningful information about deep centers, we introduce the measured DLTS activation energies and capture cross sections of interstitial titanium in silicon.

Spectroscopy of deep levels in silicon

Similarly to the study of absorption bands in silicon presented above, measured DLTS activation energies are to be assigned to a particular defect embedded in silicon. DLTS signals can be relatively easily linked to a particular defect by, for example, monitoring the disappearance of the peaks at a certain temperature, corresponding to the annealing of a well-characterized defect. In the case of interstitial titanium in silicon, up to three DLTS peaks centered around different temperatures were assigned to the impurity; see E_{40}, E_{150} and H_{180} peaks in Figure 1.13A. If electrons were injected during the forward bias pulse, DLTS peaks are denoted by an E (blue lines in Figure 1.13), whereas signals measured in p-type silicon are noted as H (since holes are the majority carriers concentration). Once the nature of the defect is identified, Arrhenius plots following the equation 1.20 are typically represented (Figure 1.13B), obtaining a slope equal to the so-called activation energy, E_a. Depending on the nature of the injected carriers employed, trap levels are reported with respect to the conduction band, $E_a = E_C - E_T$, for E-type signals; and with respect to the valence band for p-doped silicon, $E_a = E_V + E_T$ (Table 1.1).

Table 1.1: DLTS activation energies, E_a, and *apparent* capture cross sections, σ_{na}, for the three measured peaks corresponding to interstitial titanium in silicon [24]. Their assignment to a charge transition and therefore, to the donor or acceptor character of the trap, is also given.

DLTS peak	E_a [eV]	σ_{na} [cm^2]	Assignment
$E40_{Ti}$	- 0.08	6×10^{-15}	0/-
$E150_{Ti}$	- 0.27	5×10^{-16}	0/+
$H180_{Ti}$	+ 0.26	9×10^{-17}	+/++

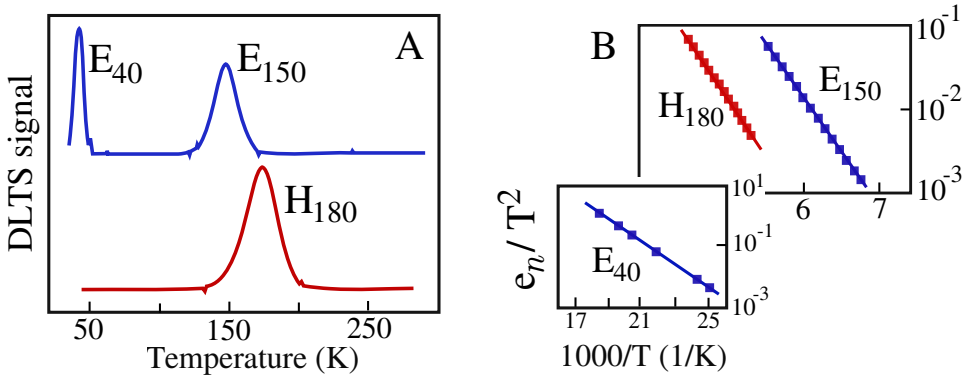

Figure 1.13: (A) DLTS signals for interstitial titanium in silicon, after [24]. (B) Arrhenius plots of the Ti-related peaks, also based on [24]. Measures in n-type silicon, with a majority of electrons as free carriers, are denoted by E (and blue lines); whereas signals arising from p-type silicon, with a majority of free holes, are denoted by H (or red lines).

In cases for which the electronic configuration of the defect is known, by means of complementary techniques and/or theoretical approaches, DLTS levels can be assigned to a certain charge transition (Table 1.1). If however, the electronic structure is to be determined, capture cross sections are said to be exploited to interpret the donor/acceptor character of the DLTS measured level. In DLTS measurements for which the capture cross sections are deduced from Arrhenius plots like the one in Figure 1.13B, the quantity σ_{na} is referred to as the *apparent* capture cross section, as indicated for the values presented in Table 1.1, extracted from [24]. A second capture cross section, σ_n, is said to be obtained by *direct* measurements if the DLTS signal from an individual trap is monitored as a function of the filling pulse duration, t_p (*e.g.* [25]). A detail analysis of the measurement techniques of capture cross sections and the comparison among different measurement methods is beyond the scope of the present manuscript. We do however note that for the DLTS activation energies, the dispersion of different published values is relatively low (see below), this not being the case for the capture cross sections, whose values tend to vary within one-two orders of magnitude even when comparing σ_n and σ_{na} (*e.g.* [25]). Published results for the DLTS levels of interstitial Ti are: for the single acceptor level, -0.08 [26], -0.08 [27], for the single donor level, -0.26 [28], -0.24 [29], -0.27 [30], -0.28 [26], -0.27 [27]; and for the double donor, +0.29 [28], +0.32 [29], +0.26 [30], +0.25 [26], +0.25 [27]. A collection of the large number of DLTS measures for primary defects in silicon can be found in [13], and for transition metal impurities in [4].

Chapter 2

Computational approaches

The Kohn-Sham theory may be regarded as the formal exactification of Hartree theory. With the exact V_{xc} all many-body effects are in principle included.

W. Kohn (1999)

In this Chapter we will introduce a theoretical framework that will be used to explore the physics of point defects throughout this thesis. We will first consider a simple effective model that reproduces the basic features of defects before moving on to more general *ab initio* methods that will allow us to obtain quantitative results. The many-body problem is enounced and depicted through a simple Linear Combination of Atomic Orbitals (LCAO)-based model (section 2.1), introducing the need for an explicit treatment of the Coulomb interaction. The general theory behind the Hartree-Fock method and the Density Functional Theory (section 2.2) is then introduced, stressing the limitations of single-particle pictures (e.g. the DFT band gap problem). A step further into accurately solving the problem of interacting electrons is analyzed through the Many-Body Perturbation Theory in the GW approximation (section 2.3). The *ab initio* approaches are finally considered to simulate isolated defects in host matrices (section 2.4), emphasizing the existence of size effects due to elastic distortions and spurious interactions of charged defect replicas. Challenges linked to the use of mean-field approaches in the specific context of point defects in semiconductors are also presented.

2.1 A simple Molecular Orbital approach

A simple Molecular Orbital approach is the name employed in the present manuscript to refer to a theoretical model proposed by Watkins and coworkers for defects in silicon (e.g. [14]). The model exploits the molecular behavior of a defect embedded in the host lattice, since only the localized-defect states are considered, neglecting the position of the band edges. The original work focused on silicon defects constituted by *dangling bonds* or broken bonds (Figure 2.1), for which the localized wavefunction was written as a linear combination of such bonds. Watkins models were based on simple symmetry considerations and they were conceived to sustain experimental evidence in the form of EPR spectra. Even if such simple models are often cited and reproduced to explain local atomic rearrangements, clear links with later electronic structure calculations are typically missing.

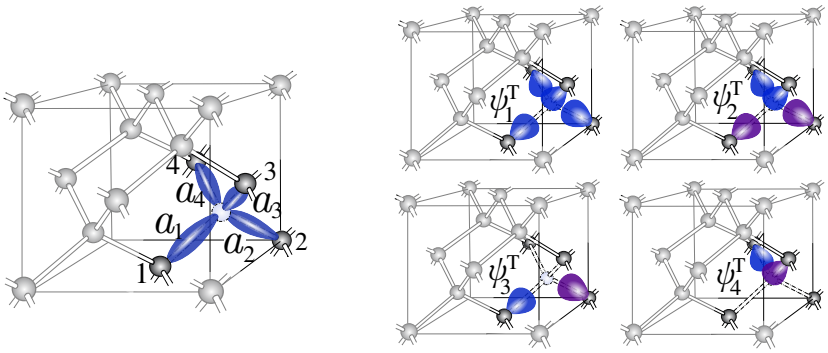

Figure 2.1: A single-electron molecular orbital model for the mono-vacancy in silicon. The dangling bonds, a_i, constituting the defects states, ψ_i^{T}, are explicitly shown. Blue and purple regions of the ψ_i^{T} denote +/- contributions of a_i respectively.

As in any electronic structure calculation, the main challenge is to determine the many body wave-function, $\Psi(\mathbf{r}_1, \mathbf{r}_2, .., \mathbf{r}_{N_\mathrm{e}}; \mathbf{R}_1, \mathbf{R}_2, .., \mathbf{R}_{N_\mathrm{n}})$, where N_n and N_e are the total number of nuclei and electrons and $\mathbf{r}_i$ and $\mathbf{R}_i$ their respective spatial coordinates. This function is solution to the stationary non-relativistic Schrödinger equation,

$$\mathcal{H}\Psi = E\Psi, \tag{2.1}$$

where the Hamiltonian operator $\mathcal{H}$ is defined (in atomic units),

$$\mathcal{H} = -\sum_i \frac{\nabla^2_{\mathbf{r}_i}}{2} - \sum_\alpha \frac{\nabla^2_{\mathbf{R}_\alpha}}{2M_\alpha} + \sum_i V_{\mathrm{nuc}}(\mathbf{r}_i) + \frac{1}{2}\sum_{i\neq j} \frac{1}{|\mathbf{r}_i - \mathbf{r}_j|} + \frac{1}{2}\sum_{\alpha\neq\beta} \frac{Z_\alpha Z_\beta}{|\mathbf{R}_\alpha - \mathbf{R}_\beta|} \tag{2.2}$$

$$V_{\text{nuc}}(\mathbf{r}) = -\sum_{\alpha} \frac{Z_\alpha e^2}{|\mathbf{r} - \mathbf{R}_\alpha|} \tag{2.3}$$

where Z_α and M_α are the atomic number and mass of the α-nucleus. Due to the complexity of the equation defined above, both adiabatic and Born-Oppenheimer approximations are typically introduced. Under these approximations, commonly referred to as the clamped nuclei approximation, the nuclei move on a Potential Energy Surface (PES) which is a solution to the electronic Schrödinger equation,

$$\mathcal{H}_{\text{elec}}(\mathbf{R})\Psi_i(\mathbf{r};\mathbf{R}) = E_i(\mathbf{R})\Psi_i(\mathbf{r};\mathbf{R}), \tag{2.4}$$

where $\mathcal{H}_{\text{elec}}$ includes the electronic kinetic energy, $\mathbf{T}_e$, the Coulomb electron-nuclei interaction $\mathbf{V}_{ne}$, the Coulomb electron interaction, $\mathbf{V}_{ee}$ and the Coulomb ionic interaction, $\mathbf{V}_{nn}$. The validity of the above equation relies on the large difference in mass between electrons and nuclei, $m_e/M_n \sim 10^{-3}$, and therefore different length and time scales of their motion.

In the case of the Molecular Orbital approach, like in any LCAO/Tight-Binding method, the electronic wavefunction of the molecule/solid is written as a linear combination of atomic orbitals, $\{\phi_\nu\}$,

$$\Psi(\mathbf{r}) = \sum_{\nu} c_\nu \phi_\nu(\mathbf{r}) \tag{2.5}$$

We note that in the above example a single atomic orbital is considered per ion, ν. The coefficients $\{c_\nu\}$ are determined by solving the Schrodinger equation 2.4, which projected in the basis set of atomic orbitals gives $\langle\phi_\mu|\,\mathcal{H}_{\text{elec}}\,|\Psi\rangle = \epsilon\langle\phi_\mu|\Psi\rangle$, and therefore a set of linear equations,

$$\sum_{\nu} c_\nu \left(\mathcal{H}_{\mu\nu} - \epsilon\,\mathcal{S}_{\mu\nu}\right) = 0, \tag{2.6}$$

where the Hamiltonian matrix elements are $\mathcal{H}_{\mu\nu} = \int \phi^*_\mu(\mathbf{r})\,\mathcal{H}_{\text{elec}}\,\phi_\nu(\mathbf{r})\mathrm{d}\mathbf{r}$, and the *overlap* matrix elements are given by $\mathcal{S}_{\mu\nu} = \int \phi^*_\mu(\mathbf{r})\,\phi_\nu(\mathbf{r})\mathrm{d}\mathbf{r}$. The accuracy and/or transferability of these methods is therefore determined by the estimation of $\mathcal{H}_{\mu\nu}$, $\mathcal{S}_{\mu\nu}$. In order to illustrate the MO model for point defects, let us consider the test-case of the Hydrogen molecule, H_2^+, for which analytical expressions for $\mathcal{H}_{\mu\nu}$, $\mathcal{S}_{\mu\nu}$ can be obtained. The $\mathcal{H}_{\text{elec}}$ for the system constituted by two ions, 1 and 2, separated by a distance, R, and with electronic coordinate $\mathbf{r}$ is, in atomic units,

$$\mathcal{H}_{\text{elec}} = -\frac{1}{2}\nabla^2_{\mathbf{r}} - \frac{1}{r_1} - \frac{1}{r_2} + \frac{1}{\mathrm{R}} \tag{2.7}$$

Where $\mathbf{r_{1,2}} = \mathbf{r} \pm \mathbf{R}/2$. If the atomic orbital basis set is composed by two 1s orbitals located at each of the ions,

$$\phi_1(\mathbf{r_1}, \mathbf{R}) = \psi_{1s}(\mathbf{r_1}, \mathbf{R}) \propto e^{-|r-R/2|/a_0}, \tag{2.8}$$

and equivalently for $\phi_2(\mathbf{r_2}, \mathbf{R}) = \psi_{1s}(\mathbf{r_2}, \mathbf{R})$, the molecular wavefunction is given by $|\psi\rangle = c_1 |\phi_1\rangle + c_2 |\phi_2\rangle$. The system of linear equations 2.6 has a non-trivial solution if, $\det(\mathcal{H}_{\mu\nu} - \epsilon\, \mathcal{S}_{\mu\nu}) = 0$, giving,

$$\epsilon_\pm = \frac{\mathcal{H}_{11} \pm \mathcal{H}_{12}}{1 \pm \mathcal{S}_{12}} \tag{2.9}$$

The derivation of such matrix elements can be found in any textbook of fundamental atomic and molecular physics. The overlap integral, for example, is easily computed in elliptical coordinates, giving, $\mathcal{S}_{12} = \int \phi_1^*(\mathbf{r_1})\, \phi_2(\mathbf{r_2}) \mathrm{d}\mathbf{r} = e^{-\mathrm{R}/a_0} \left\{1 + \mathrm{R}/a_0 + \mathrm{R}^2/3a_0^3\right\}$. The dependency of $\mathcal{H}_{\mu\nu}$, $\mathcal{S}_{\mu\nu}$ upon the inter-ionic distance, R, is shown in Figure 2.2, as well as the eigenvalues of equation 2.6. We remark that $\mathcal{H}_{11} \sim \langle\phi_1| \mathcal{H}_{\mathrm{H}} |\phi_1\rangle + 1/\mathrm{R}$, where $\mathcal{H}_{\mathrm{H}}$ is the Hamiltonian of the well-studied hydrogen atom, and thus such matrix elements can be evaluated in terms of the first ionization potential of the hydrogen atom, ϵ_{I}. From equation 2.6, the relation $c_1 \pm c_2 = 0$ is deduced, and therefore, the wavefunction corresponding to the energy levels $\epsilon_\pm$ are,

$$|\psi_\pm\rangle = \frac{1}{\sqrt{2(1 \pm \mathcal{S})}} \left[\, |\phi_1\rangle \pm |\phi_2\rangle \,\right] \tag{2.10}$$

A schematic representation of both states $|\psi_\pm\rangle$ is shown in Figure 2.2; $|\psi_\pm\rangle$ are typically known as the bonding and anti-bonding states respectively, or with respect to their symmetry transformation upon the horizontal plane of reflection, the *gerade* or *ungerade* states of the molecule. The minimum of the ϵ_+ surface at R_0 gives the equilibrium inter-ionic distance of the system at its ground state, $|\psi_+\rangle$.

We now consider the neutral molecule, H_2, for which it is assumed that the Coulomb repulsion between electrons, $\mathcal{H}_U$, can be treated as a perturbation of the Hamiltonian $\mathcal{H}_{\mathrm{elec}} = \mathcal{H}_{\mathrm{elec},1} + \mathcal{H}_{\mathrm{elec},2}$, constituted by a system of non-interacting electrons subject to the potential of ions 1 and 2 in Figure 2.2. By imposing the antisymmetry of the electronic wavefunction or the Pauli principle, six states can be built by taking into account the electronic spin,

$$\begin{aligned}
|\Psi_1\rangle &= |\psi_+\rangle_1 |\psi_+\rangle_2\ \chi_{00} \\
|\Psi_2\rangle &= |\psi_-\rangle_1 |\psi_-\rangle_2\ \chi_{00} \\
|\Psi_3\rangle &= \tfrac{1}{\sqrt{2}} \left[|\psi_+\rangle_1 |\psi_-\rangle_2 + |\psi_-\rangle_1 |\psi_+\rangle_2\right]\ \chi_{00} \\
|\Psi_{4,5,6}\rangle &= \tfrac{1}{\sqrt{2}} \left[|\psi_+\rangle_1 |\psi_-\rangle_2 - |\psi_-\rangle_1 |\psi_+\rangle_2\right]\ \{\chi_{11}, \chi_{10}, \chi_{1-1}\}
\end{aligned} \tag{2.11}$$

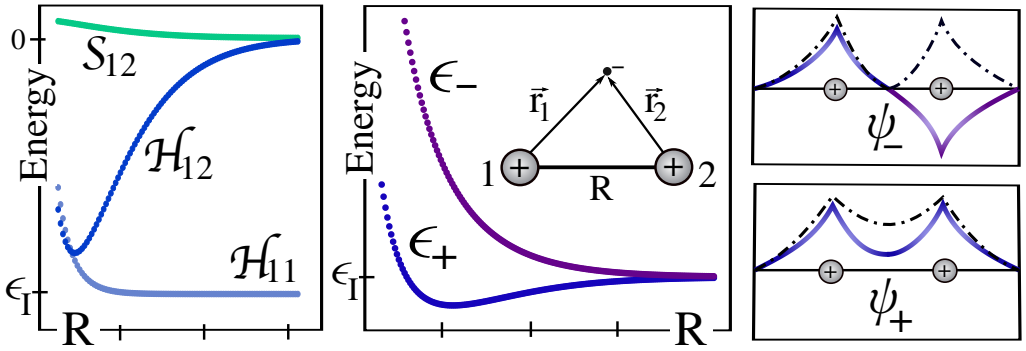

Figure 2.2: Molecular Orbital model for the H_2^+ molecule.

where, for example, χ_{00} stands for the spin singlet, $\frac{1}{\sqrt{2}}[|\uparrow\downarrow\rangle - |\downarrow\uparrow\rangle]$. The energy of each state can be determined within stationary perturbation theory as, $\epsilon_1 = 2\epsilon_+ + \langle\Psi_1|\,\mathcal{H}_U\,|\Psi_1\rangle$. In order to evaluate $\langle\Psi_1|\,\mathcal{H}_U\,|\Psi_1\rangle$, let us first consider the general case of a Slater determinant constituted by two single-electron orbitals ψ_a and ψ_b and spin variables σ and σ'. The corresponding wavefunction for electrons $(\mathbf{r}_1, s_1)$ and $(\mathbf{r}_2, s_2)$ has the form,

$$\Psi(\mathbf{r}_1, s_1; \mathbf{r}_2, s_2) \propto [\psi_a(\mathbf{r}_1)\psi_b(\mathbf{r}_2)\sigma(s_1)\sigma'(s_2) - \psi_b(\mathbf{r}_1)\psi_a(\mathbf{r}_2)\sigma'(s_1)\sigma(s_2)] \tag{2.12}$$

We note the change of notation for electronic coordinates $\mathbf{r}_{1,2}$ with respect to previous system, H_2^+. If both electrons have the same spin, $\sigma = \sigma'$, $\langle\Psi_{a\sigma;b\sigma}|\,\mathcal{H}_U\,|\Psi_{a\sigma;b\sigma}\rangle = U_{ab} - J_{ab}$, where U and J are the Coulomb and Exchange integrals respectively,

$$\begin{aligned} U_{ab} &= \int \mathrm{d}\mathbf{r_1} \int \mathrm{d}\mathbf{r_2}\, \frac{|\psi_a(\mathbf{r_1})|^2 |\psi_b(\mathbf{r_2})|^2}{|\mathbf{r_1} - \mathbf{r_2}|} \\ J_{ab} &= \int \mathrm{d}\mathbf{r_1} \int \mathrm{d}\mathbf{r_2}\, \frac{\psi_a^*(\mathbf{r_1})\psi_b(\mathbf{r_1})\psi_b^*(\mathbf{r_2})\psi_a(\mathbf{r_2})}{|\mathbf{r_1} - \mathbf{r_2}|} \end{aligned} \tag{2.13}$$

For states with opposite spin, $\sigma = -\sigma'$, $\langle\Psi_{a\sigma;b-\sigma}|\,\mathcal{H}_U\,|\Psi_{a\sigma;b-\sigma}\rangle = U_{ab}$ and $\langle\Psi_{a\sigma;b-\sigma}|\,\mathcal{H}_U\,|\Psi_{a-\sigma;b\sigma}\rangle = -J_{ab}$. The eigenvalues of the perturbed Hamiltonian $\mathcal{H}_{\text{elec}} + \mathcal{H}_U$ can thus be written as,

$$\begin{aligned} \epsilon_1 &= 2\epsilon_a + U_{aa} \\ \epsilon_2 &= 2\epsilon_b + U_{bb} \\ \epsilon_3 &= \epsilon_a + \epsilon_b + U_{ab} + J_{ab} \\ \epsilon_4 &= \epsilon_a + \epsilon_b + U_{ab} - J_{ab} \end{aligned} \tag{2.14}$$

Where a, b stand for the bonding and antibonding states $\psi_\pm$ with eigenvalues $\epsilon_\pm$. For an interatomic distance $\mathrm{R} = \mathrm{R}_0 \pm \Delta\mathrm{R}$, the level ordering can

be trivially deduced as, $\epsilon_1 \ll \epsilon_3 < \epsilon_4 < \epsilon_2$. For a larger distance, one between R_0 and the critical distance corresponding to the dissociation of the molecule, such ordering might be modified by the Coulomb contribution as, $\epsilon_4 < \epsilon_1 < \epsilon_3 < \epsilon_2$. The motivation to go through this prototype example will be evident in Chapter 4, where U and J integrals are defined to hypothesize about the level ordering of the trap states in the context of point defects in silicon.

Variations of the here-introduced LCAO method have played an important role in understanding the basic features of defects in semiconductors, often reproducing the local environment of unpaired localized electrons as described by EPR spectroscopy. In the context of primary defects in silicon, Watkins models can be considered as the first theoretical attempt to qualitatively determine the defect electronic structure. In the present work we exploit this kind of theoretical approaches to guide our first-principles calculations and to provide a general picture of the center.

2.2 The Density Functional Theory

In the previous section, an adiabatic many-body Hamiltonian was introduced for the test-case of the hydrogen molecule, H_2^+, in equation 2.7. The challenge of describing the Coulomb repulsion between electrons was considered in the case of H_2, adopting the common approximation of non-interacting electrons, $\mathcal{H}_{\text{elec}} = \mathcal{H}_{\text{e},1} + \mathcal{H}_{\text{e},2}$, with a total wavefunction $\Psi(\vec{r}_1, \vec{r}_2) = \Phi_1(\vec{r}_1)\Phi_2(\vec{r}_2)$, subject to a perturbation, $\mathcal{H}_U$. This rudimentary approach can of course be improved if $\Psi(\vec{r}_1, \vec{r}_2)$ is computed as an eigenstate of the Hamiltonian, $\mathcal{H}_{\text{elec}} = \mathcal{H}_{\text{e},1} + \mathcal{H}_{\text{e},2} + \mathcal{H}_U$. In order to do so, several methods based on the variational principle have been developed through the years; starting by the Hartree method, proposed in 1928. This principle establishes that finding the ground state of the the Schrödinger equation, $\mathcal{H}_{\text{elec}}\Psi = E\Psi$, is equivalent to minimizing the functional defined as,

$$\mathcal{F}[\Psi] = \frac{\langle\Psi|\,\mathcal{H}_{\text{elec}}\,|\Psi\rangle}{\langle\Psi|\Psi\rangle}, \tag{2.15}$$

within the subspace of possible Ψ. Among the possible trial wavefunctions we are interested in the subset of them physically acceptable, $\mathcal{P}$. The $\Psi \in \mathcal{P}$ corresponding to the $\mathcal{F}$-minimum is named the variational best solution to the quantum-mechanical Hamiltonian and the value $E_{\min}$ the corresponding variational energy,

$$E_{\min} = \min_{\Psi\in\mathcal{P}} \mathcal{F}[\Psi] \geq E_0. \tag{2.16}$$

The variational energy is therefore an upper bound of the *true* ground state of the system and Ψ an approximation of Ψ_0.

The Hartree-Fock method, proposed in 1930, postulated that if the electronic interaction is relatively small, the non-interacting picture is still valid and therefore the total wave function can be written in terms of single-electron wavefunctions or *orbitals*, $\Psi(\vec{r}_1, \vec{r}_2, .., \vec{r}_N) = \Phi_1(\vec{r}_1)\Phi_2(\vec{r}_2)..\Phi_N(\vec{r}_N)$. The exclusion principle was satisfied by rewriting the many-electron wavefunction as a Slater determinant of orthonormal single-particle orbitals,

$$\Psi_{\mathrm{S}} = \frac{1}{\sqrt{N!}} \begin{vmatrix} \Phi_1(\vec{r}_1) & \Phi_1(\vec{r}_2) & \dots & \Phi_1(\vec{r}_N) \\ \Phi_2(\vec{r}_1) & \Phi_2(\vec{r}_2) & \dots & \Phi_2(\vec{r}_N) \\ \vdots & \vdots & & \vdots \\ \Phi_N(\vec{r}_1) & \Phi_N(\vec{r}_2) & \dots & \Phi_N(\vec{r}_N) \end{vmatrix} \tag{2.17}$$

In its compact form, it can be written in terms of the parity operator P acting upon particle permutation,

$$\sum_{l}^{N!} (-1)^{P(l)} \Phi_{i_1}(\vec{r}_1)\Phi_{i_2}(\vec{r}_2)..\Phi_{i_N}(\vec{r}_N), \tag{2.18}$$

where l is defined as a particular arrangement of the N orbital subscripts (e.g. $i_1, i_2, .., i_N$; $i_2, i_1, .., i_N$, etc.). The total electronic density can be therefore expressed as a sum of such single-orbital densities, since,

$$n^{\mathrm{S}}(\vec{r}) = \langle \Psi_{\mathrm{S}}(\vec{r}_1, \vec{r}_2, .., \vec{r}_N) | \sum_{j}^{N} \delta(\vec{r} - \vec{r}_j) \, | \Psi_{\mathrm{S}}(\vec{r}_1, \vec{r}_2, .., \vec{r}_N) \rangle = \sum_{i}^{N} |\Phi_{i_n}(\vec{r})|^2, \tag{2.19}$$

showing the equivalence between electronic coordinates, $\vec{r}_j$, and single-particle orbitals, Φ_{i_n}, and therefore from now on, i_n is simply designed by i. Once the many-body system is fully described in terms of single-orbitals, the question to be addressed is: what set of $\{\Phi_i\}$ minimizes the energy functional described in equation 2.15, or even before this point, what is the form of the Hartree energy, $\langle \Psi_{\mathrm{S}} | \, \mathcal{H}_{\mathrm{elec}} \, | \Psi_{\mathrm{S}} \rangle$? Going back to the quantum-mechanical problem, the Hamiltonian $\mathcal{H}_{\mathrm{elec}}$ might be written as the sum of a single particle operator corresponding to the electron kinetic energy in the presence of nuclei, $\hat{h}_0$, and a two-particles operator, corresponding to the Coulomb interaction between electrons, $\hat{h}_e$,

$$\mathcal{H}_{\mathrm{elec}} = \sum_{j} \hat{h}_0(\vec{r}_j) + \frac{1}{2} \sum_{j \neq k} \hat{h}_e(\vec{r}_j, \vec{r}_k) \tag{2.20}$$

The single particle operator, similarly to the density operator (equation 2.19), leads to energy contributions of the form,

$$\langle \Psi_{\mathrm{S}} | \sum_j \hat{h}_0(\vec{r}_j) | \Psi_{\mathrm{S}} \rangle = \sum_i \langle \Phi_i | \hat{h}_0 | \Phi_i \rangle \tag{2.21}$$

The second expectation value for a Slater determinant is,

$$\langle \Psi_{\mathrm{S}} | \sum_j \hat{h}_e(\vec{r}_j) | \Psi_{\mathrm{S}} \rangle = \sum_{i,j} \left[\langle \Phi_i \Phi_j | \hat{h}_e | \Phi_i \Phi_j \rangle - \langle \Phi_j \Phi_i | \hat{h}_e | \Phi_i \Phi_j \rangle \right] \tag{2.22}$$

We note that for $i = j$ the Coulomb contribution exactly cancels out, eliminating the interaction of one electron with itself. This is an important result of the Hartree-Fock method, in contrast with the density functional theory formalism with its well-known self-interaction error. The variational principle can now be applied, by obtaining the single-particle orbitals such that $\Phi_k \to \Phi_k + \delta\Phi_k$ implies $\delta \langle \Psi_{\mathrm{S}} | \mathcal{H}_{\mathrm{elec}} | \Psi_{\mathrm{S}} \rangle = 0$. The variational principle leads to a set of eigenvalue equations, known as the Hartree-Fock equations,

$$\hat{F}\Phi_k = \epsilon_k \Phi_k \tag{2.23}$$

where ϵ_k is no more than a Lagrange multiplier introduced in the minimization procedure to ensure the orthonormality of the orbitals and $\hat{F}$ is the Fock operator, $\hat{F} = \hat{h}_0 + \sum_i (\hat{J}_i - \hat{K}_i)$. The operator $\hat{J}_i$ represents the classical or Hartree interaction between electronic densities, $|\Phi_i|^2$ and $|\Phi_k|^2$, whereas the exchange term, $\hat{K}_i$, is a consequence of the antisymmetry property of the wavefunction,

$$(\hat{J}_i - \hat{K}_i)\Phi_k = \int \Phi_i^*(\vec{r}_2) \hat{h}_e \left[\Phi_i(\vec{r}_2)\Phi_k(\vec{r}_1)\right] \mathrm{d}\vec{r}_2 - \int \Phi_i^*(\vec{r}_2) \hat{h}_e \left[\Phi_i(\vec{r}_1)\Phi_k(\vec{r}_2)\right] \mathrm{d}\vec{r}_2. \tag{2.24}$$

We have shown that by construction the Fock operator does depend on the single-particle orbitals, which are solution of the Hatree-Fock equations. These equations are therefore to be solved self-consistently, until, the orbitals employed to construct $\hat{F}$, $\Phi_{k,\mathrm{in}}$, are equivalent to the ones obtained after the diagonalization of the Hartree-Fock equation, $\Phi_{k,\mathrm{out}}$.

Before concluding this short introduction to the Hartree-Fock method, we focus our attention towards the physical meaning of the eigenvalues ϵ_k. It can be tempting to assign such eigenvalues to the energy levels of an electronic interacting system. It is however straightforward to demonstrate that the total Hartree-Fock energy is equal to,

$$E^{\mathrm{HF}} = \sum_k \epsilon_k - \frac{1}{2} \sum_{i,j} \left[\langle \Phi_i \Phi_j | \hat{h}_e | \Phi_i \Phi_j \rangle - \langle \Phi_j \Phi_i | \hat{h}_e | \Phi_i \Phi_j \rangle \right]. \tag{2.25}$$

The Hartree-Fock eigenvalues do therefore not correspond to single energies of interacting electrons subject to the interaction of static nuclei. They can however, be interpreted as the energies required to remove an electron from a certain one-electron state n, if one derives the Hartree-Fock energy for the system of $N-1$ electrons,

$$E^{\mathrm{HF}}(N-1) - E^{\mathrm{HF}}(N) = -\epsilon_n. \tag{2.26}$$

And equivalently for the corresponding energy to add an electron at the m orbital,

$$E^{\mathrm{HF}}(N+1) - E^{\mathrm{HF}}(N) = \epsilon_m. \tag{2.27}$$

These results are known as the Koopman's theorem, which established that ϵ_k can be assigned to orbital energies under the approximation that adding or removing one electron leaves the orbitals invariant.

In 1964, P. Hohenberg and W. Kohn proved that for any system of interacting particles in an external potential, $v(\mathbf{r})$, the density $n(\mathbf{r})$ can be used as the basic variable to describe the ground state properties of the system. In other words, the external potential is (to within a constant) a unique functional of the density; making explicit such one-to-one correspondance, if $v'(\mathbf{r}) \neq v(\mathbf{r}) + \text{constant}$, then $n'(\mathbf{r}) \neq n(\mathbf{r})$. It was also proven that the total energy of the system can be defined as a functional of the electronic charge density,

$$E[n(\mathbf{r})] = \langle \Psi^n | \, \mathcal{H}_{\mathrm{elec}} \, | \Psi^n \rangle = F[n(\mathbf{r})] + \int v(\mathbf{r}) n(\mathbf{r}) \mathrm{d}\mathbf{r}. \tag{2.28}$$

Where the universal functional $F[n(\mathbf{r})]$, independent of the external potential, includes the expectation values of the electronic kinetic and interacting terms. The energy functional $E[n]$ for the non-degenerate ground state density satisfies the variational principle; *i.e.* its global minimum corresponds to the exact ground state energy associated with $v(\mathbf{r})$. Details and proofs of the so-called Hohenberg-Kohn theorems can be found in their original paper [31].

The Hohenberg-Kohn theorems are at the very basis of the density functional theory; a formalism to compute the electronic structure of molecules and solids based on their density instead of their many-body wavefunction. From a practical perspective, describing the system of interacting particles in terms of their charge density reduces the computational expense of the calculation with respect to wave-function-based methods (such as the Hartree-Fock method), due to the exponential growth of the Hilbert space with the number of electrons. We however note that the exact form of the universal

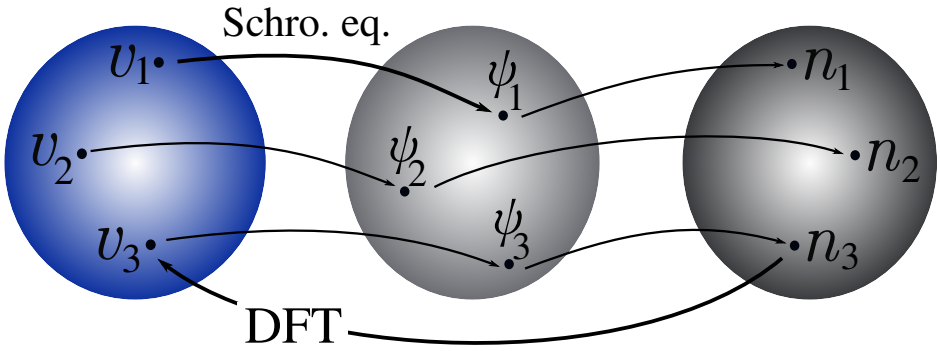

Figure 2.3: The density, n, as basic variable to describe the properties of a system of interacting particles subject to an external potential, v, is the fundamental basis of the density functional theory (DFT).

functional $F[n(\mathbf{r})]$ is unknown. An equivalent expression of the Hartree-Fock energy functional, $E[\Psi_S]$, for the density-based functional $E[n]$ is therefore to be specified. W. Kohn and L. J. Sham were able to tackle the problem in 1965 by proposing their well-known one-particle picture, described in the following section.

2.2.1 The Kohn-Sham one-particle picture

W. Kohn and S. J. Sham [32] proposed to map the real problem into an auxiliary system of non-interacting electrons with equal ground state density, whose universal function can be written in terms of three separated contributions,

$$F\left[n(\mathbf{r})\right] = T_0\left[n(\mathbf{r})\right] + E_H\left[n(\mathbf{r})\right] + E_{XC}\left[n(\mathbf{r})\right]. \tag{2.29}$$

The kinetic energy of a non-interacting particle system, $T_0\left[n(\mathbf{r})\right]$, is then simply written in terms of the auxiliary one-particle orbitals, $\Phi_i(\mathbf{r})$,

$$T_0\left[n(\mathbf{r})\right] = -\sum_i \left\langle \Phi_i \right| \frac{\nabla^2}{2} \left| \Phi_i \right\rangle, \tag{2.30}$$

The Hartree energy, $E_H\left[n(\mathbf{r})\right]$, corresponding to the classical Coulomb interaction was previously introduced with the direct term of the Fock operator, equation 2.24,

$$E_H\left[n(\mathbf{r})\right] = \frac{1}{2}\int \frac{n(\mathbf{r})n(\mathbf{r}')}{|\mathbf{r}-\mathbf{r}'|} \mathrm{d}\mathbf{r}\mathrm{d}\mathbf{r}' \tag{2.31}$$

The remaining term, the so-called exchange-correlation functional, $E_{XC}[n(\mathbf{r})]$, is defined as the missing contributions to $F[n(\mathbf{r})]$ for a system of interacting

electrons whose kinetic energy can not be approximated as the one for non-interacting particles and whose Coulomb repulsion is not a merely classical interaction. It is often referred to as a *correction* term for the so-far neglected *quantum interactions*, like the electronic exchange repulsion due to the exclusion principle. The Kohn-Sham total energy functional can therefore be written as,

$$E[n(\mathbf{r})] = T_0\left[n(\mathbf{r})\right] + E_{\mathrm{H}}\left[n(\mathbf{r})\right] + E_{\mathrm{XC}}\left[n(\mathbf{r})\right] + \int v(\mathbf{r})n(\mathbf{r})\mathrm{d}\mathbf{r}. \tag{2.32}$$

Similarly to the Hartree-Fock method, the above energy functional can be minimized with respect to perturbations $\Phi_i \rightarrow \Phi_i + \delta\Phi_i$, by introducing Lagrange multipliers imposing the orthonormality of the *orbitals*, $\langle\Phi_i|\Phi_j\rangle = \delta_{ij}$, obtaining the well-known Kohn-Sham equations,

$$\left[-\frac{\nabla^2}{2} + V_{\mathrm{KS}}(\mathbf{r})\right]\Phi_i(\mathbf{r}) = \epsilon_i\Phi_i(\mathbf{r}). \tag{2.33}$$

The effective Kohn-Sham potential, $V_{\mathrm{KS}}(\mathbf{r})$, includes three potential contributions; the external potential, the Hartree potential and the exchange-correlation potential, defined as the following functional derivative,

$$V_{\mathrm{XC}}(\mathbf{r}) = \left.\frac{\partial E_{\mathrm{XC}}[n(\mathbf{r})]}{\partial n(\mathbf{r})}\right|_{n(\mathbf{r})=n_0(\mathbf{r})} \tag{2.34}$$

Where $n_0(\mathbf{r})$ is the ground state density according to the Hohenberg-Kohn theorem, which in the one-particle picture is determined by the auxiliary one-particle orbitals, similarly to the Slater charge density in equation 2.19,

$$n_0(\mathbf{r}) = \sum_i |\Phi_i(\mathbf{r})|^2 \tag{2.35}$$

The Kohn-Sham (KS) picture can therefore be interpreted as a single electron subject to an effective *mean* potential defined by the ground state density of the interacting-particles system. The self-consistent KS equations are therefore no more than a mean field approach, but the computed ground state density is exact as long as the many-body effects are included in the exact V_{XC}. Approximations to the exchange-correlation functional, as well as the physical meaning of the auxiliary functions Φ_i and ϵ_i are quickly reviewed in the following.

Exchange-correlation functionals

As repeated multiple times, DFT is an *exact* formalism (besides the Born-Oppenheimer approximation) to determine the ground state density of the

system of interacting electrons if V_{XC} is known. The first approximation to the exchange-correlation functional was proposed in terms of a Local Density Approximation (LDA) [33], where the exchange-correlation functional was given as the one of an homogeneous gas of interacting electrons at constant density, $\varepsilon_{xc}^{\mathrm{homo}}[n(\mathbf{r})]$,

$$E_{\mathrm{XC}}^{\mathrm{LDA}}[n(\mathbf{r})] = \int \varepsilon_{xc}^{\mathrm{homo}}[n(\mathbf{r})]\, n(\mathbf{r})\, \mathrm{d}\mathbf{r}. \tag{2.36}$$

The exchange contribution, $\varepsilon_{x}^{\mathrm{homo}}[n(\mathbf{r})] = -\frac{3}{4\pi}(3\pi^2 n)^{\frac{1}{3}}$, was determined by analogy with the Thomas-Fermi approximation to the kinetic energy of the homogeneous gas; whereas the correlation energy, $\varepsilon_{c}^{\mathrm{homo}}[n(\mathbf{r})]$, was computed from accurate Monte-Carlo simulations [34]. LDA is therefore based on a simple, well-defined system and it has proven to give rise to physically accurate geometries of molecules and solids. It however presents limitations when the material presents inhomogeneities in the charge density, giving overbound structures. A significant improvement to the LDA functional was proposed by J. W. Perdew and Y. Wang [35], whose approximation to the XC-functional also included the gradient of the density. A gradient-dependent functional is better know today as the Generalized Gradient Approximation (GGA). Contrary to the uniquely-defined LDA functional, multiple GGA formulations have been proposed over the years, and extensive benchmarks can be found testing their accuracy for different systems. One of the most common GGA functionals used in the description of solids is the PBE functional, proposed by Perdew, Burke and Ernzerhof in 1992 [36]. Beyond the GGA approximation, much more complicated functionals (meta-GGA or hyper-GGA) were proposed in the search for the *chemical heaven of accuracy* (see discussion regarding the Jacob's ladder of density functional approximations for the exchange-correlation energy [37]), which are beyond the scope of the present work.

Before concluding the discussion regarding exchange-correlation functionals, we quickly introduce a last type of proposed approximations, referred to as hybrid functionals. These rather expensive functionals mix a fraction of the Hartree-Fock exact exchange functional with LDA/GGA functionals. As it was reviewed in detail above, the Hartree-Fock method computes the exchange term for a system of interacting electrons exactly. It was also proven, equation 2.22, that the interaction of an electron with itself was completely canceled out, since the exchange term compensated exactly the Hartree direct term. This is not the case in DFT, where the approximated XC-functional does not compensate the Coulomb self-interaction of electrons or the DFT self interaction problem. Hybrid functionals are therefore aimed at correcting the

SI DFT problem by partially including the self-interaction-free Hartree-Fock exchange. For the sake of completeness, we give as an example the PBE0 functional [38], which mixes the PBE exchange energy and Hartree-Fock exchange energy in a set 3 to 1 ratio, with the full contribution of the PBE correlation energy,

$$E_{\mathrm{XC}}^{\mathrm{PBE0}} = \frac{1}{4}E_X^{\mathrm{HF}} + \frac{3}{4}E_X^{\mathrm{PBE}} + E_C^{\mathrm{PBE}} \tag{2.37}$$

The usefulness of hybrid functionals in the context of point defects in semiconductors is discussed in detail along the present manuscript.

Kohn-Sham energies and Janak's theorem

The eigenvalues of the KS equation, similarly to the ϵ_k for the Hartree-Fock method, are often identified as single particle energies. Even if they have proven to give accurate descriptions of band structures of metals, the expected discrepancy between the total DFT energy and the sum of the KS energies reveals the lack of physical meaning of these auxiliary functions. An attempt to find a physical interpretation to these values was given by Janak's theorem in terms of fractional occupations,

$$n(\mathbf{r}) = \sum_i^N |\Phi_i|^2 = \sum_i^\infty f_i |\Phi_i|^2, \tag{2.38}$$

where f_i represents the occupation of the single-particle orbital Φ_i. The highest KS energy with $f_i = 1$ is said to be the highest occupied state (in analogy with the *highest occupied molecular orbital* and the *top of the valence band*), whereas the lowest unoccupied KS energy, with $f_i = 0$, would correspond to the *lowest unoccupied molecular orbital* and the *bottom of the conduction band* in the single-particle calculation. In terms of this fractionally occupied KS system, the main result of Janak's work [39] was to demonstrate that,

$$\frac{\partial E}{\partial f_i} = \epsilon_i, \tag{2.39}$$

independently of the form of the exchange-correlation functional. Much like Koopman's theorem, Janak's result is used to connect the KS energies with energy differences between systems with N and $N+1$ particles, by integrating equation 2.39,

$$E_{N+1} - E_N = \int_0^1 \frac{\partial E}{\partial f_i}\,\mathrm{d}f_i = \int_0^1 \epsilon_i\,\mathrm{d}f_i. \tag{2.40}$$

In simple terms, the above integral represents a total change in the particle number equal 1 obtained by *adding* small fractions, $\mathrm{d}f_i$, of an electron ($f_i = 1$). The sensitive aspect in such evaluation is that the eigenvalue ϵ_i is modified by a change in electronic occupation, $\epsilon_i = \epsilon_i(f_i)$, showing that $E_{N+1} - E_N \simeq \epsilon_i$ is an *approximation* of Janak's theorem.

2.2.2 Sampling the DFT potential energy surface

Within the Born-Oppenheimer approximation, it is possible to assume fixed nuclei coordinates when computing the electronic structure of the desired system. The total DFT energy does however depend on these atomic configurations, $E^{\mathrm{DFT}}(\mathbf{R}_1, \mathbf{R}_2, ..., \mathbf{R}_{N_n})$, constraining the nuclei to move along the electronic Potential Energy Surface (PES). It is thus possible to investigate the shape of such PES, finding critical points, such as minima (example of H_2^+ and the equilibrium configuration, R_0), metastable minima, etc., if the nuclei Schrödinger equation is solved. If we however consider the nuclei as classical masses, subject to an interaction energy, $E[\{\mathbf{R}_\alpha\}]$, the equations of motion simply are,

$$M_\alpha \ddot{\mathbf{R}}_\alpha = -\frac{\partial E}{\partial \mathbf{R}_\alpha} = \mathbf{F}[\{\mathbf{R}_\alpha\}]. \tag{2.41}$$

If the atomic force, $\mathbf{F}[\{\mathbf{R}_\alpha\}]$, is known, the above equation can be numerically integrated by taking a certain time step, Δt, performing the so-called *ab initio* Molecular Dynamics. As a first approach to the problem, atomic forces can be computed by finite energy differences, $E[\{\mathbf{R}_\alpha + \Delta\mathbf{R}_\alpha\}] - E[\{\mathbf{R}_\alpha\}]$, requiring to compute the electronic energy at $3N + 1$ atomic positions. Such computational expensive approximation can be overcome by exploiting the Hellmann-Feynman theorem and performing one unique calculation. The theorem establishes that the first order derivative of the energy with respect one parameter, $\partial E/\partial\lambda$, can be computed as the expectation value of the variation $\partial\mathcal{H}/\partial\lambda$. In the particular case of DFT atomic forces, it means that the evaluation of $\frac{\partial E}{\partial \mathbf{R}_\alpha}$ does not depend on any derivative of $n(\mathbf{r})$, but it is purely a classical electrostatic interaction between nuclear charges and the electronic charge density. In the present work, computed atomic forces will not be used in MD simulations, but algorithms to target critical points of the PES will be used as introduced in the following.

Structural optimization

Structural optimization seeks to find points in the DFT PES such that all atomic forces are equal zero and for which all the surrounding points are

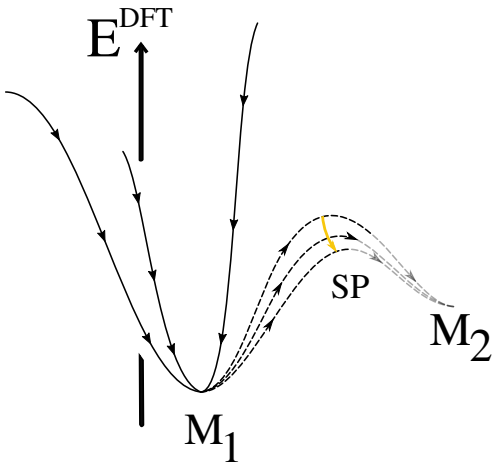

Figure 2.4: DFT potential energy surface or energy $E^{\mathrm{DFT}}[\{\mathbf{R}_\alpha\}]$ as a function of ionc clamped positions. The depicted surface is characterized by two minima, M_1 and M_2 and the saddle point, SP, of the minimal energy path between minima.

energetically less favorable (e.g. minima M1 and M2 in Figure 2.4). Among the variety of optimization techniques, we employ the Broyden-Fletcher-Goldfarb-Shanno (BFGS) algorithm [40, 41] to find equilibrium structures of point defects embedded in silicon. In very few words, the BFGS algorithm is said to be a quasi-Newton algorithm, since the Hessian matrix of second derivatives is not computed, but it is estimated by approximate gradient evaluations.

Minimum energy transition path

Another aspect of the DFT PES that is typically modeled are the transition paths between different minima (see the three transition paths betwen M1 and M2 in Figure 2.4). Among these paths, we are particularly interested in the minimum energy path MEP or the most probable path, since the energy difference between its saddle point (SP) and the minima is typically assigned to the activation energy of the thermal transition. The MEP does very often not correspond to a simple linear interpolation between the initial and final configurations, and therefore the Nudged-Elastic-Band (NEB) method [42] is usually employed. The method consists in optimizing a series of intermediate configurations or *images* starting from a tentative reaction path. It is based on a constrained energy minimization of these images by introducing spring forces between the images (or beads). The images band is therefore

subject to the parallel spring force, keeping the *beads* equally distant, and the perpendicular electronic force, *pushing* the band to go downhill towards the MPE, characterized by all forces being zero (see orange arrow in Figure 2.4). In the present work, we employ a modification of the NEB method, the Climbing-Image NEB method [43], in which one of the images is *made to climb up* to the saddle point, where it does not feel the spring force.

2.2.3 The plane-wave pseudopotential implementation

Once the fundamental theoretical aspects of DFT have been reviewed, we are in a position to describe its practical implementation to study condensed matter systems. We are particularly interested in the plane-wave representation of the Kohn-Sham scheme, since in a solid it is very convenient to require states to obey Periodic Boundary Conditions (PBC), being naturally described in the complete set of Fourier components. Among the different plane-wave-based DFT codes, we employ the ABINIT package [44], and so the computational details specified in the present section are characteristic of such package (even if they are almost equivalent to other codes such as Quantum-Espresso). Among the multiple practical technicalities of *ab initio* codes, we briefly review the plane-wave representation, the k-point sampling and the pseudopotential approximation. Further specifications, such as the Ewald summation for the ionic term, the FFT grid to determine quantities in reciprocal space, the SCF algorithms to solve self-consistently the KS equations and the spin-unrestricted calculations can be found in any book specialized in density functional theory [45].

The plane-wave representation and k-point sampling

As already mentioned above, in the case of a crystalline material, the KS potential presents the same periodicity as the crystal lattice, being $V_{\mathrm{KS}}(\mathbf{r}+\mathbf{R}) = V_{\mathrm{KS}}(\mathbf{r})$. The eigenfunctions of the KS equation are therefore Bloch wavefunctions, given by a plane wave, $e^{i\mathbf{k}\cdot\mathbf{r}}$, modulated by a periodic function, $u_{i\mathbf{k}}(\mathbf{r})$. It is thus convenient to write such function as a Fourier series,

$$u_{i\mathbf{k}}(\mathbf{r}) = \frac{1}{\sqrt{\Omega_{\mathrm{cell}}}} \sum_m c_{i,m}(\mathbf{k}) e^{i\mathbf{G}_m\cdot\mathbf{r}}, \tag{2.42}$$

where Ω_{cell} is the volume of the primitive cell, $\mathbf{G}_m$ is a vector from the reciprocal lattice and $c_{i,m}(\mathbf{k})$ are the Fourier coefficients. The KS orbitals subject to a periodic potential, $\Phi_{i,\mathbf{k}}(\mathbf{r})$, are then said to be expanded in a complete plane-wave basis set, characterized by wave-vectors $\mathbf{k}+\mathbf{G_m}$. The

KS eigevalue equations in such basis set become,

$$\sum_{m'} H^{\mathrm{KS}}_{m,m'}(\mathbf{k}) c_{i,m}(\mathbf{k}) = \epsilon_i(\mathbf{k}) c_{i,m}(\mathbf{k}), \tag{2.43}$$

whose eigenfunctions are the coefficients of the Fourier expansion. The KS eigenvalues represented against the k-vector constitute the DFT band structure of the solid (see for example the definition of ϵ_{TVB} and ϵ_{BCB} in previous section). The Hamiltonian matrix elements have a rather simple expression in reciprocal space,

$$H^{\mathrm{KS}}_{m,m'}(\mathbf{k}) = \left\langle \mathbf{k}+\mathbf{G}_m \middle| H^{\mathrm{KS}} \middle| \mathbf{k}+\mathbf{G}_{m'} \right\rangle = \frac{|\mathbf{k}+\mathbf{G}_m|^2}{2}\delta_{m,m'} + V^{\mathrm{KS}}(\mathbf{G}_m - \mathbf{G}_{m'}), \tag{2.44}$$

so the matrix diagonalization is computed in such space. Even if the plane-wave basis set is complete, containing infinite plane waves, in practice, the sum in equation 2.42 is truncated to a certain m. The reduced basis set is then defined by the *kinetic energy cutoff*,

$$E_{\mathrm{cut}} = \frac{|\mathbf{G}_{\mathrm{max}}|^2}{2}, \tag{2.45}$$

so only plane waves whose energies are lower than E_{cut} are included in the expansion. The augmentation of the energy cutoff increases the size of the basis set, increasing our precision, but also the computational resources.

In the plane-wave representation of the KS scheme, most of the quantities (like the DFT total energy) are obtained upon integration over the Brillouin zone. For a generic function $f_i(\mathbf{k})$, where i denotes a discrete band, the integral might be numerically discretized,

$$\int_{\mathrm{BZ}} f_i(\mathbf{k}) \mathrm{d}\mathbf{k} \longrightarrow \sum_{\mathbf{k}} f_i(\mathbf{k}). \tag{2.46}$$

The precision of the DFT results therefore depends on the density of our $\mathbf{k}$-grid or on the k-sampling scheme (optimized method to reduce the total number of points by intelligently selecting a few of them upon symmetry considerations).

The pseudopotential approximation

In most DFT calculations of solids, it is computationally convenient to only describe explicitly the valence electrons. This approximation to the *all-electron* calculation is therefore based on the distinction of core electrons,

tightly bound to the atomic nucleus, and valence electrons, localized farther away, almost completely responsible for the interatomic bonding (see example of the silicon atom in Figure 2.5A). Such a simplification is achieved by introducing the so-called *pseudopotentials*, which describe the interaction between valence electrons and the nuclei screened by the *frozen* core electrons. The pseudopotential is therefore characterized by a certain cutoff-radius, r_C, defining the *pseudization region* where the KS all-electron wavefunction needs to be modified. Inside such region the potential is modified so that the solution to the KS equation is a smooth and nodeless function, reducing the size of the basis set needed to describe large variations of the wavefunction (Figure 2.5B). In the case of the so-called norm-conserving pseudopotentials, the integrated electronic density corresponding to the *pseudized* wavefuntion is the same as the original wavefunction and, for $r > r_C$, the pseudopotential must coincide with the original all-electron potential. This intuitive introduction to the pseudopotential approximation is of course an oversimplification on the pseudopotential method, for a detailed description, we refer the reader to Chapter 11 of [46].

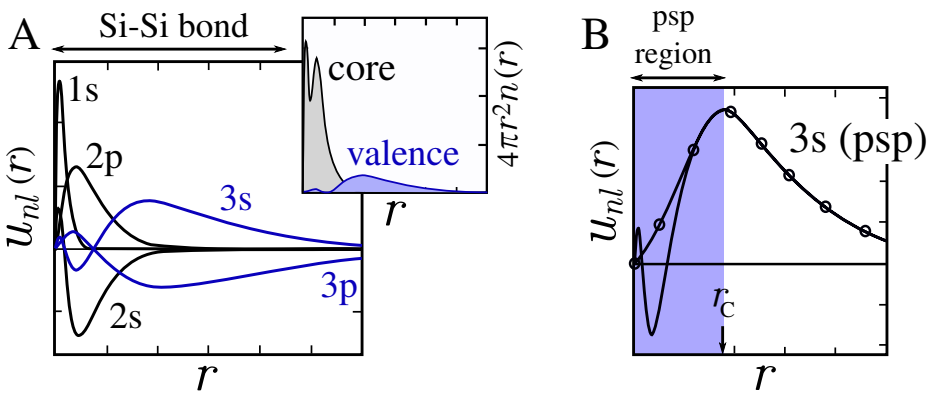

Figure 2.5: (A) Kohn-Sham radial functions of the silicon atom, after [45]. The difference between the densities corresponding to core and valence electrons is also shown. (B) A schematic representation of a psp-radial function for the 3s state of the silicon atom.

In the present work, we employed the Optimized Norm-Conserving Vanderbilt Pseudopotentials (ONCVPSP) [47], obtained using the PBE approximation for the exchange-correlation function. In particular, we have employed the 0.4 version of the PSP table found in [48] .We also referred to the detailed analysis of the accuracy of such pesudopotentials for a large variety of atomic elements made in [49].

2.2.4 The DFT band gap problem

Janak's theorem, equation 2.39, and its extrapolation to total energy differences, equation 2.40, play an important role when estimating the semiconductor bang gap or, in the interest of the present work, the relative position of the trap-induced states. As was briefly mentioned above, KS energies can reproduce the band structures of metals, but they are found to underestimate the semiconductors band gap. The underestimation of band gaps is one of DFT most challenging problems and it is typically referred to as the DFT band gap problem. We say that a band gap is underestimated by comparison with a measured band gap, which can be defined as the difference between the first ionization potential IP and the first electronic affinity, EA. From a more formal point of view, in a system with N electrons the electrical band gap can be defined as the energy difference between *charged excitations*, $E_{N-1} - E_N$ and $E_N - E_{N+1}$,

$$E_g = \text{IP} - \text{EA} = (E_{N-1} - E_N) - (E_N - E_{N+1}) \tag{2.47}$$

We note that because E_g can be defined in terms of total energy differences, one could be tempted to approximate the electrical band gap as a difference of KS energies corresponding to the highest occupied state (or top of the valence band, ϵ_{TVB}) and the lowest unoccupied state (assigned to the bottom of conduction band, ϵ_{BCB}),

$$E_g \simeq E_g^{KS} = \epsilon_{BCB} - \epsilon_{TVB} \tag{2.48}$$

From Janak's theorem or equation 2.40 we know that E_g^{KS} is only an approximation to the measured band gap and therefore we should not expect it to be accurate.

There is however another complicated aspect related to this *band gap problem*, involving the Kohn-Sham formulation of DFT, and in particular the approximations made for the exchange-correlation potential. In 1982, J. P. Perdew *et al.* proved that the *exact* exchange-correlation functional presents a piece-wise linear behavior between integer numbers of electrons [50], or in format of equation,

$$\frac{\partial E(N+1)}{\partial f_{\text{HOMO}}} = \frac{\partial E(N)}{\partial f_{\text{LUMO}}} \Longrightarrow \epsilon_{\text{HOMO}}^{N+1} = \epsilon_{\text{LUMO}}^{N} \tag{2.49}$$

In other words, and as shown in Figure 2.6, the exact exchange-correlation derivative is discontinuous at integer number of electrons. Since by construction, the approximated exchange-functionals are continuous functions of the

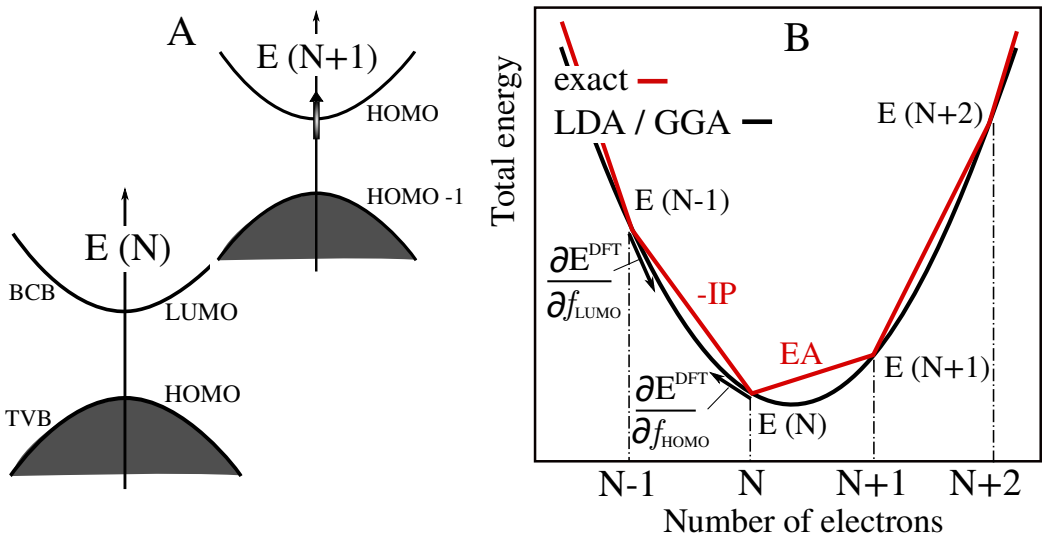

Figure 2.6: (A) Charge excitation, $N \rightarrow N+1$, and the corresponding HOMO/LUMO states for different number of electrons. (B) Convexity of LDA/GGA approximations for the echange-correlation functional upon changes in particle number.

density, there are no derivative discontinuities, and

$$\frac{\partial E^{\mathrm{DFT}}(N+1)}{\partial f_{\mathrm{HOMO}}} > \frac{\partial E^{\mathrm{DFT}}(N)}{\partial f_{\mathrm{LUMO}}} \Longrightarrow \epsilon^{N+1}_{\mathrm{HOMO}} > \epsilon^{N}_{\mathrm{LUMO}} \tag{2.50}$$

This is the reason DFT in its LDA/GGA approximation is said to be a convex formalism and the E_g^{KS} is underestimated, since ionization potentials are by construction larger than electron affinities. In the case of the Hartree-Fock method, the tendency is inverted, $\epsilon^{N+1}_{\mathrm{HOMO}} < \epsilon^{N}_{\mathrm{LUMO}}$, and so Hartree theories are said to be *concave* with respect to changes in the electronic number, typically overestimating the semiconductor band gap. Proving the lack of derivative discontinuity in the employed V_{XC} shows the limitation of DFT to estimate charged excitations or energy differences at different electronic occupations. In the ongoing discussion regarding the band gap problem, we note that even if DFT total energies are employed to compute the electrical band gap as IP - EA (equation 2.47), the estimated band gap is subject to the convexity issue of the functional. To overcome such limitation, theories beyond the density functional theory have been developed, in particular, we introduce in the following section the Many-Body Perturbation Theory, which goes one step further in solving all many-body effects.

2.3 Many-Body Perturbation Theory

So far we have presented electronic structure methods based on the one-particle picture, namely, the Hartree-Fock method and the Density Functional Theory. We have dedicated some time to show their limitations when single-particle energies are exploited to give meaningful physical quantities such as ionization potentials and electron affinities. As briefly discussed in previous sections, electrical band gaps are measured by conducting photoemission experiments, also referred to as photoelectron spectroscopy. In the case of direct photoelectron spectroscopy or photoemission experiments, a photon with energy $h\nu$ interacts with the sample, ejecting one electron, whose kinetic energy, E_{kin}, is measured (Figure 2.7). The *binding energy* or single-particle energy associated with the ejected electron is then $\epsilon_i = E_{\text{kin}} - h\nu$. We however note that because this single electron is embedded in a system of interacting electrons, correlated by the Coulomb potential, the many-body process is more accurately written in terms of total energies as, $E(N-1) - E(N) = h\nu - E_{\text{kin}}$, where $E(N)$ is the total energy of the N-particle system and $E(N-1)$ the corresponding energy for the N-1 system. The complementary process of such process, the inverse photoemession, is characterized by an electron being injected in the sample, leading to a photon emission, whose energy is subsequentely measured. The total energy exchanged in the process is then, $E(N) - E(N+1) = h\nu - E_{\text{kin}}$, where $E(N+1)$ is the energy of the (N+1)-particle system (Figure 2.7). In the case of photoelectron spectroscopy performed on semiconductors, the first ionization potential, IP $= E_{N-1} - E_N$, is typically assigned to the electronic state corresponding to the TVB or the HOMO; and similarly for the first electronic affinity, EA $= E_N - E_{N+1}$, and the BCB or LUMO; determining the energy difference IP - EA or the electrical gap. From the theoretical side, ionization potentials and electronic affinities were tentatively assigned to Hartree-Fock and Kohn-Sham eigenvalues (section 2.2.1), showing the breakdown of both theories by presenting both Koopman's and Janak's theorems. We are therefore in need of a theoretical framework capable of describing processes involving the electronic ejection or injection into the system, or in other words, capable of linking N-particle and (N$\pm$1)-particle systems: the Many-Body Perturbation Theory (MBPT).

Within MBPT, energy differences between systems with different particle numbers are assigned to the so-called quasiparticle (QP) energies. The notion of quasiparticles was first introduced by L. D. Landau in 1956 after presenting his phenomenological theory of Fermi liquids. In a system of interacting electrons, like a solid, an electron or a bare particle interacts with the other

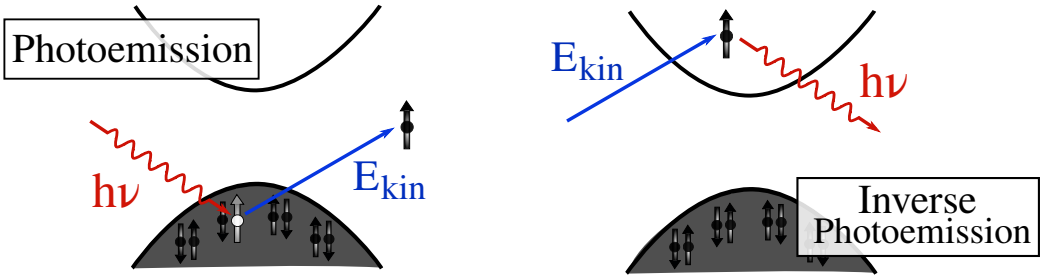

Figure 2.7: Photoemission and inverse photoemission experiments. The photon arriving to or being emitted from the sample has an energy equal hν, and the kinetic energy of the injected or ejected electron is represented by E_{kin}.

electrons via the Coulomb potential, creating an effective positively charged polarized cloud. The excitations of a system of strongly interacting particles, can then be described in terms of weakly interacting quasiparticles, or the ensemble of the bare electron and its surrounding screening charge. The formal description of these quasiparticles is based on the single-particle Green function, G, whose determination depends on the accurate calculation of the quasiparticle self-energy, Σ. A short introduction to MBPT is given in the following, with the purpose of later describing the so-called GW approximation and its practical implementation, the G_0W_0 method.

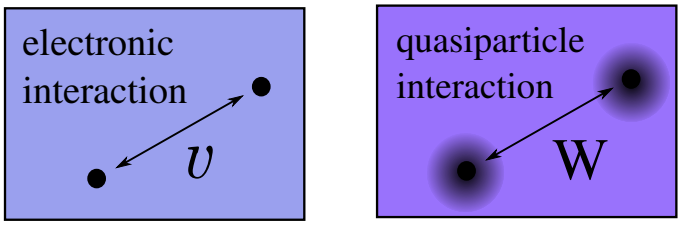

Figure 2.8: The bare Coulomb interaction, v, and the screened Coulomb interaction, W.

The one-particle Green function, G

In the context of N-body problems, we have already established that it is common to define a complete set of single particle functions, $\Phi_k(\mathbf{x})$, where $\mathbf{x}$ denotes both the space and spin variables, which are used as building functions of the global wavefunction, $\Psi(\mathbf{x_2}, \mathbf{x_1}, \ldots, \mathbf{x_N})$. The system is then

determined by a list of quantum labels, $k_1, k_2, \ldots, k_N$, and so, the N-body wavefunction can be expressed as $|k_1, k_2, \ldots, k_N\rangle$. To simplify the manipulation of such wavefunctions, the creation and annihilation operators, $a_k^\dagger$ and a_k, are typically defined, $a_k^\dagger |k_1, k_2, \ldots, k_N\rangle = |k, k_1, k_2, \ldots, k_N\rangle$, and $a_k |k, k_1, k_2, \ldots, k_N\rangle = |k_1, k_2, \ldots, k_N\rangle$. These operators act on one-single-particles functions, creating or annihilating state k. Applying this formalism to the case of free electrons, the Hamiltonian can be easily written as $\mathcal{H} = \sum_{k,l} \epsilon_{k,l} a_k^+ a_l$, and the total number of particles, $N = \sum_k a_k^+ a_k$. In practice, these operators are typically substituted by field operators, $\psi(\mathbf{x})$ and $\psi^\dagger(\mathbf{x})$, acting on space, and defined as, $\psi(\mathbf{x}) = \sum_k a_k \Phi_k(\mathbf{x})$. The time-dependence of these operators is defined within the Heisenberg picture as $\psi(\mathbf{x}, t) = e^{i\mathcal{H}t}\psi(\mathbf{x})e^{-i\mathcal{H}t}$, leading to a fundamental equation of motion,

$$i\frac{\partial\psi(\mathbf{x},t)}{\partial t} = \left[h(\mathbf{x}) + \int v(\mathbf{r},\mathbf{r}')\psi^\dagger(\mathbf{x}',t)\psi(\mathbf{x}',t)d\mathbf{x}'\right]\psi(\mathbf{x},t). \tag{2.51}$$

where v is the Coulomb interaction between particles. Let us now illustrate the form of the matrix element defined by the operator $\psi(\mathbf{x}, t)$ between states $|N\rangle$, ground state of the N-particle system, and $|N-1, s\rangle$, the eigenstate s of the (N-1) system,

$$\langle N-1, s|\,\psi(\mathbf{x},t)\,|N\rangle = f_s(\mathbf{x})e^{-i\epsilon_s t}, \tag{2.52}$$

with $\epsilon_s = E(N) - E(N-1, s)$, and $f_s(\mathbf{x}) = \langle N-1, s|\,\psi(\mathbf{x})\,|N\rangle$. Similarly, we can also connect state $|N\rangle$ to a system of N+1 electrons, $\langle N|\,\psi(\mathbf{x},t)\,|N+1, s\rangle = f_s(\mathbf{x})e^{-i\epsilon_s t}$. In the case of non-interacting electrons, where $|N\rangle$ is written as a Slater determinant, $|N-1, s\rangle = a_s\,|N\rangle$ and $|N+1, s\rangle = a_s^\dagger\,|N\rangle$, it is straightforward to show,

$$\begin{aligned} f_s(\mathbf{x}) &= \langle N-1, s|\,\psi(\mathbf{x})\,|N\rangle = \Phi_s(\mathbf{x}), \text{ if } s \text{ occupied} \\ &= \langle N|\,\psi(\mathbf{x})\,|N+1, s\rangle = \Phi_s(\mathbf{x}), \text{ if } s \text{ unoccupied} \end{aligned} \tag{2.53}$$

This result is not surprising, since we have retrieved Koopman's theorem for particle excitations. We however note that in an interacting system, the one-to-one relation between states $|N+1, s\rangle$ and single-particle orbitals, Φ_s, is no longer valid, and a different interpretation of ϵ_s and f_s is needed. With such need in mind, it is common to define the time ordered one-electron Green function,

$$i\mathrm{G}(\mathbf{x}t, \mathbf{x}'t') = \begin{cases} \langle N|\,\psi(\mathbf{x},t)\psi^\dagger(\mathbf{x}',t')\,|N\rangle\,, & t > t' \\ -\langle N|\,\psi^\dagger(\mathbf{x}',t')\psi(\mathbf{x},t)\,|N\rangle\,, & t' > t \end{cases} \tag{2.54}$$

It is said to correspond to the propagation amplitude for an added electron for positive times ($t > t'$) or an added hole for negative time ($t < t'$). If

we now introduce the full set of eigenstates of the interacting Hamiltonian (or the closure relation, $\sum_s |N \pm 1, s\rangle \langle N \pm 1, s|$), the Green function can be rewritten as,

$$\mathrm{G}(\mathbf{x}, \mathbf{x}', \tau) = \sum_s e^{-i\epsilon\tau} f_s(\mathbf{x}) f_s^\dagger(\mathbf{x}'), \tag{2.55}$$

where $\tau = t - t'$ and,

$$\begin{aligned} f_s(\mathbf{x}) &= \langle N| \psi(\mathbf{x}) |N+1, s\rangle, \quad \epsilon_s = E_{N+1,s} - E_N, \quad \text{for } \epsilon_s > \mu \\ f_s(\mathbf{x}) &= \langle N-1, s| \psi(\mathbf{x}) |N\rangle, \quad \epsilon_s = E_N - E_{N-1,s}, \quad \text{for } \epsilon_s < \mu \end{aligned} \tag{2.56}$$

If we now take the Fourier transform in time, the physical meaning of G becomes clear, since,

$$\mathrm{G}(\mathbf{x}, \mathbf{x}', \epsilon) = \sum_s \frac{f_s(\mathbf{x}) f_s^\dagger(\mathbf{x}')}{\epsilon - \epsilon_s}. \tag{2.57}$$

The poles of the previous expression exactly correspond to the excitation energies of the N-particle system or to the quasiparticle energies, and $f_s(\mathbf{x})$ can the be identified with the quasiparticle amplitude.

Equation of motion for G and the concept of self-energy, Σ

So far we have just introduced the concept of the single-particle propagator, showing explicitly its connection with quasiparticle energies. The Green function is however to be determined according to the corresponding equation of motion. For simplicity, let us neglect the exchange and correlation effects beyond the Hartree approximation. The non-interacting single particle Hamiltonian is then, $\mathcal{H}_0 = h_0 + V_\mathrm{H}$, and the corresponding Green function, G_0, solution to the equation of motion $(\epsilon - \mathcal{H}_0)\mathrm{G}_0 = \mathrm{I}$, is written in terms of single-particle orbitals, Φ_s,

$$\mathrm{G}_0 = \sum_s \frac{\Phi_s(\mathbf{x}) \Phi_s^\dagger(\mathbf{x})}{\epsilon - \epsilon_s}. \tag{2.58}$$

G_0 therefore corresponds to the propagation of a particle (hole) in a system of N+1 (N-1) non-interacting particles. If we now turn on the exchange interaction, the Green function, G^HF, is determined by,

$$(\epsilon - \mathcal{H}^\mathrm{HF})\mathrm{G}^\mathrm{HF} = (\epsilon - \mathcal{H}_0 - V_\mathrm{x})\mathrm{G}^\mathrm{HF} = \mathrm{I}. \tag{2.59}$$

From the above written equations of motion for both Hartree and Hartree-Fock Green functions, the following relation is easily obtained by multiplying by G_0 equation 2.59,

$$\mathrm{G}^\mathrm{HF} = \mathrm{G}_0 + \mathrm{G}_0 V_\mathrm{x} \mathrm{G}^\mathrm{HF}. \tag{2.60}$$

If we were to explicitly solve equation 2.59, we would find that G^{HF} or the Green function at first order of perturbation can be represented as the sum of three different Feynmann diagrams (Figure 2.9): the free particle propagator, G_0, and the Hartree and Fock diagrams, describing the interaction of one particle with itself through virtual photons. The infinite sum of Hartree-Fock diagrams leads precisely to equation 2.60, describing the propagation of G^{HF}. If we now consider higher order perturbation terms of the Coloumb interaction, the corresponding Green function, G, presents contributions of more complicated diagrams (such as, for example, the bubble diagram and the rainbow diagram at the second order expansion). The infinite sum of higher order diagrams leads to the Dyson equation for the Green function in terms of the so-called self-energy, Σ. The idea behind MBPT is then to consider the Coulomb interaction between electrons,

$$v(\mathbf{r}-\mathbf{r}') = \frac{1}{|\mathbf{r}-\mathbf{r}'|}, \tag{2.61}$$

as a perturbation of the independent-particle system (or Hartree potential), increasing the accuracy of the self energy from V_x to the *exact* Σ_{xc}.

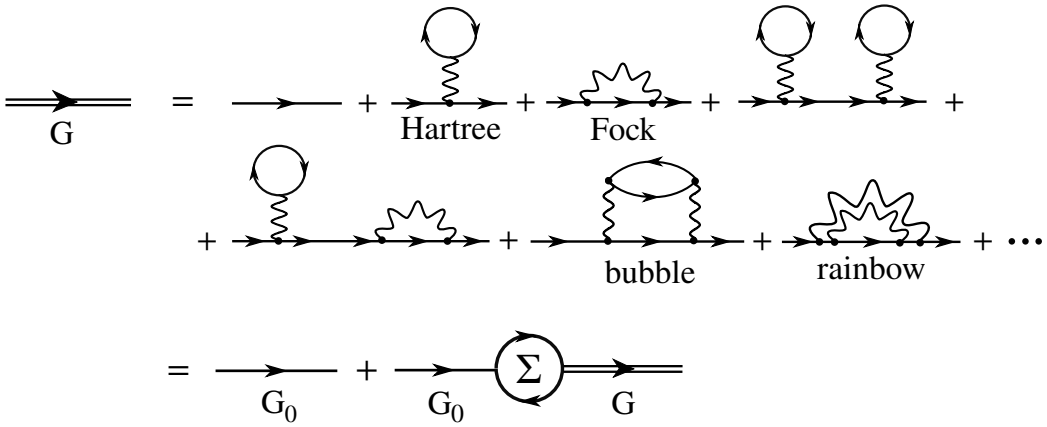

Figure 2.9: Dyson equation for the one-particle Green function, $G = G_0 + G_0\Sigma G$, represented with Feynmann diagrams.

To conclude, the equation of motion for the *dressed* Green function, introduced here as a generalization of equation 2.59, and formally derived in ref has the form,

$$[\epsilon - h_0(\mathbf{x}) - V_H(\mathbf{x})]\, G(\mathbf{x},\mathbf{x}';\epsilon) - \int \Sigma(\mathbf{x},\mathbf{x}'';\epsilon) G(\mathbf{x}'',\mathbf{x}';\epsilon) d\mathbf{x}'' = \delta(\mathbf{x},\mathbf{x}'). \tag{2.62}$$

And the corresponding Dyson equation is,

$$\mathrm{G}(\mathbf{x},\mathbf{x}',\epsilon) = \mathrm{G}_0(\mathbf{x},\mathbf{x}',\epsilon) + \int \mathrm{d}\mathbf{x}_1\mathbf{x}_2\, \mathrm{G}_0(\mathbf{x},\mathbf{x}_1,\epsilon)\Sigma(\mathbf{x_1},\mathbf{x_2},\epsilon)\mathrm{G}(\mathbf{x}_2,\mathbf{x}',\epsilon). \quad (2.63)$$

Before concluding, we note that the complex many-body character of G is due to the energy dependence of the self-energy, $\Sigma(\mathbf{x},\mathbf{x}',\epsilon)$.

The screened potential, W

In practice, the bare Coulomb interaction between electrons is substituted by a screened interacting potential, W, when determining the full interacting Green function. As one can expect for any homogenous polarizable medium, a given electronic interaction induces a response from the medium, reducing the bare interaction by the dielectric constant of the medium, ε. For any general medium, the interaction between a pair of electrons is reduced by the surrounding electrons, which act as an effective dielectric medium. The dynamically screened interaction between electrons is the defined as,

$$\mathrm{W}(\mathbf{r},\mathbf{r}',\epsilon) = \int \mathrm{d}\mathbf{r}_1\varepsilon^{-1}(\mathbf{r},\mathbf{r}_1,\epsilon)v(\mathbf{r}_1-\mathbf{r}'), \quad (2.64)$$

where ε^{-1} is the microscopic dielectric constant. The one-to-one Coulomb interaction is therefore replaced by a mean response from the medium, described by such dielectric constant. To conclude, within MBPT we aim to describe not the strong Couloumb interaction between electrons, but a screened weak interaction W between quasiparticles.

2.3.1 The GW approximation

The replacement of v by the screened potential W allowed L. Hedin to formulate in 1965 a scheme to compute the interacting Green functions by proposing a set of self-consistent equations [51], represented in the pentagon of Figure 2.10. The screened potential is written in terms of the irreducible polarizability, $\tilde{\chi}$, in the form of a Dyson equation, $\mathrm{W}= v + v\tilde{\chi}\mathrm{W}$. The irreducible polarizability is connected to the Green function through the three-point vertex function, Γ. Within the GWΓ theory an exact solution to the many-body problem is obtained if Hedin's equations are solved self-consistently, often using as the starting guess for the Green function, G_0.

In practice, and due to the computational cost of the GWΓ scheme, the vertex function is neglected or set to the identity $\Gamma = 1$, leading to the GW

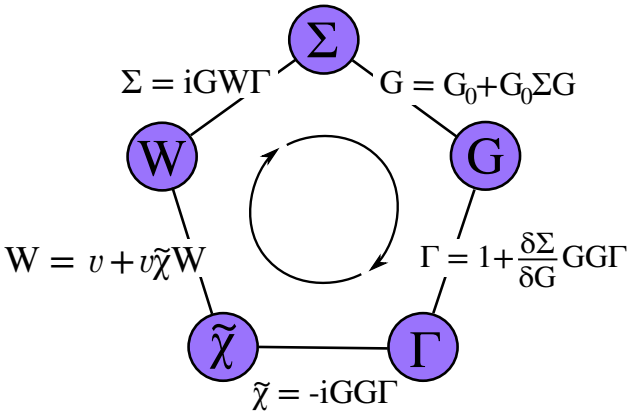

Figure 2.10: Hedin's coupled equations, constituting the GWΓ theory.

approximation. The set of equations is then reduced as follows,

$$\begin{aligned}
\Sigma(12) &= i\mathrm{G}(12)\mathrm{W}(12) \\
\mathrm{G}(12) &= \mathrm{G}_0(12) + \int \mathrm{d}34\, \mathrm{G}_0(13)\Sigma(34)\mathrm{G}(42) \\
\tilde{\chi}(12) &= -i\mathrm{G}(12)\mathrm{G}(21) \\
\mathrm{W}(12) &= v(12) + \int \mathrm{d}34\, v(13)\tilde{\chi}(34)\mathrm{W}(34)
\end{aligned} \tag{2.65}$$

where the notation $(12) = (\mathbf{x}_1, t_1, \mathbf{x}_2, t_2)$ is employed for simplicity. The self-energy is simply the product between G and W, giving the name to the GW approximation, and the neglected terms are commonly referred to as *vertex corrections*. The above scheme is also to be solved iteratively, to obtain the approximated self-energy. In practice, and as detailed in next section, the self-energy is very rarely computed self-consistently, but the *one-shot GW approximation* is typically implemented. The self-energy is therefore estimated by the initial guess of the Green function, G_0, and the corresponding screening, W_0, leading to the $\mathrm{G}_0\mathrm{W}_0$ calculation of quasiparticle energies.

2.3.2 The $\mathbf{G_0W_0}$ implementation

As already established, the practical implementation of MBPT consists in one unique evaluation of both G and W, and the estimation of the self energy as the convolution of both, $\mathrm{G}_0\mathrm{W}_0$. The *one-shot* approximation of the self-energy is justified by the reliability of the starting point: mean-field theories like Hartree-Fock or Kohn-Sham, which already include a description of the electronic interaction beyond the Hartree potential. As already shown

in equation 2.58, the independent Green function is easily expressed in terms of the single-particle orbitals, Φ_s, constituting the first step of the GW calculation. In the case of computing the many-body corrections on top of the Kohn-Sham theory, we have,

$$\mathrm{G}_0(\mathbf{r},\mathbf{r}',\epsilon) = \sum_s \frac{\Phi_s^{\mathrm{KS}}(\mathbf{r})\Phi_s^{\mathrm{KS}\,\dagger}(\mathbf{r}')}{\epsilon - \epsilon_s^{\mathrm{KS}} + i\eta\mathrm{sign}(\epsilon_s^{\mathrm{KS}} - \mu)}, \tag{2.66}$$

where the spin-dependence has been dropped, and only the spatial variable is considered. The second step in the calculation is to compute both the irreducible polarization, $\tilde{\chi}_0$, and the screened potential, W_0, according to Hedin's equations 2.65. The estimated self-energy is then evaluated, $\Sigma_0 = i\mathrm{G}_0\mathrm{W}_0$, and so, it is possible to write the quasiparticle equation,

$$\left(-\frac{\nabla^2}{2} + V_n(\mathbf{r}) + V_{\mathrm{H}}(\mathbf{r})\right)\Phi_i^{\mathrm{qp}}(\mathbf{r}) + \int \mathrm{d}\mathbf{r}'\Sigma_0(\mathbf{r},\mathbf{r}',\epsilon_i^{\mathrm{qp}})\Phi_i^{\mathrm{qp}}(\mathbf{r}') = \epsilon_i^{\mathrm{qp}}\Phi_i^{\mathrm{qp}}(\mathbf{r}) \tag{2.67}$$

We note that in practice, the above equation is solved by approximating the quasiparticle wavefunctions as the Kohn-Sham single-particle orbitals, $\Phi_i^{\mathrm{qp}}(\mathbf{r}) = \Phi_i^{\mathrm{KS}}(\mathbf{r})$, and the quasiparticle energies, ϵ_i^{qp}, are computed as a first order correction to the Kohn-Sham starting point,

$$\epsilon_i^{\mathrm{qp}} = \epsilon_i^{\mathrm{KS}} + \langle\Phi_i|\,\Sigma_0(\epsilon_i^{\mathrm{qp}}) - V_{\mathrm{xc}}\,|\Phi_i\rangle \tag{2.68}$$

Within the $\mathrm{G}_0\mathrm{W}_0$ approach there is then a one-to-one correspondence between the KS eigenvalues and the computed QP energies. In most of the GW calculations of band structures, the dependency of Σ with the quasiparticle energy is linearized, and the expression, $\epsilon_i^{\mathrm{qp}} = \epsilon_i^{\mathrm{KS}} + Z_i\,\langle\Phi_i|\,\Sigma_0(\epsilon_i^{\mathrm{KS}}) - V_{\mathrm{xc}}\,|\Phi_i\rangle$, is solved instead. The renormalization factor, Z_i, is simply,

$$Z_i = \left[1 - \langle\Phi_i|\,\frac{\delta\Sigma_0(\epsilon)}{\delta\epsilon}\bigg|_{\epsilon=\epsilon_i}\,|\Phi_i\rangle\right]^{-1} \tag{2.69}$$

Obtaining the quasiparticle eigenvalues is the last step of the GW calculation, since the quantity Σ_0, and hence the screened potential, W_0, are assumed to be previously computed. In the following we briefly describedsome technical details regarding the calculation of the dielectric matrix through the non-interacting response function χ_0 and the dependency of the screened potential with ϵ.

Converged quasiparticle band structures

After neglecting the vertex contribution, the irreducible polarizability is easily written in terms of the Green function in equation 2.66 as $\chi_0(12) =$

$-i\mathrm{G}(12)\mathrm{G}(21)$,

$$\chi_0(\mathbf{r}_1,\mathbf{r}_2,\epsilon)=\sum_{i,j}\Phi_i(\mathbf{r}_1)\Phi_i^\dagger(\mathbf{r}_2)\Phi_j(\mathbf{r}_2)\Phi_j^\dagger(\mathbf{r}_1)\left[\frac{1}{\epsilon-(\epsilon_i-\epsilon_j)-i\eta}-\frac{1}{\epsilon-(\epsilon_i-\epsilon_j)+i\eta}\right] \tag{2.70}$$

with the condition of i being an occupied KS state, whereas j runs over the unoccupied states. The number of *empty bands* employed in the description of χ_0 is therefore one of the convergence parameters to account for in a GW calculation, typically needing at least a 1:10 proportion between occupied versus empty bands [52]. The requirement of including such large number of bands makes the calculation extremely expensive, explaining the lack of benchmarks and/or consistent studies of certain systems in the literature (e.g. point defects in semiconductors). Furthermore, the independent-particle polarizability is in practice computed in the reciprocal and frequency domain, and so, *oscillator matrix elements* of the form,

$$\mathrm{M}_{ij}(\mathbf{q}+\mathbf{G})=\int \mathrm{d}\mathbf{r}_1\Phi_i(\mathbf{r}_1)\Phi_j^\dagger(\mathbf{r}_1)\mathrm{e}^{-i(\mathbf{q}+\mathbf{G})\cdot\mathbf{r}_1} \tag{2.71}$$

must be determined, giving a dielectric matrix of the form $\varepsilon_{\mathbf{G}_1,\mathbf{G}_2}(\mathbf{q},\omega)$. The number of **G**-vectors employed to describe the polarizability thus constitutes the second convergence parameter to be considered in GW calculations. We finally note that the dependency of the here-mentioned parameters is often not independent and a joint convergence study is required.

Computing the screened potential, $\mathbf{W_0}$

The computation of the self-energy is commonly split into the exchange contribution, Σ_x, and the correlation term, Σ_c, with $\Sigma(\epsilon)=\Sigma_\mathrm{x}+\Sigma_\mathrm{c}(\epsilon)$. While the estimation of the exchange term is straightforward, $\Sigma_\mathrm{x}=i\mathrm{G}v$, the evaluation of the second terms needs the convolution integral of G and $\mathrm{W}_p=\mathrm{W}-v$,

$$\Sigma_\mathrm{c}(\mathbf{r}_1,\mathbf{r}_2,\epsilon)=\frac{1}{2\pi}\int \mathrm{d}\epsilon' e^{i\eta\epsilon'}\mathrm{G}(\mathbf{r}_1,\mathbf{r}_2,\epsilon+\epsilon')\mathrm{W}_p(\mathbf{r}_1,\mathbf{r}_2,\epsilon') \tag{2.72}$$

The energy dependencence of W_p is often given by a plasmon-pole model [53, 54], according to which the imaginary part of ε^{-1} can be approximated as a single-pole function in the frequency domain, ϵ. In the present work, the Godby-Needs plasmon model is employed as implemented in the ABINIT package.

2.3.3 Many-body effects in semiconductors

To conclude the present section on MBPT, let us note that eigenvalues of the quasiparticle equation 2.67 correspond by construction to ionization potentials, IPs, and electronic affinities, EAs. The GW approximation is then Koopman's compliant, since,

$$\epsilon^{\mathrm{GW}}_{\mathrm{HOMO}} = \mathrm{E}^{N} - \mathrm{E}^{N-1} = \mathrm{IP}, \tag{2.73}$$

and similarly,

$$\epsilon^{\mathrm{GW}}_{\mathrm{LUMO}} = \mathrm{E}^{N+1} - \mathrm{E}^{N} = \mathrm{EA}. \tag{2.74}$$

The electrical band gap, E_g, is then equal to the energy difference,

$$E_g = \epsilon^{\mathrm{GW}}_{\mathrm{LUMO}} - \epsilon^{\mathrm{GW}}_{\mathrm{HOMO}}, \tag{2.75}$$

where ϵ^{GW} are eigenvalues of a single particle equation, which accounts for all many-body effects through the exchange-correlation self-energy, Σ_{xc}. GW calculations of semiconductors are therefore expected to give accurate estimates of electrical gaps, as reported by the the seminal work of M. van Schilfgaarde *et al.* [55], in which many-body corrections were constructed from the LDA approximation: the GW@LDA scheme.

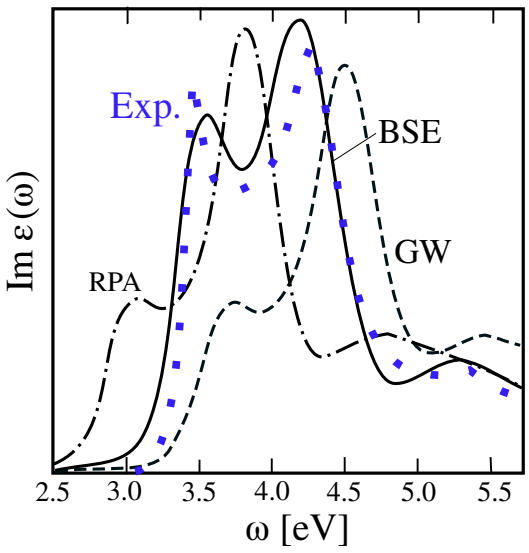

Figure 2.11: Silicon absorption spectrum after [56].

It is also important to emphasize the fact that the GW approximation leads to the accurate description of charged excitations, for which the number

of particles is changed by one, *i.e.* N-1 and N+1 excitations. Exploiting the quasiparticle eigenvalues to predict neutral excitations, characterized by the creation of an excitation (or a electron-hole pair), is therefore an approximation and it needs to be justified. In general terms, when a photon is absorbed, the binding energy between the paired electron and hole needs to be taken into account. Such attractive electrostatic interaction is said to justify the fact that measured optical band gaps are smaller than electrical gaps, ${E_g}^{\text{opt}} < E_g$. Neutral excitations are solutions of the Bethe-Salpeter equation (BSE), which consists of an effective Schrödinger equation for the electron-hole pair [57]. Even if a review of the BSE theory is beyond the scope of the present manuscript, we note that in the case of the semiconductors, the BSE optical band gap is effectively smaller than the GW electrical gap [56].

2.4 *Ab initio* calculations of point defect properties in practice

Local "imperfections" in realistic crystalline samples are found in a diluted regime, characterized by isolated non-interacting defects. In order to simulate such conditions, single point-like defects are embedded in large matrices reproducing the host atomic structure. Depending on the choice of such matrix, *ab initio* approaches are distinguished between the cluster method, for which the defect is introduced in a finite cluster emulating the solid structure, or the large-cell approach, which is constituted by multiple unit cells arranged according to the primitive vectors of the lattice, subject to the Periodic Boundary Conditions (PBC). In order to guarantee an atomistic model of isolated defects, the dimension of the host matrix needs to be sufficiently large to avoid size effects or non-physical interactions at the matrix borders, but it has to be computationally affordable, since the translational invariance of the solid can no longer be exploited. To emphasize this particular point, we quote M. Cardona again (foreword of [58] from 2007):

"Although the field of defects in semiconductors is at least 60 years old, it had to wait, in order to reach maturity, for the colossal increase in computer power that has recently taken place, following the predictions of Moore's law. The ingenuity of computational theorists in developing algorithms to reduce the intractable many-body problem of defect and host to one that can be handled with existing and affordable computer power has also played a significant role."

Even nowadays, counting on rather large affordable matrices, size effects are still traceable due to the long-range elastic distortions induced by defects in covalent materials (section 2.4.1). Furthermore, in the case of PBC-based calculations, mitigation strategies need to be taken into account to overcome the long-range spurious Coulomb interaction between defect replicas (section 2.4.2). Besides these sources of non-physical interactions, intrinsic to the large-cell approach, estimated defect properties might be subject to the DFT band gap problem, *i.e.* the concavity or lack of piece-wise linearity in available exchange-correlation functionals (section 2.4.3), for which different correction schemes have been proposed (section 2.4.4).

In the case of silicon, state-of-the-art calculations typically employ large cubic cells containing from 216 atoms to 1000 atoms, and they are typically sampled only at $\mathbf{k} = \Gamma = (0, 0, 0)$, or in fewer cases, employing the smallest Monkhorst-Pack grid [59] centered at Γ, with a total of 8 k-points. Assuming that the solid band structure is sufficiently folded for a cell of 216 atoms, the KS orbitals are simply,

$$\Phi_i(\mathbf{r}) = \frac{1}{\sqrt{\Omega_{\text{cell}}}} \sum_m c_{i,m}\, e^{i\mathbf{G}_m \cdot \mathbf{r}}, \tag{2.76}$$

and the energy density of states for the crystal is well-represented at Γ, $\epsilon_i(\mathbf{k} = \Gamma)$.

2.4.1 Size effects due to elastic distortions

Artifacts associated to the finite size of the defective cell are known to be introduced due to the long range ionic relaxations in the host lattice. In the vacancy-related defects case, for example, broken bonds are known to recombine into defect states, lowering their energy by inducing large atomic displacements of first neighbor atoms, and by consequence, second or even third neighbors of the vacancy. In the case of large metallic ions introduced at interstitial position (or if the atom is big enough, at substituional position), might provoke local expansions of the lattice in order to accommodate the impurity. The range of these defect-associated distortions and the consequent non-physical elastic contributions do not follow a simple rule of thumb, and so this issue needs to be addressed for each individual defect. Elastic distortions for three common centers in silicon, the substitutional phosphorous, the vacancy and the vacancy-phosphorous complex (the E-center) are shown in Figure 2.12. Relaxation patterns are especially relevant for the vacancy and the E-center, whereas they are almost negligible for the dopant element. Shallow impurities do however introduce rather delocalized states (section 1.1.2),

whose effective radius might be larger than the cell parameter. The electronic density, $|\Phi_{\mathrm{KS}}^{\mathrm{Shallow}}|^2$, might then interact with the replicas of the defective cell, introducing a non-physical contribution due to the overlap between periodic images (Figure 2.12). A relatively recent work [60] showed that the shallow KS eigenvalue associated with substitutional phosphorus is converged within 1 meV for a cell containing 10648 atoms. Within the scope of the present work, we are not interested in accurately describing shallow centers, but the electronic activity associated with deep states. As depicted in Figure 2.12, when a P atom traps a mobile vacancy, constituting the phosphorus-vacancy complex, the P impurity does no longer introduce a shallow state, but several deep localized states. Seeing the comparative effective radius between shallow and deep states, it is safe to conclude that the tails of $\Phi_{\mathrm{KS}}^{\mathrm{Deep}}$ are normally contained within any silicon cell, whose lattice parameter is at least ~ 20 Å (corresponding to a cubic cell of 64 atoms).

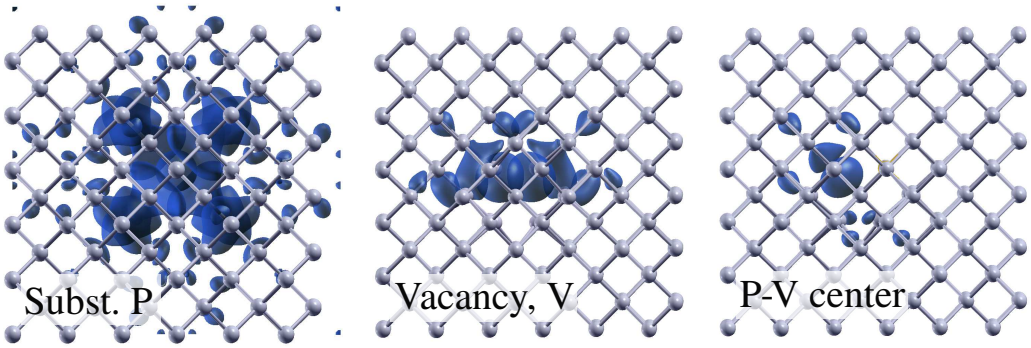

Figure 2.12: Defect electronic density corresponding to the substitutional phosphorous, the mono-vacancy, and the phosphorous-vacancy complex. KS isosurfaces in a 216-atoms silicon cell for three defect-induced states are shown in blue. The plotted probability density, $|\Phi_{\mathrm{KS}}|^2$, corresponds to $\frac{1}{9}$ of the maximum isosurface value calculated for each defect.

Historically, convergence tests for deep centers were based on the tendency of formation energies upon variations on the number of host atoms (see, for example, convergence studies for the silicon vacancy [61, 62, 63, 64]). Besides targeting total energy convergences, one could also check the energy tendency of a single KS state within the semiconductor band gap, similarly to the example given above for the P shallow state. In our case, since KS defect states are not aimed to be determined with a precision of 1 meV, size effects are discussed in terms of total energy differences or the collective behavior of KS eigenvalues in a defective cell. For a given cell size, we re-

mark that finite size effects are responsible for the broadening of the defect induced states. As described at the very beginning of the manuscript, defect states are delocalized in **k-**space, introducing constant energy bands in the solid band structure. However, artifacts of defective cell calculations induce the nonphysical dispersion $\epsilon_{\mathrm{T}}(\mathbf{k})$. Two common schemes to overcome such band broadening are: either to average the eigenvalue over the BZ, or to sample at Γ only, considering that such k-point exploits the defect symmetry completely. A second issue related to the KS eigenvalues in a defective cell is the determination of the host crystal band edges, ϵ_{TVB} and ϵ_{BCB}, since in defective cells the *band gap narrowing* effect is commonly found, characterized by an artificial lift of the host band degenerate states. For this reason, eigenvalues of the defective cell are often shifted to match bulk states deep in the valence band, where the spurious defect interaction does not affect the host energy band structure.

2.4.2 Spurious interaction between charged defects

As it has been established, the study of point defects in semiconductors requires to simulate several trap electronic occupations or different charge states of the defect. In order to avoid the divergence of the electrostatic energy for a charged defective cell calculation, a homogeneous neutralizing background charge is usually employed: the compensating charged jellium. This technique allows the study of charged defects by accurately describing, for example, ionic relaxations patterns at different charge states, but it does however introduce the spurious interaction between charged defect images. In other words, in addition to the artificial elastic interactions, charged defective cells are characterized by including a fictitious electrostatic interaction in our DFT calculations. The total energy of a charged cell is therefore *artificially shifted* by a certain quantity, $\Delta E^{\mathrm{elect}}$, corresponding to the Coulomb interaction between two rather localized charged densities, separated by a distance L (or the lattice parameter of the defective cell). A second drawback of the charged defective cell calculations is the change of the *reference electrostatic potential* due to the interaction between the charged defect and the compensating jellium, which *fixes* the KS absolute energies and, in particular, determines the host band edges. A second correction must therefore be taken into account when comparing KS DOS for differently charged cells, often referred to as the potential alignment correction, ΔV.

In the case of defect studies whose main quantity of interest is the formation energy of charged centers, applying a correction scheme to DFT quantities is fundamental to achieve accurate values. There is therefore a need

to revisit the expression for the charged defect formation energies, which is defined in its more general form as,

$$E_f^q\ [\mathrm{Si, d}] = E_{\mathrm{DFT}}^q\,[\mathrm{Si, d}] - \sum_I n_I \mu_I + q\,[\epsilon_{\mathrm{TVB}} + \mathcal{E}_{\mathrm{F}}]\,, \tag{2.77}$$

where $E_{\mathrm{DFT}}^q\,[\mathrm{Si, d}] = E_{[\mathrm{Si,\,d}^q]} - E_{[\mathrm{Si,\,bulk}]}$ and the presence of the ionic reservoir is introduced by the chemical potentials, μ_I. The term E_{DFT}^q is therefore subject to the spurious electrostatic interaction induced in the particular system [Si, d^q]; so the electrostatic correction $\Delta E^{\,\mathrm{elect}}$ is typically added to the above expression. Furthermore, describing the position of the valence band is fundamental to accurately determine the electronic chemical potential, $\mu_e = \epsilon_{\mathrm{TVB}} + \mathcal{E}_{\mathrm{F}}$. To overcome the delocalization of the band edges in a charged defective cell, it is common to include a potential alignment correction, ΔV,

$$E_f^q\ [\mathrm{Si, d}] = E_{\mathrm{DFT}}^q\,[\mathrm{Si, d}] + \Delta E^{\,\mathrm{elect}} - \sum_I n_I \mu_I + q\,[\epsilon_{\mathrm{TVB}} + \mathcal{E}_{\mathrm{F}} + \Delta V]\,. \tag{2.78}$$

So far we have only introduced the correction terms in the formation energy expression, without tackling the problem of determining such contributions. From a historical point of view, the first expression for this term was given by Leslie and Gillan [65], when they made the assumption that a charged defect induces a point-like charge distribution. Because such charge distributions are not isolated systems, the spurious Coulomb interaction was written in terms of the Madelung constant, α_{m} [66],

$$\Delta E^{\,\mathrm{elect}} = -\frac{\alpha_{\mathrm{m}} q^2}{2\varepsilon L}, \tag{2.79}$$

where L is the lattice parameter of the cell, or the distance between point-like distributions; and ε the dielectric constant of the solid. Having the above monopole correction in mind, it is evident that because of the long-range character of the Coulomb interaction, slow convergence with respect to the size of the cell is expected. We also notice that within this point charge model, higher order terms in the multipole expansion can be added to expression 2.79. The multipole expansion as the electrostatic correction to the charged defect formation energy, $\Delta E^{\,\mathrm{elect}}$, is often referred to as the Makov-Payne correction scheme [67]. On the second correction term, the simplest scheme is again to align KS eigenvalues obtained for the charged defective and the neutral *pure* cells, giving the resulting absolute shift as ΔV, Chapter 2 [58]. We note that in the case of defective charged cells, the misalignment between KS DOS is consequence of two different *artifacts* of the calculation: the atomic relaxation or elastic contributions (also observed

in a neutral defective cell), and the induced variation of the electrostatic potential when charging the cell. More *sophisticated* schemes to accurately describe both energy corrections terms have been proposed over the years, see work of [68, 69], including the effort to find a link between the potential alignment and the electrostatic correction.

2.4.3 Defect properties subject to the DFT band gap problem

The above introduced quasiparticle approach to study materials properties (section 2.3) shows the limitations of mean-field theories, such as DFT, to describe certain many-body effects. Because of the notorious underestimation of electrical band gaps or particle-excitations, KS states computed on a defective cell, or even DFT total energy differences at different charge states, poorly describe optical or electronic properties of the center. Furthermore, occupation of localized states within the band gap might suffer from the Self-Interaction problem and so other physical properties computed from DFT total energies might also be compromised. Ideally, one should extend the estimation of single-quasiparticle energies to the description of the total energy of the system, like in the case of Hartree-Fock and the Density Functional Theory, allowing an exploration of a PES which accounts for all many-body effects. However, in practice, these calculations are computationally very expensive, particularly in the case of defective cells, and so single point calculations at critical points of the PES (defined with a mean-field approach) are usually performed. Defect geometries are therefore not optimized at the MBPT level of accuracy, but at the accuracy level of the employed exchange-functional. The error on the local defect geometry is considered small due to the good description of the local symmetry by DFT, but many-body effects might become relevant in the subtle energy differences at difference ionic configurations.

Both the Self-Interaction problem and the concavity of the employed functional (section 2.2.4) are especially relevant when determining the CTLs for a given center. Besides the finite-size effects and the spurious interaction between charged defects, the underlying DFT band gap problem also needs to be taken into account when determining $\Delta E^{q,q'}_{\mathrm{DFT}}$ in equation 2.78. Among the proposed schemes to overcome such limitation, we distinguish the use of hybrid functionals, the development of the Marker Method and finally, the inclusion of many-body corrections. Hybrid functionals are one of the reference methods to compensate the DFT self interaction problem, by introducing a

certain fraction, α, of the exact Hartree exchange (equation 2.37). Because they have proven to give accurate band gaps for semiconductors, they are expected to accurately locate defects states within their respective band gaps for a chosen flavor of the functional, tuned by the parameter α. Circumventing the approximations regarding the exchange-correlation potential and the lack of a unified transferable expression, we aim for an exact treatment of the electronic interaction within the many-body perturbation theory, as introduced in the following.

The Marker Method, as an approach to accurately compute CTLs, has been extensively used in the context of point defects in silicon, so we quickly review its bases. The main idea behind this method is to correct the underestimated term, $E^{q}_{\mathrm{DFT}}[\mathrm{Si,d}] - E^{q\pm1}_{\mathrm{DFT}}[\mathrm{Si,d}]$, by introducing an empirical shift. It is based on the assumption that two defects with, and we quote Chapter 3 [58], "similar electronic properties", induce the same absolute error when determining DFT energy differences at different q. It is assumed that if for a certain marker, M, there is a good experimental reference for its CTL, then the energy correction is given by,

$$\Delta_{\mathrm{M}} = \mathcal{E}(0/-)_{\mathrm{M}} - \left(E^{-1}_{\mathrm{DFT}}[\mathrm{Si,M}] - E^{0}_{\mathrm{DFT}}[\mathrm{Si,M}]\right). \tag{2.80}$$

The unknown acceptor level for the defect under study is then,

$$\mathcal{E}(0/-)_{\mathrm{d}} = \Delta_{\mathrm{M}} + \left(E^{-1}_{\mathrm{DFT}}[\mathrm{Si,d}] - E^{0}_{\mathrm{DFT}}[\mathrm{Si,d}]\right). \tag{2.81}$$

As mentioned in Chapter 3 [58], several bold assumptions are made in order to obtain the above equation. Recalling the definition for the CTL in terms of formation energies, $E^0_f = E^-_f$, it should be clear that both correction terms due to the spurious electrostatic interaction between defects, $\Delta E^{\mathrm{elect}}$ and ΔV, need to be included both for the defect and the marker. It is therefore common to assume that these contributions are equivalent for both systems, canceling out in the final expression 2.81. On the other hand, establishing which marker is adequate for a given defect needs an already preconceived idea of its energy levels or the use of a rather general marker, whose *electronic equivalency* with the studied defect might be strongly questioned. We also remark that the Marker Method (MM) is an empirical method, and not a full *ab initio* approach.

2.4.4 The DFT + GW combined approach

In 2009, P. Rinke *et al.* [70] proposed a combined LDA + GW scheme to compute formation energies avoiding the DFT band gap problem. The

idea behind the method is to minimize the DFT self-interaction problem, very prominent in defective cells, by including many-body corrections. The method establishes that for any generic defect, d, formation energies at different charge states are safely computed with respect to E_f^q, if at charge q the defect does not present occupied states in the band gap. From the definition of formation energy, given in equation 2.77, the energy E_f^{q-1} can be estimated using E_f^q as starting point, by simply computing E($\mathbf{g}^{q-1}, q-1$) - E($\mathbf{g}^q, q$) - μ_e, where $\mathbf{g}^q$ and $\mathbf{g}^{q-1}$ are the equilibrium ionic geometries at charge states q and $q-1$ respectively. Regarding the employed notation, we remark that the defect state $q-1$ corresponds to the N+1 number of particles state with respect to charge state q. As represented in the coordination diagram of Figure 2.13a, the energy difference E($\mathbf{g}^{q-1}, q-1$) - E($\mathbf{g}^q, q$) can be split into two energy contributions: (1) the vertical transition E($\mathbf{g}^q, q-1$) - E($\mathbf{g}^q, q$), at constant equilibrium atomic geometry, $\mathbf{g^q}$; and (2) the ionic relaxation at constant electronic occupation, given by E($\mathbf{g}^q, q-1$) - E($\mathbf{g}^{q-1}, q-1$). The formation energy at $q-1$, can then be written as,

$$E_f^{q-1} = E_f^q + \mathrm{EA}(\mathbf{g}^q, q) + \Delta E_{\mathrm{relax}}^{q-1} - \mu_e, \tag{2.82}$$

where EA($\mathbf{g}^q, q$) is the first electronic affinity computed at charge state q, describing by construction the energy difference in (1), and $\Delta E_{\mathrm{relax}}^{q-1}$ is the relaxation energy given to the lattice, (2). If the the formation energy at charge state $q-2$ is also to be computed, its expression is straightforward,

$$E_f^{q-2} = E_f^{q-1} + \mathrm{EA}(\mathbf{g}^{q-1}, q-1) + \Delta E_{\mathrm{relax}}^{q-2} - \mu_e. \tag{2.83}$$

So far we have considered a generic defect at charge states q, $q-1$ and $q-2$, without discussing the defect charge neutrality. We however note that for the majority of point defects, the reference electronic occupation corresponding to an empty trap does often not correspond to the neutral state.

The DFT + GW approach also constitutes the perfect scheme to avoid the DFT band gap problem when computing CTLs. Continuing the description of the generic defect, d, the CTL $\mathcal{E}^{q/q-1}$, can be safely estimated as,

$$\mathcal{E}^{q/q-1} = \mathrm{EA}(\mathbf{g}^q, q) + \Delta E_{\mathrm{relax}}^{q-1} - \mathrm{IP}_{\mathrm{TVB}}. \tag{2.84}$$

Being aware of the spurious interaction between charged defects (section 2.4.2), we note that total energy correction, $\Delta E^{\mathrm{elect}}$, is not needed, since it cancels out when $\Delta E_{\mathrm{relax}}^{q-1}$ is estimated. Regarding the second correction, or the potential alignment correction, ΔV, the electrostatic error in the individual KS eigenvalues is most likely transferred to the QP eigenvalues, and so, it

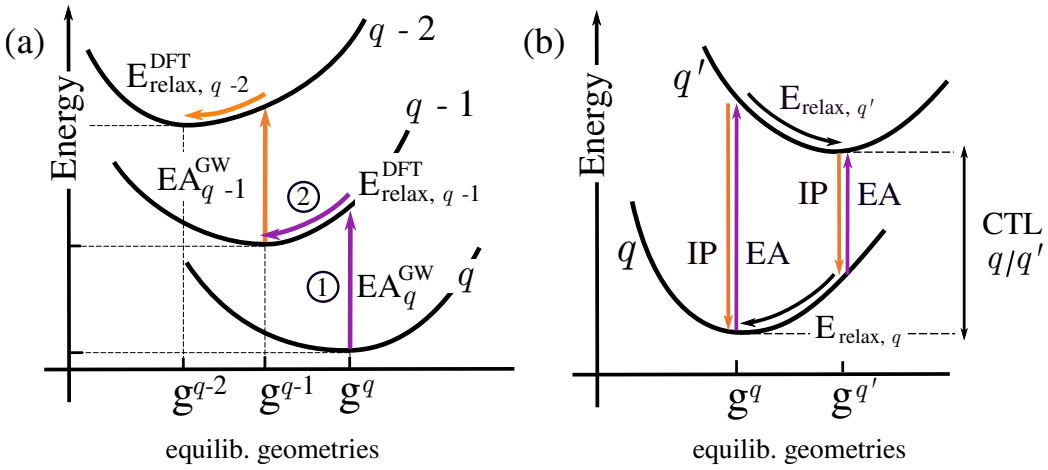

Figure 2.13: Coordination diagram illustrating the DFT + GW combined approach to estimate formation energies at charge states $q+1$ and $q+2$ (a). Coordination diagram showing the four possible paths to compute the CTL $\mathcal{E}^{\,q/q'}$ within the DFT + GW method (b).

needs to be taken into account when specifying ionization potentials and electronic affinities with respect to the $\mathrm{IP}_{\mathrm{TVB}}$ in a defective charged cell. We now remark another aspect of the DFT + GW approach; the fact that any CTL $\mathcal{E}^{\,q/q'}$ can be computed through four different paths (represented in Figure 2.13b), leading to the equality,

$$\begin{aligned}\mathcal{E}^{\,q/q'} + \mathrm{IP}_{\mathrm{TVB}} &= \mathrm{EA}(\mathbf{g}^q, q) + \Delta E^{\,q'}_{\mathrm{relax}} = \mathrm{IP}(\mathbf{g}^q, q') + \Delta E^{\,q'}_{\mathrm{relax}} = \\ &= \mathrm{EA}(\mathbf{g}^{q'}, q) + \Delta E^{\,q}_{\mathrm{relax}} = \mathrm{IP}(\mathbf{g}^{q'}, q') + \Delta E^{\,q}_{\mathrm{relax}}.\end{aligned} \tag{2.85}$$

Practical issues and error avoidance regarding the existence of these four paths is discussed in detail in Chapter 5, where numerical examples for a catalog of defects in silicon iare provided.

Examples of DFT + GW calculations are rarely found in the literature due to the computational challenge of performing GW calculations in large supercells. The method has been exploited to estimate accurate CTLs in the context of crystalline silicon for the self-interstitial defect in the seminal work of P. Rinke [70], where many-body corrections were obtained on top of LDA, a GW@LDA calculation; or for the interstitial carbon impurity [71], employing a GW@HSE approach (HSE being a hybrid functional). We also remark the early work on charged oxygen-related defects in amorphous silica [72] and the case of the carbon vacancy in SiC [73], both based on GW@LDA calculations. Besides determining the accuracy of the approach by comparing

estimated CTLs with experimental evidence, in [70], the formation energy of the neutral silicon interstitial was also matched to diffusion Monte Carlo calculations; and in [73], energy barriers of the transformation V_{Si} into $V_C C_{Si}$ were corrected by performing GW calculations at the saddle point geometry, obtaining activation energies in agreement with annealing experiments.

Chapter 3

Unraveling iconic centers in silicon: linking atomistic modeling with experiments

EPR experiments can reveal much about the electronic and mechanical properties of the defects, shedding valuable insight into their role in altering the macroscopic properties of the solids in which they are incorporated

G. D. Watkins (1975)

Atomistic modeling should be the key asset to guide the identification of defects in electronic devices whenever characterization techniques are inconclusive. As a general idea, comprehensive full theoretical models, contrary to experimental techniques, allow to explore an infinite number of physical conditions and/or parameters of the system, providing a complete characterization of the center. The increase of computational power, together with the development of affordable algorithms, made DFT-based methods the perfect approach to construct a quantitative model for defects in semiconductors. However, the existence of differently converged parameters and flavors of the exchange-correlation functionals has transformed DFT studies of defects in silicon into numerical experiments; limiting the analysis to comparing the estimated defect properties to measured quantities in order to validate the choice of the employed set of computational parameters. In the present work, we take one step back, taking simple symmetry-based models as the starting

point of our theoretical analysis. Once the fundamental physics of the center is understood, computational methods are employed to quantify the model, linking the atomistic modeling with different characterization techniques.

The need to guide *ab initio* calculations with simple theoretical models is the main conclusion of the present chapter, throughout which we present the cases of the titanium impurity (section 3.1) and the E-center in silicon (section 3.2). In section 3.1, we question the long-established degrading power of transition metals (TMs) in silicon by considering the possible existence of an impurity-induced band in Ti-doped silicon, capable of enhancing the efficiency of silicon-based solar cells. Our theoretical analysis of the center starts by revisiting the phenomenological model proposed by Ludwig and Woodbury, based on simple symmetry considerations and sustained by EPR spectroscopy. We then quantify the model within a mean-field approach, explicitly showing the correspondence between the two theories, grounding the basic features of the center. Only then, state-of-the-art simulations with the inclusion of many-body effects are performed, investigating the hypothesis of photon-absorption enhancing efficiency in Ti-doped silicon photodiodes. From an opposite perspective, the degrading effect of transition metals in silicon-based devices as isolated impurities is confirmed within a pure first-principles approach under the DFT+GW method.

In section 3.2, we analyse the relevance of the silicon E-center for several technologically relevant processes, like the Dark-Current Random Telegraph Signal in image sensors. The former might be defined as a burst noise in electronic devices commonly linked to the finite-temperature dynamics of crystallographic defects, motivating an extensive exploration of the potential energy surface at different *temperature regimes*. Our DFT and NEB calculations, in excellent agreement with EPR spectroscopy, provide new insight into the defect dynamics, and in particular into the vacancy-mediated dopant diffusion mechanism in silicon. The success of our computational investigation relies on the molecular-orbital model presented by Watkins, whose simple symmetry arguments predicted the Jahn-Teller effect, responsible for the basic features of the center. We unequivocally confirm such Jahn-Teller model by quantifying the electronic excitations within the molecular-orbital picture, assigning the transitions to measured infrared bands.

3.1 Degrading defects or photon-absorption-enhancing centers? The case of Titanium

From a common perspective, transition metals (TMs) in silicon are known to introduce several *deep levels* in the semiconductor gap, reducing the efficiency of silicon-based devices through the so-called non-radiative transitions or the SRH recombination process [4]. In the particular case of silicon photovoltaic devices, their eventual promotion to be widely used required a large-scale manufacturing process characterized by low cost, lower purity silicon samples [74, 75], consciously growing contaminated-silicon wafers containing 3d TMs like titanium, copper and iron. There was therefore a motivation to determine a *tolerable* contamination which did not degrade the solar-cell performance. Among the considered impurities, titanium was said to severely impact the cell efficiency, since an occurrence of $2{\cdot}10^{14}$ cm^{-3} resulted in a 63% performance-loss [75]. From an opposite perspective, Olea *et al.* [76] presented experimental evidence that Ti can be implanted in silicon in concentrations above 10^{18} cm^{-3}, proving the possibility that Ti-doped silicon could serve as an intermediate-band material, increasing the efficiency of the third generation of solar cells (the so-called intermediate-band (IB) solar cell [77, 78]). The basic idea behind such IB-materials is to intentionally dope the sample with an impurity center, which induces a partially filled state within the forbidden gap (Figure 3.1). Photons with *insufficient energy* with respect to the E_g are then still able to pump electrons from the valence band (VB) to the defect-related band (IB) [77]. Two photon-absorption paths can therefore co-exist: the direct excitation from VB to CB (3 in Figure 3.1) and the IB-mediated excitation (1 and 2 in Figure 3.1), triggered by *below band gap photon absorptions*. One can therefore question at what concentrations titanium is a degrading impurity or an efficiency-enchaining center in silicon-cell photovoltaic devices. Luque *et al.* [79] postulated that a delocalization of the intermediate band can be obtained for a sufficiently large density of impurities, allowing the trapped electronic density to be extended throughout the crystal. This statement has been criticized by [80], but supported by measurements in Ti-doped silicon [81, 82, 83]. Two central questions are therefore to be assessed by theoretical considerations: the existence of an optically-active Ti-related band within the silicon gap and the possibility of a localized-delocalized state transition (referred to as an insulator-metal transition in [84]), guaranteeing the prevention of non-radiative transitions.

Historically, transition metals in silicon have been extensively characterized as degrading impurities, targeting their capability to capture and/or

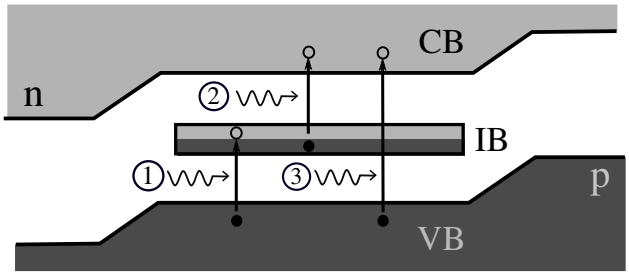

Figure 3.1: Schematic band structure of an intermediate-band-material-based solar cell, adapted from [78]. (1) and (2) represent photon absorption transition with energies lower than E_g, whereas (3) represents above band gap photon absorption.

release free carriers through non-radiative transitions. Pioneer EPR studies [85] already revealed that TMs could be found at different charge states (ranging from +2 to -1), indicating the ability of such impurities to interact with the electronic reservoir. Further analysis of the EPR spectrum allowed Ludwig and Woodbury [86] (LW) to postulate that TMs in silicon have a preference for tetra-folded atomic conformations, since they mostly appear at substitutional sites and tetra-interstitial sites. As explicitly shown in Figure 3.2, at both lattice positions, the TM is then surrounded by four nearest neighbors or silicon atoms 1, 2, 3 and 4, whose interatomic distances $d_{\mathrm{Ti-Si}_n}$ were established to be equivalent for all n, defining a local geometry with point-group symmetry T_d [86]. Moreover, by monitoring the interaction of unpaired electrons with an external magnetic field, they observed that TMs had a preference for large spin values, being S often larger than the usual 1/2 for a single unpaired electron and 0 for a close-shell configuration. Interstitial manganese, $\mathrm{Mn_I}$, for example, presented spin values of 5/2, 2 and 3/2 at charge states +2, +1 and 0 respectively. As a generalization of the substantial number of EPR spectra collected for different TMs, an atomistic model regarding the electronic configuration of TMs, explaining the observed magnetic properties was proposed (details in section 3.1.1). In a few words, the so-called Ludwig-Woodbury model establishes that the isolated-atom configuration $4s^2 3d^n$ is modified when TMs are embedded in the diamond lattice as follows: the five 3d orbitals are filled with n + 2 electrons at interstitial position, whereas, they are occupied by n - 2 electrons at substitutional sites, since the remaining four electrons contribute to the tetra-folded Ti-Si bonds. The 3d states are therefore responsible for the TMs electronic activity, *pushing* the 4s states higher in energy, into the conduction band. It was further postulated that 3d states split according to the electrostatic repulsion with nearby silicon atoms into a doublet (e-states) and a triplet (t_2-states), with

$\epsilon_e < \epsilon_{t_2}$, for a substitutional configuration, whereas $|\epsilon_{t_2} < \epsilon_e|$ for an interstitial position. The absolute magnitude of the energy splitting, $\epsilon_{t_2} - \epsilon_e$, was assumed small, singly filling both e and t_2 states before forming electronic pairs (Figure 3.2). In other words, the Coulomb repulsion between two electrons whose densities are spatially equivalent is larger than the splitting of the 3d states, preserving Hund's principle. The LW model was first sustained by the observed EPR spectrum for V^{2+}, $Cr^{+,0}$, $Mn^{2+,+,0}$, $Fe^{+,0}$, Ni^{+} at interstitial positions; and Cr^0, $Mn^{+,2-}$ at substitutional positions, where the notation TM^q is employed (with q the charge state of the impurity). Later EPR investigations [87] revealed a spin value equal 3/2 for positively charged titanium at interstitial position, also consistent with the model.

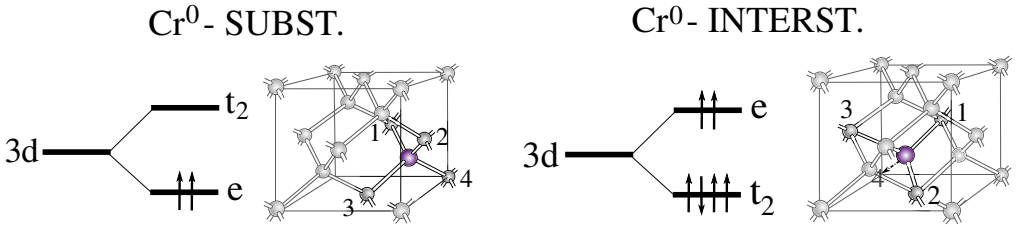

Figure 3.2: The Ludwig-Woodbury model for 3d Transition Metals in silicon. Electronic configuration for neutral chromium at both substitutional (left) and tetrahedral-interstitial (right) positions. The four nearest neighbors to the TM are explicitly marked; silicon atoms 1, 2, 3 and 4.

In alignment with the variety of charge/spin values reported by Ludwig and Woodbury, DLTS spectroscopy (*e.g.* [4]) revealed that most of the 3d TMs introduce up to three *deep* levels, being present at charge states +2, +1, 0 and -1. The existence of multiple trap levels, confirmed for various TMs and by different independent measurements (*e.g.* [4]) is the main argument to sustain the degrading power of these metallic impurities in silicon-based devices. In the specific case of Ti, as already introduced in section 1.3.3, three levels have been consistently reported for Ti_I; a double donor at E_V + 0.29-0.32 eV [28, 29, 30, 26, 27, 24], a single donor at E_C - 0.24-0.28 eV [28, 29, 30, 26, 27, 24] and a single acceptor level E_C - 0.08 eV [26, 27, 24]. A fourth level at E_V + 0.51-0.55 eV has also been reported [29, 30, 27] and assigned to interstitial Ti, reconsidering the position of the double donor level and hence questioning the existence of a triple donor level. Substitutional titanium, on the other hand, is known to be electronically inactive, since no deep levels have been reported for the center [4]. It is precisely such difference between the electronic properties at both sites in the lattice (*i.e.* Ti_I

and Ti_S), that allowed to unequivocally determine their relative occurrence, concluding that Ti in silicon is mainly found at interstitial position. Note the employed notation: TM_I and TM_S for tetra-interstitial and substitutional positions.

On the theoretical side, early density-functional-theory-based calculations [88, 89] confirmed the fundamentals of the LW framework or the magnetic properties at different charge state and atomic site. They however established that early TMs at interstitial position (namely, titanium and vanadium) presented lower spin values of 1 and 1/2 at charge states $Ti_I^{0,-}$, $V_I^{+,0}$, than the predicted 2 and 5/2. Later first-principles studies [90, 91, 92] agreed on such magnetic properties, focusing their work on the degrading nature of the impurities by estimating their CTLs, investigating the link with DLTS activation energies. From a different perspective, computational approaches have also been used to investigate the possibility of Ti-doped silicon being an intermediate-band material [93, 84, 94]. In [93, 84], *different concentrations* of the impurity in silicon have been modeled by performing PBE calculations on cubic defective cells containing from 64 to 512 atoms. Variations on the defect-related KS eigenvalues on the energy density of states obtained for different regimes led them to conclude that Ti can effectively be used to dope silicon and the third generation of solar cells. Besides questioning the validity of their approach to simulate a disorder doped semiconductor with a set of identical defect replicas, a unique theory addressing at the same time the degrading effect and the photon-absorption enhancement in photovoltaic devices by Ti-contamination is still missing.

In the current section, our *ab initio* characterization of titanium in silicon is presented, carefully detailing the methodology employed throughout this thesis to represent/determine certain defect properties. Throughout this section, we also established the general comparison between the numerical investigation of point-like defects and experimental values at different levels of approximation: In section 3.1.2, structural properties evaluated within standard DFT in the PBE approximation are compared to EPR measurements, confirming the symmetry of the defect-related orbitals and the distortions triggered in the surrounding lattice. In section 3.1.3, optical and electronic properties are evaluated with the inclusion of many-body effects in the form of the GW approximation, tentatively assigning infrared absorption bands to estimated charged excitations. Finally, in section 3.1.4, we determine the *deep levels* of interstitial titanium in silicon within the DFT+GW combined approach, establishing a one-to-one correspondence with DLTS activation energies. Our *ab initio* theoretical picture, in contrast with previous studies, is

guided by long-standing symmetry-considerations (section 3.1.1), providing new insight into the defect finite-temperature dynamics, and a new perspective of its degrading power *versus* its photon-absorption-enhancing capabilities if implanted in solar cells.

3.1.1 Transition metals subject to tetra- and octa-hedral fields: symmetry considerations

The success of the phenomenological LW model when predicting the measured spin value relies strictly on the filling of the TM 3d shell. Ludwig and Woodbury did however rely on previous theoretical investigations when discussing the origin and inversion of the 3d orbitals splitting at substitutional and interstitial positions. We cite, for example, the seminal work of J. D. Duntiz and L. E. Orgel [95], regarding the electronic properties of TM oxides. According to their symmetry-based model, when a TM is subject to an octahedral field, imposed by six negative ions surrounding the TM, the degeneracy of the five 3d states is broken depending on their spatial orientation with respect to the surrounding ions (Figure 3.3B). Orbitals with quadratic representations z^2 and x^2-y^2, oriented towards the negative ions, are less stable than the t_2-states, which point in the directions where the electrostatic repulsion is minimized. If, on the other hand, the TM is surrounded by four negative ions, placed at the vertices of a regular tetrahedron, within a simple electrostatic-repulsion treatment the levels are inverted with respect to the ortahedral field. Luwdig and Woodbury applied the model for TMs subject to tetrahedral and octahedral fields to TMs in silicon, by stating that even if at both substitutional and interstitial sites the TM presents four nearest neighbors (Figure 3.2), the six second neighbors at interstitial position are capable of destabilizing the doublet, favoring the t_2 states. In Figure 3.3A we show the positions of both second and first neighbors to the interstitial TM in the silicon lattice, as well as the x, y, z axis according to which the directionality of the 3d orbitals is considered (Figure 3.3B). The t_2 states xz and yz are not represented, but they are analogous to the xy state in the corresponding perpendicular planes. The splitting of 3d states is only confirmed by EPR spectroscopy in a rather *indirect way*, leaving the door open to sustain and quantify the model within a first-principles approach.

Before concluding, we note that a symmetry-based model allowed J. D. Duntiz and L. E. Orgel [95] to consider perturbations of the crystal fields upon structural distortions of the surrounding negative ions. In the case of the octahedral field, if the two atoms along the z-direction are displaced

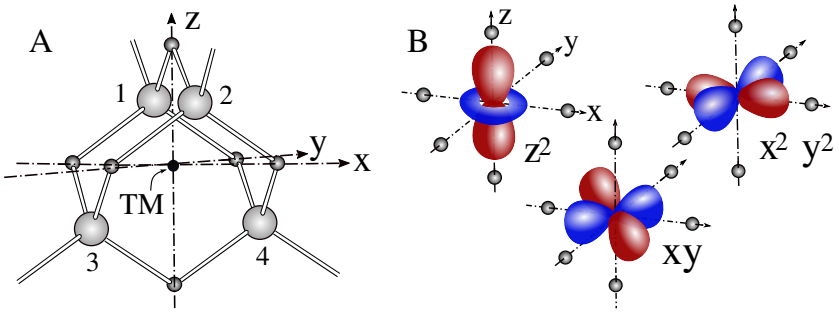

Figure 3.3: (A) TM at tetrahedral-interstitial position in the silicon lattice. First and second neighbors are represented in light grey (atoms 1, 2, 3 and 4) and with smaller dark grey circles respectively. (B) Quadratic representations of 3d states z^2, x^2-y^2 and xy, oriented according to the x, y z axis imposed by the TM second nearest neighbors.

farther away from the TM, the degeneracy of the doublet and the triplet is lifted, being $\epsilon_{xz} = \epsilon_{yz} < \epsilon_{xy}$ for the t_2 states, and $\epsilon_{z^2} < \epsilon_{x^2-y^2}$ for the more energetic doublet. Such symmetry-breaking mechanism of orbitally degenerated systems is commonly referred to as the Jahn-Teller effect, since in 1937 H. A. Jahn and E. Teller showed that any non-linear molecule is unstable upon degeneracy of molecular orbitals at static equilibrium. These systems therefore present at least one symmetric axis along which the molecule may distort in order to lower its energy. In the context of point defects in semiconductors, symmetry-breaking atomic distortions are also referred to as Jahn-Teller distortions, in analogy with a molecule embedded in a dielectric medium, with dielectric constant, ϵ_{host}. In other words, the degeneracy of defect-induced states might trigger local reconfigurations in the lattice as the one showed in Figure 2.2.2 for the silicon mono-vacancy.

3.1.2 Ground state electronic properties *vs.* EPR spectroscopy

The first ground state property typically targeted when numerically studying defects in silicon is the DFT optimized geometry at different charge states. The description of different local configurations by different computational approaches is often validated or proved wrong by comparing the paramagnetic electronic configurations to EPR spectroscopy. Even if such link has demonstrated to be a strong validation of the employed set of numerical parameters, it is limited to paramagnetic centers, leaving the estimated configuration for paired states at the predictive level. In the case of 3d-TMs

in silicon, total DFT energies have been exploited to determine the optimal spin values at different charge states. In the case of interstitial titanium at charge states +1, 0, -1 spin-unrestricted calculations [90, 91, 92] estimated the ground state spin values to be 1, 3/2, 1/2 respectively; whereas at substitutional position, S=0, 1/2 for charge states 0 and -1. They also reported a highly symmetric tetrahedral configuration (*e.g.* with point-group symmetry T_d) independently of the charge state and the position in the lattice. Even though these spin values are consistent with EPR spectroscopy for Ti_I^+, and the Ludwig-Woodbury model for $Ti_I^{0,-}$ and $Ti_S^{0,-}$, these theoretical models were *blind* to the underlying electronic structure of the defect. In other words, theoretical models purely based on total-DFT-energies typically fail to give a complete picture of the center, since no effort to actually describe the defect-related states is made.

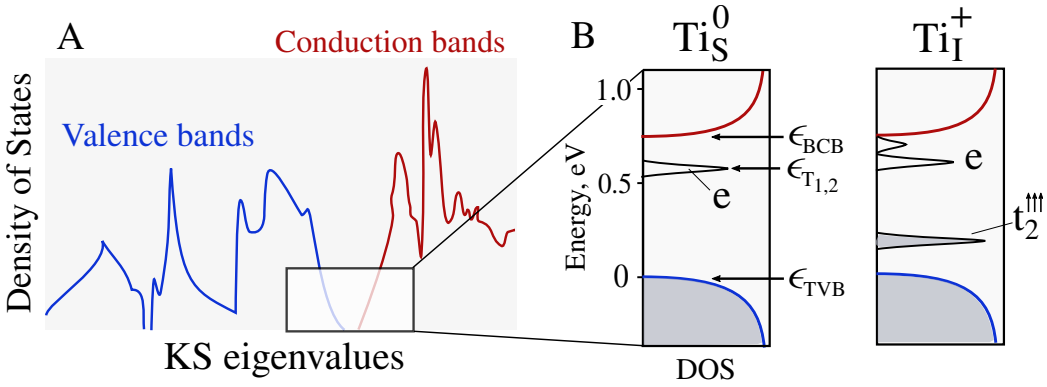

Figure 3.4: (A) KS energy density of states (DOS) for crystalline silicon. (B) KS DOS of two silicon supercells containing a neutrally charged titanium impurity at substitutuinal position, Ti_S^0; and a positively charged Ti at interstitial position, Ti_I^+ respectively. Trap states are named according to the Ludwig-Woodbury model for TM in silicon; states e and t_2. In the case of Ti_I^+, it consists of the spin-polarized projected DOS, $\epsilon_i\,(\sigma =\uparrow)$. Filled states represent the occupied KS orbitals, determined from a PBE-based calculation.

A stronger correspondence between the LW model and the numerical calculation can be made through a detailed investigation of the KS eigenvalues and eigenfunctions, which are expected to reproduce the main features of the defect electronic structure; namely, the number, degeneracy and form of the localized states. As shown in the KS energy density of states in Figure 3.4A, among all the possible defect-induced states, we focus our attention on the band-gap energy region of the host material, since nearby localized states are

responsible for the fundamental structural properties of the defect. In order to analyze the KS energy density of states of Ti_S^0 and Ti_I^+, in Figure 3.4B we represent a superposition of two sets of KS eigenvalues computed for the pure silicon cell containing 216 atoms and the defective cell sampled at Γ. In order to avoid size-effects and spurious interactions between charged defects, a rigid shift, ΔV is applied to the defective DOS according to *e.g.* Chapter 2 [58]. In the case of substitutional Ti, two degenerate states $\epsilon_{T_{1,2}}$ are obtained within the crystal band edges. These unoccupied KS states are located close to the BCB and they are candidates to be Ti-induced states. Similarly for the DOS for interstitial Ti, a triplet of occupied states, responsible for S = 3/2, and a more energetic unoccupied doublet of states is obtained within the host BG.

Even if the degeneracy and relative energy position of these KS states can be linked to the LW model, a solid final correspondence can be established by analyzing the symmetry of the real-space projection of the KS eigenstates, $\Phi_{KS}(\mathbf{r})$ (Figure 3.5). In the case of substitutional Ti, our numerical simulations show that the doublet effectively corresponds to the e-states described by the LW model, since they present spatial distributions z^2 and x^2-y^2, avoiding the Ti-Si bonds. At the PBE level of theory, we therefore reproduce the level ordering predicted by the simple theoretical model, locating the five 3d states below the symmetric 4s orbitals and the splitting of the 3d states; $\epsilon_e < \epsilon_{t_2}$. In the case of interstitial Ti, the localized states do however not correspond to the predicted representations xy, xz and yz, but to a linear combination of the former, here-named as a singlet a_1 and a doublet e (Figure 3.5). The computed t_2 states are oriented in order to avoid the Ti second nearest neighbors (located along the x, y, z axis), being partially located within the Ti-Si bonds. The more energetic doublet is unequivocally assigned to the e-states since they are analogous to the ones plotted for Ti_S, oriented along the x, y, z axis. Finally, the unnamed singlet state located between the e-doublet and the BCB is actually a bulk state, whose energy has been lowered artificially by fictitious elastic interactions, artifact commonly referred to as the *band gap narrowing*. The electronic configuration for Ti_I^+ is then proved to be $t_2^{\uparrow\uparrow\uparrow}$ (or $t_{2\,a_1}^{\uparrow}\ t_{2\,e}^{\uparrow\uparrow}$), in alignment with the simple symmetry-based models.

Before concluding, we remark the limitation of the employed mean-field theory, for which the *approximated* silicon BG, $\epsilon_{BCB} - \epsilon_{TVB}$, is as expected (section 2.2.1), smaller than the measured BG for silicon, E_g = 1.17 eV. The estimated position of defects states within the silicon BG is therefore compromised by the DFT band gap problem. In the case of substitutional Ti, for example, the defect is known to be electronically inactive, not introducing

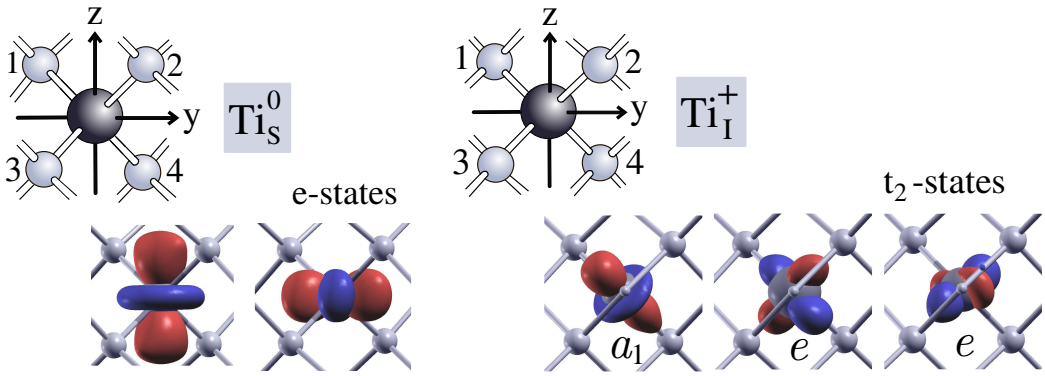

Figure 3.5: Titanium-related defect states in silicon. Isosurfaces of $\Phi_{\mathrm{KS}}(\mathbf{r})$ for both e-states for $\mathrm{Ti}_{\mathrm{S}}^{0}$ and t_2-states for interstitial $\mathrm{Ti}_{\mathrm{I}}^{+}$, computed within the PBE approximation, are shown. Both systems present T_d geometries, with four equivalent distances between Ti and its nearest silicon neighbors, equal to 2.51 Å and 2.48 Å for $\mathrm{Ti}_{\mathrm{S}}^{0}$ and $\mathrm{Ti}_{\mathrm{I}}^{+}$ respectively. One second neighbor is represented in the case of interstitial Ti, shared by the Si atoms 2 and 3.

trap states in the BG, contradicting our PBE calculation.

The Jahn-Teller effect in trapping impurities from first-principles

After carefully assigning the KS-localized states to the ones described by the LW model for the precursor charge states $\mathrm{Ti}_{\mathrm{S}}^{0}$ and $\mathrm{Ti}_{\mathrm{I}}^{+}$, further understanding of the center can be sought by charging/discharging the defect. In other words, one might expect that changes in the electronic occupation of the e-doublet and the t_2-triplet are unstable upon distortions of the highly symmetric T_d configuration. If an electron is added to Ti at substitutional position, $\mathrm{Ti}_{\mathrm{S}}^{-}$, a PBE-based optimized structure relaxation reveals an inward regular expansion of the Ti first silicon neighbors, since the interatomic distance $d_{\text{Si-Ti}}$ is decreased from 2.51 Å at neutral charge state, to 2.49 Å at negative charge state. Even if the T_d symmetry seems to be preserved, we notice that because the e-states are oriented towards the second neighbors, the Jahn-Teller distortion occurs within the second shell of the impurity. The unpaired electron, localized at the orbital x^2-y^2 triggers a relaxation of the four second neighbors located within the xy plane towards the impurity. The effect of such symmetry rupture is rather small, since the length-difference between both interatomic distances is barely 0.02 Å. In the case of interstitial Ti, small anisotropic relaxations are obtained within the impurity first shell in the form of a C_{3v}-distortion, since one of the nearest atoms (atom 4 in Figure 3.6) is responsible for the symmetry-breaking mechanism. The new

distorted structure is named according to point-group symmetry considerations, as later detailed in Chapter 4, while we now investigate the implications of the here-described electron-lattice coupling. At charge state +2 (or configuration d^2), one of the four nearest silicon atoms moves far away from the impurity, constituting an elongated tetrahedron with $d_{\text{Ti-Si}_4} > d_{\text{Ti-Si}_{1,2,3}}$ (Figure 3.6). This new local geometry, energetically favors two t_2 states over the third one, being $\epsilon_e < \epsilon_{a_1}$, and so resulting in an electronic structure, $t_{2e}^{\uparrow\uparrow}$. If on the contrary an electron is added to the precursor positive state, achieving charge neutrality, Ti_i^0 or d^4, the degeneracy of states t_2 is broken differently, being $\epsilon_{a_1} < \epsilon_e$ (Figure 3.6). The obtained flattened configuration, $d_{\text{Ti-Si}_1} < d_{\text{Ti-Si}_{2,3,4}}$, has therefore a band structure characterized by $t_{2a_1}^{\uparrow\downarrow}\ t_{2e}^{\uparrow\uparrow}$. If yet another electron is added to the center, the structural relaxation is inverted, obtaining an elongated tetrahedron at negative charge state, with electronic configuration $t_{2e}^{\uparrow\downarrow\uparrow\downarrow}\ t_{2a_1}^{\uparrow}$. From a general perspective, we can conclude that the T_d symmetry is only stable at charge states for which each t_2 state is equally filled; namely, charge states +4 (zero occupation), +1 ($t_2^{\uparrow\uparrow\uparrow}$) or -2 (double occupation, $t_2^{\uparrow\downarrow\uparrow\downarrow\uparrow\downarrow}$). For any other electronic occupation, a spontaneous symmetry-breaking or Jahn-Teller effect in the form of a distorted tetrahedron, which breaks the degeneracy of the 3d-triplet orbitals, is to be expected.

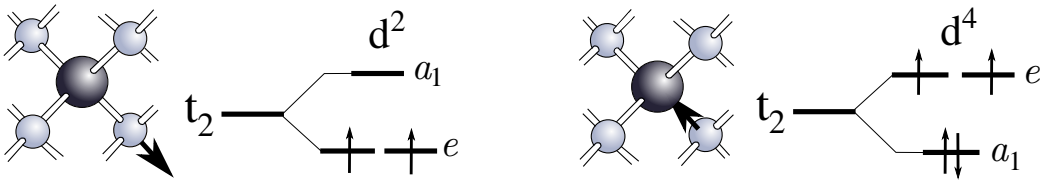

Figure 3.6: Proposed Jahn-Teller effect in the form of a C_{3v} distortion for interstitial titanium. Two senses of the distortion for charge states +2 and 0 or electronic occupations d^2 and d^4 are represented: (left) elongated tetrahedron, E, (right) flattened tetrahedron, F.

The splitting of the t_2 states has been previously considered within different scopes, like the case of transition metals oxides [95], for which the distortion of the octahedral field lifts the degeneracy of the xy, yz, xz orbitals (section 3.1.1). In the context of Ti in silicon, the existence of small distortions in the case of interstitial Ti were hypothesized [90], but never confirmed, since it was insinuated that the employed BO-adiabatic approximation was incapable of predicting such phenomena. Within a DFT+U study [92] a symmetry-breaking mechanism was reported uniquely for the neutral charge state, obtaining an equivalent symmetry as the one described

in the present work. We have however showed a general picture for the spontaneous symmetry-breaking mechanism, concluding that the symmetric T_d configuration is exclusively stable at charge states +4, +1 or -2. At the PBE level of theory, we report a rather small magnitude of the Jahn-Teller distortion ranging from 0.02 to 0.04 Å at charge states +2, 0, -1, certainly questioning the reliability of such local reconfigurations. The existence of the here-described C_{3v} distortions is however consistent with the general Jahn-Teller theorem, which predicts the instability of highly symmetric configurations for *uneven* electronic occupations. Moreover, the Jahn-Teller distortion is source of a non-negligible electron-lattice coupling, which is postulated to be responsible for the non-radiative transitions [22, 23].

Table 3.1: Proposed Jahn-Teller mechanism for interstitial titanium in silicon. The sense of the C_{3v} distortion (elongated, E, or flattened, F) is indicated for different trap occupations or charge states ranging from +4 to −2 (even if $\mathrm{Ti_I}$ is only observed at charge states, $q = +2, \pm 1, 0$). The interatomic distances, estimated within the PBE approximation, are also collected. At charge state +3, the T_d geometry found from simulations is in disagreement with the general JT model. All values are given in Å.

q	+4	+3	+2	+1	0	−1	−2
Trap occupation	Zero	↑	↑↑	↑↑↑	↑↑↑↓	↑↑↑↓↓	↑↑↑↓↓↓
JT distortion	T_d	C_{3v}-F	C_{3v}-E	T_d	C_{3v}-F	C_{3v}-E	T_d
$d_{\text{Ti-Si}_i}$	2.47	2.48	2.49	2.48	2.45	2.49	2.46
$d_{\text{Ti-Si}_{j,k,l}}$	2.47	2.48	2.48	2.48	2.48	2.45	2.46

Further investigation of the symmetry breaking mechanism is conceived by realizing that the distorted T_d geometry induces four equivalent C_{3v} configurations, which under equilibrium conditions are equally probable to coexist. At finite temperature, the defect can therefore reorient, describing the metastable-switching phenomenon. In Figure 3.7, we show the minimum energy path, computed with the CI-NEB algorithm, for the reorientation mechanism. Even if changes in atomic positions of the four nearest silicon atoms are rather subtle, the existence of four minima in the PES is visible by the relative orientation of the t_2 states along the MEP (plots of electronic density in Figure 3.7). At the PBE level of accuracy, activation energies between equivalent minima are equal to 8 meV for $\mathrm{Ti_I}^{+2,0,-1}$. Since the estimated activation energies are significantly smaller than $k\mathrm{T_{RT}}$, we postulate

that interstitial Ti is capable of freely reorient between different distorted tetrahedra at temperatures far below RT, hence making the characterization of the hypothesized symmetry breaking mechanism difficult. We also note that in the case of interstitial Ti, only the EPR spectrum at single positive state has been reported, for which no JT distortion is predicted. Exhaustive explorations of the PES, guided by simple theoretical models, beyond the usual optimal structure relaxation studies, is one of the main contributions of the present work.

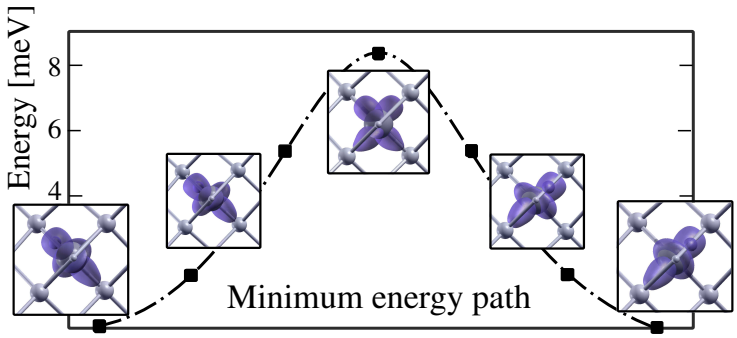

Figure 3.7: Proposed reorientation mechanism for Ti_I^0 in silicon. The Minimum Energy Path (MEP) between equivalent atomic distortions determined for a PBE-energy surface is represented with black squares, whereas the line is a guide to the eye. Electronic densities corresponding to the occupied spin-down projected state are plotted in blue along the MEP.

To summarize, we have proposed a Jahn-Teller model for interstitial Ti in silicon, consistent with long-standing symmetry-considerations and our *ab initio* calculations. The complete picture of the center is constructed by a careful analysis of the symmetry of KS Ti-related orbitals in silicon and the respective degeneracy of the KS states at different atomic distortions. Such investigation is presented opposed to most of previous theoretical models which limit their defect characterization to total DFT energy differences.

3.1.3 Optical and electronic properties with the inclusion of many-body effects

Quasiparticle calculations performed on top of the KS picture account for many-body effects when determining defect properties. In general terms, many-body effects for defects in semiconductors are rarely found in the literature due to the computational expense of the calculation (convergence of Σ_{xc} with respect to the number of empty bands, section 2.3.2). In the case

of point defects in silicon, only a few calculations have yet been reported, namely [70, 71], where the electronic activity of selected centers was evaluated within the DFT+GW combined approach (section 2.4.4). With even less occurrence (to the best of our knowledge), many-body corrections have only been exploited to estimate the measured infrared absorption bands in silicon in [96], where the C-C complex was investigated. As indicated in section 2.3.3 and depicted in Figure 2.11, differences in quasiparticle energies can be assigned to neutral excitations if the electron-hole interaction is small, which can be assumed to be the case of crystalline silicon due to its high macroscopic dielectric constant ($\epsilon_\infty \sim 12.0$). This particular point has been addressed in detail for defects in SiC, for which a joint study of BSE and GW calculations has been performed to characterize excitations involving defect states [97]. Such comparative analysis allowed the authors to estimate the electron-hole interaction energy, being around 0.2 eV for different studied transitions, for a semiconductor with a similar dielectric constant than silicon. In the present thesis, we give a first theoretical insight to neutral excitations involving defect-states in silicon within the GW approximation, leaving the characterization of excitonic effects for future works.

In the case of the titanium impurity in silicon, we show the quasiparticle (QP) energy DOS at both substitutional and interstitial positions in Figure 3.8. Due to the one-to-one correspondance between the KS eigenvalues and the quasiparticle energies (equation 2.67), it is possible to identify the defect-induced QP eigenstates by analyzing the symmetry of $|\Psi_{\mathrm{KS}}(\mathbf{r})|^2$. In agreement with different characterization techniques [4], substitutional titanium does not introduce defect states within the band gap (*i.e.* it is not electronically active), since $\mathrm{EA}_{\mathrm{BCB}}$ is lower in energy than EA_{e}. By comparing the QP DOS with the one previously obtained within the PBE approximation for $\mathrm{Ti_S}$ (Figure 3.4B), we have shown that not only the electrical gap, E_g, is augmented, but also the *correct* level ordering is obtained (states e are moved up into conduction band). At interstitial position, both densities of states are qualitatively equivalent, since trap states $\mathrm{t_2}$ and e are located within the silicon gap. We also show the symmetry breaking mechanism described at the PBE level for the neutral charge state, Ti_I^0, characterized by the electronic configuration, $\mathrm{t}_{2\,a_1}^{\uparrow\downarrow}\ \mathrm{t}_{2\,e}^{\uparrow\uparrow}$. As already described above, the partial occupation of the $\mathrm{t_2}$ states leads to a small distortion of the defect geometry in the form of an elongated tetrahedron, with one of the Si-Ti atomic distances larger than the others. Evidence of such distortion in the GW DOS is the fact that, $\epsilon_{a_1} < \epsilon_e$ for Ti_I^0. The position of the ϵ^{GW} corresponding to defect-induced states within the Si BG allow us to confirm that interstitial Ti is electronically active, introducing more than one charge transition level.

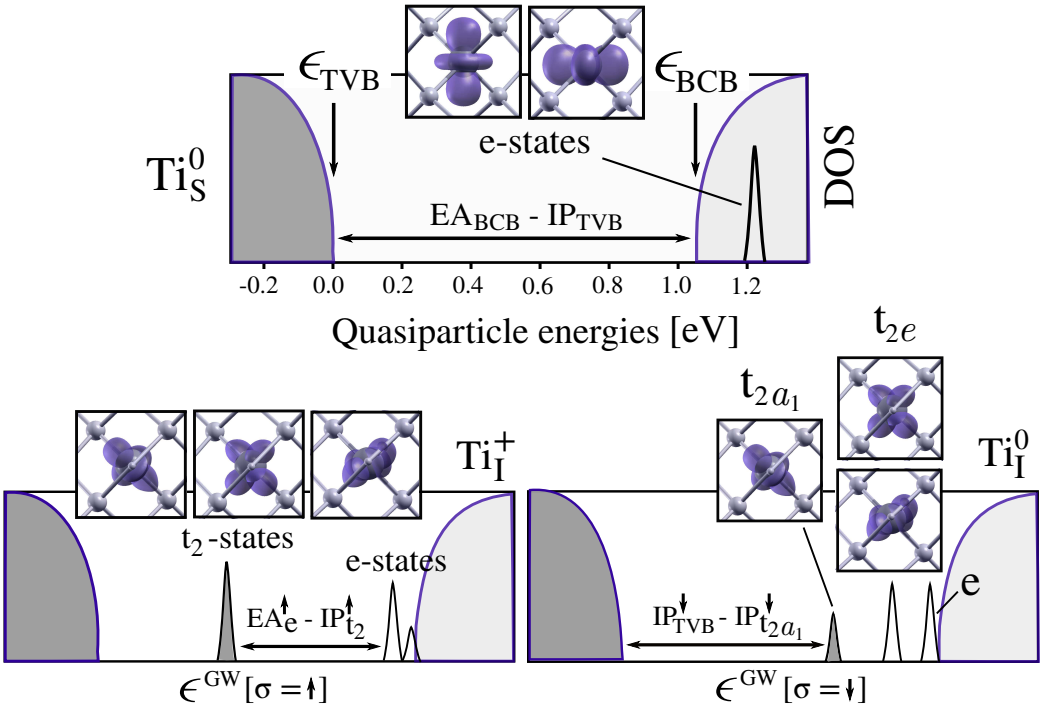

Figure 3.8: Quasiparticle energy density of states for substitutional and interstitial titanium in silicon. Spin-unrestricted GW calculations are performed for Ti_I. Electronic densities in blue correspond to the KS states employed to construct G_0, W_0. Specific electronic transitions are denoted with their respective electronic affinities (EA) and ionization potentials (IP).

Among the previous DFT studies interested in the degrading power of the impurity [90, 91, 92], only in the latest work the electronic structure of the defect was investigated. According to their analysis, only the triplet t_2 states was found to lay within a rather small electrical gap ($E_g \sim 0.7$ eV in [92], Figure 1). On the side of theoretical works postulating the efficiency-enhancement of the impurity, KS energy DOS were plotted in [93], where the identification of KS states with defect-related states is rather unclear and the employed mean-field approach underestimates the band gap considerably. In the same line of analysis, [84] plotted the KS energy DOS within a LDA+U method, postulating that the defect-induced states within the gap had a silicon s and p character, in clear disagreement with our approach.

So far we have merely commented on the relative energy position of ionization potentials and/or electron affinities corresponding to the Ti-related

states, with respect to IP_{TVB} and EA_{BCB}. A quantification of the electronic activity of both centers can be obtained through the estimation of the CTLs within the DFT+GW approach as introduced in the following, since we now focus on the correspondence between charged excitations and possible optical bands. In the particular context of the IB-materials, for which a partially filled band needs to be induced within E_g, we can strongly stipulate that Ti must be implanted at interstitial positions to achieve photon-absorption enhancement. At interstitial position, we have however shown evidence of electron-phonon coupling (responsible for non-radiative transitions) through the Jahn-Teller effect and consequent splitting of the t_2 states. According to Luque *et al.* [79], recombination centers can be mitigated if their concentration is sufficiently large to induce a localized to delocalized transition of the center-related states. In the case of interstitial Ti, for which the t_2 states are highly localized, with an effective radius of 8 Å, we estimate the required critical concentration to be $6{\cdot}10^{20}$ cm^{-3}. The effective radius is here estimated as the critical point beyond which the presence probability is smaller than $\frac{1}{10}\rho_{max}$. The presented rough estimation of the critical Ti concentration for IB-material applications is in very good agreement with the carrier lifetime increment for silicon wafers doped with Ti in the 10^{20}-10^{21} cm^{-3} concentration range [82]. At the diluted regime, for which the presented calculations are performed, the precursor state Ti_I^+ (characterized by the absence of Jahn-Teller distortions) induces an occupied triplet state at 0.4 eV with respect the TVB, and a triplet of empty states at 1.0 eV. Assuming a small electron-hole interaction, neutral excitations within such energy ranges are here estimated, and hence, supporting the photon-absorption-enhancement evidence presented in [81, 82, 83] for Ti-doped silicon as an IB-material.

Table 3.2: Estimated critical Ti concentration required to induce a localized/delocalized transition of the t_2 states, whose relative positions are here computed as IP_{t_2} - IP_{TVB} for the occupied triplet and EA_{t_2} - IP_{TVB} for the empty triplet at positive charge state.

Critical Ti concentration	Empty t_2 triplet	Occupied t_2 triplet
$6{\cdot}10^{20}$ cm^{-3}	1.0 eV	0.4 eV

To summarize, we have obtained the energy density of states for interstitial titanium impurities in silicon including many-body effects within the GW approximation, in contrast with previous mean-field employed approaches. At the diluted regime, or in the limit of non-interacting impurities,

for which the presented calculations are performed, we have positioned the quasiparticle energies of the center-induced states in the semiconductor band gap guided by the symmetry analysis performed on the KS wavefunctions. From the real-space extension of the localized electronic density, we have estimated the critical concentration for which the point-like defect looses its isolated character, inducing an intermediate-band with promising technological applications.

3.1.4 Computed CTLs *vs.* DLTS activation energies

Since the degrading effect of transition metal impurities in silicon samples is unquestionable (*e.g.* [4]), the electronic properties, and in particular the CTLs, are often the main targeted quantity of first-principles studies. In the context of Ti in silicon, previous computed CTLs [90, 91, 92] were determined from DFT total energies, and so the empirical Marker Method (section 2.4.3) was employed to avoid the band gap problem. The CTLs were therefore computed as a difference of DFT energies, $E^{q}_{\mathrm{DFT}}\left[\mathrm{Si},\mathrm{d}\right] - E^{q\pm1}_{\mathrm{DFT}}\left[\mathrm{Si},\mathrm{d}\right]$, accounting for both the energy of adding/removing an electron to a certain defect-state and for the energy loss through lattice relaxation (or change in atomic distortion). The employed method was therefore not capable of resolving the changes in occupation of defect orbitals, or the 3d states in the considered case, for a given charge transition. Besides comparing the resulting CTLs between different approaches, the set of employed computational parameters (besides the ones in a standard DFT calculation), the ΔV, the $\Delta E^{\mathrm{elect}}$, the Δ_{M} and even the U/J values for the LDA+U study reported in [92], were validated with DLTS activation energies (section 1.3.3).

Continuing the ongoing discussion, DLTS activation energies, typically referred to as *deep levels*, do also correspond to electronic transitions of the form $\epsilon_{\mathrm{T}}^{\uparrow\downarrow} \leftrightharpoons \epsilon_{\mathrm{T}}^{\uparrow}$. They can be therefore assigned to the single-electron energy, ϵ_{T}, or quasiparticle eigenvalue, IP_{T}, plus a certain lattice contribution if a change in the defect geometry occurs. In the case of interstitial Ti, the electronic configuration at negative charge state, Ti^{-}, is (omitting the splitting of the t_2 states) $\mathrm{t}_2^{\uparrow\downarrow\uparrow\downarrow\uparrow}$. This deep trap, or charge state of the defect, can emit one electron to conduction, $\mathrm{t}_2^{\uparrow\downarrow\uparrow\downarrow\uparrow} \rightarrow \mathrm{t}_2^{\uparrow\downarrow\uparrow\uparrow}$, leading to the charge transition, -1 $\rightarrow$ 0, being measured as an *acceptor level* (0/-) by the DLTS peak E40 (Table 1.1). If a second electron is emitted to conduction, $\mathrm{t}_2^{\uparrow\downarrow\uparrow\uparrow} \rightarrow \mathrm{t}_2^{\uparrow\uparrow\uparrow}$, the donor level (0/+) is detected by the E150 peak. In the case of p-type doped silicon, the injection of positive carriers results in the H180 peak, assigned to the double donor level (++/+), since it corresponds to the transition $\mathrm{t}_2^{\uparrow\uparrow\uparrow} \rightarrow \mathrm{t}_2^{\uparrow\uparrow}$. To conclude with the discussion of the widely used misleading

term of *deep levels*, previous total-DFT-based calculations with the inclusion of empirical parameters were capable of reproducing the position of charge transition energies with respect to band edges in agreement with DLTS spectroscopy for interstitial Ti.

In the present work, CTLs are estimated within the DFT+GW approach, naturally identifying the nature of the electronic transitions. The donor level (0/+) is, for example, estimated as,

$$\mathcal{E}^{+/0} = \mathrm{IP}^{0}_{\mathrm{t_2}\,a_1} - \mathrm{IP}_{\mathrm{TVB}} + \Delta E^{+}_{relax}, \tag{3.1}$$

where the quantity $\mathrm{IP}^{0}_{\mathrm{t_2}\,a_1} - \mathrm{IP}_{\mathrm{TVB}}$ is represented in the quasiparticle DOS in Figure 3.8, and ΔE^{+}_{relax} accounts for the DFT ionic relaxation at positive charge state going from the distorted flattened tetrahedron to the regular one. The level $\mathcal{E}^{+/0}$ can also be estimated in terms of the first electronic affinity at positive charge state, $\mathrm{EA}^{+}_{\mathrm{t_2}} - \mathrm{IP}_{\mathrm{TVB}} - \Delta E^{0}_{relax}$, where ΔE^{0}_{relax} describes the distortion of the tetrahedron at neutral charge state. Besides the two donor levels, located at $\mathrm{E_v}$ + 0.46 eV and $\mathrm{E_v}$ + 0.81 eV, we also report a single acceptor level, $\mathcal{E}^{0/-}$ in the upper region of the band gap, $\mathrm{E_c}$ - 0.08 eV (Figure 3.9A). Due to the position of the CTLs and the charge states involved, we tentatively conclude that interstitial Ti in silicon can be present at up to four different charge states, depending on the position of $\mathcal{E}_{\mathrm{F}}$. Formation energies for these electronic occupations are represented in Figure 3.9B, according to equations 2.82, 2.83. The non-shaded region in the diagram E^{q}_{f} vs $\mathcal{E}_{\mathrm{F}}$ corresponds to energy intervals of thermodynamic stability at different charge states. Since the goal of this representation it is not to estimate absolute values of E^{q}_{f}, but simply to determine the CTLs, relative values of formation energies are plotted.

Furthermore, as it has been widely established, calculated CTLs are comparable to DLTS levels (Figure 3.9B), revealing a one-to-one correspondance between the estimated levels and the measured activation energies [26, 27, 28, 29, 30]. When such correspondance is quantitatively analyzed, we however notice that relatively large shifts are obtained for the double donor and single acceptor (0.1-0.2 eV), questioning the validity of the first-principles parameter-free approach and/or the assignment of DLTS activation energies to the reported charge transitions (Table 3.3). The later argument is sustained by the postulated existence of a fourth CTL, due to the measured DLTS level, $\mathrm{E_v}$ + 0.51-0.55 eV [29, 30], which by all means could correspond to the double donor computed level. In order to clarify this point, CTLs for interstitial vanadium in silicon are also computed, due to the electronic equivalence between $\mathrm{Ti_I^{+}}$ and $\mathrm{V_I^{2+}}$ (also referred to as isoelectronic centers). As

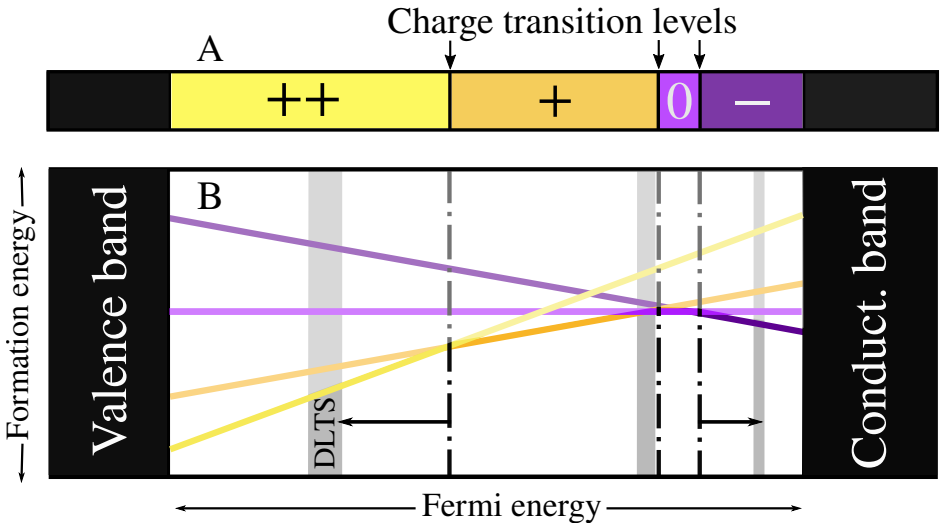

Figure 3.9: Charge transition levels for interstitial titanium within the DFT+GW combined approach (A). The formation energy E_f^q for $q = [+2, +1, 0, -1]$ vs. the Fermi energy $\mathcal{E}_\mathrm{F} \in [\mathrm{IP_{TVB}}, \mathrm{EA_{BCB}}]$ is also represented (B). The DLTS activation energies and their respective dispersion within different measurements [26, 27, 28, 29, 30] are also shown.

collected in Table 3.3 , the computed single donor for interstitial vanadium is slightly lower than the one for Ti, whereas the double donor is located higher in energy with respect to (++/+) for titanium. The tendency of reducing the energy difference between donor levels with the increase of atomic number has also been reported by DLTS spectroscopy, proving the validity of the comparative analysis. The large absolute errors of the double donor levels for both $\mathrm{Ti_I}$ and $\mathrm{V_I}$ seems therefore to indicate an intrinsic limitation of the employed method, which is further discussed in Chapter 5.

Within the DFT+GW approach, we have confirmed the degrading power of interstitial Ti in silicon by estimating the position of the Fermi energy for which the trap captures/releases free carriers from the electronic reservoir. By employing this specific method, the electron-lattice coupling is explicitly examined through the relaxation term, ΔE_{relax} in equation 3.1. Even if CTLs reveal information regarding the electronic activity of the center, further characterization is achieved through the evaluation of the non-radiative capture cross sections (Chapter 5). To conclude, the DFT+GW approach also allows to determine regions of the band gap or positions of the Fermi level for which optical transitions are visible. In the ongoing case, the optical transition between the valence band and the $\mathrm{t_2}$ states, described by

Table 3.3: Charge transition levels for interstitial titanium (Ti) and interstitial vanadium (V), here computed within the DFT+GW combined approach, collected against DLTS activation energies [26, 27, 28, 29, 30, 98, 99, 100]. The double donor level is given from the TVB, whereas the single double and acceptor levels are given with respect to the BCB. All values are in eV.

	Double donor level		Donor level		Acceptor level	
	Ti	V	Ti	V	Ti	V
DLTS	+0.25-0.32	+0.30-0.34	−0.24-0.28	−0.43-0.45	−0.08	−0.16-0.18
DFT+GW	+0.46	+0.22	−0.24	−0.26	−0.17	−0.06

$EA^{+}_{t_2} - IP_{TVB}$ (at the diluted regime) is therefore only possible at positive charge state, or at the Fermi energies comprised between $\mathcal{E}^{++/+}$ and $\mathcal{E}^{+/0}$.

3.2 Understanding the finite-temperature dynamics of the silicon E-center

The E-center is one of the most abundant point-like defects in n-type doped silicon since it consists of a silicon vacancy trapped next to a donor element; most commonly phosphorous, P, arsenic, As, and antimony, Sb (Figure 3.11a). It is known to be electronically active [*e.g.* 13], introducing an acceptor level (-/0) in the silicon gap at $\sim E_c$ - 0.45 eV independently of the dopant atomic number. A donor level (0/+) has also been measured for the phosphorus-vacancy complex (here denoted as the PV center) at E_v + 0.27 eV [101], overcoming the difficulty of tracking the emission of minority carriers with DLTS spectroscopy (*i.e.* the emission of holes in a n-type doped semiconductor). The existence of such level has still not been experimentally proved for As- and Sb-doped silicon, but it has been postulated from theoretical approaches [101]. Besides its electronic activity, E-centers can play important roles in specific performance losses and long term degradation processes due to the mobility of vacancies at relatively low temperatures. As it has been established, the effective dopant diffusion mechanism in silicon presents two main contributions depending on the intrinsic defect assisting the dopant mobility: the vacancy-mediated and the self-interstitial-mediated mechanisms [*e.g.* 13, 102]. Uncontrolled dopant diffusion can lead to the depopulation of doped regions in an electronic device, preventing the desired concentration of free carriers. The complexes arsenic-vacancy and antimony-vacancy (or AsV and SbV), are considered crucial

in dopant diffusion as the vacancy-mediated contribution seems to be comparable to or even higher than the interstitial-mediated mechanism [102]. Furthermore, the phosphorous-vacancy complex is postulated to be at the origin of the Dark Current-Random Telegraph Signal [103, 104, 105, 106] in image sensors, based on the CMOS photodiodes. It is characterized by sudden transitions between two or several discrete current levels, resulting in a step-like output signal as the one in Figure 3.10, in absence of incoming photons (*i.e.* dark current). The randomness of the signal has been widely attributed to the variation in the recombination rates of deep levels due to the metastable-switching process. In particular, the E-center reorientation at room temperature is postulated to be responsible for this characteristic output signal, whose existence constitutes an uncontrollable source of error by inducing a burst noise in the measured current. Since the possibility for a center to exhibit and/or participate to the aforementioned phenomena relies strictly on the details of its potential energy surface (PES), linking the macroscopic output RTS with one specific point-like defect has served as a motivation for the present theoretical study.

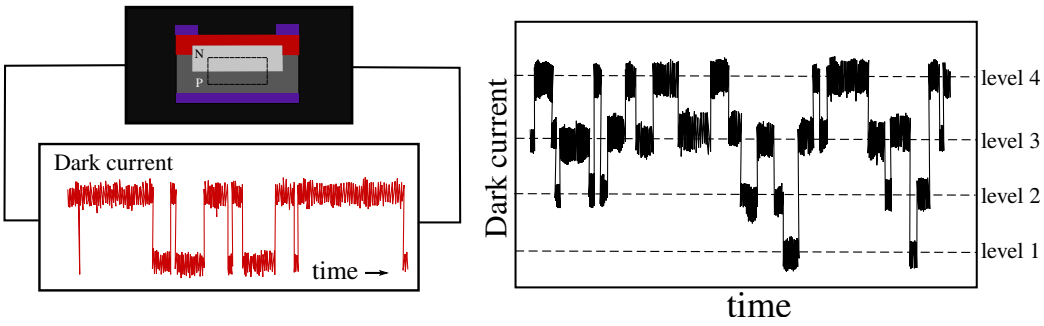

Figure 3.10: Dark current random telegraph signals in photodiodes. A two-level (in red) and four-level (in black) output signals are shown.

The E-center was first characterized by Watkins and Corbett during a series of Electronic Paramagnetic Resonance (EPR) studies of point defects in silicon [17, 19]. They reported that the ground state configuration of the neutral E-center presents a *pairing* geometry: one of the three interatomic distances between the three silicon atoms adjacent to the vacancy is shorter than the other two (Figure 3.11). Moreover, in [17, 19] two temperature regimes were distinguished. At low temperature stress measurements revealed the existence of three degenerate ground state geometries: P_1, P_2 and P_3 (Figure 3.11), separated by an *energy barrier* of 60-70 meV. Later optical absorption studies [107] of PV^-, AsV^- and SbV^- showed a ground state dis-

tortion of opposite sign. In this configuration, known as *resonant*, one of the silicon bonds is longer than the other two (R in Figure 3.11). The change of the atomic relaxation pattern with the charge state, together with the presence of degenerate ground states was explained by a simple single-electron orbital model [108], according to which the PES is predicted to exhibit the form of a *Mexican hat*. Furthermore, Watkins hypothesized [108] that the *energy barrier* between equivalent minima for the neutral systems actually corresponds to the energy difference between pairing and resonant configurations. At higher temperatures, energy barriers of 0.90 up to 1.30 eV, for P, As, Sb were observed. Such barriers were assigned to the *reorientation of the vacancy-dopant axis*, *i.e.* the reorientation of the whole vacancy-dopant complex. It was also postulated that this reorientation process, followed by a *dopant-vacancy exchange* would characterize the vacancy-mediated dopant diffusion.

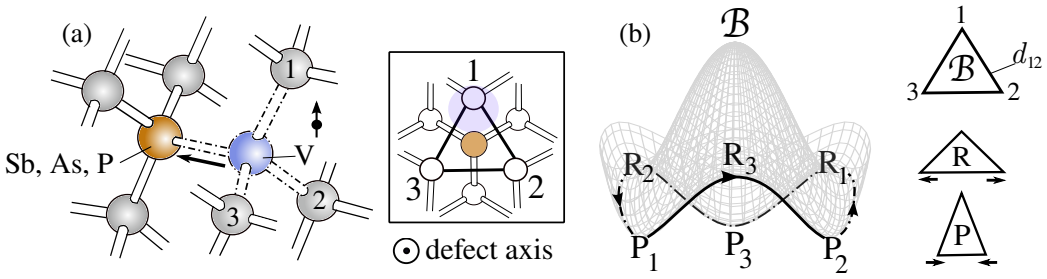

Figure 3.11: (a) The silicon E center and its projection along the vacancy-dopant axis. The probability density for the unpaired electron at neutral charge state is also shown. (b) Watkins *et al.* model for the E-center potential energy surface at the neutral charge state. Three geometries are distinguished depending on the relative interatomic distances between atoms 1, 2 and 3: the symmetric breathing configuration ($\mathcal{B}$), the pairing configuration (P), and the resonant bond configuration (R). P_i and R_i denote the pairing and resonant geometries with unpaired distances $d_{jk} < d_{ij} = d_{ik}$ and $d_{jk} > d_{ij} = d_{ik}$, respectively.

On the modelling side, the energy ranking of these configurations is not consistent between different studies [109, 110, 111, 101, 112, 113]: the ground state geometry for the PV center was found to be a pairing configuration for both neutral and negative charge states in [109] (see also Ref. [110] for the neutral charge state) but a resonant one in [111]. Later studies reported a rather flat PES with multiple *metastable* minima, comprising pairing, resonant and, in some cases, also breathing ($\mathcal{B}$, in Figure 3.11) configura-

tions [101, 112]. Only for the AsV center the measured atomic distortion at neutral and negative charge states (pairing and resonant distortions respectively) has been correctly reproduced [113]. In all the aforementioned works, the assessment for metastability has been only based on total energy calculations with no further exploration of the actual PES shape. This leaves the question open about the ground state geometry and the temperature-dependent dynamics of the E-center in silicon, and of the capacity of computational modelling to reproduce experimental findings [17, 19].

In the present work, by means of state-of-the art DFT-based methods we obtain the ground state geometry for different charge states, in line with Watkins *et al.* observations(section 3.2.1). The presence of Jahn-Teller distortions is further confirmed by accurately describing and analyzing the electronic structure of vacancy-dopant complexes by means of many-body perturbation theory within the GW approximation. The PES shape is explored by single-point total energy calculations on interpolated geometries and by using the Climbing Image Nudged Elastic Band (CI-NEB) method (section 3.2.2). Within this approach, we are able to reproduce the model proposed by Watkins *et al.*: three pairing degenerate minima and three resonant degenerate saddle points, with the higher energy maximum breathing mode lying at the top of the *Mexican hat* potential. Finally, by using the CI-NEB algorithm we found energy barriers for the reorientation of the whole vacancy-dopant complex in very good agreement with the experimental measurements (section 3.2.3). For the exchange mechanism, for which no direct experimental measure is available, our results suggest a rethinking of this diffusion mechanism: the barrier, higher than what previously postulated, seems to indicate a relevant vacancy-mediated contribution only for the case of Sb.

3.2.1 Ground state electronic structure: a Jahn-Teller model

We confirm that the geometry of the silicon E-center at different charge states is fully described by changes in the interatomic distances between atoms 1, 2 and 3 in Figure 3.11, *i.e.* the vacancy's first silicon neighbours. We report a pairing configuration (P in Figure 3.11) as the ground state for the PV^0, AsV^0 and SbV^0 centers and a resonant geometry (R) for the negative charge states (Table 3.4), in agreement with the experimental evidence [17, 19, 107]. The breathing mode configuration ($\mathcal{B}$ in Figure 3.11) is the ground state for the three centers at positive charge state (or empty trap), in agreement with

previous hypothesis [108]. The characteristic interatomic distance, d_{ij}, for PV^+, AsV^+ and SbV^+ is equal to 3.54 Å, 3.59 Å and 3.63 Å respectively. The increase of the interatomic distance with the dopant atomic number is due to the subtle relaxation of the dopant towards the vacant site; going from its ideal substitutional site to a slight interstitial position. The dopant net displacement at positive charge state is equal to 0.06 Å, 0.22 Å and 0.43 Å, in ascending order of the dopant atomic number. Such tendency is observed for all charge states, with a lower absolute displacement for 0 and -1 cases due to the increase of electronic density at the vacant site. Such behaviour is not visible by EPR spectroscopy, it does however have an important implication on the impurity diffusion mechanism, as discussed in later sections.

Table 3.4: Relevant interatomic distances d_{ij} for the E-center at neutral and negative charge states, corresponding to ground state geometries pairing and resonant respectively. All values are given in Å.

Center	$q = 0$		$q = -1$	
	d_{ij}	$d_{jk} = d_{ik}$	d_{ij}	$d_{jk} = d_{ik}$
PV	2.99	3.58	3.54	2.84
AsV	3.05	3.61	3.55	2.87
SbV	3.11	3.65	3.55	2.97

The change in structural configuration or atomic distortion with the charge state can be explained through the *partial* electronic occupation of the trap-induced levels or the Jahn-Teller effect (introduced in previous section for titanium in silicon). According to H. A. Jahn and E. Teller atomic distortions like pairing and resonant geometries are energetically more favorable than highly symmetric configurations (*i.e.* the breathing configuration), for which degeneracy of defect-orbitals is expected. The investigation of the electronic configuration of the E-center was first performed by Watkins [108] by means of a simple one-electron molecular orbital (MO) model. Within such level of theory, trap-induced states were written as a linear combination of the three dangling bonds a_1, a_2 and a_3, located in atoms 1, 2 and 3 respectively. As established in previous sections, such simple approach captures the molecule-like behavior of the point defect, being able to describe the symmetry of the localized trap-induced electronic states. On the other hand, it remains an oversimplification of the system, since only three silicon atoms are considered, ignoring the influence of the surrounding silicon diamond structure. In the case of the breathing mode configuration, *i.e.* before the

Jahn-Teller distortions, the lowest electronic level corresponds to the highly symmetric state $S = (a_1+a_2+a_3)/\sqrt{3}$, whereas states $A = (2a_1-a_2-a_3)/\sqrt{6}$ and $B = (a_2-a_3)/\sqrt{2}$ are higher and degenerated in energy (see Figure 3.12). If the empty trap (in the current case, the single positively charged E-center) gets occupied by one or two electrons, the system undergoes a structural reconfiguration in the form of a Jahn-Teller distortion, breaking the degeneracy of states A and B. The state A is favored by the pairing configuration, P, ($\epsilon_A < \epsilon_B$), whereas the state B is lower in energy in the case of the resonant configuration, R. More details on the matrix elements, that allowed Watkins to postulate the energy levels diagram in Figure 3.12, are discussed in the following Chapter. For now, we focus on the qualitative description of the trap-induced states and their relative energy ordering with respect to changes in the atomic configurations.

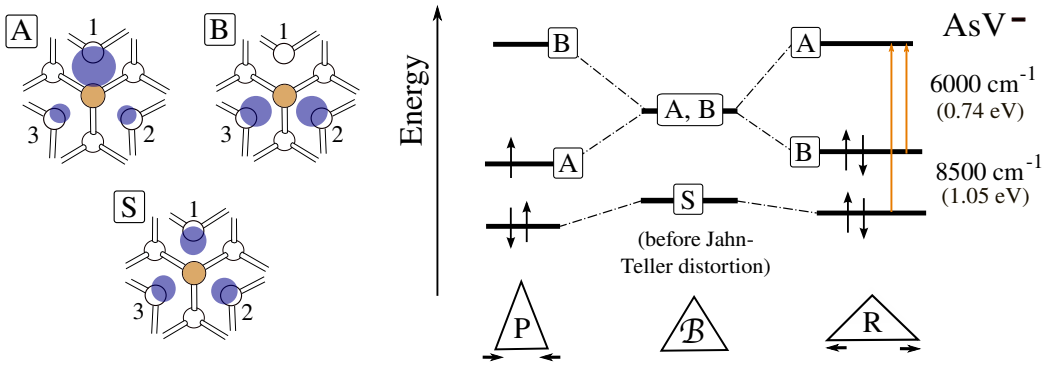

Figure 3.12: The single-electron-orbital model for the E-center proposed by Watkins [17, 19]. The probability density for the electronic states S, A and B and their relative energy position at different atomic configurations are shown. The measured absorption bands [107] and their corresponding electronic transition assignments within Watkins' model for AsV^- are also shown.

A simple MO model like the one proposed by Watkins is able to predict, for example, that at neutral charge state the unpaired electron is mainly located at one of the silicon neighbouring atoms (atom 1 in Figure 3.12), as described by state A and observed by EPR spectroscopy [17, 19]. It is however limited to the description of localized levels, overlooking the presence of bulk delocalized states, and to the use of empirical parameters when estimating the relative position of the trap levels. The splitting of the defect levels A and B after the spontaneous distortion was confirmed by optical absorption experiments [107] on the AsV^- center, where two absorption bands were reported at 0.74 eV and 1.05 eV. They were assigned to electronic ex-

citations from an occupied localized state (S and B levels in Figure 3.12) to the unoccupied state A. Unfortunately, only values for the smaller band were reported for the other two dopants. However, Watkins speculated that their defect-induced optical bands should be very similar to the ones for AsV^{-}, seeing the similarity between electronic configurations. Even though the electronic structure of the E-center is a clear evidence of the Jahn-Teller effect, no quantitative description has so far been given due to the limitations of previously used mean-field approaches [109, 110, 111, 101, 112, 113], incapable of describing particle excitations.

Optical and electronic properties from state-of-the-art calculations

Our DFT calculations qualitatively reproduce the point defect electronic structure obtained by means of simple symmetry arguments; *i.e.* the degeneracy of the localized levels A and B in the absence of Jahn-Teller distortions and the splitting and exchange of such levels for the pairing and resonant configurations. Moreover, the electronic density distributions of the Kohn-Sham states A and B are in good agreement with the simple MO model (see Figure 3.12). The inclusion of crystal field effects when using the supercell approach, in contrast with Watkins' simple MO model, allows us to give an exhaustive picture of the electronic structure of the E-center. We remark that the highly symmetric S state does not appear as a disentangled localized state, but it hybridizes with the silicon bulk states, becoming part of the valence band for all charge states. Defect-induced levels A and B are always found to be within the forbidden silicon gap. On the other hand, the electronic state coming from the donor atom is completely disentangled from both bulk states and localized trap states S, A and B; it is located deep in the valence band, at approximately 0.5 eV from the top of the valence band. In order to provide a quantitative description of the band structure, Many-Body perturbation corrections in the GW approximation (section 2.3.1) are computed on top of the DFT eigenvalues. In Figure 3.13, we show the quasiparticle Density Of States (DOS) for the E-center embedded in silicon (similarly to the ones presented for Ti_S and Ti_I). We remark once more that the electronic densities of localized states, plotted in Figure 3.13, correspond to Kohn-Sham states, thanks to the one-to-one correspondence between the KS scheme and the QP eigenvalues (equation 2.67).

As the electron-hole interaction is small, quasiparticle energy differences between empty and occupied states (ionization potentials and electronic affinities) can be exploited to meaningfully estimate vacancy-dopant-complex-

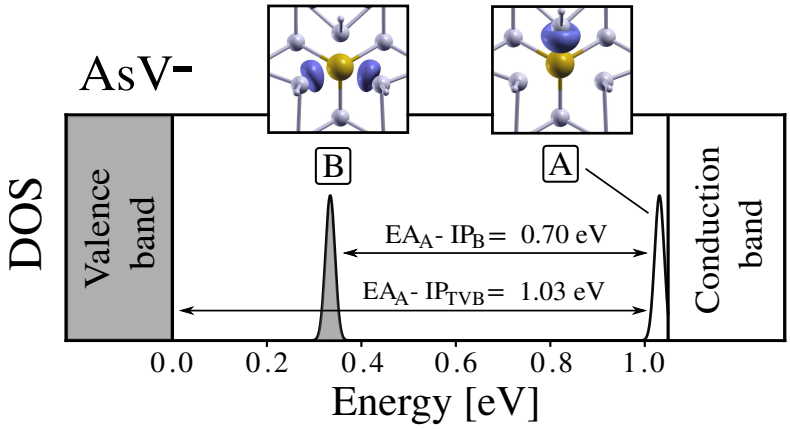

Figure 3.13: The quasiparticle density of states for the AsV^- center. Calculated optical absorption bands (EA_A-IP_B and EA_A-IP_{TVB}) and their assignation to single-particle transitions together with the electronic density of the corresponding DFT states A and B.

related optical absorption bands. In the case of the AsV^- center the energy difference between the first ionization potential (IP_B) and the first electronic affinity (EA_A) can be assigned to the 6000 cm^{-1} (0.74 eV) absorption peak reported in [107], confirming that such transition occurs from the occupied defect state B to the unoccupied localized state A (Figure 3.13). In the case of the 8500 cm^{-1} (1.05 eV) band, we assign the measured absorption band to an electronic excitation involving the top of the valence band and the localized level A (here described as EA_A - IP_{TVB}). We remark that the previous assignment made by Watkins was limited to a MO model, and therefore the position of the top of the valence band was neglected from the electronic structure prediction (Figure 3.12).

We estimate the absorption bands for PV^- and SbV^- to be located at 0.72 eV and 1.04 eV and 0.60 eV and 0.89 eV respectively (Table 3.5), confirming that the E-center has similar electronic properties independently of the dopant, as postulated in [107]. Within the presented Many-Body approach, we note that an absolute error of less than 12% is obtained with respect to the available optical measurements for the singly negative E-center. The predicted one-particle excitation bands at charges states 0 and +1 are also given in Table 3.5. Our estimation of the first excitation energies, in good agreement with experience, appears to be the numerical confirmation of the Jahn-Teller effect for the silicon E-center. It also allows to uniquely assign the presence of E-centers in a n-type doped silicon by its characteristic absorption signature when *complex* optical absorption spectra are measured,

Table 3.5: First excitation energies within Many-Body perturbation theory in the form of the GW approximation for the E-center at charge states 0, ± 1. A and B stand for the localized defect states, whereas TVB stands for the top of the valence band.

Charge state		Center PV		AsV		SbV	
+ 1	$EA_{A,B} - IP_{TVB}$	0.59	–	0.60	–	0.49	–
0	$EA_B - IP_A$	0.66	–	0.62	–	0.56	–
	$EA_B - IP_{TVB}$	0.88	–	0.85	–	0.75	–
-1	$EA_A - IP_B$	0.72	0.76[1]	0.70	0.74[1]	0.60	0.68[1]
	$EA_A - IP_{TVB}$	1.04	–	1.03	1.05[1]	0.89	–

[1]Measured absorption bands [107]

including excitations within different point defects, like the one showed in Figure 1.9.

Besides estimating neutral excitations or absorption bands involving defect-induced states, quasiparticle energies can be employed to compute charge transition levels or, as they are commonly referred to, the trap levels in the forbidden gap. In Figure 3.14, the CTLs measured as DLTS activation energies for the PV center [101] are represented, dividing the silicon gap in three regions corresponding to the defect charge states 0, ±1. Within the DFT+GW combined approach (section 2.4.4), such CTLs can be computed as a vertical charged excitation (1), followed by a change in the defect geometry (2). In the coordination diagram of Figure 3.14, the PES at each charge state is represented schematically as having one unique minimum at breathing, $g^{\mathcal{B}}$, pairing, g^{P}, and resonant, g^{R}, geometries respectively. The CTL $\mathcal{E}^{+/0}$ might then be estimated as the first electronic affinity at positive charge state, minus the energy difference between breathing and pairing configurations at neutral charge state. The second deep level, $\mathcal{E}^{0/-}$, is similarly computed starting at the pairing geometry at neutral charge state.

Exploiting quasiparticle energies to estimate both optical and electronic properties allows to picture CTLs as changes in the partial occupation of defect states (often involving a relaxation of the ionic positions), hence reinforcing the idea that neutral excitations are only observed for certain Fermi energies. The E-center donor level can be interpreted as the occupation

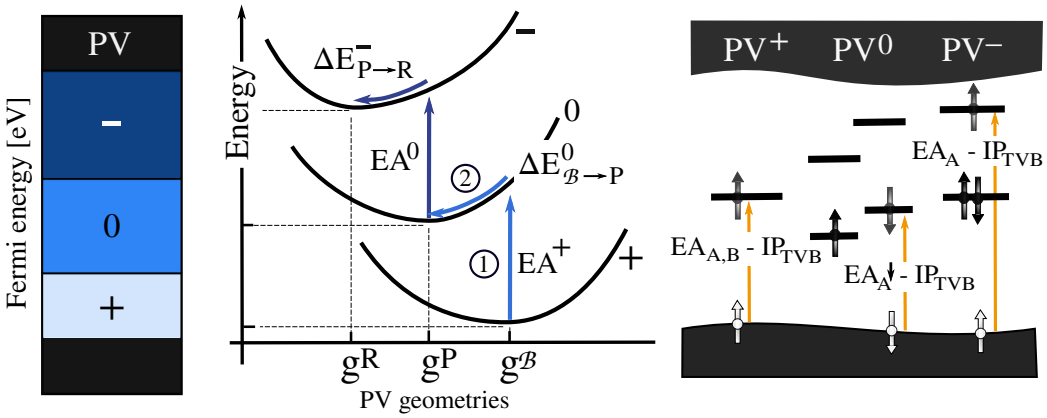

Figure 3.14: Optical versus electronic properties of the PV center estimated as charged excitations or quasiparticles energies. Represented charge transition levels are taken as the DLTS activation energies reported in [101].

of degenerate states A and B at positive charge state, whose energy variation $E^{N+1}-E^{N}$ at constant geometry is given (with respect to TVB) as $EA_{A,\,B} - IP_{TVB}$. Then, if $\mathcal{E}_F < \mathcal{E}^{+/0}$, the neutral excitation from the TVB to states A, B might be observed until the charge transition $+ \rightarrow 0$ occurs, partially filling state A. The E-center acceptor level therefore corresponds to the full occupation of state A, with vertical energy contribution $EA_A^{\downarrow} - IP_{TVB}$. We note that the *later* atomic relaxation P $\rightarrow$ R is responsible for the inversion of levels A and B, the later being fully occupied at negative charge state. Within the band gap region, $\mathcal{E}^{+/0} < \mathcal{E}_F < \mathcal{E}^{0/-}$, a neutral excitation from TVB to the partially empty state A is in principle allowed unless an extra electron is added to the system, originating the second charge transition, $0 \rightarrow -$. The importance of correctly assigning CTLs to the occupation of specific defect-states is therefore remarked when absorption bands are measured only at certain positions of the Fermi level. A similar reasoning as the one presented here for the PV center allow us to unequivocally assign the three measured absorption bands for the silicon divacancy to one-particle excitations (Chapter 4).

Estimated CTLs for the E-center within a full *ab initio* parameter-free approach are collected in Table 3.6. The proximity among the deep levels for the three impurities, similarly to the optical bands, is a conclusive evidence that the three centers are governed by the same Jahn-Teller effect. Our computed values are in fair agreement with previous theoretical studies, which in contrast with the here employed formalism, included an empirical parameter to circumvent the DFT band gap problem (*i.e.* the Marker Method, intro-

duced in section 2.4.3). The deviation of 0.1-0.2 eV between the estimated CTLs and the corresponding DLTS activation energies is consistent with the absolute error here reported for interstitial Ti and V in silicon. A consistent analysis of such intrinsic error of the DFT+GW combined formalism will be discussed in detail in section 5.1.

Table 3.6: Charge transition levels for the silicon E-center here computed within the DFT+GW combined approach, collected against the estimated values by the Marker Method (MM) [101] and DLTS activation energies. The donor level is given from the TVB, whereas the acceptor level is given with respect the BCB. All values are in eV.

	Donor level			Acceptor level		
	DFT+GW	MM	DLTS [101]	DFT+GW	MM	DLTS [114]
PV	+0.29	+0.22	+0.27	−0.45	−0.36	−0.45
AsV	+0.31	+0.24	–	−0.39	−0.35	−0.47
SbV	+0.35	+0.27	–	−0.28	−0.31	−0.44

To summarize, we have numerically confirmed the Jahn-Teller model proposed by Watkins within a simple molecular-orbital approach at different levels of theory. Breathing, pairing and resonant geometries are obtained as ground state minima of the energy surfaces at positive, neutral and negative charge states for a PBE description of the electronic exchange-correlation contribution. Optical and electronic properties of the three centers have been also investigated with the inclusion of many-body effects, unequivocally establishing the equivalence of the electronic structures of PV, AsV and SbV in silicon, sustained by experimental evidence (infrared OA and DLTS spectroscopy).

3.2.2 The Mexican hat potential energy surface at low temperatures

We now focus our attention on the energy landscape of the E-center at low temperatures, studied by EPR stress studies [17, 19] in the case of the neutral charge state. As hypothesized by [17, 19], we found three pairing configurations, P_1, P_2 and P_3 in Figure 3.11, as ground state minima of the potential energy surface (P_i is characterized by an unpaired distance $d_{jk} < d_{ij} = d_{ik}$). The unpaired electron is therefore mainly located in silicon atom i at the

pairing configuration P_i (see the form of the localized state A in Figures 3.12 and 3.13). Even though the three distortions are geometrically equivalent, the electronic jumps between atoms 1, 2 and 3 modify the magnetic moment of the center, making the transitions between pairing configurations visible through EPR spectroscopy [17, 19]. The lifetime of each distortion was estimated by compressing the bulk in a given spatial direction (prioritizing one of the three orientations) and studying the recovery time of the back-reorientation. The low-temperature regime reorientation barriers were estimated to be within 60-70 meV [17, 19] and it was later postulated [108] that such energy barriers actually correspond to the energy difference between the pairing and the resonant geometries. A NEB calculation between points P_1 and P_2 finds the R_3 geometry (resonant configuration characterized by unpaired distance $d_{12} > d_{31} = d_{32}$) as the saddle point of the transition path (see Figure 3.15), proving Watkins' hypothesis regarding the height of the energy barriers between equivalent minima. We estimate the energy difference between pairing and resonant configurations to be 36 meV, 31 meV and 28 meV for PV^0, AsV^0 and SbV^0 respectively. As in Ref. [113] the "disagreement" between the calculated barrier, 20 meV for the AsV^0 complex, and the measured value [19], 70 meV, was attributed to size effects, we performed calculations on a 511 atoms supercell. We obtained a very similar value of about 38 meV for all three dopants, showing that size effects are particularly important for the SbV complex.

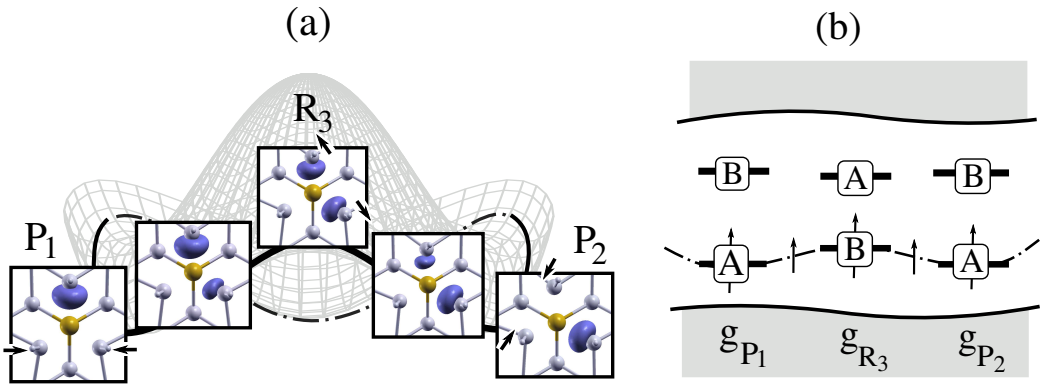

Figure 3.15: Symbolic representation of the minimum energy path between equivalent pairing configurations for the PV^0 center. The highest occupied Kohn-Sham state (a) and the relative position of the trap-induced levels A and B (b) at different atomic positions are also shown.

The potential energy surface for the E center at neutral charge state is therefore characterized by three pairing geometries as degenerate minima, sep-

arated by three resonant configurations as saddle points (Figure 3.16). Along the Minimum Energy Path (MEP), despite structural changes between pairing and resonant configurations seeming "negligible", the unpaired electron localizes at different atomic sites (see the electronic density plots that follow the symbolic paths $P_1 \rightarrow R_3 \rightarrow P_2$ in Figure 3.15). At the saddle point, the system adopts a resonant configuration for which the half-filled electronic orbital becomes state B, as expected from a Jahn-Teller system (Figure 3.15). If we consider a set of configurations along a straight path between a pairing and resonant configuration with the same characteristic unpaired distance, the system is forced to pass through a highly symmetric configuration, close to the breathing mode geometry ($\mathcal{B}$ in Figure 3.11), overcoming an energy barrier of $\sim$ 60-100 meV (Figure 3.16). According to the above results, the PES of the E-center exhibits the shape of a *Mexican hat*, in agreement with Watkins ideas and measurements. At room temperature, the barriers between pairing configurations are comparable to $k\mathrm{T_{RT}}$ and the neutral E-center can reorient by circling around the *Mexican hat*. These reorientations can therefore not be responsible for the Random Telegraph Signal, since at room temperature an average configuration of the three Jahn-Teller distortions is observed, corresponding to a highly symmetric geometry [17, 19].

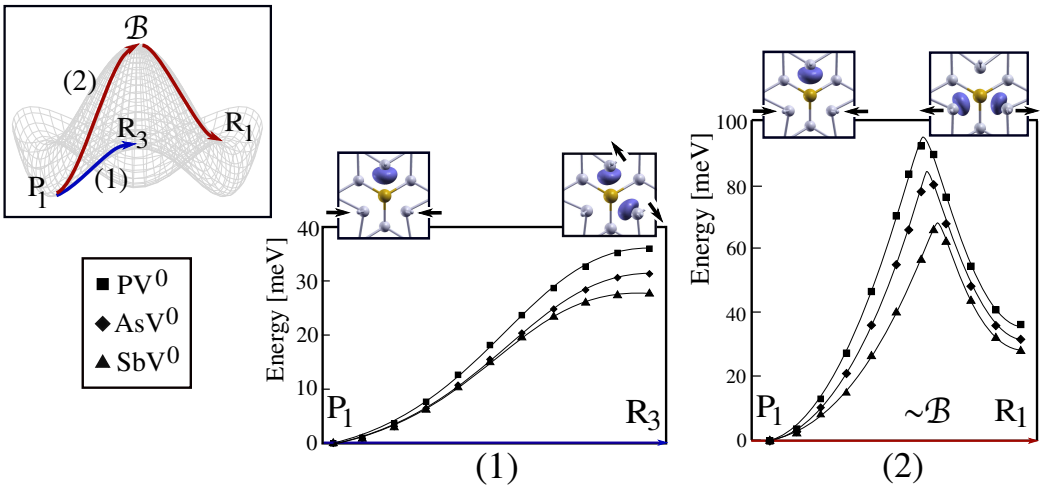

Figure 3.16: The potential energy surface at low temperature for the neutral E-center. Transition paths (1) and (2) between pairing and resonant configurations for the three dopants are shown. The electronic density for the unpaired electron at different atomic configurations is also shown. Points are obtained within the NEB algorithm (1) and single point DFT calculations (2). Lines are a guide for the eye.

For the negative charged E-centers the *Mexican hat* is inverted: pairing and resonant configurations becomes, respectively, saddles and minima points. The energy barriers to jump from one minimum, R configuration, to another one is of 62 meV, 48 meV and 25 meV for PV^-, AsV^- and SbV^- respectively (511 atoms supercell) at the DFT level of approximation. As in the neutral case, size effects are important when computing such reorientation barrier, resulting in up to 20 meV energy difference between 215 and 511 silicon supercells. Reorientation barriers at both charge states are presented in Table 3.7. Positively charged E-centers exhibit a single minimum that corresponds to the breathing configuration, $\mathcal{B}$. The rather small reorientation barriers (or energy differences between pairing and resonant configurations) for charge states 0 and -1 are the possible cause of previous works claiming the E-center was a *multi-stable* center. However, we have shown that a good understanding of the system and the origin of the distortions is sufficient to prove such studies wrong. To conclude, we remark that any Jahn-Teller potential energy surface is easily predicted by simple symmetry-based considerations, giving a qualitative description of the defect-induced states and its relative energy ordering with respect to atomic distortions. Even if so far we have focused on the numerical side of the characterization, in the following chapter a general theory to model Jahn-Teller systems is introduced and applied to more complex systems.

Table 3.7: Reorientation barriers at low temperatures at neutral and negative charge states for all three dopants, computed in this work (t.w.) and other works (o.w.) as the total energy difference between pairing and resonant configurations. All values are given in meV.

	$q=0$			$q=-1$	
	t.w.	o.w.	Exp.	t.w.	o.w.
PV	38	–	62 [17]	62	–
AsV	36	20 [113]	60 [19]	48	40 [113]
SbV	38	–	70 [19]	25	–

Underestimation of the reorientation barriers

The systematic underestimation of the barriers, 40 meV for all three dopants, against the 60 to 70 meV measured by Watkins *et al.* [17, 19], is a signature of the well known Self-Interaction problem in standard DFT exchange and correl-

ation functionals. Such well-known problem of DFT is typically encountered, in the particular case of point defects, when computing the charge transition levels (section 2.4.3). From a broader perspective, a pure DFT calculation will most probably fail when energetically comparing different configurations of partially occupied traps, since it requires an accurate treatment of the electronic interaction that is limited in a mean-field approximation. Among the different schemes that have been proposed to correct such shortcoming, we are particulary interested on the combined DFT+GW approach, previously exploited to correct total energy differences in point defects studies [70, 72, 73]. In a few words, total energy differences for different atomic configurations are safely determined by DFT only in the case of non-occupied traps (process (2) indicated by the violet arrow in Figure 3.17), computing energy differences between different trap occupations at a given point defect geometry within a GW approach (process (1) represented by a orange arrow in Figure 3.17).

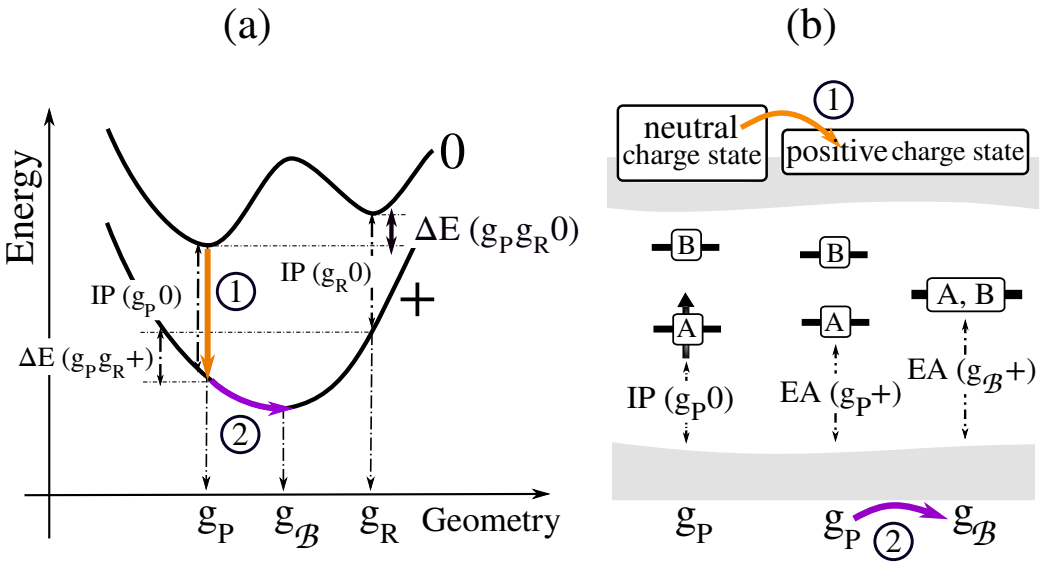

Figure 3.17: The coordination diagram for the silicon E-center at neutral and positive charge states (a). The electronic structure of relevant points in the diagram are also shown (b). The transition between the two minima of the parabolas, indicated in the diagrams with orange and purple arrows, is composed by the loss of one electron at pairing configuration and neutral charge state (1) and posterior atomic relaxation from pairing to breathing configurations at positive charge state (2).

In the present case, we are not interested in determining the energy differ-

ence between different charged geometries, but in the subtle energy difference between two different geometries at constant trap occupation, ΔE (g_P, g_R, 0) in Figure 3.17a. By definition, the ionization potential computed within the GW method for the pairing configuration (g_P) at neutral charge state can be written as the total energy difference,

$$\mathrm{IP}\,(g_P, 0) \;=\; \mathrm{E}\,(g_P, 0) \;-\; \mathrm{E}\,(g_P, +). \tag{3.2}$$

By computing the same quantity at the resonant configuration, the reorientation barrier at neutral charge state can be written as,

$$\Delta\mathrm{E}\,(g_P, g_R; 0) \;=\; \mathrm{IP}\,(g_P, 0) \;-\; \Delta\mathrm{E}\,(g_P, g_R; +) \;-\; \mathrm{IP}\,(g_R, 0). \tag{3.3}$$

The quantity ΔE (g_P,g_R; +) is the difference in energy between the pairing and resonant configurations at positive charge state (empty trap) and therefore can be safely estimated within DFT. All energy differences required to *accurately* compute the reorientation barriers at neutral charge state are represented in Figure 3.17a. Since the electronic structure of the E-center should be perfectly known by now, we also show processes (1) and (2) in terms of transitions in the trap-induced levels in Figure 3.17b.

In the case of the PV center (where the elastic contributions are minimal at 216 atoms), such difference in ionization potentials, IP (g_P, 0) − IP (g_R, 0), is equal to 65 meV and the corresponding reconfiguration energy, ΔE (g_P,g_R; +), is 10 meV, given an overall reorientation barrier of 75 meV. Similarly, a value of 71 meV is obtained for the AsV center. These values reinforce the idea of DFT limitations when computing certain properties of point defects. The limitations and drawbacks of the above presented DFT+GW combined approach will be discussed in more detail in future sections.

To conclude, we have extensively explored the PES of the E-center at neutral and negative charge states, finding the *Mexican hat* shape hypothesized by Watkins. The comparison of the estimated reorientation barriers between equivalent Jahn-Teller distortions with EPR activation energies have allowed us to identify the limitations of the PBE-functional when describing certain defect properties, due to the DFT well-known self-interaction problem. We have then proven that within a higher level of treatment of the Coulomb electronic repulsion (or within the GW approximation), the underestimated barriers are *correctly* shifted with respect to experiment.

3.2.3 The energy landscape at high temperatures: complex reorientation and exchange

The present section is dedicated to the two mechanisms underlying the vacancy-mediated dopant diffusion: the defect reorientation and the vacancy-dopant exchange (see Figure 3.18). The first process involves the reorientation of the vacancy-dopant axis, through the movement of the vacancy to second (vacancy positions 2 and 2' in Figure 3.18) and third neighbour positions (denoted 3) with respect to the impurity. Such mechanism was first proposed by [17, 19], after performing EPR stress studies at high temperatures. They obtained the lifetime of each defect-axis orientation, corresponding to activation energies that were comprised between 0.9 and 1.3 eV, for dopant-increasing atomic number. As in the case of low temperature studies, a characterization of the atomic process and its energy landscape at high temperatures is possible by EPR spectroscopy due to the change in magnetic moment between the initial and final configurations (see configurations 1 and 1' in Figure 3.18). It was also postulated that the reorientation mechanism constituted the bottleneck process for vacancy-mediated diffusion, since the energy expense for the dopant-vacancy exchange was believed to be close to 0.33 eV (activation energy for the monovacancy diffusion in silicon [16]).

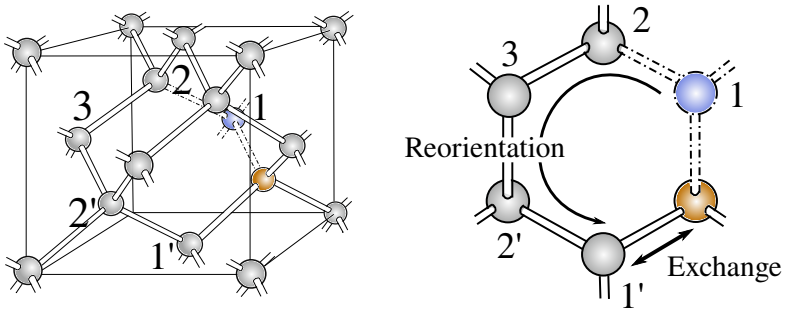

Figure 3.18: The vacancy-mediated dopant diffusion mechanisms: the reorientation of the defect and the exchange vacancy-dopant.

The high temperature dynamics of the E-center is studied through the mechanisms of defect reorientation and dopant-vacancy exchange within the CI-NEB algorithm (see section on sampling the DFT PES 2.2.2). The exchange of positions between the dopant and the vacancy is a direct symmetric process, as shown in Figure 3.19. The decrease of the energy barrier with the increase of the dopant size is explained by the ground state geometry of the E-center. As mentioned in section 3.2.1, the dopant slightly moves from its ideal substitutional position towards the vacant site. Such effect increases

with the dopant size, as it is evident by the low energy barrier obtained, in particular, for the antimony-vacancy exchange. In contrast with the simple exchange process, the reorientation of the defect axis requires the movement of the vacancy to different sites of the lattice before arriving to its final configuration. The electronic and structural configurations at second and third neighbour positions are studied as intermediate states of the reorientation process. Two different minimum energy paths must therefore be characterized ($1 \rightarrow 2$ and $2 \rightarrow 3$), with their respective energy barriers. The relative stability of the second neighbour and third neighbour configurations present opposite tendencies with the dopant size. The E-center is barely stable at third neighbour configuration in the case of the PV^0 center, finding an energy barrier of 26 meV, whereas the energy expense to leave such configuration is about 0.16 eV in the case of the antimony (transition $3 \rightarrow 2$ in Figure 3.19). As it is shown in Figure 3.19, such behaviour is inverted in the case of the second neighbour configuration, obtaining energy barriers to return to the first neighbour site of 11 meV for SbV^0 and 0.11 eV for PV^0 (transition $2 \rightarrow 1$ in Figure 3.19). The reorientation barrier observed by EPR stress studies at high temperatures [17, 19] is here estimated as the energy difference between the ground state configuration of the E-center and the saddle point of the $2 \rightarrow 3$ transition (see Figure 3.19).

The theoretical values obtained in Table 3.8 clearly show that the diffusion of the whole vacancy-dopant complex is energetically more expensive in the case of the PV center than postulated by Ref. [17] from the mono-vacancy diffusion. The activation energy for the exchange mechanism is comparable to the 0.33 eV barrier for the mono-vacancy diffusion only in the case of antimony. We remark that the energy path for the exchange antimony-vacancy is characterized by a *positive* barrier of 0.26 eV, in big contrast with the negative value previously published by [115]. In a few words, the systematic study presented in Table 3.8 allows to confirm the energy expense of the reorientation process measured at high temperatures and to better estimate the exchange barrier, unmeasurable by EPR studies, and therefore unknown from experimental characterization. While a detailed study of the diffusion mechanism of the E-center is beyond the scope of the present work, our results indicate that vacancy-mediated diffusion would be the primary diffusion mechanism for large dopant-atomic numbers, as it has been experimentally proved in Ref. [102].

For what concerns the possible contribution of the E-center to the Random Telegraph Signal, we refer to the measurements of I. H. Hopkins and G. R. Hopkinson [103] on proton-irradiated *charge-couple devices* (CCD), where

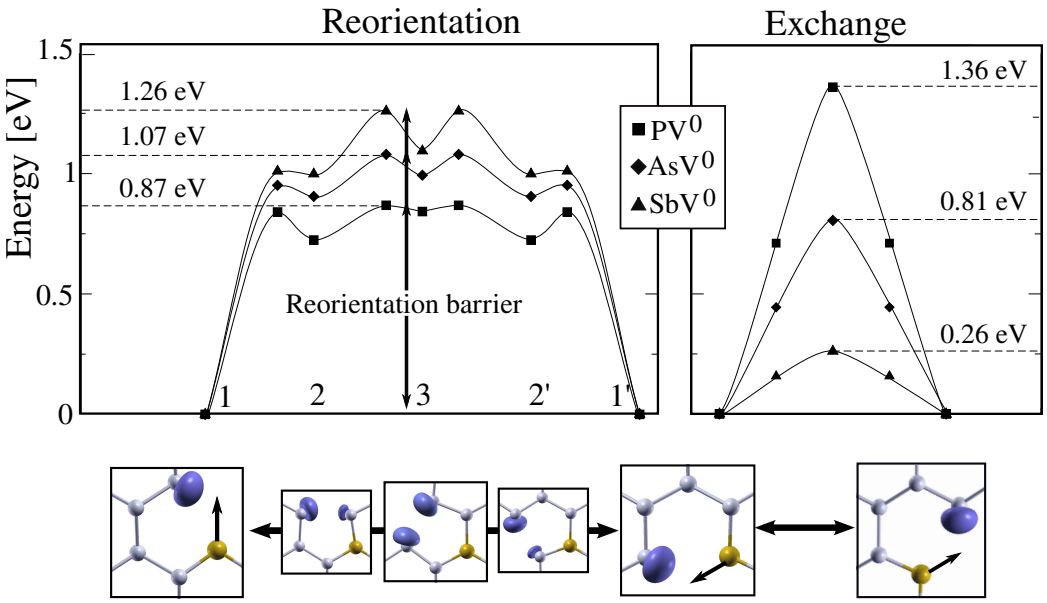

Figure 3.19: The energy landscape of the E-center at high temperatures: activation energies for the reorientation of the vacancy-dopant axis and exchange. The probability density for the unpaired electron along both processes is shown. Only relevant points, corresponding to local minimum and saddle points, are shown in the case of the reorientation process. Lines are guides to the eye. Activation energies for the first-neighbor-complex dissociation (transition $1 \rightarrow 2$) and the complete reorientation process (transition $1 \rightarrow 3$), as well as the ones for the exchange mechanism are listed in Table 3.8.

Table 3.8: Exchange barriers, first neighbours binding energies and reorientation barriers at high temperatures for PV^0, AsV^0 and SbV^0. Values are given in eV. t.w. stands for this work, whereas o.w. stands for other works.

Dopant	**Exchange barrier**		1st neighb. binding energy		**Reorientation barrier**		
	t.w.	o.w.	t.w.	o.w.	t.w.	o.w.	Exp.
P	1.36	1.05 [115], 1.29 [116]	0.84	1.05 [115]	0.87	0.8 [116]	0.93 [17]
As	0.81	0.65 [115]	0.95	1.17 [115]	1.07	1.0 [113]	1.07 [19]
Sb	0.26	-0.05 [115]	1.01	1.45 [115]	1.26	–	1.28 [19]

the two-level RTS was assigned to the presence of the PV center. In the original work, the observed burst noise was linked to the reorientation between equivalent geometries at room temperature, justifying the variation of the

dark current with the atomic reorientation by exemplifying the P→V center as a dipole moment subject to an electric field. The one-to-one relation between the RTS and the reorientation of the P→V axis at room temperature was strongly supported by the so-said similar *kinetics* presented by both phenomena [103], since the magnitude of the RTS activation energies, 0.94 eV and 0.95 eV for the down and up levels respectively, was equivalent to the reorientation barrier estimated by Watkins of 0.93 eV [17]. Our computed energy barrier for the PV center reorientation process confirms both Watkins' measurement and its identification with a particular atomic-scale mechanism. Our result seems by consequence to support the early work of I. H. Hopkins and G. R. Hopkinson [103]. We however note that later studies, and in particular [105], reported a different characteristic time constant for such signal on P-doped silicon, but it was still assigned to the presence of the PV complex due to correlation between the dissociation temperature of the center and the characteristic T above which the RTS was disappearing. The work presented in [104, 106] also focused on the temperature-dependence arguments, leaving aside the measured time constants. Seeing that in most of proton- or neutron-irradiated devices small clusters are known to dominate over the creation of point-like-defects, it seems like purely temperature-based justifications are insufficient to prove a one-to-one correspondence between RTS and defects, given the vast catalog of possible defects. To conclude, we remark the fact that both AsV and SbV centers present similar reorientation barriers as the one discussed for the PV complex (see Table 3.8), being consequently candidates for RTS defects in As- and Sb-doped silicon. However, to the best of our knowledge, only the work of [117] has so far presented a comparative study of P- and As- doped devices, where the vast catalog of created defects and/or clusters of defects prevented the one-to-one correspondence with single point-like defects. Even if a description of RTS activation energies like the one performed by I. H. Hopkins and G. R. Hopkinson was done, a further and more detailed examination of how reorientations between equivalent configurations are capable of originating a macroscopic response in the device is required.

To conclude, we have explored the energy landscape for the vacancy-dopant axis reorientation observed at higher temperatures, finding activation energy barriers in very good agreement with experiments. Moreover, the computed exchange barriers offer a new insight on the vacancy-mediated diffusion. In particular, in the case of the SbV complex, they support the long time belief that Sb diffuses in silicon mainly through a vacancy-mediated mechanism.

3.3 Computational details

The ABINIT package [44], version 8.10.1, was used to perform all the presented calculations. Kohn-Sham real space wavefunctions and electronic densities are plotted using the XCrySDen package [118].

Both metallic impurities and the E-center have been embedded in a 216/215 atoms-cell for all calculations, except for certain geometry relaxations performed on a bigger cell of 512/511 atoms, as specified in section 3.2.2. The Brillouin zone was sampled at gamma and the Perdew-Burke-Ernserhof exchange-correlation functional [36] was chosen for all the presented results. The ONCVPSP norm-conserving pseudopotentials [48] from the pseudo-dojo platform were taken. We remark that for As (Z = 33) and Sb (Z = 51) elements, part of the core electrons were put in valence, and therefore 15 valence electrons were explicitly considered instead of the 5 electrons for the phosphorous atom. Similarly for titanium and vanadium, with isolated atomic configurations, [Ar] $3d^2 4s^2$ and [Ar] $3d^3 4s^2$, twelve and thirteen electrons were respectively self-consistently *relaxed*. An energy cutoff for the plane wave basis set of 762, 1306 and 1225 eV has been employed for the PV, AsV and SbV centers embedded in silicon bulk. In the case of interstitial titanium and vanadium, the energy cutoff was fixed to 1088 eV.

Defect geometries at different charge states have been optimized by means of the BFGS algorithm, with a convergence threshold of 1 meV/Å. The PES is explored by both the climbing-NEB method, with a total energy convergence threshold of 1 meV, and by single-point total energy calculations. All geometries discussed in the present work were obtained without any symmetry constraints. Saddle points of the *Mexican hat* energy surface for the E-center were determined on a 216-atoms cell by standard structural relaxation and the NEB method, obtaining indistinctly the atomic distortions collected in Table 3.9. Reorientation barriers estimated on the 512-atoms cell purely rely on the BFGS algorithm to correctly describe saddle point geometries.

Prior to the determination of W_0 and G_0, two consecutive DFT calculations are performed: a full self-consistent calculation with few empty bands, followed by three scf cycles generating the later required large number of empty bands. The cutoff energy to determine such *building* Kohn-Sham eigenfunctions is the same as the one employed in the above detailed DFT calculations. We employ a cutoff energy of 82 eV to describe the dielectric matrix for the Many-body corrections computed on top of the Kohn-Sham

Table 3.9: Relevant interatomic distances d_{ij} for the E-center at neutral and negative charge states, corresponding to saddle points geometries resonant and pairing respectively for a 216-atoms cell. All values are given in Å.

Center	$q = 0$		$q = -1$	
	d_{ij}	$d_{jk} = d_{ik}$	d_{ij}	$d_{jk} = d_{ik}$
PV	3.61	3.28	2.76	3.36
AsV	3.64	3.36	2.79	3.39
SbV	3.71	3.53	2.87	3.44

energies. In order to assure convergence of the GW exchange-correlation self-energy, we use a very large ratio of 10:1 empty bands versus occupied bands. Size effects and spurious interactions between charged defective cells are considered in the case of QP DOS, shifting IP and EA values according to the non-defective silicon cell. Charge transition levels computed within the DFT+GW combined formalism are obtained from the neutral charge state, defining the vertical transitions as IP^0 and EA^0 (except for the double donor level for Ti_I and V_I, for which IP^+ and ΔE^{2+} are employed).

Chapter 4

On the modeling of Jahn-Teller effects in silicon

This process of model-building, essentially that of discarding all but essentials and focusing on a model simple enough to do the job but not too hard to see all the way through, is possibly the least understood and often the most dangerous of all the functions of a theoretical physicist

R. W. Anderson

As established by the Jahn-Teller theorem, the instability of localized orbitally degenerate atomic configurations upon distortions with respect to a given symmetry transformation is a universal effect for all non-linear atomic systems. In the context of point defects in semiconductors, such universal mechanism is source of electron-phonon coupling and hence, thermal electronic transitions within the technologically unwanted recombination centers. Within an even more specific scope, confined symmetry-breaking mechanisms in an infinite crystal are responsible for local atomic reorientations, since they often allow finite-temperature dynamics between different/equivalent Jahn-Teller distortions. In the case of silicon, which is often assumed to be well-characterized, such effect has been widely exemplified in the case of the mono-vacancy within a point-group-theoretical treatment, and later quantification by first-principles calculations. Such comprehensive characterization of Jahn-Teller distortions in silicon is however an exceptional case, since as presented in the previous Chapter, this universal mechanism is not fully un-

derstood (case of the E-center) or even neglected (Ti impurity) in existent *ab initio* studies.

In the present Chapter, we present a general theoretical framework to study Jahn-Teller effects in silicon, based on the *ab initio* quantification of simple symmetry-based models. We demonstrate that within these toy-models the estimated basic features of the center, such as the symmetry of the defect-orbitals and variations of the defect electronic structure with atomic distortions, allow us to establish a solid correspondence with EPR measurements. Symmetry considerations are then employed to guide the state-of-the-art *ab initio* characterization, providing a stronger *grounded* comparison with experimental data. In addition, the validation of first-principles simulations by both fundamental constrains and experimental evidence enables us to evaluate the quality or accuracy of the calculations.

More precisely, we target the characterization of Jahn-Teller effects for rather complex centers in silicon, for which the symmetry, sense and magnitude of the distortions are still source of controversy in the *ab initio* community. The Chapter begins with the presentation of a symmetry-based generalized model for the $C_{3v} \rightarrow C_{1h}$ distortions of the trimer or the E-center (section 4.1), taking as starting point Watkins' original model. In section 4.2, an equivalent model for the $D_{3d} \rightarrow C_{2h}$ mechanism is proposed for the divacancy or the bi-trimer. Within such model, pairing and resonant distortions are again either minima or saddle points of the energy surface, providing an extra degree of comparison with EPR reorientation barriers, in contrast with previous studies. A complete understanding of the center allows us to revisit the long-standing assignment of the optical absorption bands with the inclusion of many-body effects. The universality of the model is farther proved when tetrahedral Jahn-Teller distortions for the vacancy and heavy transition metals (Pt, Au) in silicon are considered (section 4.3). The $T_d \rightarrow D_{2d}$ mechanism for such centers is a clear example of the importance of the Jahn-Teller effect, since large lattice relaxations might induce larger level-splitting than the on-site Coulomb repulsion,favouring double occupations. We conclude with the description of multiple symmetry-breaking mechanisms, $D_{2d} \rightarrow C_{2v}^{\mathrm{V}}$, $D_{2d} \rightarrow C_{2v}$ and $D_{2d} \rightarrow D_2$, explaining the reorientation of the Pt^- center at cryogenic temperatures and providing an explanation for the absence of EPR signals for the Au^0 center.

4.1 A toy-model for the silicon E-center

A simple one-electron model for the silicon E-center [108] was introduced in the previous Chapter as a theoretical model capable of qualitatively reproducing the experience. It was however noted that as a molecular-orbital approach, empirical parameters were required if *meaningful* values were to be compared with the measured optical absorption bands and/or reorientation barriers at low temperatures. The success of such model was to correctly describe the localized trap-induced electronic states (states A and B in Figure 4.1) and their relative position in energy upon atomic distortions (degeneracy and reversal of states A and B at geometries $\mathcal{B}$, P and R). In other words, the Jahn-Teller effect was naturally characterized by the three dangling bonds located at the three silicon neighbours of the vacancy (atoms 1, 2 and 3 in Figure 4.1).

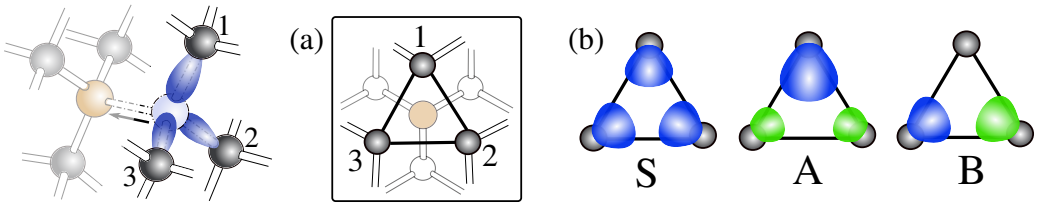

Figure 4.1: The silicon E-center projected on the vacancy-dopant axis (a) and the eigenstates of the trimer (b) constituted by the first silicon neighbours of the vacancy or atoms 1, 2 and 3.

Even though Watkins' model (section 4.1.1) was enough to guide our *ab initio* exploration of the PES, it presents a couple of limitations that should be taken into consideration when extrapolating such simple model to the study of more complex defects. In the following, we present our generalization of the original model (section 4.1.2), allowing us to establish a full qualitative correspondence with experience, but explicitly showing that without an empirical input or a more sophisticated treatment of the electronic Coulomb repulsion, basic features such as the ground state geometry at a given charge state remain inconclusive.

4.1.1 Watkins' original model

In a few words, Watkins' model for the silicon E-center was simply based on the trimer constituted by silicon atoms 1, 2 and 3, each contributing with a broken bond, here denoted as a_1, a_2 and a_3. By first considering an

equilateral conformation, $d_{12} = d_{13} = d_{23}$, matrix elements between different dangling bonds were said to be non-zero and equivalent, $\langle a_i | \mathcal{H}_0 | a_j \rangle = -\gamma$. The eigenstates of the resulting equilateral-trimer-Hamiltonian, $\mathcal{H}_0$, were then obtained as a linear combination of $\{a_i\}$: S $\sim a_1+a_2+a_3$, A $\sim 2a_1-a_2-a_3$ and B $\sim -a_2 + a_3$ (note the change of notation with respect [108]), represented in Figure 4.1b. In this new basis set, $\mathcal{H}_\mathbf{0}$ is trivially,

$$\mathcal{H}_0 = \begin{array}{c} \\ \langle B| \\ \langle A| \\ \langle S| \end{array} \begin{array}{c} |B\rangle \quad |A\rangle \quad |S\rangle \\ \begin{pmatrix} \epsilon_{\mathrm{A,\,B}} & 0 & 0 \\ 0 & \epsilon_{\mathrm{A,\,B}} & 0 \\ 0 & 0 & \epsilon_{\mathrm{S}} \end{pmatrix} \end{array} \tag{4.1}$$

It was then shown that for any given equilateral trimer, or any given hopping γ, the eigenvalues for states A and B, $\epsilon_{\mathrm{A,\,B}}$, are degenerate and higher in energy than ϵ_{S}. Led by the experimental evidence of pairing distortions as ground state geometries [17, 19], Watkins [108] aimed to reproduce the Jahn-Teller effect in the form of a distorted trimer by proposing a *perturbative* Hamiltonian, $\mathcal{H}_{\mathrm{JT}}$. Since the distorted trimer is defined upon one horizontal plane of reflection, σ_{Q} in Figure 4.2, the Jahn-Teller Hamiltonian, $\mathcal{H}_{\mathrm{JT}}$, was approximated as a linear perturbation of the trimer, Q_{A}, with respect to σ_{Q}. In other words, $\mathcal{H}_{\mathrm{JT}}$ was constructed as an *even* distortion with respect to one of the three equivalent σ_{Q}, explicitely breaking the three-fold symmetry of the equilateral trimer. States A and S are also even upon such perturbation; whereas state B is *odd* under the trimer plane of reflection, giving off-diagonal terms equal to zero, $\langle \mathrm{B}| \mathcal{H}_{\mathrm{JT}} |\mathrm{A,\,S}\rangle = 0$. The other non-zero terms were determined by Watkins [108] to be,

$$\mathcal{H}_{\mathrm{JT}} = \begin{array}{c} \\ \langle B| \\ \langle A| \\ \langle S| \end{array} \begin{array}{c} |B\rangle \quad\quad |A\rangle \quad\quad |S\rangle \\ \begin{pmatrix} -VQ_{\mathrm{A}} & 0 & 0 \\ 0 & +VQ_{\mathrm{A}} & \frac{V}{\sqrt{2}}Q_{\mathrm{A}} \\ 0 & \frac{V}{\sqrt{2}}Q_{\mathrm{A}} & 0 \end{pmatrix} \end{array} \tag{4.2}$$

As it is implied in equation 4.2, both states A and S are no longer eigenstates of the distorted trimer, but they are combined into new states A'$\sim \lambda\mathrm{A} + \gamma\mathrm{S}$ and S'$\sim \gamma\mathrm{A} + \lambda\mathrm{S}$, with $\lambda > \gamma$. As expected, states B and A' present a different tendency with respect to the *sign* of the applied linear perturbation as, $\langle \mathrm{B}| \mathcal{H}_{\mathrm{JT}} |\mathrm{B}\rangle = -VQ_{\mathrm{A}}$; whereas $\langle \mathrm{A'}| \mathcal{H}_{\mathrm{JT}} |\mathrm{A'}\rangle = \langle \lambda\mathrm{A} + \gamma\mathrm{S}| \mathcal{H}_{\mathrm{JT}} |\lambda\mathrm{A} + \gamma\mathrm{S}\rangle \sim (1 + \sqrt{2}\gamma)VQ_{\mathrm{A}}$, in the case of $|\lambda|^2 \sim 1$. The degeneracy of states A and B is not only lifted, but $\epsilon_{\mathrm{A'}} < \epsilon_{\mathrm{B}}$ for $Q_{\mathrm{A}}(+)$ (or a pairing distortion) and *viceversa* for $Q_{\mathrm{A}}(-)$ (resonant geometry), as it is sustained by experimental evidence. We also show that within the linear regime considered by Watkins, a similar energy shift of the trap levels A and B upon the Jahn-Teller distortions is

expected.

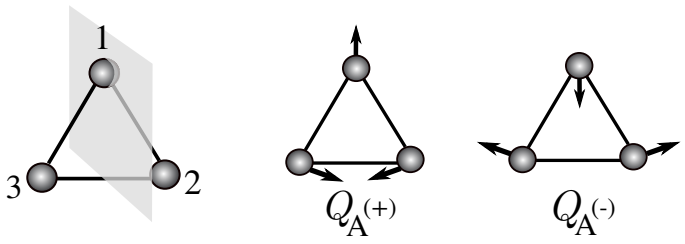

Figure 4.2: Atomic distortions described by Watkins' model [108] for the silicon E-center. The horizontal plane of reflection, σ_Q, for both static distortions is also shown.

To conclude, Watkins' model is capable of reproducing the observed Jahn-Teller effect because the Hamiltonian, $\mathcal{H}_0 + \mathcal{H}_{JT}$, accounts for atomic distortions upon simple symmetry considerations. A generalization of his model would consist in writing the trimer Hamiltonian with an explicit parameterization of interatomic distances, d_{ij}, naturally describing changes in the atomic configuration (see section 2.1 on the simple Molecular Orbital approach). Furthermore, the model $\mathcal{H}_{JT}$ is restricted to one given reflection or distortion plane, σ_Q, overlooking the existence of three equivalent distorted trimers. The transition from positive distortion Q_A^+ (pairing geometry) to negative distortion Q_A^- (resonant configuration) is therefore forced to pass through $Q_A = 0$, or the high symmetric configuration. Watkins was aware of such limitation, when he wrote that pairing and resonant geometries were minima and saddle points of the PES within the $Q_A - Q_B$ plane [108], making explicit the need for a second parameter, Q_B, but without including it in his model of $\mathcal{H}_{JT}$. The Hamiltonian in equation 4.2 can therefore not reproduce the transition path between equivalent atomic distortions (or equivalent Q_A^+ with respect to three equivalent planes of symmetry σ_Q). We finally note that at this level of theory, without an expicit treatment of the electronic interaction and/or the delimitation given by the host lattice, the model is not capable of predicting whether the pairing or the resonant configurations are the actual minima of PES at different charge states. The fact that in Watkins' theoretical work the *correct* geometry was assigned to charge states 0 and -1 was induced from experimental evidence.

4.1.2 A generalization of Watkins' model: full correspondence with experience

We now introduce our generalization of Watkins' approach or our *toy-model* for the silicon E-center, also based on the trimer formed by atoms 1, 2 and 3 in Figure 4.1. As in any LCAO-based approach, the defect-induced localized states can be written as,

$$\psi^{\mathrm{T}}(\mathbf{r}) = \sum_{i}^{N} c_i a_i(\mathbf{r}) \tag{4.3}$$

Where N is the number of host atoms contributing to the trap-states, ψ^{T}, with a dangling bond, a_i. Interatomic distances between atoms constituting the defect, d_{ij}, are constrained by the diamond structure, and therefore equilibrium interatomic distances are limited to $d_{\text{Si-Si}} \pm \Delta d_{ij}$. In other words, since the system constituted by atoms i is not confined to the lattice potential, our model will never describe the equilibrium distances, $d_{ij\,0}$ (as it was shown for the hydrogen molecule in Figure 2.2). The goal of the present approach is therefore not to determine the position of the PES minima, but to qualitatively describe the form ($\{c_i\}$) and relative energy differences of ψ^{T} states. Assuming that within the range in configuration space Δd_{ij}, off-diagonal matrix elements $\mathcal{S}_{ij}$ are small, we consider $\mathcal{S} = \mathbb{I}$, and since the diagonal terms of the Hamiltonian $\mathcal{H}_{ii}$ are almost constant (see their dependency upon the interatomic distance R in Figure 2.2), the reference of energy is set to zero. Furthermore, the basis set, $\{a_i\}$, employed within the *toy-model* does not present the directionality expected from a sp^3 hybridization (dangling bonds in Figure 4.1), but the orbitals are characterized as s-like, with off-diagonal matrix elements,

$$\langle a_i | \, \mathcal{H} \, | a_j \rangle = -\gamma_{ij} = -\gamma_0 e^{-\alpha d_{ij}}. \tag{4.4}$$

The above $\mathcal{H}$ is therefore parameterized according to three interatomic distances d_{ij}. The eigenstates of $\mathcal{H}$ for an equilateral trimer are the same as the ones predicted by Watkins and plotted in Figure 4.1b, with $\epsilon_{\mathrm{A,\,B}} < \epsilon_{\mathrm{S}}$. In Figure 4.3, eigenvalues of the *breathing configuration* or equilateral trimer are marked with $\mathcal{B}$.

Starting from the equilateral configuration, and relying on experimental evidence, we investigate the Jahn-Teller mechanism by breaking the symmetry of the $\mathcal{B}$-trimer with respect to an horizontal reflection plane, σ. Pairing, P, and resonant, R, distortions are then considered by explicitly modifying the set of interatomic distances, making $d_{ij} < d_{ik} = d_{jk}$ for P_σ and

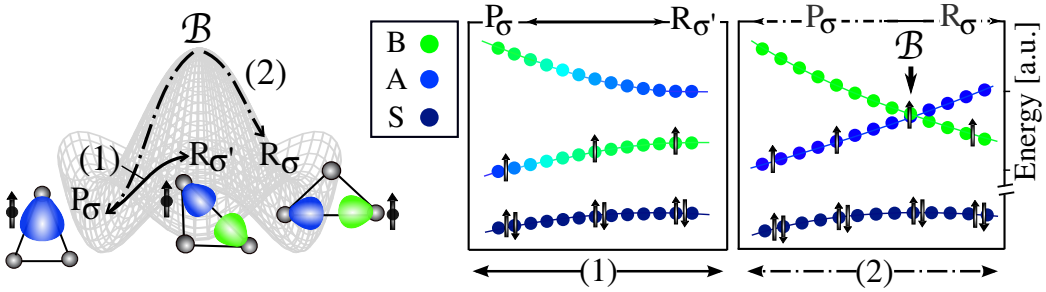

Figure 4.3: Eigenvalues of the trimer at different interatomic distances along σ-unrestricted (1) and σ-restricted (2) paths of the schematic *sombrero*. The symmetry character of the corresponding eigenstates S, A and B is indicated with the color legend.

$d_{ij} > d_{ik} = d_{jk}$ for R_σ. In Figure 4.3, we show the relative energy difference of the trimer eigenvalues at different atomic configurations along the σ-restricted transition path (also denoted as path 2) between pairing (P_σ) and resonant (R_σ) distortions. We assign a blue color to eigenvalues corresponding to *even* eigenstates (states S and A) upon the reflection plane of distortion, σ, an a green color to the B state, for being *odd* under such transformation. Since no confining potential is considered, no minimum of the PES is actually obtained, and so any σ-constrained distortion breaking the symmetry of the breathing configuration, $\mathcal{B}$, is referred to as a Jahn-Teller distortion and is generally denoted as $P_{\sigma,\sigma',\sigma''}$ and $R_{\sigma,\sigma',\sigma''}$ (in contrast with the minima of the E-center PES $P_{1,2,3}$ and $R_{1,2,3}$). Transition path 2 therefore represents different *magnitudes* of the distortion in the positive sense (or P configuration) versus the negative sense (or R conformation). Given the three-fold symmetry of the precursor $\mathcal{B}$ state, a second transition path is investigated when modifying the symmetry plane along the path, $\sigma \rightarrow \sigma\prime$ (path 1 in Figure 4.3). The color of the trimer eigenstates gradually changes from blue to green or *viceversa* along $P_\sigma \leftrightarrow R_{\sigma'}$. In practice, once the initial and final sense, orientation and magnitude of the transition path are conceived, a linear interpolation between initial and final interatomic distances is represented. We also note that Watkins' eigenstates of the distorted trimer S' and A', defined as S'$\sim \gamma$A$+\lambda$S and A'$\sim \lambda$A$+\gamma$S, are also obtained within our toy-model. However, for small perturbations $\lambda \gg \gamma$ and therefore S'$\sim$ S and A'$\sim$ A, and thus we did not rename the states of the trimer in previous discussions.

To summarize, we have fully characterized the PES of the trimer, going one step beyond Watkins' model, since it was limited to the σ-restricted path.

In relation with the neutral E-center, we assume an occupation equal three (up and down arrows in Figure 4.3), explicitly showing that the breathing geometry, $\mathcal{B}$, represented in path 2 of Figure 4.3, corresponds to the inflection point for states A and B, since the corresponding HOMO *abruptly* goes from being a pure A state for a pairing configuration (left side of $\mathcal{B}$) to a B state for a resonant configuration (right side of $\mathcal{B}$). In the case of the second considered path, or atomic transition 1, the HOMO state of the system *gradually* changes from a state A (at a pairing configuration defined upon σ) into a state B (for a resonant configuration R with respect to a different reflection plane, $\sigma\prime$), in agreement with our numerical calculations for the E-center (Chapter 4). Our toy-model for the trimer therefore reproduces the underlying physics of the point defect, in terms of form and energy order of the trap-states, existence of multiple minima and/or metastability of the PES. To this point, we have estimated the electronic structure for a system of non interacting electrons arising from an atomic trimer. In the case of an electronic occupation equal four or the negative state of the silicon E-center, for which an explicit treatment of the electronic interaction might be relevant, a system of interacting electrons within the trimer is considered in the following.

Interacting electrons: the ground state geometry of the trimer

The toy-model based on the one-electron Hamiltonian in equation 4.4 introduced in the previous section allowed us to determine the electronic structure of a trimer for a system of non-interacting electrons. The question that can now be raised is whether it is possible to establish within the toy-model for the trimer the ground state geometry of the silicon E-center at different charge states or different electronic occupations. The neutral charge case was already introduced in the previous section when an electronic occupation equal three was employed to exemplify different transition paths between pairing and resonant configurations (Figure 4.3). For such case, even if a minimum of the PES is missing for a certain *magnitude* of the Jahn-Teller distortion, we observe that $\epsilon_{\mathrm{A}} < \epsilon_{\mathrm{B}}$ for a similar *magnitude* of distortion, showing a preference for a pairing configuration at the given electronic occupation. On the other hand and similarly to the test-cases of H_2^+ and H_2 molecules presented in Chapter 2, there is a motivation to estimate the Coulomb interaction to compare the ground state properties of the trimer at electronic occupation equal three and four. Within our toy-model, we consider that electrons one and two are occupying state S, without interacting with electrons three and four, which are occupying higher energy states A and/or B. We are thus interested by two electrons subject to the

Hamiltonian $\mathcal{H}_1 + \mathcal{H}_2 + \mathcal{H}_U$, where the trimer Hamiltonian $\mathcal{H}_1$ is defined in equation 4.4 and $\mathcal{H}_U$ is the Coulomb interaction between electrons three and four. Equivalently to equation 3.7, six antysimmetric states can be written as,

$$\begin{array}{l} |\Psi_{\mathrm{A}}\rangle = |\mathrm{A}\rangle_1 |\mathrm{A}\rangle_2 \ \chi_{00} \\ |\Psi_{\mathrm{B}}\rangle = |\mathrm{B}\rangle_1 |\mathrm{B}\rangle_2 \ \chi_{00} \\ |\Psi_{\mathrm{AB,\,S}}\rangle = \frac{1}{\sqrt{2}} \left[|\mathrm{A}\rangle_1 |\mathrm{B}\rangle_2 + |\mathrm{B}\rangle_1 |A\rangle_2 \right] \chi_{00} \\ |\Psi_{\mathrm{AB,\,T}}\rangle = \frac{1}{\sqrt{2}} \left[|A\rangle_1 |\mathrm{B}\rangle_2 - |\mathrm{B}\rangle_1 |\mathrm{A}\rangle_2 \right] \{\chi_{11}, \chi_{10}, \chi_{1-1}\} \end{array} \tag{4.5}$$

The eigenvalues, prior to the perturbation $\mathcal{H}_U$, are equal to $2\epsilon_{\mathrm{A}}$, $2\epsilon_{\mathrm{B}}$ and $\epsilon_{\mathrm{A}} + \epsilon_{\mathrm{B}}$ for both singlet, S, and triplet, T, states. For a distorted trimer (see tendency of eigenvalues in Figure 4.3), the electronic ground state wavefunction is Ψ_{A} for a pairing configuration ($\epsilon_{\mathrm{A}} < \epsilon_{\mathrm{B}}$) and Ψ_{B} for a resonant geometry ($\epsilon_{\mathrm{A}} > \epsilon_{\mathrm{B}}$). The energy of such states can be estimated in terms of the Coulomb integral U (Chapter 2), as $2\epsilon_{\mathrm{A}} + U_{\mathrm{AA}}$ and $2\epsilon_{\mathrm{B}} + U_{\mathrm{BB}}$, naturally wondering whether state Ψ_{B} lowers the energy of state Ψ_{A} for a similar magnitude of distortion. Now, since both states A and B are defined as rather simple linear combinations of dangling bonds, we can evaluate these integrals in terms of such constituent elements; namely $\langle \Psi_{\mathrm{B}} | \mathcal{H}_U | \Psi_{\mathrm{B}} \rangle = \frac{1}{4} \langle a_2(\mathbf{r_1}) - a_3(\mathbf{r_1}), a_2(\mathbf{r_2}) - a_3(\mathbf{r_2}) | \mathcal{H}_U | a_2(\mathbf{r_1}) - a_3(\mathbf{r_1}), a_2(\mathbf{r_2}) - a_3(\mathbf{r_2}) \rangle$. For an *equilateral trimer*, we find, however,

$$2 \langle \Psi_{\mathrm{A}} | \mathcal{H}_U | \Psi_{\mathrm{A}} \rangle = 2 \langle \Psi_{\mathrm{B}} | \mathcal{H}_U | \Psi_{\mathrm{B}} \rangle = U_{ii} + U_{ij} + 2J_{ij} - 4F_{ij} \tag{4.6}$$

Where the above integrals are defined for simplicity in the following notation, $U_{ij} := \left[a_i^*(\mathbf{r_1}) a_i(\mathbf{r_1}) a_j^*(\mathbf{r_2}) a_j(\mathbf{r_2}) \right]$ and $J_{ij} := \left[a_i^*(\mathbf{r_1}) a_j(\mathbf{r_1}) a_j^*(\mathbf{r_2}) a_i(\mathbf{r_2}) \right]$. The reminding integrals F do not correspond to either a Coulomb or Exchange integrals, since they are of the form, $F_{ij} = [a_i^*(\mathbf{r_1}) a_i(\mathbf{r_1}) a_i^*(\mathbf{r_2}) a_j(\mathbf{r_2})]$. It should be clear that equation 4.6 is obtained after assuming the three dangling bonds are equivalent (i.e. $U_{ij} = U_{ji} = U_{ik} =$ etc). The terms U_{AA} and U_{BB} must therefore break the degeneracy when the system undergoes a Jahn-Teller distortion, making $U_{ij} \neq U_{ik}$, etc. We conclude that without explicitly solving the integrals in equation 4.6 for a distorted trimer, it is not possible to hypothesize about the ground state of the trimer for an electronic occupation equal four.

To conclude, from simple symmetry considerations we have proven that the neutral and negative trimer are both characterized by a *Mexican hat* energy surface, in alignment with experimental evidence. We have however explicitly shown that the treatment of the electronic Coulomb repulsion at this level of theory limits a further comparison with EPR spectroscopy or a definitive assignment of the *true* ground state minima. A quantification of

the toy-model is hence necessary if a stronger comparison with experience is sought after, as shown in previous Chapter for the numerical investigation of the E-center at the PBE level of approximation. The success of the full theoretical study for the silicon E-center has motivated the joint toy-model-*ab initio* characterization of selected centers in silicon, providing comprehensive pictures validated with experience.

4.2 A long standing controversy: the silicon divacancy

Contrary to the E-center, the silicon divacancy is an intrinsic point-like defect since it consists of a vacancy adjacent to another vacancy (see Figure 4.4). It is a very common center in both n-type and p-type irradiated silicon [13] and it is known to introduce three DLTS levels in the semiconductor band gap, which have been assigned to the charge transitions (+/0), (0/-) and (-/2-) [13]. Similarly to the E-center, previous theoretical attempts to characterize the defect [119, 120, 121, 122, 123, 124, 125, 126, 127, 128, 129, 130] are not only incapable of reproducing the experience, but the contradictions among the published results revealed the sensitivity of the Jahn-Teller distortion to the employed exchange-correlation functional or, with a broader term, the electronic interaction treatment. The motivation to study this defect is therefore to make a clearer theoretical model, supported by the experimental measurements. Furthermore, due to its structural resemblance with the E-center, we can consider the divacancy as a model comprising two trimers facing each other, as shown in Figure 4.4.

The structural similarity between the E-center and the divacancy was first postulated by Watkins and Corbett, since early EPR studies [18, 17] on doped silicon. The silicon divacancy is associated with two *different* EPR signals measured after irradiating p-type and n-type silicon: the G6 and G7 spectra [18], which have been assigned to charge states, V_2^+ and V_2^-. Evidence of pairing distortions ($d_{23} < d_{12} = d_{13}$, with $d_{ij} = d_{i'j'}$, see Figure 4.4) were reported for both systems; for which it was postulated that the localized electrons were filling an extended orbital between atoms 1 and 1' (or more generally, i and i'). Reorientation barriers analogous to the ones discussed for the trimer at low temperatures were estimated to be 0.073 eV and 0.056 eV for V_2^+ and V_2^- respectively. Complementary theoretical considerations allowed Watkins [108] to postulate that the same Mexican hat PES obtained

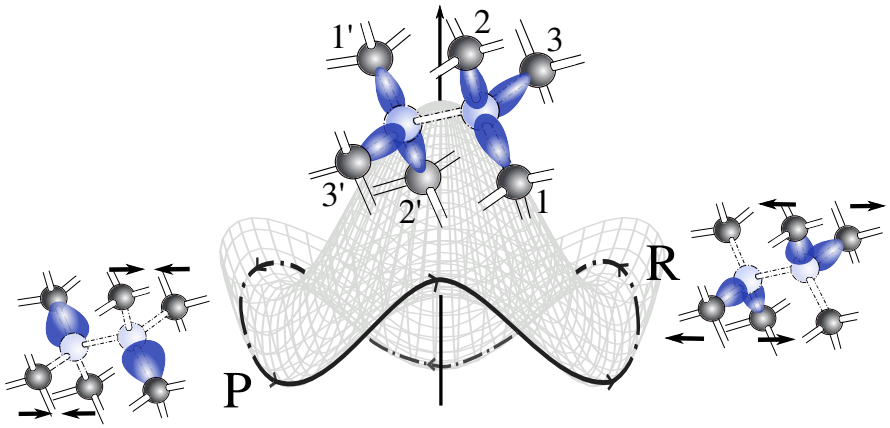

Figure 4.4: The silicon divacancy and its potential energy surface at positive charge state according to Watkins' model. The electronic density for the unpaired electron is shown.

for the E-center at neutral charge state could also describe singly charged divacancies (Figure 4.4), and so, a second *sense* of the Jahn-Teller distortion was included in the model: the resonant configuration, R. Later joint theoretical and EPR studies [131] investigated further the wavefunction of the unpaired electron and its link with the measured spectrum, questioning the symmetry previously established by Watkins. Both infrared absorption and photoconductivity measurements were performed on irradiated silicon by [9]. Their analysis of the dependence of each measured absorption band upon the existence of photoconductivity and/or the position of the Fermi level above/below which a given signal was disappearing allowed [12] to tentatively assign the 1.8-μm, 3.3-μm and 3.9-μm bands to three electronic excitations arising from the silicon divacancy-induced states.

The big effort made by the *ab initio* community during the past three decades to characterize the ground state geometry of the divacancy is an unequivocal sign of the complexity in modelling such center. A resonant-bond model as the ground state Jahn-Teller distortion for the negative state was proposed by [119, 120, 122], criticized by Watkins in [121] and supported by later calculations [130]. In [123] only the neutral charge state was considered, reporting a resonant distortion as the global minima, whereas a pairing configuration was found to be the ground state for all three charge states in [125, 126, 127]. To add more incoherence, a mixed structure with an S_2 geometry was reported for V_2^- in [124], a resonant configuration for states 0, $\pm$ 1 was postulated in [128] and a drastic dependency with the XC-functional was indicated by [129] when describing simultaneously pairing and resonant

configurations as ground state geometries for charge state 0 and -1.

Even though a pairing configuration has been succesfully described by [125, 126, 127] for both $V_2^{\pm}$, no effort was made to investigate the shape of the PES and the role of the resonant-bond geometry in the global theoretical model remains unclear. The possibility of both configurations being metastable was briefly commented in [119, 128]. If Watkins' hypothesis is correct [108], as it was for the E-center, the resonant distortion would however be the saddle point of the transition between equivalent pairing configurations, and the difference in energy between both geometries would determine the reorientation energy barrier.

In the following, we present a toy-model for the silicon divacancy (section 4.2.1), based on two facing trimers, which reproduces the *Mexican hat* energy surface postulated by Watkins. The model is then rediscussed in terms of point-group theory with the pretext of further comparing with previous models, but it is ultimately employed to describe the Jahn-Teller effect as the symmetry breaking mechanism $D_{3d} \rightarrow C_{2h}$. The toy-model is later quantified at the PBE level of approximation (section 4.2.2), explicitly showing different degrees of comparison with experience. We can therefore judge the quality or accuracy of the symmetry-guided *ab initio* calculations to resolve Jahn-Teller distortions, in contrast with previous studies. We conclude with the assignation of the measured optical bands within our bi-trimer picture with the inclusion of many body effects (section 4.2.3).

4.2.1 A toy-model for the divacancy

As already mentioned above, the silicon divacancy can tentatively be modeled as two facing trimers T and T', as shown in Figure 4.5. A total number of six dangling bonds must be taken into account and therefore the Hamiltonian can be written as,

$$\mathcal{H} = \begin{pmatrix} \mathcal{H}_{\mathrm{T}} & \mathcal{H}_{\mathrm{C}} \\ \mathcal{H}_{\mathrm{C}} & \mathcal{H}_{\mathrm{T'}} \end{pmatrix} \tag{4.7}$$

where $\mathcal{H}_{\mathrm{T}}$ and $\mathcal{H}_{\mathrm{T'}}$ are the Hamiltonian corresponding to both trimers, and thus identical to equation 4.4. The off-diagonal terms, included in $\mathcal{H}_{\mathrm{C}}$, account for the *coupling* between trimers and so,

$$\mathcal{H}_{\mathrm{C}} = \begin{pmatrix} -\gamma_{11'} & -\gamma_{12'} & -\gamma_{13'} \\ -\gamma_{21'} & -\gamma_{22'} & -\gamma_{23'} \\ -\gamma_{31'} & -\gamma_{32'} & -\gamma_{33'} \end{pmatrix} \tag{4.8}$$

where $\gamma_{ij'}$ are defined for interatomic distances $d_{ij'}$ between atoms belonging to different trimers. Since the defect is embedded in the silicon lattice, characteristic interatomic distances (at the PBE level of theory) are, $d_{ij} = d_{i'j'} = 3.87$ Å, $d_{ij'} = 4.53$ Å and $d_{ii'} = 5.96$ Å. Since $\gamma_{ij} = \gamma_{i'j'} > \gamma_{ij'}, \gamma_{ii'}$ prior to defect relaxation, we consider that each trimer preserves its *identity*, *i.e.* the expected Jahn-Teller distortions will be symmetric for both trimers, being d_{ij} always equal to $d_{i'j'}$, as postulated by Watkins and shown in Figure 4.4. The six eigenstates for two facing equilateral trimers are represented in Figure 4.5. The notation employed to name such eigenstates is based on the toy-model for the trimer, introduced in section 4.1. Since the form of the trimer-eigenstate (orbitals S, A and B in Figure 4.3) is the same for both trimer T and T', the bi-trimer orbitals are named according to the symmetry transformation upon inversion (transformation T $\leftrightarrow$ T'). State S + S', for example, is even upon such transformation, whereas S - S' is odd.

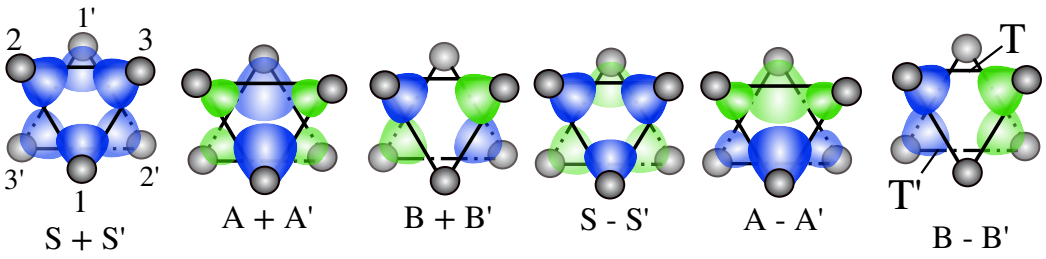

Figure 4.5: The divacancy toy-model based on a bi-trimer and its corresponding eigenstates.

As already stated several times, we assume that the divacancy PES can be described by a bi-trimer toy-model limited to the constraint $d_{ij} = d_{i'j'}$. Such assumption is based on experimental evidence [18] and the difference in magnitude of γ_{ij} versus $\gamma_{ij'}$, imposed by the surrounding lattice. We can therefore guide the exploration of the divacancy or bi-trimer potential energy surface by the model developed for the silicon E-center or a single trimer. In Figure 4.6 we represent the six energy levels obtained for the *breathing geometry*, $\mathcal{B}$, or the equilateral trimers configuration. Highly symmetric states S + S' and S - S' are lowest in energy, with $\epsilon_{\text{S+S'}} < \epsilon_{\text{S-S'}}$. States A - A' and B - B' are higher and degenerate in energy, as well as states A + A' and B + B', with $\epsilon_{\text{A+A'}} > \epsilon_{\text{A-A'}}$. Similarly as for the single trimer, a Jahn-Teller distortion in the form of pairing (P) or resonant (R) configuration breaks the symmetry of the system, lifting the degeneracy of all four states. Furthermore, since the three-fold symmetry is present also in this case, a PES characterized by three equivalent minima is also expected. Transition paths

1 and 2 explored for the trimer can thus also be conceived for the divacancy and so in Figure 4.6 a similar color-legend as the one defined for the trimer in Figure 4.3 is employed. We note that besides the transformation upon the plane of reflection, σ, for which the distinction blue/green is made, the transformation under the inversion symmetry is also considered when using the filled/empty pattern.

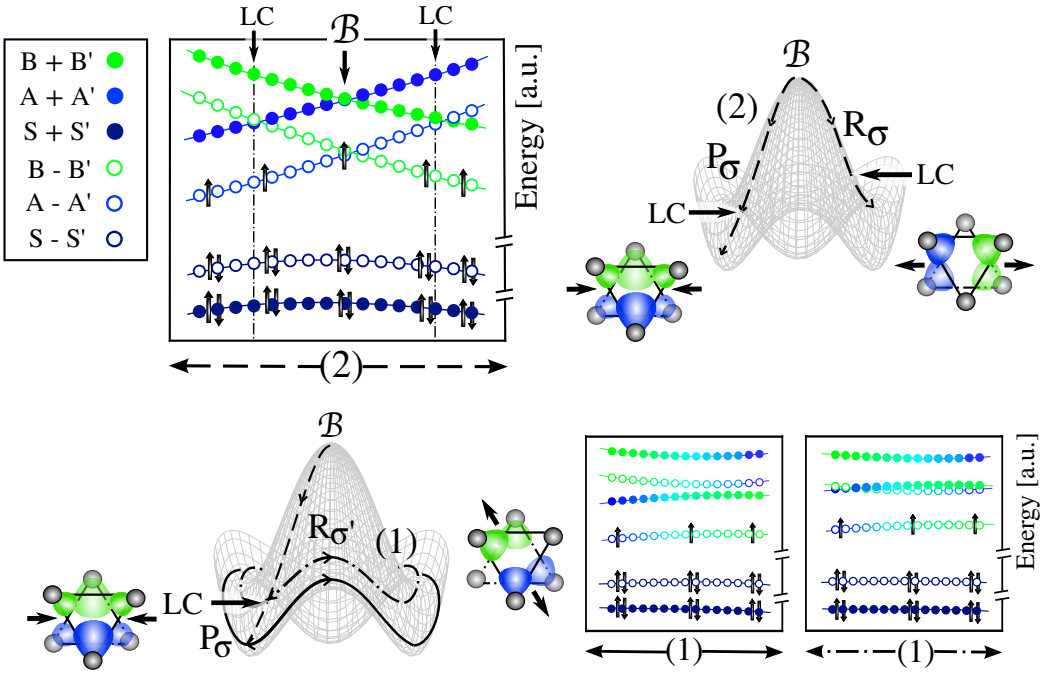

Figure 4.6: Eigenvalues of the bi-trimer within the divacancy toy-model along two different transition paths (1) and (2) between pairing and resonant distortions.

Assuming an electronic occupation equal five (*e.g.* divacancy at positive charge state), path 2 in Figure 4.6 shows how the HOMO goes from being the A - A' state for a pairing-like distortion (left side of $\mathcal{B}$) to the B - B' state for a resonant-like configuration (right side of $\mathcal{B}$) along the σ-constrained transition. Two regimes appear for the transition path 2, marked by the level-crossing (LC) of states A + A' and B - B' for a positive distortion (P) and states B + B' and A - A' for the opposite sense of distortion (R). In other words, if the distortion in both trimers is sufficiently large to overcome the *coupling* terms, a level crossing would energetically favor both states A over states B for a large pairing geometry and *viceversa*. We note again that at this level of approximation it is not possible to conclude which *magnitude*

of the *pairing or resonant* distortions are the *actual* minima/saddle points of the divacancy PES. The *sombrero* PES in Figure 4.6 is a pure schematic representation of path 2; since the point marked as LC could by all means already correspond to the actual minimum.

A second path is considered by going around the *sombrero* (see again path 1 for the trimer in Figure 4.3), characterizing the transitions between equivalent minima. In this case, we have distinguished two different regimes, by showing a transition between *large* distortions (black line) and *critic* distortions (dotted line), for which the level-crossing is still very subtle. In the case of having an electronic occupation equal five or the positively charged divacancy (Figure 4.6), the difference between such paths is unnecessary, since the HOMO will gradually change from state A - A' to state B - B' for both considered paths. In the case of a higher electronic occupation (especially for occupation equal 7 or the negatively charged divacancy) it does however become relevant due to the proximity of the two intermediate eigenstates.

As it was briefly mentioned above, the intra- and inter-trimer hoppings, γ_{ij} and $\gamma_{ij'}$, were defined upon the characteristic interatomic distances of a divacancy embedded in the silicon lattice. For a Jahn-Teller distortion with unpaired distances d_{12} and $d_{1'2'}$, and therefore $d_{13} = d_{23} = d_{1'3'} = d_{2'3'}$, two different inter-trimer hopppings are obtained, since $-\gamma_{ij} = -\gamma_0 e^{-d_{ij}/a_0}$. The intra-trimer hoppings, defined equivalently as $-\gamma_{ij'} = -\gamma_0 e^{-d_{ij'}/a_0}$, are also modified by the symmetry breaking, since the intra-trimer distances become: $d_{33'} \neq d_{11'} = d_{22'}$ and $d_{12'} \neq d_{13'} = d_{23'}$. For a pairing distortion, characterized by $d_{12} < d_{13} = d_{23}$, the intra-trimer hoppings become, $d_{33'} > d_{11'} = d_{22'}$ and $d_{12'} < d_{13'} = d_{23'}$. In the case of a resonant geometry, the inequalities are inverted, being $d_{12} > d_{13} = d_{23}$, $d_{33'} < d_{11'} = d_{22'}$ and $d_{12'} > d_{13'} = d_{23'}$. Once the magnitude and orientation (either σ or σ') of the initial and final distortions of the considered path are defined, the respective hoppings are computed upon their interatomic distances. The subset of atomic configurations constituting the path are obtained by linearly interpolating the initial and final configurations. The importance of the inter-trimer hopping was commented when discussing the level crossing of eigenstates upon the magnitude of the Jahn-Teller distortion (Figure 4.6). In the limit case for which the inter-trimer hopping is set to zero (case of two non-interacting trimers), *gerade* and *ungerade* eigenstates upon inversion will be indistinguishable, degenerate in energy. The pairing/resonant distortion in each trimer would be capable of lifting the degeneracy of states A and B, but not between A - A' and A + A'. Such limit case is prevented by the silicon lattice environment, but it could still question the validity of the constrain $d_{ij} = d_{i'j'}$ in the regime

prior to the level crossing. In other words, in the present work the possibility of having a configuration lower in energy by breaking the inversion symmetry upon the two trimers in the region between the two LC points is not considered.

The divacancy from a point-group symmetry perspective

Applying a similar one-electron model as the one introduced in section 4.1, Watkins *et al.* [18] wrote the six localized levels of the divacancy as a linear combination of the broken bonds a_i, where $i = 1, ..3, 1', ..3'$, being capable of ordering such levels upon symmetry considerations. To be specific, he employed a perturbative Hamiltonian, similar to the one in equation 4.2, to establish the electronic structure at a given Jahn-Teller distortion. Since both Jahn-Teller distortions (pairing and resonant geometries) present a C_{2h} point-group symmetry, he labeled the trap-induced states with their respective symmetry representation (see Figure 4.7).

Table 4.1: Character table for the C_{2h} point-symmetry group. The notation employed in section 4.2.1 is also included.

C_{2h}	E	C_2	σ_h	i	bi-trimer
a_g	1	1	1	1	A + A' or S + S'
b_g	1	-1	-1	1	B + B'
a_u	1	1	-1	-1	B - B'
b_u	1	-1	1	-1	A - A' or S - S'

Before discussing the electronic occupation within Watkins model, a more detailed discussion regarding point-group symmetries and their representations is given in the following. In Table 4.1, the transformations of the four group representations (b_u, a_u, a_g and b_g) under the four characteristic symmetry operations are shown. The symmetry operations in the case of C_{2h} are: the identity (E), the horizontal plane of reflection (σ_h in Figure 4.7), the π rotation around an axis perpendicular to σ_h (C_2) and the inversion of elements $j \leftrightarrow j'$ (i). The states denoted by a are symmetric under a π rotation, whereas the b states are antisymmetric. The distinction *gerade* (g) and *ungerade* (u) is made for symmetric and antisymmetric states upon inversion (note that, for example, $b_u \sim a_1 - a_{1'}$ and on the contrary, $a_g \sim a_1 + a_{1'}$). The fact that any symmetry operation (*e.g.* σ_h) is actually a combination of the other two, *i.e.* $C_2 \bigotimes i = \sigma_\mathrm{h}$, is exploited in the use of a two-letter convention

to name each representation univocally. We note that the convention used when naming the toy-model states was based on the σ_{h} and i operations, since A and B kind states have opposite parity upon the reflection plane (σ_{h}) and the distinction A + A' and A - A' are the *gerade-ungerade* notation for the inversion transformation (i). States S and A are indistinguishable under such symmetry transformations, as indicated in Table 4.1. However, since the highly symmetric states S are always lower in energy (Figure 4.6) and they are not precursors of the symmetry-breaking mechanism, they are typically not included in the discussion, naming states A + A' and A - A' as a_g and b_u unequivocally.

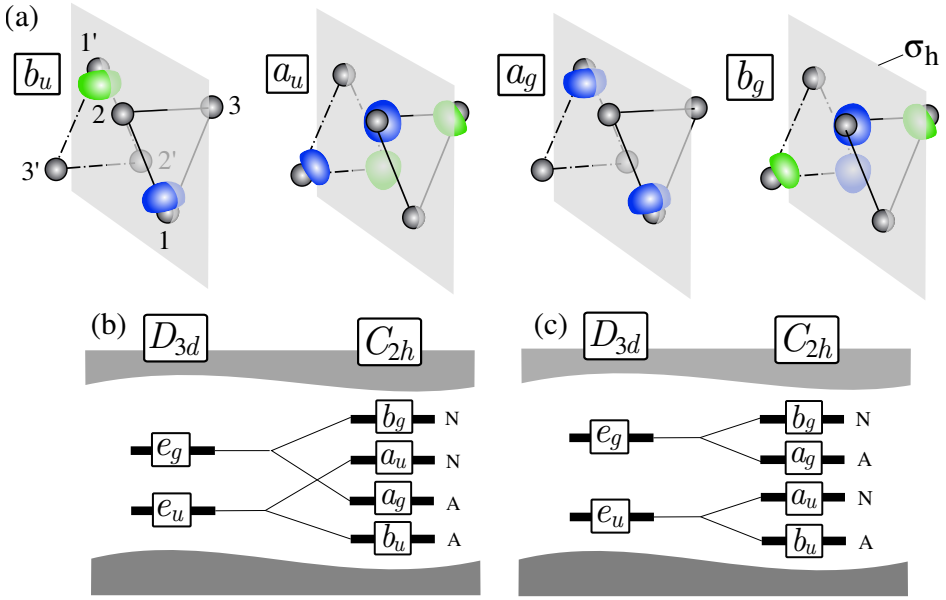

Figure 4.7: The trap-induced states of the divacancy named upon symmetry transformations (a). Electronic structure for the divacancy according to [125] for *large* (b) and *small* (c) pairing Jahn-Teller distortions.

Watkins' original model for the divacancy [18, 108] was guided by the experimental evidence of a pairing Jahn-Teller distortion for both charged states $\mathrm{V}_2^{\pm}$. It was then stated that since the same sense of distortion was observed for charged states $\pm$, both states A were to be occupied and lower in energy with respect to states B (see level ordering for *large* pairing distortions in Figure 4.6). The electronic occupation was therefore postulated to be $a_g^1 b_u^0$ and $a_g^2 b_u^1$ for the centers VV^+ and VV^- respectively. We remark that even if the form of Watkins orbitals is in agreement with our toy-model, he estimated the order of the A states, as being $\epsilon_{b_u} < \epsilon_{a_g}$ for all possible magnitudes

of the pairing distortion in disagreement with our toy-model (Figure 4.6). This remark was already stated by early theoretical analysis of [131] and its comparison with EPR spectroscopy and first principles calculations [125, 126] obtaining *large* paring distortions for both charge states (Figure 4.7), as discussed in detail in the following.

The divacancy potential energy surface

The energy surface represented in Figure 4.8 might be regarded as a summary of the emerging conclusions from the divacancy toy-model. Such energy surface, corresponding to the HOMO of the bi-trimer for an electronic occupation equal five, reveals the existence of three equivalent minima in the form of Jahn-Teller distortions with respect to the three symmetry-planes of the equilateral trimers. Along the transition paths between equivalent minima, the symmetry character of the HOMO is modified, being even with respect to σ_{h} at the minima (blue color) and odd at the saddle points (green color).

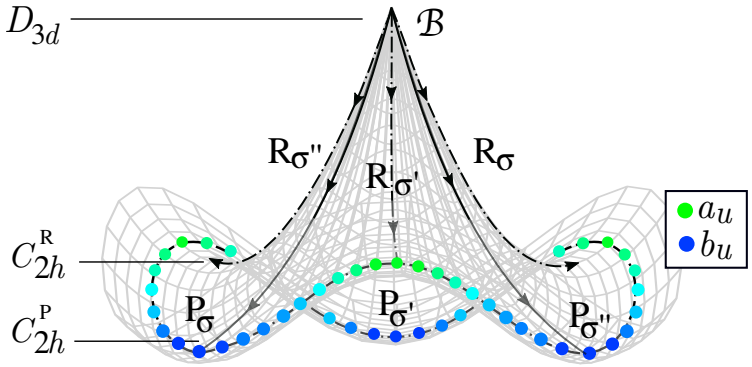

Figure 4.8: The silicon divacancy potential energy surface at positive charge state within our bi-trimer toy-model. The energy surface corresponds to the ϵ_{HOMO} at different atomic configurations. Note the change of filled/empty pattern with respect to previous section (*i.e.* $b_u \equiv$ A - A' and $a_u \equiv$ B - B').

The breathing configuration, $\mathcal{B}$, is located at the peak of the PES, representing the instability of the orbitally-degenerate configuration. One could however wonder about the form of the *top* of the *tent*: is the abrupt peak shape expected in the actual point defect PES? Within our toy-model, such shape has a simple explanation in terms of the *avoided level crossing*, which can be easily illustrated for a two level system. We consider a general two-state Hamiltonian describing the energy levels of states a_u and b_u, E_a and

E_b, along a path connecting two regimes where $E_a < E_b$ and $E_a > E_b$,

$$\mathcal{H} = \begin{pmatrix} E_a & w \\ w^* & E_b \end{pmatrix} \tag{4.9}$$

Since by construction states a_u and b_u have opposite signs upon the plane of reflection σ, any hermitan matrix conceived in a σ-constrained space, $\mathcal{H}_\sigma$, has off diagonal terms equal zero, $\langle a_u | \mathcal{H}_\sigma | b_u \rangle = 0$. In other words, if the above defined Hamiltonian commutes with the reflection upon σ operator, states a_u and b_u are symmetry protected, leading to no avoiding crossing ($w = 0$) and the system abruptly goes from one state to the other. If however the Hamiltonian 4.9 does not preserve symmetry, $w \neq 0$, and the new eigenvalues are of the form $E_\pm = \frac{1}{2}(E_a + E_b) \pm \frac{1}{2}\sqrt{(E_a - E_b)^2 + 4|w|^2}$. The crossing is thus avoided, smoothing the inflection point of the transition between states a_u and b_u. Returning to the shape of the bi-trimer PES, any of the three paths passing by the breathing configuration, $\mathcal{B}$ preserves the symmetry, leading to level crossing. Any other path, obtained by the intersection of the conical shaped surface and any plane not passing by $\mathcal{B}$, is characterized by an avoiding level crossing. In the case of the actual point defect PES, it is difficult to hypothesize whether a symmetry protected inflection point can exist, since contributions from the lattice or higher order of theory might give $w \neq 0$ for the silicon divacancy.

In the present work, we have therefore developed a toy-model for the silicon divacancy, demonstrating that the center is also characterized by a *Mexican hat* energy surface. Pairing and resonant distortions for the trimer and bi-trimer are hence described by a general model of symmetry-breaking mechanisms: $C_{3v} \rightarrow C_{1h}$ and $D_{3d} \rightarrow C_{2h}$ respectively. The particular complexity when characterizing the Jahn-Teller effect for the divacancy is explained by the level crossing of the partially occupied defect states for increasing atomic distortions. At this level of theory, in the case of large pairing distortions and an electronic occupation equal one (for example), we propose an electronic configuration $b_u^\uparrow$ (A - A'), in clear disagreement with Watkins' original model, $a_g^\uparrow$ (A + A'), but sustained by symmetry considerations.

4.2.2 Quantitative analysis and link with EPR spectroscopy

Our first-principles characterization of the silicon divacancy, guided by the simple qualitative analysis, had as first objective to explore the PES at positive and negative charge states, linking the theoretical model with EPR

spectroscopy results. At the PBE level, we confirm that the ground state geometry of the silicon divacancy at both singly charge states is a pairing Jahn-Teller distortion, whose characteristic interatomic distances are collected in Table 4.2 (note that at this level of theory, $d_{ij} = d_{i'j'}$, as assumed for the toy-model). Further exploration of the divacancy PES allowed us to identify the resonant configurations as the saddle points of the transition path between pairing-equivalent minima, and thus interatomic distances for such geometry are also included in Table 4.2. Finally, in order to have a reference for the magnitude of the Jahn-Teller distortions, interatomic distances for the neutral E-center (vacancy-phosphorus complex isoelectronic to the VV^+) are also collected in the Table. A direct comparison of the three pairing geometries allow us to conclude that both isoelectronic systems present similar magnitudes of the Jahn-Teller distortion, whereas such distortion is *quenched* for the negative charge state of the divacancy.

Table 4.2: Relevant interatomic distances d_{ij} for the E-center (phosphorous-vacancy complex) at neutral charge state and the divacancy at singly charge states, computed within the PBE approximation. All values are given in Å.

Center	Pairing		Resonant	
	d_{ij}	$d_{jk} = d_{ik}$	d_{ij}	$d_{jk} = d_{ik}$
PV^0	2.99	3.58	3.59	3.20
VV^+	3.07	3.64	3.66	3.36
VV^-	3.28	3.43	3.51	3.30

As predicted by the toy-model, differences in the sense and magnitude of the atomic distortions result in different band structures or different ordering of the defect-induced states. From the spatial projection of the wavefunction and/or electronic densities (Figure 4.9), we can identify the Kohn-Sham eigenfunctions with our toy-model states, showing that simple symmetry-based considerations were enough to qualitatively describe the electronic structure of the divacancy. At this level of theory, and including the description of the surrounding lattice, two different level-orderings for the pairing configuration are reported according to the two magnitudes of the distortion predicted as minima for the two charge states. As represented in Figure 4.9, the largest perturbation, corresponding to the positive charge state, is characterized by the slight inversion of states a_g and a_u (or the level-crossing point, LC, in Figure 4.6). Independently of the relative positions of such unoccupied states, the unpaired electron is located at state b_u or A-A', which within the mean-

field approach is positioned below the top of the valence band. At negative charge state, the quenched pairing distortion is not enough to favor both A-like states over the B-like states, locating the unpaired electron in state a_u or B-B'. The level-ordering of defect-states is also investigated for the resonant configuration, R, for $q = +1$ (Figure 4.9). Since the magnitude of such distortion is rather quenched for all three systems considered in Table 4.2, it is not surprising that the Jahn-Teller effect is not capable of overcoming the LC point for a negative sense of the distortion, and so, we find b_u lower in energy than b_g or B+B'.

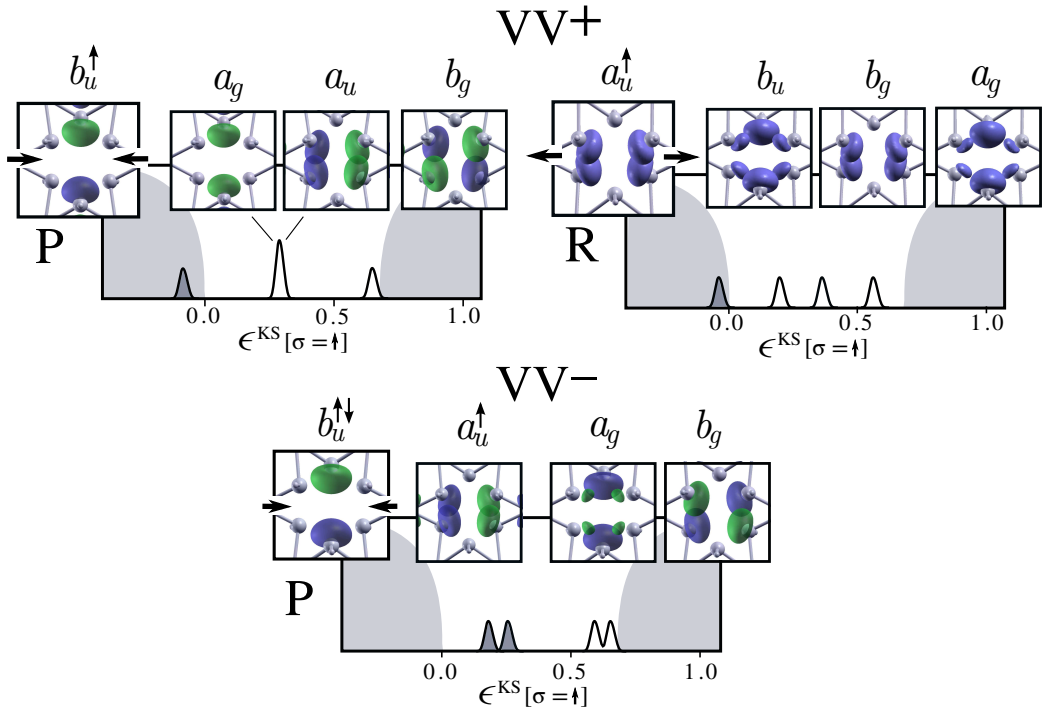

Figure 4.9: Spin-projected Kohn-Sham density of states for the pairing geometry at both single charge states of the divacancy and for the resonant configuration at positive state, estimated within the PBE approximation. The wavefunction corresponding to the defect-states for the P configurations and the electronic density for the R distortion are also shown. Defect states are named according to point group C_{2h} transformations. Filled states are represented as filled levels in the DOS plot and/or by up and down arrows subscripts of the defect names, *e.g.* $b_u^{\uparrow}$ for the VV^+ at pairing configuration. Kohn-Sham eigenvalues are given in eV. Black arrows indicate the plane and sense of distortion for both P_1 and R_1 (or P_σ and R_σ for the toy-model).

At positive charge state we report an electronic configuration $b_u^{\uparrow}$, supported by both symmetry-based considerations and PBE calculations, in contrast with Watkins simple model, reporting $a_g^{\uparrow}$. Independently of this disagreement, both models predict the electronic density for the unpaired electron to be described by an extended orbital between atoms i and i' (or a σ-even-state). At negative charge state, Watkins postulated that the unpaired electron was located at the b_u state, being the overall configuration, $a_g^{\uparrow\downarrow}b_u^{\uparrow}$. Besides the fact that this level-ordering contradicts again the *gerade/ungerade* ranking predicted by our toy-model, Watkins was reporting a large pairing distortion, where all three localized electrons were in σ-even-states (or extended orbitals between equivalent atoms under inversion). At the PBE level, we obtain an electronic occupation $b_u^{\uparrow\downarrow}a_u^{\uparrow}$, for which the unpaired electron is described by a σ-odd-state for a small pairing distortion.

Our *ab initio* calculations also contradict previous first-principles calculations investigating the electronic structure of the negative divacancy [125, 126], since they both obtained electronic configurations $b_u^{\uparrow\downarrow}a_g^{\uparrow}$ for a pairing distortion. At the LDA level of approximation, S. Ogüt *et al.* [125] did emphasize that the level-crossing of states a_g and a_u was only obtained if size effects were minimized, increasing the cluster size from $Si_{36}H_{42}$ to $Si_{316}H_{158}$ and concluding that the smallest cluster for which $\epsilon_{a_g} < \epsilon_{a_u}$ was $Si_{206}H_{158}$. In [126], by using a similar cluster method and a local density functional, they did however also report the structure $b_u^{\uparrow\downarrow}a_g^{\uparrow}$ for the *small* cluster $Si_{146}H_{98}$. In the present work, size effects are minimized by increasing the 216-atoms cubic cell to a 512-atoms cell, observing small variations in the interatomic distances, modifying the level-ordering of defect-induced states only in the case of the positive charge state (obtaining $\epsilon_{a_u} < \epsilon_{a_g}$ for the smaller cell). A further remark can be made if the work of Sieverts *et al.* [131] is brought into the discussion, since they argued that if VV^- was identified with the a_g state, the theoretical values for the hyperfine parameters were far too low compared to the experimental values, resulting in a poor description of the system. We can therefore conclude that unequivocally assigning the a_g or b_u orbitals to the VV^- center is a non-trivial task. Because of the limitations of the employed theoretical approach[131] (EHT calculations), the authors argued about the reliability of the computed hyperfine parameters, explicitly stating the need for a higher level of theory. One possible strategy would be to resolve the hyperfine structure directly from *ab initio* calculations (as implemented in the Quantum-Espresso package [132]) to finally and unequivocally assign the a_g or b_u orbital to the negative state of the divacancy, determining the magnitude of the Jahn-Teller distortion.

Table 4.3: Proposed electronic structure for the negative divacancy characterized by a pairing distortion. For reference [131], the crossed configuration indicates a lack of agreement with the defect-orbital assigned to the unpaired electron.

Watkins [18]	Sieverts [131]	Cluster calculations [125, 126]	This work
$a_g^{\uparrow\downarrow} b_u^{\uparrow}$	~~$a_g^{\uparrow}$~~	$b_u^{\uparrow\downarrow} a_g^{\uparrow}$	$b_u^{\uparrow\downarrow} a_u^{\uparrow}$

Further comparison with experiment is possible when the reorientation process between equivalent pairing minima is investigated (Figure 4.10). At positive charge state, the unpaired electron goes from a b_u state for the P_2 configuration to a a_u orbital at the R_3 saddle point of the transition, confirming the form of the PES hypothesized by simple symmetry considerations (Figure 4.8). The activation energy for such process is computed to be 40 meV, equivalently to the results for the E-center, underestimating the experimental value of 73 meV. The MEP for the transition between small pairing distortions is also obtained (Figure 4.10), being the electronic transition $b_u^{\uparrow\downarrow} a_u^{\uparrow} \rightarrow a_u^{\uparrow\downarrow} b_u^{\uparrow}$. The estimated reorientation barrier is equal 2 meV, far underneath the experimental value of 56 meV. Even if our first-principles calculations are capable of reproducing the EPR investigation for the positive center, it is possible that the PBE description of the negative state is erroneous, non-physically quenching the pairing distortion, wrongly describing its electronic configuration. One can then be tempted to conclude that the absence of level-crossing in the quenched pairing distortion and the large underestimation of the reorientation barrier are both product of a poor description of the negative system. We however note, that in the case of large pairing distortions [125], the reorientation barrier, reported as a Jahn-Teller energy for both pairing and resonant geometries, is double the experimental value.

Even more notorious than the description of different magnitudes of the Jahn-Teller distortion between different approaches is the estimation of different senses of the distortion among the published results (Table 4.4). As established in the introduction, during the past three decades the senses of the C_{2h} distortion at charge states 0, ± 1 have been under debate in the *ab initio* community. As a general trend, the energy difference between pairing and resonant distortions for the neutral and negative divacancy is estimated to be within 10 meV at the LDA level of approximation, questioning the ability of such mean-field approach to accurately describe the electronic

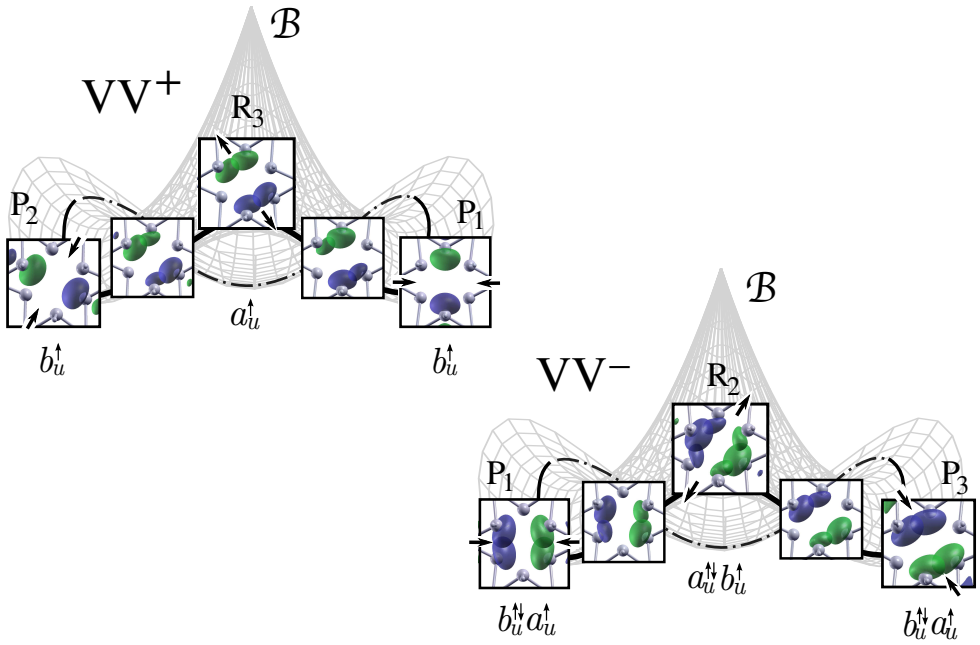

Figure 4.10: Reorientation of divacancy between equivalent pairing distortions at both single charge states, investigated within the PBE approximation. The wavefunction corresponding to the unpaired electron is plotted along the MEP and the electronic configuration is indicated. The plane of symmetry σ_h defining the direction of the symmetry breaking (directions 1, 2 and 3 or planes σ, σ' and σ'' in Figure 4.8) and the sense of the distortion (P or R) is also represented with black arrows.

occupation of the divacancy orbitals and hence the corresponding atomic distortion. Furthermore, previous studies did often neglect the investigation of the overall Jahn-Teller mechanism, overlooking the form of the PES (and postulating the mestastability of both P and R distortions [128]) and/or the geometry of the precursor charge states ± 2. In the present work, we report a full theoretical picture for the charge excitations of the divacancy (or the systems $VV^{\pm 1}$, $VV^{\pm 2}$) consistent with symmetry considerations and quantified within the PBE approximation (Figure 4.11).

We describe a breathing configuration for the empty trap or charge state +2 and the half-filled trap or state -2, characterized by equivalent interatomic distances 3.63 Å and 3.40 Å. At neutral charge state, we obtain resonant configurations as the global minima of the PES, and pairing distortions as the saddle points of the reorientation mechanism. The inversion of the Mexican hat energy surface when an electron is added to the positive divacancy

Table 4.4: Proposed ground state geometries for the silicon divacancy at charge states ranging from +2 to -2 (being $q = +2$ not thermodynamically stable [13]). The configurations $\mathcal{B}$, P, R and M stand for breathing (D_{3d}), pairing (C_{2h}), resonant (C_{2h}) and mixed pairing-resonant distortions respectively. The XC-functional characterizing the reported calculations are specified (where t.w. stands for this work). If different sizes of the cluster/cell were employed, the results for the largest system are collected.

	[18]	t. w.	[120]	[123]	[124]	[125]	[126]	[128]	[129]	[129]	[130]
	Exp.	PBE	LDA	LDA	LDA	LDA	LDA	LDA	LDA	PBE	LDA
+2	-	$\mathcal{B}$	-	-	$\mathcal{B}$	-	-	-	-	-	-
+1	P	P	P	-	M	P	P	R	P	P	R
0	-	R	-	R	M	P	P	R	R	P	R
−1	P	P	R	-	M	P	P	R	R	P	R
−2	-	$\mathcal{B}$	-	-	$\mathcal{B}$	$\mathcal{B}$	-	-	$\mathcal{B}$	$\mathcal{B}$	-

is consistent with the inversion of minima and saddle points of the E-center PES obtained for the charge transition 0 → -1. The estimated energy difference between minima and saddle points is however 2 meV, in alignment with previous mean-field calculations, poorly differentiating between electronic configurations $b_u^{\uparrow\downarrow}$ for a pairing distortion and $a_u^{\uparrow\downarrow}$ for a resonant geometry. We might then conclude that even if the PBE calculation is perfectly consistent with our toy-model, the obtained flattened Mexican hat energy surface (Figure 4.11) might be an artefact in any standard DFT calculation. This statement is sustained by our understanding of the center, allowing us to compare the underestimated difference $\mathrm{E}^{\mathrm{PBE}}\{\mathrm{g}^{\mathrm{R}}\}$ - $\mathrm{E}^{\mathrm{PBE}}\{\mathrm{g}^{\mathrm{P}}\}$ with the observed reorientation barrier at negative charge state (Figure 4.11). It therefore seems that in order to accurately quantify the toy-model for the divacancy one needs to go beyond the LDA or PBE description of the electronic interaction, fully optimizing the Jahn-Teller distortion with a higher level of theory.

To summarize, a deep understanding of the center from simple symmetry considerations and DFT-based calculations have allowed us to build a consistent model for the charged excitations of the silicon divacancy. Within such picture, the long-standing debate of pairing *versus* resonant distortions as ground state geometries is resolved in favor of a description where such configurations represent minima or saddle points of the energy surface. With the full characterization of the PES, new degrees of comparison with experiment are possible (*i.e.* EPR reorientation barriers), letting us judge the

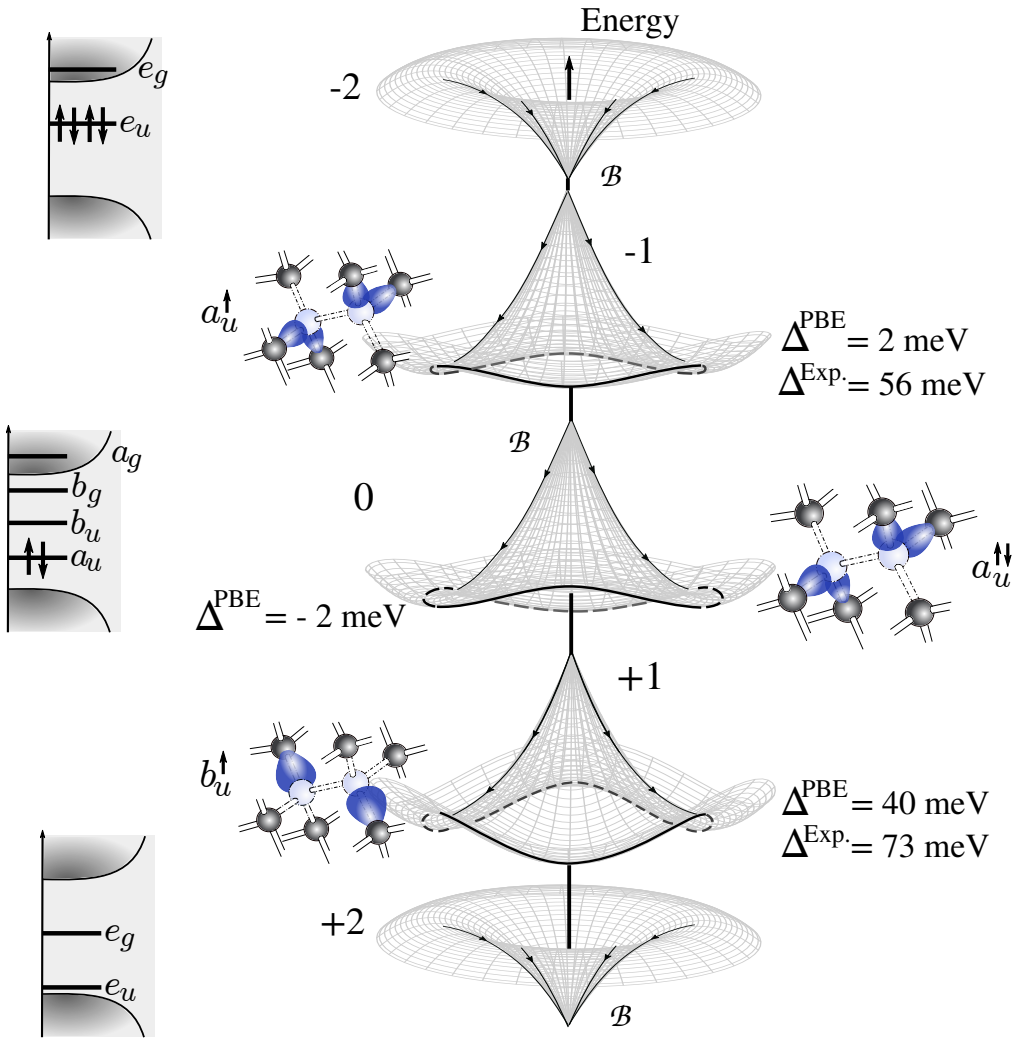

Figure 4.11: Charged excitations of the silicon divacancy computed from *ab initio* calculations in the PBE approximation and sustained by symmetry considerations. The reorientation barrier or the energy difference between both senses of the C_{2h} distortion is denoted by Δ, and estimated as a difference in total energies $E^{PBE}\{g^R\}$ - $E^{PBE}\{g^P\}$. Schematic single-particle band structures are represented for close-shell configurations or charge states 0, ± 2.

quality of standard DFT calculations. In particular, in the case of the negative divacancy, we conclude that an accurate description of the center requires of a higher level of theory with respect to the employed PBE approximation.

4.2.3 On the assignment of the optical absorption bands

The three optical absorption bands 1.8, 3.3 and 3.9 μm reported in the pioneering study of Y. Y. Fan and A. K. Ramdas in irradiated silicon [9] were unequivocally associated to the divacancy over five decades ago by employing complementary characterization techniques [12]. The assignment of such bands to specific electronic transitions within the vacancy-related states was tentatively proposed by [12] within Watkins molecular-orbital model [18]. Due to the limitations presented by such simple approach, we dedicate the present section to revisiting the previous (and only) established correspondence.

As determined during the first series of experiments [9], the observed infrared bands were not visible for any Fermi-level in the band gap, but the electronic excitations occurred for a certain charge state of the defect (Figure 4.12). This is the reason, the 3.9 μm band was assigned to the positive divacancy by [12], since it disappears for Fermi energies above the single donor level, $\mathcal{E}^{+/0}$. Equivalently, the 3.3 μm band was associated to the double negative charge state, since it only becomes visible for $\mathcal{E}_{\mathrm{F}} > \mathcal{E}^{-/2-}$. Finally, the remaining band, 1.8 μm, was observed for several charges states of the divacancy, namely $q = +1$, 0, -1. With all these considerations and having in mind the level-ordering in Watkins model for the highest four orbitals, $\epsilon_{a_g} < \epsilon_{b_u} < \epsilon_{a_u} < \epsilon_{b_g}$ (Figure 4.12c), the 3.9 μm band was assigned to an excitation from the valence band to the partially unoccupied a_g state; the 1.8 μm was described as a transition from a *valence-like* state to the unoccupied b_u state, and the 3.3 μm was simply said to be associated with the promotion of an electron from the fully occupied state b_u to *other excited states* [12]. We remark that within such model and as depicted in Figure 4.12, it is impossible to describe the position of the valence band, simply assigning the starting point of the transition the highly symmetric states a_g (S + S') and b_u (S - S').

In the present work, and similarly to the previous correspondence, we assign the 3.9 μm band to an excitation from the valence band to the first partially unoccupied state b_u at positive charge state (or transition α in Figure 4.12). Such correspondence is based on its dependence on the Fermi-level and our theoretical model positioning the b_u-state lower than the a_g-level (in disagreement with Watkins' model). Furthermore, we estimate the charged

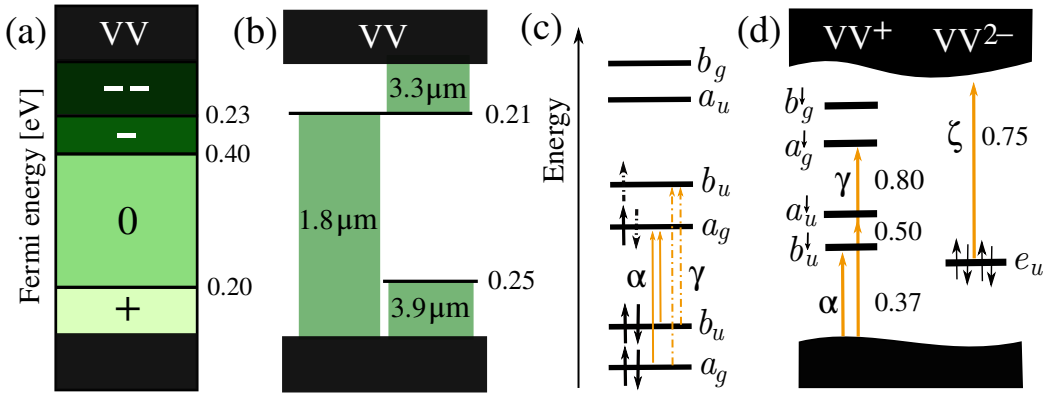

Figure 4.12: (a) Deep levels in the silicon gap corresponding to different charge states of the divacancy obtained by DLTS spectroscopy [13]. (b) The Fermi-energy dependence of the infrared bands 1.8 μm (0.69 eV), 3.3 μm (0.34 eV) and 3.9 μm (0.31 eV) found by [9] (depicted diagram is based on [12]). (c) Divacancy energy levels for the positive and negative states within Watkins model [18] and tentative assignment of the measured bands. (d) Quasiparticle energies for the divacancy at charge states +1, -2 and this work tentative assignment for the observed excitations.

transition $\mathrm{EA}^{+}_{b_u}$-$\mathrm{IP}_{\mathrm{TVB}}$ to be equal 0.37 eV, in close agreement with the measured band (Table 4.5). In the case of the 1.8 μm band, we tentatively associate the excitation to a transition from the valence band to the first or second fully unoccupied state at positive charge state (levels a_u and a_g within the proposed model). We however note that the accurate inclusion of many-body effects within the GW approximation forces us to decrease the defective cell size to a 216 atoms-cell, for which no level-crossing is found at the underlying PBE level. For is the reason, the level ordering of the divacancy states in diagram 4.12 differs from the one depicted in the DOS of Figure 4.9. One has to therefore keep in mind that the cost of including an accurate treatment of the electronic interaction is to artificially quench the Jahn-Teller distortion due to size effects that can be difficult to avoid. As a consequence of such limitation, the charged excitations $\mathrm{EA}^{+}_{a_u}$-$\mathrm{IP}_{\mathrm{TVB}}$ and/or $\mathrm{EA}^{+}_{a_g}$-$\mathrm{IP}_{\mathrm{TVB}}$ are tentatively assigned to the measured neutral excitation (Table 4.5).

Finally, and thanks to our theoretical model including the description of high charge states, we assign the 3.3 μm band to an electronic transition from the fully occupied state e_u at charge state -2 to the conduction band (ζ-transition in Figure 4.12). Such association disagrees strongly with Watkins' previous correspondence, since he was not taking into account the highly

Table 4.5: Tentative assignment of the measured optical bands with the electronic transitions depicted in Figure 4.12, estimated as quasiparticle energy differences, EA - IP, for a non-converged 216-atoms cell.

Transition	α	γ	ζ
EA - IP	0.37 eV	0.50, 0.80 eV	0.75 eV
Opt. band	0.31 eV (3.9 μm)	0.68 eV (1.8 μm)	0.37 eV (3.3 μm)

symmetric electronic configuration at charge state -2, characterized by two degenerate orbitals e_u and e_g, non the position of the conduction band (Figure 4.9). Our proposed transition is entirely based on the fact that the band is only observed at Fermi energies above the double acceptor level, since our estimation in terms of quasiparticle energies significantly overestimates the electronic excitation.

4.3 The *invisible* Jahn-Teller effect in silicon

Heavy transition metals, such as platinum and gold, are less and less frequent trapping impurities in silicon wafers, due to the increased control in the manufacturing process [4]. From a fundamental perspective, early EPR studies of substitutional Pt^- did report deviations from the well-established Ludwig-Woodbury model for transition metal impurities [133], observing a Jahn-Teller effect disrupting the substitutional tetrahedral symmetry. The missing EPR spectra for its isoelectronic center, Au^0, fed the interest to characterize such challenging systems with complementary techniques [134, 135] and/or simple symmetry-based models [136, 137]. Previous first-principles studies on gold have focused on determining the electronic activity of the defects [138, 139], giving little insight into its basic properties and the symmetry-breaking mechanism. A parallel study of both centers at different levels of theory might therefore be regarded as the natural conclusion to the present Chapter.

In contrast with early 3d transition metals with a preference for a *perfect* substitutional lattice position with Td-symmetry, EPR spectra for Pd^- and Pt^- revealed a slight shift of the impurities from the substitutional site (Figure 4.13a), giving a global C_{2v}-geometry [133]. Furthermore, the wavefunction of the unpaired electron was not located at the foreign element, but within two of the four nearest silicon neighbours (atoms 1, 2, 3, 4 in

Figure 4.13), contrary to the well-studied cases of early 3d transition metals (plots of 3d orbitals in 3.5). This interpretation of the EPR signal was supported by [135], who did also perform stress-alignment measurements, observing a defect-reorientation mechanism at temperatures as low as T $\sim$ 2 K for the Pt^- center. The evidence of rather small reorientation barriers, together with the fact that Pt^- and Au^0 are isoelectronic centers, allowed [140] to hypothesize about the missing EPR signal for neutral gold. It was established that since the two metals are neighbours in the periodic table, they present similar electronic structures when embedded in silicon and hence, Au^0 would also present a C_{2v} symmetry. In the case of gold, the Jahn-Teller distortion would however not be *static*, as in the case of platinum, but the system would (and we quote [140]) *tunnel* between two trigonal distortions, resulting on a tetrahedral distortion with $g_\perp$ close to zero. A similar magnitude for the g-tensor-main-value was found in [134], where Zeeman studies were reported for both excitation spectra at 793 and 611 meV. From their detailed investigation of the electronic structure, they concluded that substitutional neutral gold in silicon is a paramagnetic center, with S = $\frac{1}{2}$, capable of *freely reorienting* between *static distortions* at T = 1.9 K. One could therefore question whether neutral gold is effectively describing a dynamical Jahn-Teller effect (*i.e* non-observable static distortions) and consequently, the origin of $g_\perp \cong 0$.

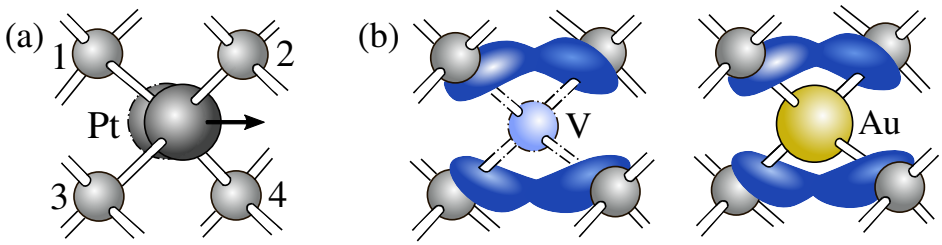

Figure 4.13: (a) Geometry of the Pt^- center proposed by [133]. (b) Schematic representation of the *vacancy model* for the mono-vacancy (V) and substitutional gold (Au). Electronic densities corresponding to a trap-induced state are depicted in blue.

From a theoretical perspective, a simple molecular-orbital model was first developed to support the experimental evidence of a C_{2v}-distortion for the Pd^- and Pt^- centers [136, 137]. The theoretical investigation was based on the well-established vacancy model [141], which did also describe a C_{2v} geometry for the silicon mono-vacancy at negative charge state. The analogy between the two systems was established by arguing that the closed shells

$4d^{10}$ (for Pd) and $4f^{14}$, $5d^{10}$ (for Pt) are located deep into the silicon valence band, and hence, the defect-states of the TMs arise from the four broken bonds in silicon atoms 1, 2, 3 and 4 (Figure 4.13b). The vacancy model was also applied to neutral gold, with electronic configuration, [Xe] $4f^{14}$ $5d^{10}$ $6s^1$, simply stating that the center presented one extra charge with respect Pt. For both systems, the C_{2v}-geometry at negative charge state (neutral state for Au) was explained through two consecutive symmetry breaking mechanisms, $T_d \rightarrow D_{2d} \rightarrow C_{2v}$, lifting completely the degeneracy of the t_2-states, postulated to be located within the semiconductor gap. To conclude, it was remarked that even if the symmetry-point group at different charge states was equivalent for the vacancy and the TM, the sense of the distortion was opposite with respect to each other, presenting electronic structures with different level-ordering (similarly to the discussion for the divacancy, summarized in Figure 4.9).

Among the *ab initio* community, little attention has been given to the Pd, Pt and Au centers in silicon. In the case of substitutional gold, the main focus of the published work [138, 139] was to determine the CTLs as an energy difference of DFT-total energies, so a full picture of the center was not given. In [138], it was stated that the Au-center was slightly distorted from the T_d position into a C_{2v}-geometry, without further investigating the ground-state basic features of the defect. In [139], the geometry of the center was obtained at charge states ranging from +1 to -3, reporting a $\sim D_{2d}$ symmetry for all electronic occupations, except for the neutral state, for which a D_2 geometry was described. From the computed CTLs, they argued that gold presents Anderson-negative-U properties, being unstable at paramagnetic states, justifying the missing EPR signal for Au_S^0. This result is however not consistent with DLTS levels E_V + 0.35 eV and E_C - 0.56 eV, widely assigned to the charge transitions 0/+ and 0/-, and neither with the optical measurements reported in [134]. Even if Pt- and Au-contamination is typically under control in silicon-based devices, the degrading power of such impurities is unquestionable, since even at small concentrations of 10^{12} cm^{-3}, they are responsible for faulty devices due to the enhanced dark current [4], motivating our work to clarify the contradictory interpretations for the missing EPR signal for gold.

In the present work, we propose a theoretical framework equivalent to the one previously introduced for the divacancy to investigate the reorientation of the Pt^- center at very low temperatures between static C_{2v}-distortions and the possibility of neutral gold exhibiting dynamical Jahn-Teller distortions. Due to the hypothesized similarity of the Jahn-Teller distortions for

the mono-vacancy and the metallic impurities, our investigation of the centers is performed and consequently presented as follows: In section 4.3.1, we expose the symmetry-breaking mechanism constituted by two consecutive Jahn-Teller distortions $T_d \rightarrow D_{2d} \rightarrow C_{2v}$, proposed in Watkins' vacancy model. To ground the basic features of the center, we extensively analyse the symmetry of the vacancy-related orbitals at different atomic distortions, establishing a solid correspondence with our *ab initio* characterization. The understanding of such simple defect is later exploited to model the D_{2d}-distortions for the Pd, Pt and Au centers (section 4.3.2), comparing the magnitude of the distortions, the symmetry of the KS wavefunctions and ultimately, the reorientation barriers. Our detailed analysis of the intermediate geometry in the overall symmetry-breaking mechanism, contrary to previous theoretical considerations, allows us to demonstrate the equivalence of the energy surface $T_d \rightarrow D_{2d}$ with the ones previously presented for the trimer and bi-trimer. We finally investigate the Jahn-Teller distortions for all the studied centers at electronic occupation equal three (section 4.3.3), which was associated to the C_{2v} type of distortions in Watkins model. In the case of neutral gold, we propose an alternative explanation for the non-measurable EPR-signal, linked to the description of a *new* symmetry of the ground state in the form of D_2-distortions. Furthermore, we investigate the complex shape of the energy surface for the Pt^- center, characterized by six equivalent minima and two reorientation processes, whose accurate description is beyond a CI-NEB algorithm. In such context, we propose the symmetry character of both reorientation mechanisms, assigning the D_2-distortion to the saddle point between two equivalent C_{2v}-distortions, successfully reproducing the measured reorientation at cryogenic temperatures.

4.3.1 The vacancy model

The first theoretical model for the silicon vacancy was proposed by Watkins [141], predicting once again the form and relative energy position of the defect-induced states within a simple molecular orbital approach. In contrast with the silicon E-center, the localized electronic states are described as a linear combination of four dangling bonds, arising from the vacancy first neighbours. The system therefore presents a four-fold symmetry instead of the three-fold transformations extensively discussed for the trimer and bi-trimer. According to Watkins, at charge state +2 or empty trap the PES presents a single minimum corresponding to a T_d geometry, for which three out of the four defect-states are degenerate in energy (Figure 4.14). The main contribution of the model is to describe the instability originated by the partial occupation of the t_2 states, leading to two consecutive Jahn-Teller

distortions, required to lift completely the degeneracy of the triplet. The symmetry breaking mechanisms postulated by Watkins were sustained by EPR spectroscopy for the paramagnetic states $q = \pm 1$ and they were later confirmed by first-principles calculations [61, 62, 63, 64]. At both charge states +1 and 0, the system adopts a D_{2d} geometry, characterized by a paired inward relaxation, for which the six interatomic distances follow, $d_{24} = d_{13} = d_{\mathrm{JT}} < d_{12} = d_{14} = d_{23} = d_{34}$ (Figure 4.14). At charge states +1, 0, the t_2-states are therefore unfolded in a b_2-state and the e-doublet. If yet another electron is added to the center, a second Jahn-Teller distortion in the form of a C_{2v} configuration was predicted to lift the degeneracy of states e. The new geometry, observed at charge state -1, is characterized by interatomic distances, $d_{24} = d_{\mathrm{JT}} < d_{13} = d_{\mathrm{JT}_2} < d_{12} = d_{14} = d_{23} = d_{34}$ (Figure 4.14).

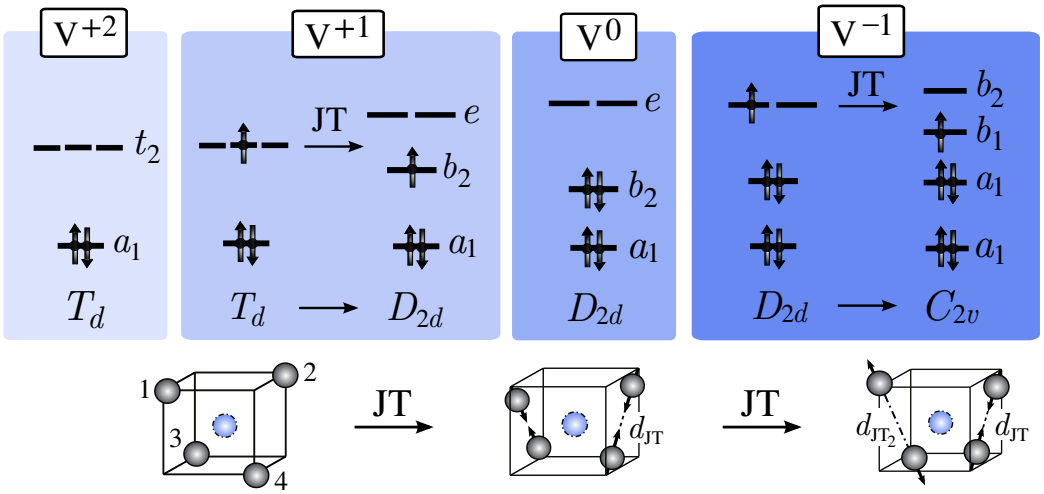

Figure 4.14: Watkins vacancy model [141] characterized by two Jahn-Teller distortions, lowering the symmetry of the tetrahedral system from a T_d geometry to a D_{2d} configuration and consecutively to a C_{2v} conformation.

From simple symmetry considerations, or within our toy-model, the degeneracy of the defect states at different atomic configurations T_d, D_{2d} and C_{2v}, is reproduced. In the case of the D_{2d} geometry, for instance, the lowest defect-state simply corresponds to $\sim a_1 + a_2 + a_3 + a_4$ (Figure 4.15). Such highly symmetric state is labeled as a_1 according to the point-group transformations collected in Table 4.6. The second non-degenerate state, or state b_2, has the form $\sim -a_1 + a_2 - a_3 + a_4$, for a symmetry-breaking mechanism constrained by interatomic distances, $d_{13} = d_{24} = d_{\mathrm{JT}}$. Due to the three-fold degeneracy of the C_2-symmetry transformation characterizing the precursor

T_d configuration, one can already postulate the existence of three equivalent D_{2d} geometries, with paired distances, $d_{13} = d_{24} = d_{\mathrm{JT}}$ or $d_{12} = d_{34} = d_{\mathrm{JT}}$ or $d_{14} = d_{23} = d_{\mathrm{JT}}$ at this level of theory. Further analysis of the reorientation process between equivalent minima is given in the following, since we now simply focus on introducing the Jahn-Teller distortions and their relevant symmetry elements. The b_2 state is even with respect to both dihedral planes, σ_d, (one of them represented in Figure 4.15) and the parallel rotation axis, C_2; whereas it is odd under a S_4 transformation and the two rotation axis, C_2', perpendicular to the main axis, C_2 (also represented in Figure 4.15).

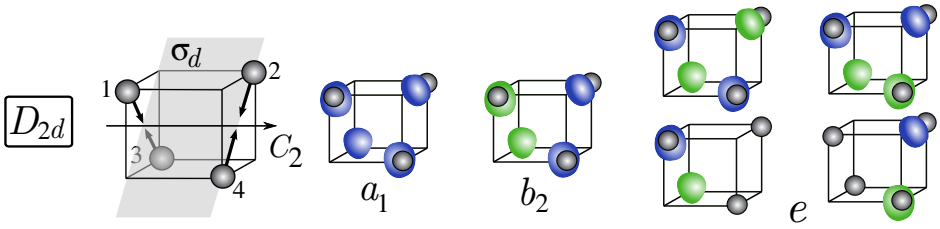

Figure 4.15: Trap-induced states for the vacancy at D_{2d} configuration within a simple MO approach labeled according to point-group transformations.

The obtained degenerate states are labelled according to the *irreducible representation of size two*, e; since these states do not transform to themselves under certain symmetry transformations. State $a_1 - a_3$, for instance, goes to states $\pm(a_2 - a_4)$ if the rotation constrained by the C_2'-axis is applied to the system. The values listed in Table 4.6 for such representation are thus defined as the trace of the matrix of order two, containing 0, 1, -1 transformations under a given symmetry operation. In the ongoing example of the two rotations C_2', the diagonal terms are equal zero (since state $a_1 - a_3$ does not go to itself under the operation) and both off-diagonal terms are equal to ± 1 depending on the direction of the rotation axis. The trace of the matrix is then equal to zero, as listed in Table 4.6. In the case of symmetry operations like the identity, for which diagonal terms are non-zero (state $a_1 - a_3$ is even under such transformation), the trace of the corresponding matrix is equal 2. We finally notice the equivalence of states $a_1 - a_2 - a_3 + a_4$ and $a_1 + a_2 - a_3 - a_4$ (proposed by the original Watkins model) and our states $a_1 - a_3$ and $a_2 - a_4$ at this level of approximation.

If the symmetry of the system is lowered through the mechanism $D_{2d} \rightarrow C_{2v}$, the trap-induced states remain invariant at this level of theory (Figure 4.16), being relabelled according to the symmetry representations listed in Table 4.6. At this new atomic configuration, characterized by $d_{24} = d_{\mathrm{JT}} <$

Table 4.6: Character tables for the D_{2d}, C_{2v} and D_2 point-symmetry groups.

D_{2d}	E	$2S_4$	C_2	$2C_2'$	$2\sigma_d$
a_1	1	1	1	1	1
a_2	1	1	1	-1	-1
b_1	1	-1	1	1	-1
b_2	1	-1	1	-1	1
e	2	0	-2	0	0

C_{2v}	E	C_2	σ_v	σ_v'
a_1	1	1	1	1
a_2	1	1	-1	-1
b_1	1	-1	1	-1
b_2	1	-1	-1	1

D_2	E	C_2'	C_2''	C_2'''
a	1	1	1	1
b_1	1	1	-1	-1
b_2	1	-1	1	-1
b_3	1	-1	-1	1

$d_{13} = d_{\mathrm{JT}_2}$, states $a_1 - a_2 - a_3 + a_4$ and $a_1 + a_2 - a_3 - a_4$ are no longer eigenstates of the Hamiltonian, since they are not compatible with a transformation under σ_v, defined as the vertical plane, parallel with the principal axis. States $a_1 - a_3$ and $a_2 - a_4$ are differentiated as states b_1 and b_2, depending on their behaviour with respect both perpendicular planes σ_v and σ_v'. Furthermore, state b_1 is lower in energy with respect to b_2, because σ_v' contains the interatomic direction defining d_{JT_2}. We remark that states denoted as a_1 and b_2 for the D_{2d} geometry, are both now labeled as a_1, since they are indistinguishable under the C_{2v} operations, similarly to states A+A' and S+S' (A-A' and S-S') in the case of the divacancy. Before concluding, we notice that within these simple considerations, six minima of the PES can be expected, since for each distortion with respect the three equivalent C_2 axis, each C_{2v} geometry co-exists for $d_{24} = d_{\mathrm{JT}} < d_{13} = d_{\mathrm{JT}_2} \rightleftharpoons d_{24} = d_{\mathrm{JT}_2} < d_{13} = d_{\mathrm{JT}}$.

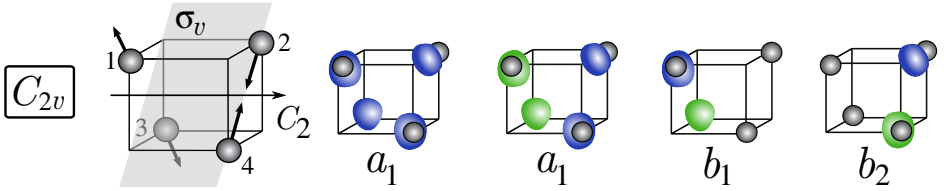

Figure 4.16: Trap-induced states for the vacancy at C_{2v} geometry within a simple MO approach labelled according to point-group transformations.

The Jahn-Teller effect for the silicon vacancy has historically served as

the test-case-study to analyse the convergence of *ab initio* calculations regarding size of the cell/cluster, number of k-points, form of the defective cell, etc. [61**?** , 63, 64]. Among the published works, the most recent one [64] investigated the ground state geometry at charge states ranging from +2 to -2, in alignment with Watkins model. At the LDA level of approximation, they did also confirm the electronic negative-U properties properties of the center, postulated in the seminal work of Baraff, Kane and Schlüter [142] and sustained by experimental evidence [143]. In a few words, an Anderson negative-U system is characterized by the formation of a localized electronic pair, capable of inducing a large lattice relaxation, overcoming the Coulomb repulsion between the electrons. The paramagnetic states of the Anderson-center are therefore said to be *thermodynamically unstable*, since the Jahn-Teller distortion causes the level inversion between the double and single donor/acceptor levels ($\mathcal{E}^{++/+} > \mathcal{E}^{+/0}$ and $\mathcal{E}^{-/--} < \mathcal{E}^{-/0}$).

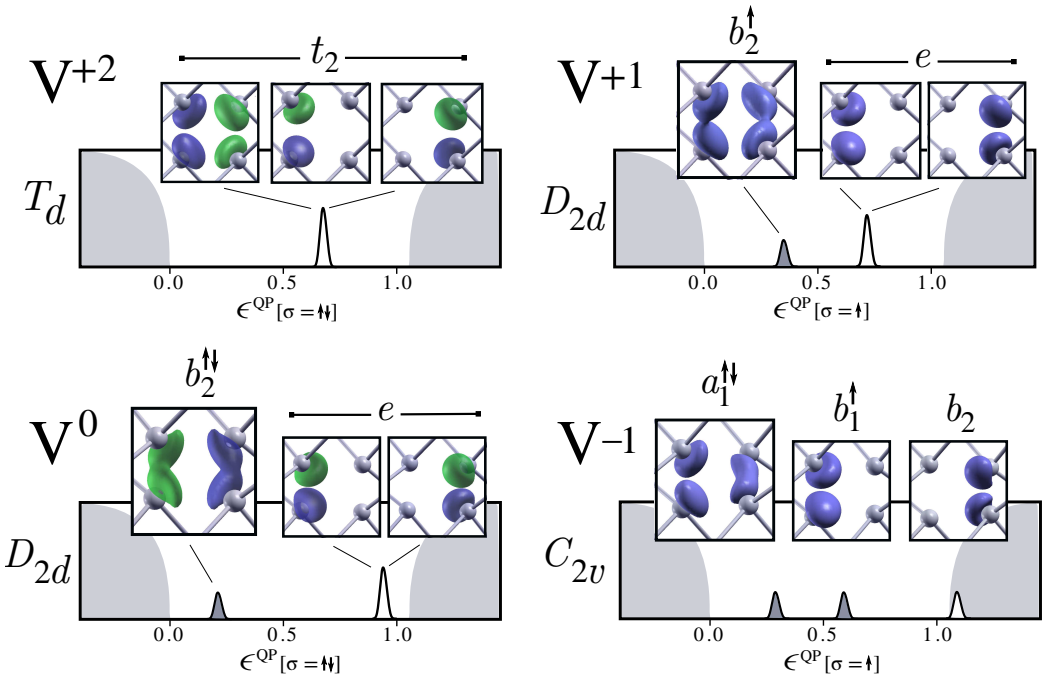

Figure 4.17: Spin-unrestricted quasiparticle density of states for the vacancy at charge states +2 and 0 and spin-restricted states for the singly charged states, ±1. The Kohn-Sham wavefunction of the defect-induced states is shown for the paired systems, whereas the electronic density is represented for the $V^{\pm 1}$. The point group symmetry is specified at each atomic distortion and the localized states are named accordingly. Computed quasiparticle energies within the GW approximation are given in eV.

In the present work, besides revisiting Watkins model through an extensive point-group-symmetry analysis, we have also performed state-of-the-art first-principles calculations, establishing a one-to-one correspondence between the two theories (Figure 4.17). As depicted, at the PBE level of theory, the degeneracy and real-space projection of the KS eigenstates are in perfect alignment with previous symmetry considerations. The inclusion of many-body effects, in contrast with the work presented in [64], allows us to *directly* postulate that the vacancy is a negative-U center, since $\mathrm{IP}^{0}_{b_2} < \mathrm{IP}^{+}_{b_2}$ (Figure 4.17). Such energy difference reveals the stability of the electronic pair, $b_2^{\uparrow\downarrow}$, through lattice relaxation or the thermodynamic stability of the neutral charge state over the single charge state. Further information regarding the magnitude of the Jahn-Teller distortions is provided in the following, since the motivation for the present section was simply to ground the vacancy model at different levels of theory to guide the investigation of more complex systems (Pt, Au).

4.3.2 Transition Metals exhibiting Jahn-Teller tetrahedral distortions

From our first-principles study of the Pd, Pt and Au centers in silicon at charge states +2, +1 and 0 (+3, +2 and +1 for Au), we confirm that these TMs are characterized by tetrahedral Jahn-Teller distortions, triggered by the partial occupation of the defect-states located in the nearest silicon atoms. For an empty trap, t_2^0, the precursor state presents a T_d symmetry, with equivalent interatomic distances, d_{ij}, between the silicon atoms. For an electronic occupation equal one ($\mathrm{t}_2^{\uparrow}$, corresponding to charge states Pt^{+}, Pd^{+}, Au^{+2}) or two ($\mathrm{t}_2^{\uparrow\downarrow}$ or Pt^{0}, Pd^{0}, Au^{+}), we report a D_{2d}-geometry, whose characteristic interatomic distances are collected in Table 4.8. The distance d_{JT}, represented in Figure 4.14, corresponds to interatomic distances between *paired* atoms, being different from the other four characteristic d_{ij}. Relevant interatomic distances are also included for the mono-vacancy, V, as a reference for the sense and magnitude of the D_{2d}-distortion. From the distances collected in Table 4.8, we conclude that the Jahn-Teller distortion for the TMs occurs in the same sense as for the mono-vacancy, since $d_{\mathrm{JT}} < d_{ij}$. The magnitude of the distortion is almost equivalent for all four systems for an electronic occupation equal one, since the two d_{JT} are consistently ~ 0.1 Å smaller than the remaining four d_{ij}. In the case of the electronic pair, $\mathrm{t}_2^{\uparrow\downarrow}$, the lattice-relaxation is much more prominent for the vacancy nearest neighbours, $\sim$ 0.5 Å, than for the metallic impurities, $\sim$ 0.2 - 0.3 Å. Independently of the magnitude of the D_{2d}-distortions described by silicon atoms 1, 2, 3 and 4,

the TMs remain unperturbed at the perfect substitutional site.

Table 4.8: Relevant interatomic distances d_{ij} between the nearest silicon atoms for the Pd, Pt, Au and vacancy (V) centers, computed within the PBE approximation. Electronic occupations of the precursor t_2 states (prior to JT distortions) are indicated in parenthesis. All values are given in Å.

Center	T_d (t_2^0)	D_{2d} ($t_2^{\uparrow}$)		D_{2d} ($t_2^{\uparrow\downarrow}$)	
	d_{ij}	d_{JT}	d_{ij}	d_{JT}	d_{ij}
Pd	3.90	3.78	3.93	3.65	3.95
Pt	3.88	3.76	3.90	3.63	3.93
Au	3.99	3.89	4.02	3.79	4.05
V	3.76	3.49	3.66	3.07	3.54

The electronic configuration for the here-studied impurities is therefore $b_2^{\uparrow}$ and $b_2^{\uparrow\downarrow}$, as predicted for the mono-vacancy at charge states +1 and 0 (Figure 4.17). In Figure 4.18 we quantify the simple symmetry-based model at the PBE level of theory (wavefunctions and electronic densities of the defect-related states) and within MBPT, by representing the quasiparticle energy density of states for Au^{+2} and Pt^{+}. The KS-states are in excellent agreement with the ones depicted for the vacancy, confirming that substitutional Pt and Au in silicon can be simply modelled as single missing atoms. We can therefore conclude that the first symmetry-breaking mechanism in metallic impurities, $T_d \rightarrow D_{2d}$, is identical to the one described and observed for the vacancy. Our results slightly contradict Watkins model [136, 137], for which the spontaneous Jahn-Teller distortions were *directly* described for an electronic occupation equal three, establishing that the intermediate tetragonal distortion (D_{2d}) had an opposite sense with respect the one described here. According to their theoretical considerations, the e doublet would therefore be lower in energy and occupied by the three electrons, before lowering the symmetry to a C_{2v} configuration. We can therefore conclude with the original part of our investigation, carefully investigating the *intermediate-step-geometry* in the overall symmetry-breaking mechanism $T_d \rightarrow D_{2d} \rightarrow C_{2v}$.

We conclude the present section by analysing the reorientation mechanism between the three equivalent D_{2d}-distortions for all the considered systems. Contrary to the *trigonal* centers (E-center, divacancy), the three equivalent minima of the PES are not defined by three equivalent σ_{h}-planes, but with respect to three perpendicular C_2 axis, here identified with the coordination

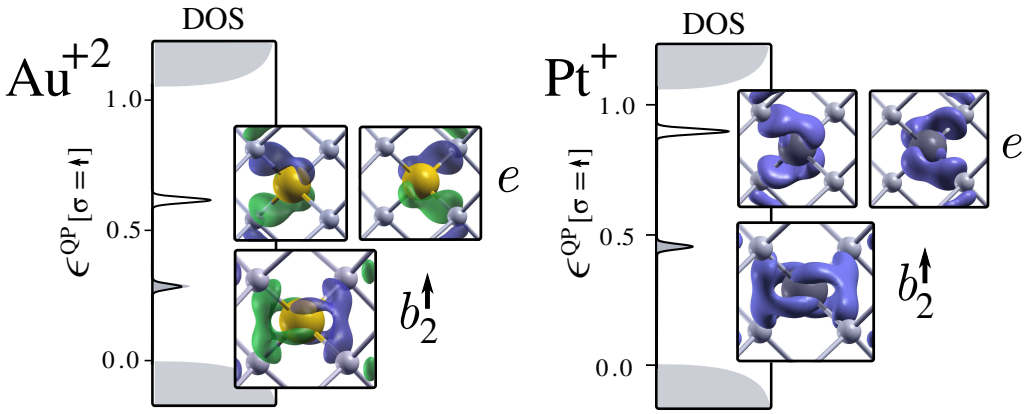

Figure 4.18: Spin-restricted quasiparticle energy density of states for Au^{+2} and Pt^{+}, both presenting D_{2d}-distortions and hence, and electronic occupation, $b_2^{\uparrow}$. The KS wavefunction and the electronic density for the partially occupied b_2 and empty e states are respectively shown for Au^{+2} and Pt^{+}. Estimated values within the GW approximation are given in eV.

axis: $D_{2d}^{x<}$, $D_{2d}^{y<}$ and $D_{2d}^{z<}$ (Figure 4.19). The superscript $<$ denotes the sense of the D_{2d}-distortion, since the ground state geometries for the studied centers follow $d_{\mathrm{JT}} < d_{ij}$. Moreover, by simple symmetry considerations or within our toy-model, we postulate that the saddle points characterizing the reorientation process correspond to opposite senses of the D_{2d}-distortion, $D_{2d}^{>}$, defined by $d_{\mathrm{JT}} > d_{ij}$. Even more precisely, and equivalently for the trimer (and bi-trimer), the saddle point of the transition $D_{2d}^{\mathrm{i}<} \leftrightarrow D_{2d}^{\mathrm{j}<}$, defined to any two i, j axis, corresponds to the distortion $D_{2d}^{\mathrm{k}>}$, defined with respect to the third symmetry-axis, k (Figure 4.19). A C_2-restricted path (or transition $D_{2d}^{\mathrm{i}<} \leftrightarrow D_{2d}^{\mathrm{i}>}$), in analogy with the σ-restricted path for the trimer, would force the system to pass through the highly symmetric T_d configuration, characterized by the degeneracy of the t_2 states. The shape of the PES for $V^{+1,0}$, $Pd^{+1,0}$, $Pt^{+1,0}$ and $Au^{+2,+1}$ is therefore here postulated to be identical to the one extensively investigated for the E-center and divacancy in silicon upon exchange of the symmetry elements $C_2 \leftrightarrow \sigma_{\mathrm{h}}$, defining the Jahn-Teller mechanism.

The *ab initio* exploration of the PES confirms the simple symmetry model, obtaining $D_{2d}^{>}$-distortions as saddle points of the MEP, whose activation energies are collected in Table 4.9. We remark the similarity of the barriers for Pd and Pt at charge states +1 and 0, and a general proximity in the order of magnitude for all the studied centers. In the case of the vacancy, the fact that the energy expense of the reorientation is increased at least by a factor of ten

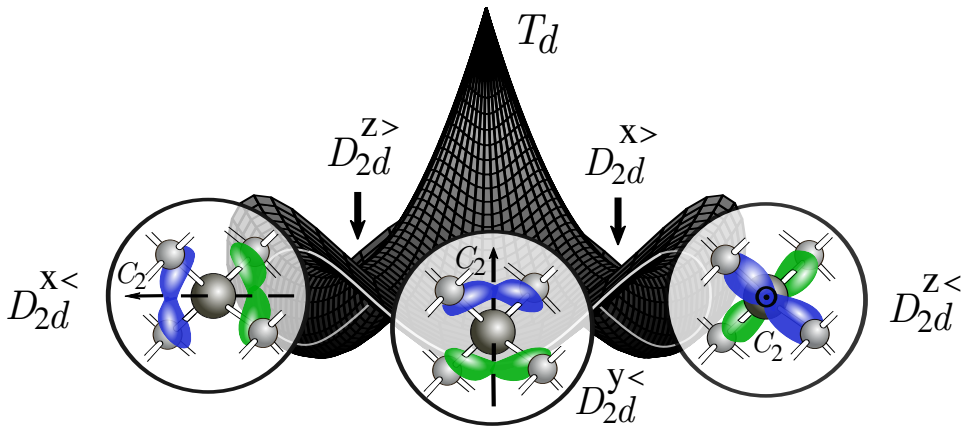

Figure 4.19: Proposed symmetry model for the $T_d \rightarrow D_{2d}$ mechanism, particularized for the Pt center at charge states +1, 0. The electronic wavefunction corresponding to the partially occupied ($b_2^{\uparrow}$) or fully occupied ($b_2^{\uparrow\downarrow}$) states for the three minima are also depicted.

when an electron is added to the system was already observed experimentally through EPR spectroscopy [141] and confirmed by *ab initio* calculations [144]. Since similar tendencies are obtained for the metallic impurities, we originally report that the D_{2d} lattice relaxation is energetically stabilized by the constitution of an electronic pair, $b_2^{\uparrow\downarrow}$, similarly to for the silicon vacancy. We do however report ionization potentials corresponding to states $b_2^{\uparrow}$ and $b_2^{\uparrow\downarrow}$ to be within 0.05 eV with respect to each other for $Au^{+2,+}$ and $Pt^{+/0}$ respectively. Contrary to the silicon vacancy, the D_{2d}-distortions are therefore not sufficiently large to overcome the Coulomb repulsion between the paired electrons and the paramagnetic states are thermodynamically stable (*i.e.* Pt and Au centers do not present negative-U properties in silicon).

Table 4.9: Activation energies between equivalent D_{2d}-distortions for Pd, Pt, Au and the mono-vacancy at electronic occupations ${b_2}^{\uparrow}$ and $b_2^{\uparrow\downarrow}$. All values are given in eV.

Trap occupation	Pd	Pt	Au	V		
${b_2}^{\uparrow}$	0.04	0.04	0.02	0.02	0.013[1]	0.05[2]
$b_2^{\uparrow\downarrow}$	0.16	0.15	0.10	0.20	0.23[1]	0.32[2], 0.20[2]

[1]Measured reorientation barriers [141] [2]Other works [144, 145]

To summarize, we have proven that Jahn-Teller distortions in the sur-

rounding of heavy transition metals, such as platinum and gold, can be simply modelled in the same way as the case of a single missing atom. Besides comparing the magnitude of the Jahn-Teller distortions and the reorientation barriers among the studied defects, we have proposed a general shape for the $T_d \rightarrow D_{2d}$ energy surface, equivalent to previous models for the $C_{3v} \rightarrow C_{1h}$ for the E-center and $D_{3d} \rightarrow C_{2h}$ for the divacancy. We finally notice that the reorientation process between equivalent D_{2d}-distortions was exclusively discussed for the vacancy by precedent theoretical studies, without investigating any further the symmetry of the transition path.

4.3.3 Multiple symmetry-breaking mechanisms

For a trap-occupation equal three, our *ab initio* approach reproduces the C_{2v}-distortion for the Pd^- and Pt^- centers as the ground state geometries, postulated from EPR measurements [133, 135]. In agreement with experimental observations and Watkins' simple model [136, 137], the sense of the distortion is opposite to the one described by the mono-vacancy, since the four interatomic distances d_{ij} are smaller than the *paired* distances $d_{\rm JT}$, $d_{\rm JT_2}$ (Figure 4.20). Two senses of the C_{2v} distortion are therefore to be distinguished (similarly to the Pairing and Resonant distortions for the E-center, divacancy; or the $D^{>}_{2d}$, $D^{<}_{2d}$ distortions at charge states $Pt^{+,0}$), so in the following we denote by $C^{\rm V}_{2v}$ the Jahn-Teller described by the vacancy, with $d_{ij} > d_{\rm JT}, d_{\rm JT_2}$ (Figure 4.20). Since the sense of the distortion conditions the level-ordering of the defect-induced states, we notice that in the case of the Pt^- center, the b_1, b_2 states are lower in energy than the symmetric a_1 state, locating the unpaired electron in a b_2-state, $b_1^{\uparrow\downarrow} b_2^{\uparrow}$, contrary to the vacancy electronic configuration, $a_1^{\uparrow\downarrow} b_1^{\uparrow}$ (Figure 4.20).

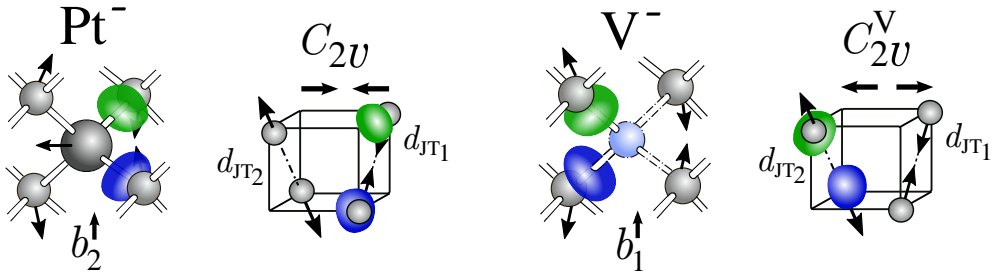

Figure 4.20: C_{2v}-distortions for Platinum in silicon and the mono-vacancy at negative charge state (or electronic occupation equal three). The wavefunction of the unpaired electron is also represented.

In Table 4.10 we present the interatomic distances between the metal or

vacancy first silicon neighbors at the PBE level of approximation for both the C_{2v} and C_{2v}^{V} distortions. Even if the defect electronic density is located at nearest Si atoms, triggering the Jahn-Teller relaxations, we estimate a small shift of the metallic impurities from their substituional sites as depicted in Figure 4.20, in alignment with EPR spectroscopy [133]. Such effect was vaguely described from first-principles calculations in the case of gold at neutral charge state, postulating a small deviation of 0.03 Å [138]. Within the present approach, we however report a larger *net movement* equal 0.17, 0.13, 0.09 Å for Pd^{-}, Pt^{-}, Au^{0} respectively along the C_2 axis and in the direction of the d_{JT_2} distance.

Table 4.10: Relevant interatomic distances d_{ij} between the nearest silicon atoms for the C_{2v}-geometry, estimated within the PBE approximation. All values are given in Å.

C_{2v}	Pd^{-}	Pt^{-}	Au^{0}	V^{-}
d_{JT}	3.79	3.79	3.99	2.83
d_{JT_2}	4.15	4.11	4.16	3.39
d_{ij}	3.75	3.73	3.88	3.46

The equivalence or universality among the potential energy surfaces for the $C_{3v} \rightarrow C_{1h}$ (E-center), $D_{3d} \rightarrow C_{2h}$ (divacancy) and $T_d \rightarrow D_{2d}$ (previous section) mechanisms is clearly broken in the case of the $T_d \rightarrow C_{2v}$ mechanism, due to the existence of six equivalent minima and two different reorientation processes. As depicted in Figure 4.21, for each of the three possible orientations of the C_2-symmetry-axis (here identified with the coordinate axis), two different configurations or orientations +/- can co-exist upon the inversion $d_{\mathrm{JT}_1} \rightleftharpoons d_{\mathrm{JT}_2}$. The center might hence not only reorient with respect to the C_2-symmetry-axis, but also with respect the +/- sense of such direction. Even if such small reconfigurations were assigned to the reorientation of the Pt^{-} center at very low temperatures [133], no further investigation of the transition path has been performed within simple molecular-orbital approaches, nor within an *ab initio* approach. In the case of neutral gold, characterized by the non-measurable EPR signal and for which the C_{2v}-distortion was merely postulated to be the ground state geometry [140, 134], a reorientation barrier equal 0.11 eV between equivalent C_{2v} configurations was reported in [138]. Such large reorientation barrier is however not consistent with the absence of EPR spectrum for gold in silicon, since that would imply that static C_{2v} Jahn-Teller distortions would be observed at temperatures comparable to RT

(when Pt^- was observed to freely reorient at T $\sim$ 2 K).

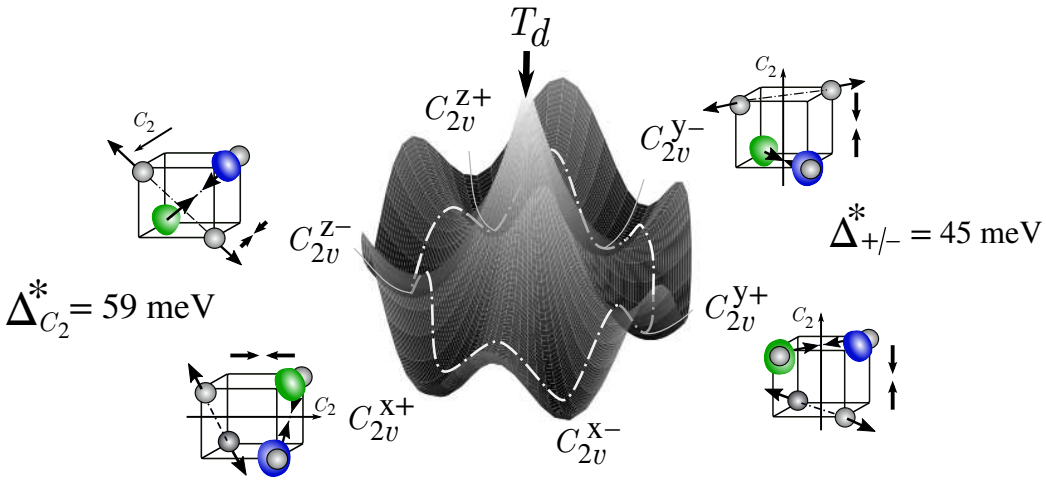

Figure 4.21: Schematic six-minima energy surface corresponding to the $T_d \rightarrow C_{2v}$ mechanism. Activation energies, Δ^*, estimated with the CI-NEB algorithm at the PBE approximation, for the two reorientation processes ($C_{2v}^{x+} \leftrightarrow C_{2v}^{z-}$ and $C_{2v}^{y+} \leftrightarrow C_{2v}^{y-}$) are indicated.

In the present work, as a first step into characterizing the energy surface of the Pt^- center, we *blindly* estimate the MEP between equivalent minima within a CI-NEB calculation, obtaining activation energies, $\Delta^*_{C_2}$ = 60 meV and $\Delta^*_{+/-}$ = 40 meV (Figure 4.21). The height of the +/- barrier is however clearly overestimated with respect to EPR measurements, from which it was deduced that the center could freely reorient at temperatures as low as $\sim$ 2 K between "two equivalent trigonal distortions". A closer look into the symmetry-character of the computed transitions reveals that the estimated saddle point presents a $\sim D_{2d}$-geometry. This result however contradicts the general observed trend of the SP being of the same *symmetry order* as the minima (as it has been extensively studied for the $C_{3v} \rightarrow C_{1h}$, $D_{3d} \rightarrow C_{2h}$ and $T_d \rightarrow D_{2d}$ cases). One could therefore question the validity of the numerical optimization and whether it is correctly describing the symmetry-character of the reorientation process, postulating the need to further investigate the shape of the PES for the Pt^- center.

In the case of neutral gold, Au^0, our first-principles calculations reveal that the C_{2v} distortion does not correspond to the global minimum of the PBE-potential energy surface, but we find a D_2 geometry instead, characterized by six *paired* distances, d_{JT_1} = 3.81 Å, d_{JT_2} = 3.95 Å and d_{JT_3} = 4.08 Å.

The obtained geometry might be regarded as a D_{2d} distortion, followed by a rotation of the paired atoms in opposite senses as depicted in Figure 4.22a. Such symmetry-breaking mechanism has been previously reported by [139] within a LSDA approximation. They did however not perform a proper analysis of the geometry, simply stating that "the distortion is enough to lift the degeneracy of the three defect states". As shown in the character tables collected in Table 4.6, the D_2 symmetry has the same number of irreducible representations or symmetry elements then the C_{2v} point group, so it has the correct construction to lower the symmetry of the D_{2d} geometry. Within our simple toy-model, we have modeled the $D_{2d} \rightarrow D_2$ mechanism, for which the resulting eigenstates have been named according to symmetry considerations (Figure 4.22). As depicted, the degeneracy of the e states is lifted, resulting in three defect-states b_1, b_2 and b_3, defined with respect to the three symmetry-axis C_2', C_2'' and C_2'''. If the geometry of the center is so that $d_{\mathrm{JT}_1} = d_{13} = d_{24} < d_{\mathrm{JT}_2} = d_{12} = d_{34} < d_{\mathrm{JT}_3} = d_{14} = d_{23}$, then $C_2' \equiv \hat{x}$, $C_2'' \equiv \hat{y}$ and $C_2''' \equiv \hat{z}$ and $b_1 \sim a_1 + a_3 - a_2 - a_4$, $b_2 \sim a_1 + a_2 - a_3 - a_4$ and $b_3 \sim a_1 + a_4 - a_2 - a_3$, as depicted in Figure 4.22a within the toy-model and Figure 4.22c within the PBE approximation. Equivalently to the C_{2v}-distortions, six equivalent D_2 geometries can co-exist, depending on the relative orientation of the symmetry elements. In Figure 4.22c, for instance, we have represented two equivalent distortions with $C_2''' \equiv \hat{z}$, and opposite orientations of the C_2' and C_2'' axis: $\hat{x} \leftrightarrow \hat{y}$. The lack of energy barrier between both D_2 and C_{2v} distortions for the Au^0 center, together with the small energy difference of 9 meV between both geometries, indicates that this second type of distortions might play a relevant role in the reorientation mechanism of the Pt^- center.

By twisting the already characterized C_{2v} geometry for the Pd^- and Pt^- centers as the starting point of the structural optimization, the minimization algorithm also finds as *critical points* of the PES the D_2 and the C_{2v}^{V} symmetries. One could therefore question the existence of different local minima and/or the metastability of the metallic impurities. Since however such geometries present the same *symmetry order* than the six-fold global minima of the PES, we postulate that they actually correspond to the saddle points of the two reorientation processes. The C_{2v}^{V} distortion, similarly to the model for the D_{2d}-energy surface, corresponds to the saddle point of the reorientation mechanism with respect to the C_2 symmetry, whereas the D_2 symmetry characterizes the transition between +/- orientations. Such assignment is supported by symmetry considerations (or within our toy-model), the activation energies obtained as total energy differences (giving $\Delta_{C_2} = \mathrm{E}\{\mathrm{g}^{C_{2v}^{\mathrm{V}}}\} - \mathrm{E}\{\mathrm{g}^{C_{2v}}\}$ = 21 meV and $\Delta_{+/-} = \mathrm{E}\{\mathrm{g}^{D_2}\} - \mathrm{E}\{\mathrm{g}^{C_{2v}}\} = 4$ meV for the Pt^- center) and

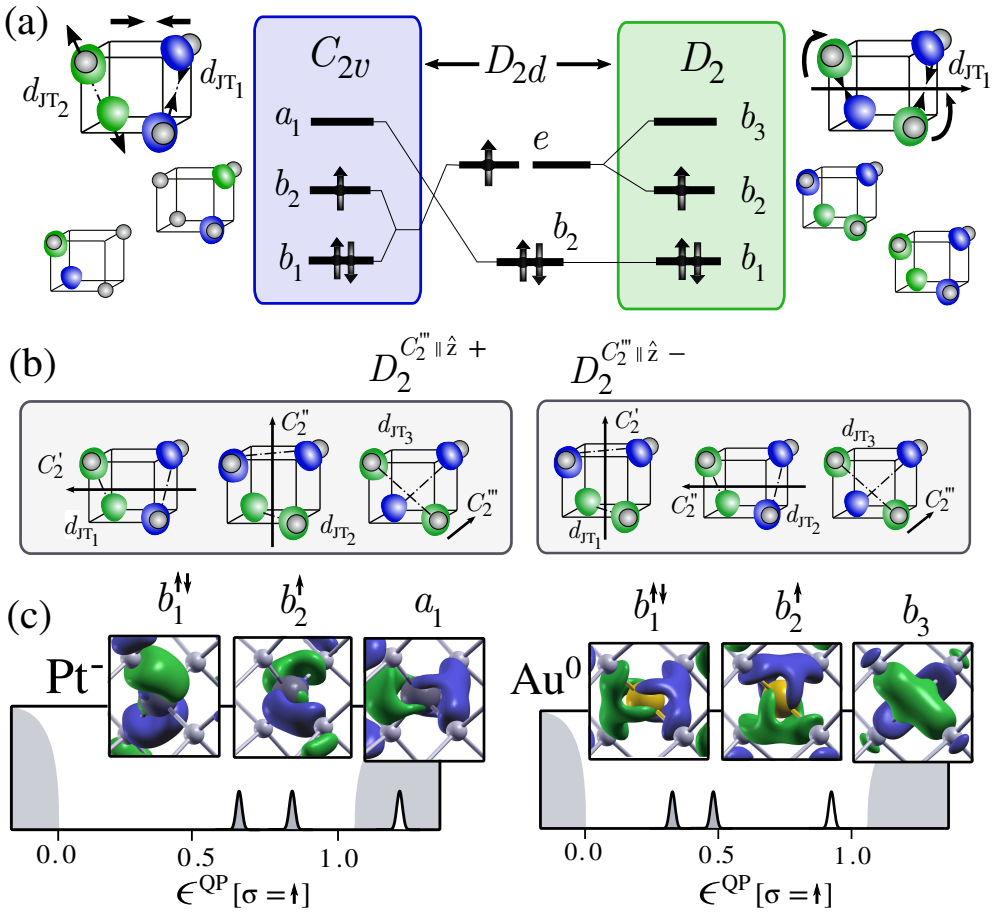

Figure 4.22: (a) Jahn-Teller model for the $D_{2d}^{<} \to C_{2v}$ and $D_{2d}^{<} \to D_2$ mechanisms. (b) Two out of six equivalent D_2 distortions, restricted to $C_2''' \equiv \hat{z}$. (c) Spin-restricted quasiparticle density of states for the PBE-defined ground state geometries of the Pt^- and Au^0 centers. The real-space projection of the KS wavefunctions are also shown.

the first-principles exploration of the *symmetry-imposed* transition paths (*i.e.* lack of energy barrier in the transition $C_{2v} \leftrightarrow D_2$ and $C_{2v} \leftrightarrow C_{2v}^{V}$).

In Figure 4.23, we have depicted our model for the reorientation processes of a C_{2v} center by placing the six minima of the energy surface on the six vertices of a regular octahedron, under the restriction that +/- orientations can not be positioned in adjacent nodes. The reorientation of the center with respect the C_2-axis is therefore given by the edges of the octahedron, whereas the transitions +/- are represented by the union of non-adjacent nodes. Furthermore, we postulate that any line representing a reorientation

process can be mediated by two different geometries or distortions. In the case of the $C_2^{\mathrm{x},+/-} \leftrightarrow C_2^{\mathrm{z},+/-}$ reorientation (depicted as a regular square in Figure 4.23), any of the four depicted transitions is characterized by a $C_{2v}^{\mathrm{V}y+}$ or a $C_{2v}^{\mathrm{V}y-}$ distortion. If on the other hand, we linearly interpolate between the $C_2^{\mathrm{x},+/-}$ and the $C_{2v}^{\mathrm{V}\mathrm{x},+/-}$ distortions, the system is forced to pass through a highly symmetric configuration, obtaining an energy barrier equal 0.14 eV. The transition between +/- orientations is depicted in Figure 4.23 for the $C_2^{\mathrm{z},+} \leftrightarrow C_2^{\mathrm{z},-}$ distortions. The saddle point of the MEP corresponds to either of the D_2 geometries with the restriction $C_2'''' \equiv \hat{z}$, imposing that the largest interatomic distance d_{JT_3} for the D_2 distortion is aligned with the d_{JT_1} and d_{JT_2} distances characterizing the C_{2v} geometry. Two more transitions paths might be considered, by forcing the transitions $C_2^{\mathrm{z},+/-} \rightarrow D_2$, for $C_2'''' \equiv \hat{x}$ and $C_2'''' \equiv \hat{y}$. Even if both transitions are characterized by non-zero energy barriers, they are inequivalent, due to the difference in energy cost to align the d_{JT_1} (distortion with $C_2'''' \equiv \hat{x}$) and d_{JT_2} (distortion with $C_2'''' \equiv \hat{y}$) distances with the d_{JT_1} and d_{JT_2} for the C_{2v} configuration.

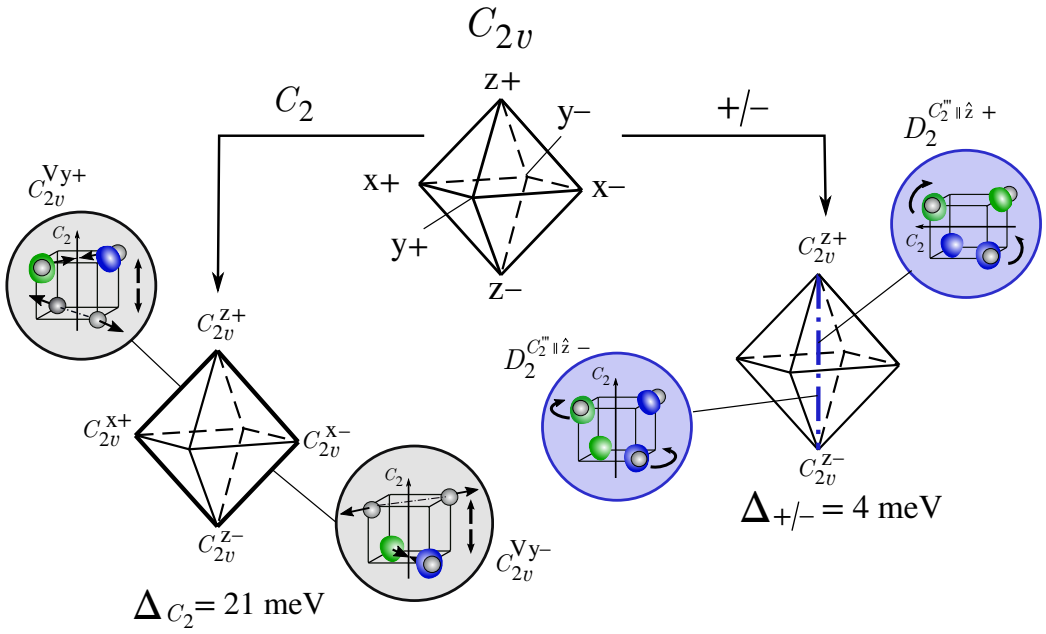

Figure 4.23: Theoretical model for the two reorientation processes of the Pt^- center in silicon, characterized by C_{2v} Jahn-Teller distortions. Transitions between different C_2-symmetry axis are defined by C_{2v}^{V} distortions, whereas the smaller +/- reorientations are given by D_2 distortions. Activation energies are determined at the PBE level of approximation as total energy differences, *e.g.* $\Delta_{+/-} = \mathrm{E}\{\mathrm{g}^{D_2}\} - \mathrm{E}\{\mathrm{g}^{C_{2v}}\}$.

We have hence proven once more that a *blind ab initio* characterization of the defect PES is not capable of describing the most basic features of the center. From simple symmetry considerations we have deduced the reorientation processes of the Pt^- center, building for the first time a consistent model for its energy surface. In Table 4.11, energy barriers for both reorientation mechanisms between equivalent C_{2v} distortions, estimated as total energy differences $E\{g^{C^V_{2v}}\} - E\{g^{C_{2v}}\}$ and $E\{g^{D_2}\} - E\{g^{C_{2v}}\}$, are collected. Activation energies are however still overestimated with respect to experimental evidence, questioning again the actual accuracy of the employed mean-field calculations. In the case of neutral gold, our *ab initio* calculations predict a D_2 distortion as the ground state geometry of the energy surface, with C_{2v} distortions as saddle points, defining an energy barrier of 9 meV. At this level of approximation, one has to therefore question whether the absence of EPR spectrum for gold in silicon is due to the estimated symmetry of the static Jahn-Teller minima of the PBE-energy surface (in contrast with previous discussions), or whether the center is characterized by a dynamical Jahn-Teller effect (in the form of D_2 or even C_{2v} distortions).

Table 4.11: Total energy differences between the reference C_{2v} geometry and the C^V_{2v} and D_2 distortions. All values are given in meV.

	Pd^-	Pt^-	Au^0
C^V_{2v}	21	21	–
D_2	7	4	-9

We conclude by restating the complexity of the Jahn-Teller effect in the studied centers for an electronic occupation equal three, for which three different symmetry-breaking mechanisms are described: $D_{2d} \rightarrow C^V_{2v}$ (monovacancy), $D_{2d} \rightarrow C_{2v}$ (negatively charged platinum) and $D_{2d} \rightarrow D_2$ (neutral gold). In the case of Pt^-, we have further investigated the shape of the energy surface, proposing a symmetry-resolved path for the observed small reorientations at low temperatures. The height of the computed barrier makes us however question once more the quality or accuracy of the mean-field calculations when describing Jahn-Teller effects in silicon. In the same line of thought, we also report a D_2 symmetry for neutral gold in silicon, which is barely 9 meV lower in energy than the previously proposed C_{2v} geometry. From a general perspective, we can question whether our symmetry guided *ab initio* characterization is capable of predicting the static or dynamic nature

of Jahn-Teller effects in silicon whenever the experimental evidence is inconclusive.

4.4 Computational Details

General computational details on the here performed *ab initio* calculations were already introduced in section 3.3. In the particular case of the silicon divacancy, we employ a large 512-atoms cell to investigate basic structural properties and a 680 eV energy cutoff. The inclusion of many-body corrections forces us to reduce the size of the cell, artificially quenching the Jahn-Teller distortions as collected in Table 4.12.

Table 4.12: Relevant interatomic distances d_{ij} for the divacancy at singly charge states embedded on a 216- and 512-atoms cells. All values are given in Å.

	$q = +1$		$q = -1$	
	d_{ij}	$d_{jk} = d_{ik}$	d_{ij}	$d_{jk} = d_{ik}$
216-atoms cell	3.21	3.66	3.32	3.49
512-atoms cell	3.07	3.64	3.28	3.43

Transition metals are embedded on a 216-atoms cell, and an energy cutoff of 1088 eV is employed to describe the D_{2d} geometries, whereas a 1578 eV cutoff was chosen to characterize the C_{2v} and D_2 distortions. All presented quasiparticles energies are obtained for an energy cutoff equal 1088 eV.

Chapter 5

Electronic activity of point defects in semiconductors: past, present and future

Thus electrons are raised by the light into conduction band, wander around until they find an F-center, and then stick there

Pohl (1937)

In the field of point defects in semiconductors, and especially defects in silicon, most of the theoretical studies are focused on determining the electronic activity of these *trapping impurities* due to its *immediate* technological interest. In terms of the long-established SRH model, one might then think that defects in semiconductors are fully characterized if the position of the induced deep levels ($E_V+ E_T$ or $E_C+ E_T$) and their respective non-radiative capture cross sections (σ_n) are determined. For what concerns silicon, a lot of effort has been dedicated to computing the charge transition levels (CTLs) of diluted centers by developing different computational approaches, evaluating their accuracy by comparison with the DLTS activation energies. Throughout this thesis, we have however extensively discussed the limitations of these studies, often offering a poor description of the basic features of the center and overlooking complementary information given by EPR spectroscopy and OA measurements.

In the present Chapter, we revisit established models to evaluate the electronic activity of defects in semiconductors, basing our analysis on our understanding of selected centers in silicon (Chapters 3, 4). Since only preliminary

results are given, this Chapter might be regarded as the natural perspectives of the present work. In section 5.1, we briefly compare the existent computational methods to estimate deep levels in semiconductors, before discussing the accuracy of the DFT+GW approach when the resulting CTLs are compared to DLTS energies. Furthermore, the barely discussed lack-of-energy-conservation issue of the method is reconsidered by providing numerical examples for selected centers in silicon. In section 5.2, we provide a historical overview of the so-called multi-phonon theories to evaluate non-radiative capture cross sections, giving special attention to the latest *ab initio*-based models.

5.1 Accuracy of computed deep levels by state-of-the-art calculations

Intrinsic limitations of the commonly employed mean-field approaches to characterize defects in semiconductors (*i.e.* self-interaction problem and the DFT band gap problem) are responsible for the poor description of deep levels in the band gap (Chapter 2). As introduced in Chapter 2, three methods have been proposed by the community to circumvent such issues, namely: the Marker method, the use of hybrid functionals and the DFT+GW combined method. With the existence of three *competitive* methods, it is surprising that to this date (and to the best of our knowledge) no comparative study or benchmark has been systematically performed on selected defects in semiconductors. In the case of silicon, the election of the Marker method to estimate most of the reported CTLs (with the exception [70, 71]) has therefore no formal or comparative justification (other than perhaps, limitations in the computational resources). In the present thesis, because we aim for a full *ab initio* parameter-free approach, we have employed the DFT+GW method.

Even if such method does not require any empirical shift (equation 2.81, in the context of the Marker Method), nor the choice of a certain fraction or parameter α (needed to define the hybrid functionals, equation 2.37), we still have to face the election of the *ab initio* code, the exchange-correlation functional, the pseudopotential, the electrostatic correction for charged supercells, etc. One is then confronted with the general reproducibility issues in first-principles calculations [146] and the estimation of absolute errors in such studies. In the case of CTLs, here computed as specified in the Computational Details section 3.3, deep levels for Ti and E-center were estimated to be between 0.1-0.2 eV off with respect to the corresponding DLTS activ-

ation energies. We can therefore question whether such absolute error is the expected accuracy of the method or whether there is an intrinsic limitation that needs to be corrected/taken into account.

Among the published works exploiting the DFT+GW combined method, in [147, 148] a lack of energy conservation in the electronic-capture-release closed cycle was reported and corrected. Before giving numerical examples of such issue and analyzing the proposed correction schemes, let us simply consider the electronic-capture-release cycle for the well known case of the silicon E-center and its two deep levels in the gap. As depicted in Figure 5.1, the energy exchanged through the electron release/capture process might be estimated as the energy difference between the minima of the parabolas, *i.e.* difference in energy at the two ground state geometries at different charge states. As it is represented, each charge transition might then be determined through two different paths (P_1 and P_2 in Figure 5.1), starting at different atomic distortions and evaluating the relaxation energy, ΔE, at two different charge states. Furthermore, for each transition path, one can determine the electronic excitation as an electron capture (in the form of an electronic affinity, EA) or an electron release (determined by an ionization potential, IP). One single charge transition level may then be computed through four different equivalent paths, given a net energy difference equal zero (close cycle represented in black in Figure 5.1).

In practice, the lack of energy conservation or numerical deviations among different equivalent paths were reported in the works of [147, 148]. In [147], discrepancies from the equality IP(0) = EA(+) at fixed atomic configuration were consistently studied at different levels of theory (HF, LDA, G_0W_0, etc), allowing them to conclude that the GW approximation is slightly concave and proposing to estimate the vertical transition or electronic excitation as the average of the estimated EA and IP. The later work of [148] reported differences of 0.1-0.2 eV between QP energies, estimating deep levels as the average between both CTLs obtained for paths P_1 and P_2 (taking either the IP or EA for the vertical transition).

In the present work, we also report a lack of energy conservation for the studied defects in silicon, as illustrated for the E-center (phosphorous-vacancy complex) in Table 5.1. For both donor (+/0) and acceptor (-/0) levels, we observe the inequality $\mathrm{IP}(q) \neq \mathrm{EA}(q-1)$ at fixed atomic distortions. Moreover, the QP eigenvalues reveal the slight concavity issue of the G_0W_0 method reported in [147], since IPs are systematically smaller than EAs. Furthermore, if one tries to compute the total energy exchanged in

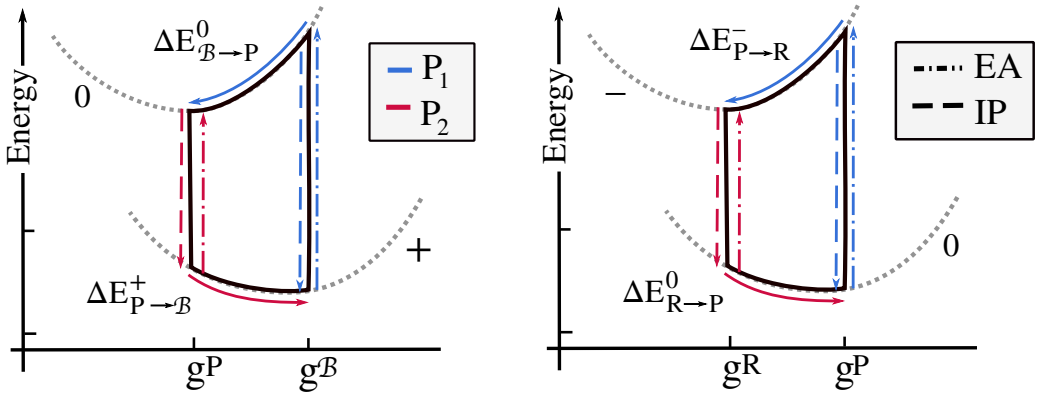

Figure 5.1: Coordination diagrams illustrating the energy exchange in charge transitions $+1 \leftrightarrow 0$ and $0 \leftrightarrow -1$ for the silicon E-center. Two different paths to estimate the CTLs (P_1 and P_2) are differentiated in blue and red respectively. The vertical transition for each path can be computed as an electron capture (EA) or an electron release (IP) at different charged states (*e.g.* IP(+), EA(0)). In black, the close energy cycle with a net energy exchange equal zero.

close cycles by describing both vertical transitions in Paths 1 and 2 exclusively with IPs or EAs, one finds that $\mathrm{IP}(q, \mathrm{g}^q) + \Delta\mathrm{E}^{q-1}(\mathrm{g}^q \to \mathrm{g}^{q-1}) \neq \mathrm{IP}(q, \mathrm{g}^{q-1}) - \Delta\mathrm{E}^{q}(\mathrm{g}^{q-1} \to \mathrm{g}^q)$, and equivalently for the EAs. In other words, besides the lack of precision when determining excitation energies or changes in the particle number, Paths 1 and 2 are numerically non equivalent, which might be attributed to the difference of the underlying KS wavefunctions employed to estimate G_0 and W_0 at two different atomic geometries.

Table 5.1: Vertical transitions energies (IPs or EAs) from $\mathrm{IP}_{\mathrm{TVB}}$ and relaxation energies (ΔE) employed to compute the CTLs induced by the PV center through the two different paths depicted in diagram 5.1.

CTL	Path 1			Path 2		
+/0	$\mathrm{EA}^{+}\{\mathrm{g}^{\mathcal{B}}\}$	$\mathrm{IP}^{0}\{\mathrm{g}^{\mathcal{B}}\}$	$\Delta\mathrm{E}^{0}_{\mathcal{B}\to\mathrm{P}}$	$\mathrm{EA}^{+}\{\mathrm{g}^{\mathrm{P}}\}$	$\mathrm{IP}^{0}\{\mathrm{g}^{\mathrm{P}}\}$	$\Delta\mathrm{E}^{+}_{\mathrm{P}\to\mathcal{B}}$
	0.60	0.47	0.12	0.40	0.22	0.07
0/−	$\mathrm{EA}^{0}\{\mathrm{g}^{\mathrm{P}}\}$	$\mathrm{IP}^{-}\{\mathrm{g}^{\mathrm{P}}\}$	$\Delta\mathrm{E}^{-}_{\mathrm{P}\to\mathrm{R}}$	$\mathrm{EA}^{0}\{\mathrm{g}^{\mathrm{R}}\}$	$\mathrm{IP}^{-}\{\mathrm{g}^{\mathrm{R}}\}$	$\Delta\mathrm{E}^{0}_{\mathrm{R}\to\mathrm{P}}$
	0.80	0.70	0.19	0.44	0.34	0.13

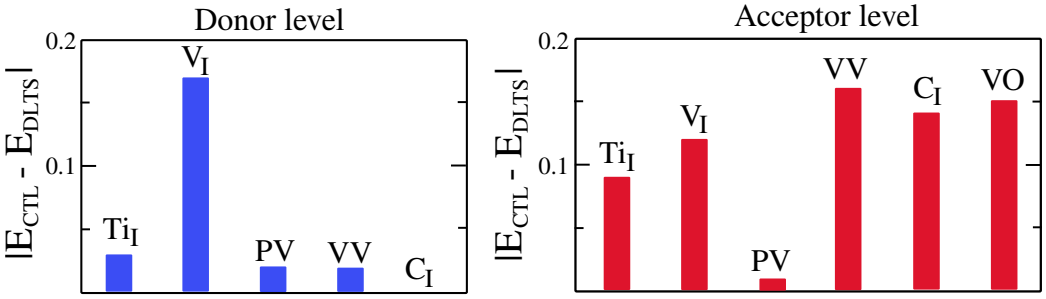

Figure 5.2: Absolute error of the computed single donor and acceptor levels for selected centers in silicon: interstitial titanium (Ti_I), interstitial vanadium (V_I), the phosphorous-vacancy complex (PV), the divacancy (VV), interstitial carbon (C_I) and the oxygen-vacancy complex (VO). The energy difference $|E_{CTL} - E_{DLTS}|$ corresponds to the deviation of the estimated CTLs within the DFT+GW approach from the corresponding DLTS activation energies. Experimental values for PV, C_I and VO were taken from [13, 101, 114]. In the case of centers for which multiple DLTS activation energies have been reported (Ti_i [26, 27, 28, 29, 30] , V_I [98, 99, 100], VV [13]), the reference level was assigned to the corresponding mean value. Vertical transitions have been determined at neutral charge state, *i.e.* IP^0 for donor levels, EA^0 for acceptor levels, whereas relaxation energies have been estimated as DFT-total energy differences at constant singly charged states, ΔE^+, ΔE^-. All values are in eV.

One can therefore question the best strategy to estimate CTLs within the DFT+GW approach, minimizing the intrinsic error of the method. Trying to keep the formalism as general as possible, we have computed vertical excitations exclusively from the neutral charge state and atomic distortion g^0 for selected defects in silicon, avoiding the inclusion of an *arbitrary* electrostatic correction (which might play a significant role in the inequality $IP(q) \neq EA(q-1)$). In Figure 5.2, we have plotted the energy difference $|E_{CTL} - E_{DLTS}|$ for single donor and acceptor levels, which might be interpreted as the absolute error of the estimated CTLs. Besides the challenging studied cases of the Ti_I, V_I, PV, VV centers, we have computed the CTLs levels for interstitial carbon (C_I) and the A-center (VO), since our our PBE-structural optimization is consistent with the fully understood defect-induced states and atomic distortions from EPR measurements [10, 149]. Even if an extension of the present investigation to a larger catalog of defects is recommended, one can already foresee that single donor levels are more accurately estimated than single acceptor levels, or more generally, computed ionization potentials seem to be closer to the *true* QP energies than electronic affinit-

ies. If the better estimation of IPs over EAs in HF-related theories was to be consistently proved, an even more accurate framework to estimate CTLs could be established.

To conclude, as in any DFT-based study, one has to be careful with the intrinsic error of computed values, which might be mitigated with the election of the pseudopotential, the exchange-correlation functional, etc., or in some cases, might be consequence of an underlying limitation of the theory. In the particular case of CTLs, we have shown the lack of energy conservation in electron-capture-release cycles. Acceptor levels estimated from electronic affinities seem to be systematically computed with a 0.1-0.2 eV error bar, which corresponds to a $\sim$10% of the silicon band gap. Prior to the performance of more numerical studies, one might be tempted to propose to exclusively estimate CTLs using IPs, after establishing a general scheme for the electrostatic correction of QP energies.

5.2 Non-radiative transitions under the scope

Evidently, introducing deep levels in the band gap is the fundamental condition for a defect to be electronically active. Among the catalogue of centers, there is however experimental evidence supporting that not all centers are equally harmful or equally efficient when degrading the performance of electronic devices. One is therefore interested in the probability of defects to capture/release free carriers non-radiatively or more specifically, by the capture cross sections (σ_n) of the defect-induced levels. From a historical perspective, Huang and Rhys reported their seminal work evaluating radiative and non-radiative cross sections in the context of point defects in alkali-halide materials in 1950 [8]. The main ideas of such early investigations were later taken by D. V. Lang [23], who published his widely known *non-radiative capture and recombination by multiphonon emission* theory in 1977, becoming the referent theoretical framework for thermal transitions within trapping centers. Due to the unquestionable influence of both theories in nowadays *ab initio* modelling, we dedicate section 5.2.1 to review the main ideas behind both works, before discussing recent first-principles estimations of the non-radiative σ_n in section 5.2.2.

5.2.1 Early theoretical frameworks

Due to the non-radiative character of the thermal transitions in recombination centers, one can only be certain of their occurrence through indirect

evidence. It is the case, for example, of the absorption-emission photon cycle within a given center, for which the number of absorbed photons is different from the number of emitted quanta. This phenomena, often refereed to as quenched luminescence, is widely explained by the existence of competing processes, capable of de-exciting the electron non-radiatively, dissipating the excitation energy through lattice vibrations. Throughout this section, it is therefore important to keep in mind that radiative and non-radiative transitions were historically studied together, employing similar theoretical frameworks to model the role of electron-photon coupling and the electron-lattice coupling in defect-localized processes.

The first conclusive evidence of trapped electrons being coupled with the crystal lattice was provided by Pohl in the form of *considerable widths* of the absorption curves of F-centers in alkali-halides [6]. In such early interpretation, as a consequence of the F-center electron-crystal coupling, lattice phonons were said to be created/annihilated when a photon-induced electron transition occurred. For a given electronic transition, the broadening in the absorption frequencies spectra was then identified with a larger or smaller number of exchanged lattice quanta (see, for example, the dotted lines with respect the bold line in Figure 5.3, representing photon-absorbed transitions). In such context, the first quantitative theory of the absorption curves was reported by K. Huang and A. Rhys (1950) in their seminal work, *Theory of light absorption and non-radiative transitions in F-centers* [8], where the radiative transition probability was estimated by explicitly considering both the electronic and ionic degrees of freedom. Further understanding of the de-excitation mechanisms was intended when they computed the non-radiative transition probability, setting a reference framework to still nowadays determine the σ_c for deep levels in semiconductors.

As in any quantum-mechanical system with initial and final states $|i\rangle$ and $|f\rangle$, one can think of estimating the transition probability $i \to f$ in terms of the Fermi-Golden rule,

$$P_{i\to f} \propto |M_{ij}|^2 \delta(E - E_{if}), \tag{5.1}$$

where M_{if} denotes the matrix elements describing the nature of the transition and E_{if} stands for the total energy exchanged in the process. Due to the complexity to compute M_{ij} for both electronic and ionic degrees of freedom, in practice, or as exemplified by Huang and Rhys, one can make a first simplification by considering the Franck-Condon approximation. The system initial and final states can then be written as a product state, *e.g.*

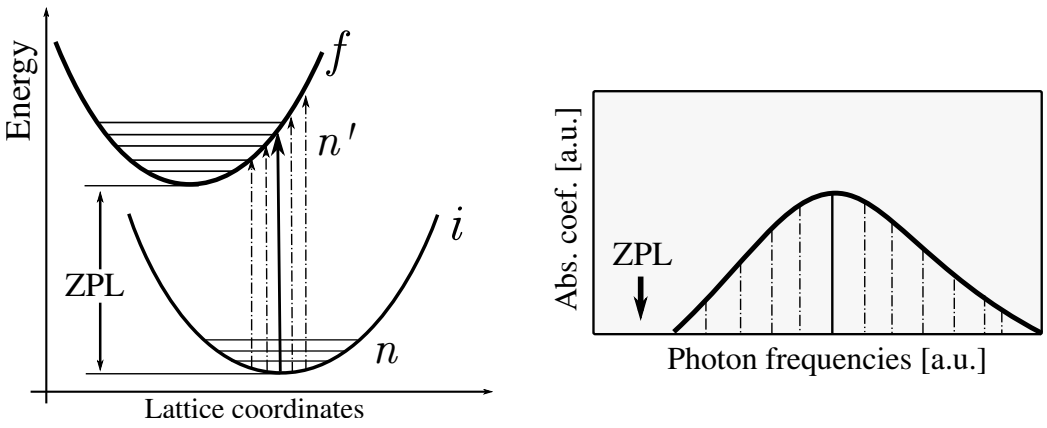

Figure 5.3: (Left) Coordination diagram constituted by two parabolas representing two electronic states i and f, for which the vibronic states, n, n' are also depicted. Photon-induced absorption transitions between both parabolas are represented with black arrows. (Right) Schematic absorption curve corresponding to the radiative transitions represented in the coordination diagram. The Zero-Phonon-Line is explicitly marked for both diagrams.

$|i\rangle \rightarrow |\phi_i\rangle\,|\chi_i\rangle$, where $|\phi_i\rangle$ and $|\chi_i\rangle$ are the electronic and ionic wavefunctions respectively. In the case of a radiative transition, the Franck-Condon principle might be understood by the fact that a photon-mediated electronic transition is vertical, *i.e.* it does not involve any changes in the surrounding lattice, and hence,

$$M_{if} \propto \langle i|\,\vec{d}\,|f\rangle \rightarrow \langle\phi_i|\,\vec{d}\,|\phi_f\rangle\,\langle\chi_i|\chi_f\rangle\,, \tag{5.2}$$

where $\langle\phi_i|\,\vec{d}\,|\phi_f\rangle$ denotes the dipole matrix element between two electronic states, responsible for the observed absorption band; and $\langle\chi_i|\chi_f\rangle$ is the vibronic term. Because the theory intended to model the annihilation/creation of phonons in radiative transitions, the initial and final ionic wavefunctions were specified by two quantum numbers, the electronic state (i, f) and the vibrational state (n, n'); so for simplicity from now on we will use the following notation, $|n\rangle \equiv |\chi_{i,n}\rangle$ and $|n'\rangle \equiv |\chi_{f,n'}\rangle$ (Figure 5.3). The vibronic term, later called the line shape factor or vibrational factor, $F(\nu)$, was written as a function of the photon frequency, ν, by summing over all possible quantum states of the final configuration, n',

$$F(\nu) = \sum_{n'} |\,\langle n|n'\rangle\,|^2 \delta(h\nu - (E_{f,n'} - E_{i,n})), \tag{5.3}$$

giving the transition probability $P_{i\rightarrow f}(\nu) = |\,\langle\phi_i|\,\vec{d}\,|\phi_f\rangle\,|^2 F(\nu)$. The success of the Huang-Rhys early work was precisely to develop an expression for

the vibronic term within the *continuum approximation for the lattice*, describing the ionic crystal as a dielectric medium. In such model, all normal coordinates, q_j, were be characterized by the same longitudinal frequency, ω_l, and the electronic transitions within the F-center were described by different magnitude of perturbations in the coordinates.

Within the same theoretical framework, Huang and Rhys wrote an analogous expression of M_{ij} (equation 5.2) for the non-radiative transition, stating that *when there is no perturbation term, the transition probabilities can still be obtained by perturbation methods*. In simpler words, the matrix elements for non-radiative transitions were identified with the non-adiabatic terms, neglected in the Born-Oppenheimer approximation or the nuclei kinetic related-terms, K_N. In the following, we reproduce the derivation reported in [8] to determine $P_{i\to f}$, starting from the definition of the electronic and ionic equations in the Born-Oppenheimer approximation,

$$\begin{aligned}\left[\hat{K}_e + \hat{V}_e + \hat{V}_{en} - E_\alpha\right]\phi_\alpha = 0 \\ \left[\hat{K}_n + \hat{V}_n + E_\alpha - E_{\alpha n}\right]\chi_{\alpha,n} = 0\end{aligned} \tag{5.4}$$

where E_α is the potential energy surface obtained at frozen ionic positions and electronic state α and $E_{n\alpha}$ is the total energy of the electronic and ionic system. The perturbative term is then,

$$(\hat{H} - E_{\alpha,n})\phi_\alpha\chi_{\alpha,n} = K_n\phi_\alpha\chi_{\alpha,n} - \phi_\alpha K_n\chi_{\alpha,n} \tag{5.5}$$

and the corresponding matrix elements, $\langle fn'|\,\hat{H} - E_{i,n}\,|in\rangle$, can be simply derived by writing K_n in terms of the normal coordinates, $K_n = -\sum_j \partial^2/2\partial q_j^2$. If one neglects second order derivative terms,

$$P_{i\to f}(p) \propto \sum_{n'}\left|\sum_j \langle f|\,\frac{\partial}{\partial q_j}\,|i\rangle\,\langle n'|\,\frac{\partial}{\partial q_j}\,|n\rangle\right|^2 \delta\left(p\hbar\omega_l - (E_{f,n'} - E_{i,n})\right) \tag{5.6}$$

In contrast with the radiative transition, the exchange in energy is entirely dissipated through $p = \sum_j \Delta n_j$ lattice-phonons, which in the approximation of the *continuum lattice* were reduced to one single longitudinal frequency, ω_l. Similarly to the tedious derivation for the radiative line shape factor, Huang and Rhys obtained an expression for the vibronic term, which will not be copied here, but can be found in [8].

The main contributions of the pioneering work of Huang and Rhys are therefore to provide a full quantum-mechanical formalism to describe transitions involving both the electrons and the lattice and to derive the first

analytical expressions for the finite-temperature radiative and non-radiative probabilities. The theory was however quickly criticized for being limited to a single frequency model, being generalized to many-frequency models by [150, 151] shortly after the publication of the first paper. An incommensurable amount of works have since then been published with the objective of estimating the radiative and/or non-radiative probabilities (*e.g* [152, 23, 153]), most of them invoking the seminal work of Huang and Rhys. Since giving a detailed review of such theories is beyond the scope of the present thesis, we simply aim to contextualize certain recurrent ideas that are often linked with the Huang-Rhys model or to the non-radiative transition probability; namely, the multi-phonon emission concept and the Huang-Rhys factor.

Even if Huang and Rhys commented on the dissipation or creation of *several lattice quanta* and they formulated that the energy conservation in non-radiative transitions was restricted to $p\hbar\omega_l$, they did not discuss any further the phenomenology of the studied transitions. It was, to the best of our knowledge, M. Lax the first author to use the term *multi-phonon process* [154], after contextualizing the theoretical formalism to an electron being trapped by a defect level located in the middle of the semiconductor band gap. More concretely, referring to the electron-capture process, he wrote:

"*that the electron not only must come to the vicinity of the center, it must on arrival perform the unlikely task of disposing of perhaps 0.5 eV (and it may take ten phonons to carry away this energy)*"

This is the reason that (even nowadays) the electron-capture by an impurity is said to be accompanied or mediated by simultaneous emission of a number of phonons (*i.e.* the so-called non-radiative transitions through multi-phonon emission theories).

The motivation of M. Lax to understand the *multi-phonon processes* or the lattice-relaxation process can be tracked back to his early work [150], where he worked on the generalization of the Huang-Rhys model to a many-frequency model and he represented certain definitions or parameters of the model in one-dimensional coordination diagrams. Thanks to such simple graphical representations, changes in the lattice coordinates or normal modes were simply associated to lattice-relaxation energies. With this interpretation of radiative and non-radiative transitions, M. Lax naturally defined an S-factor (similar to the one defined in Huang-Rhys work), explicitly relating dissipation energies with exchanged lattice-quanta for a given transition. The one-dimensional diagrams and the S-factor were later widely reproduced,

with the later eventually becoming the famous Huang-Rhys factor.

One-dimensional coordination diagrams, like the ones depicted in Figure 5.4 for radiative and non-radiative transitions are an extreme simplification of the Huang-Rhys original work, especially in the considered case of the two electronic surfaces having the same curvature, ω. They are however often employed to understand lattice-related process, like the measured Stokes shift or difference between the photon absorbed and emitted frequencies by a given center, which is associated to the change of the optimized atomic positions at different electronic states. Assuming that such modification in the lattice positions can be described by a change in the normal mode, Q_0, the Huang-Rhys factor, is symply defined as (*e.g.* [7]),

$$\hbar\omega S = \frac{1}{2}\omega^2 Q_0^2 \tag{5.7}$$

As represented in Figure 5.4, within such simple model, the Stokes shift can be trivially related to the curvature of the electronic energy surfaces and the above-defined Huang-Rhys factor.

In the case of non-radiative transitions, the electron-lattice process is often depicted as two intersecting parabolas, as represented in Figure 5.4. Within such model, the non-radiative transitions are simply approximated as thermally-activated processes, defined by an energy barrier, $\mathrm{E_B}$, which can be written in terms of the S-factor, the curvature ω and the energy shift between both parabolas, $\mathrm{E_0}$ (Figure 5.4). The transition probability can thus be simply estimated as,

$$P_{i\to f} \propto \exp(-\mathrm{E_B}/kT) \tag{5.8}$$

A similar expression in the context of charge-electronic-transfer in chemical reactions was postulated by the Marcus theory [155] and by K. Huang [8], when he took the high temperature limit of his original non-radiative transition probability. In the limit of high temperatures or the classical limit, there is therefore a general consensus of the characteristic rate of *multi-phonon* processes following a simple Arrenhius law.

To summarize, the term *non-radiative transitions* encapsulates the large variety of possible non-visible processes in solids or molecules, responsible for degrading phenomena in electronic devices, such as quenched luminescence or free-carrier recombination through trap states. The pioneering work of Huang and Rhys constitutes the first attempt to model the non-radiative

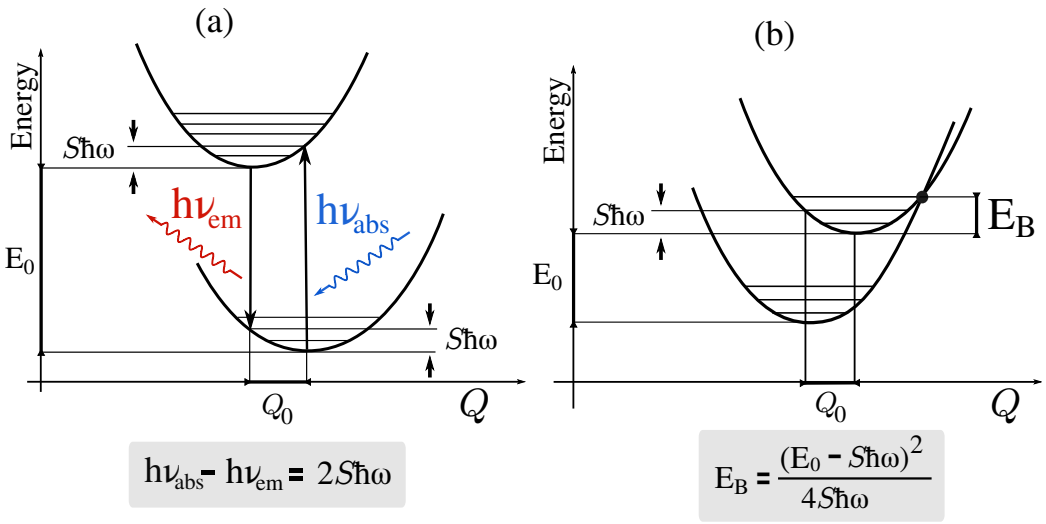

Figure 5.4: One-dimensional coordination diagrams for (a) radiative and (b) non-radiative transitions defined in the energy, E, *versus* normal coordinate, Q, plane. The represented parabolas have the same curvature, ω, and are relatively displaced by E_0 units of energy and Q_0 difference in normal coordinates. The Huang-Rhys factor, S, defined as $\hbar\omega S = \frac{1}{2}\omega^2 Q_0^2$, is also depicted and related to the Stokes shift ($h\nu_{\text{abs}} - h\nu_{\text{em}}$) for radiative transitions and the energy barrier (E_B) for non-radiative transitions.

transition probability, for the particular case of F-centers in alkali-halides. Since then, multiple theories have been proposed, trying to generalize the Huang-Rhys formalism to multiple-frequency models, but without defining a universal theoretical framework. Only at the high-temperature limit, a characteristic expression in the form of an Arrenhius law is often widely adopted.

Multi-phonon theories linked to DLTS spectroscopy

Due to its unquestionable importance in the field of thermal recombination in semiconductors, we give special attention to the work of Henry and Lang, titled *Non-radiative capture and recombination by multiphonon emission in GaAs and GaP* [23], often considered as the reference multi-phonon theory. In their seminal work, they presented a formalism to determine the probability of electron-capture by a trap level from the bulk bands non-radiatively, which is still employed nowadays to correct DLTS activation energies. Within their simple formalism, the capture of an electron from conduction (C) to a bound state (T) is explained through the lattice vibrations causing the free and

bound state to cross. The transition rate for electron capture, C $\rightarrow$ T, was written as,

$$w = \frac{2\pi}{\hbar}\text{ave}_{n_c}\sum_{n_t} |\left\langle tn_t\right| \mathcal{H} \left|cn_c\right\rangle|^2 \delta(\varepsilon_c - \varepsilon_t), \tag{5.9}$$

where the global wavefunctions $|\text{T}\rangle$ and $|\text{C}\rangle$ are written in terms of the electronic states, $|t\rangle$ and $|c\rangle$, and the lattice states, $|n_t\rangle$ and $|n_c\rangle$. Restricting the calculation to one single vibrational mode, with frequency ω, and a net displacement given by the occupations n_t and n_c, the energy exchanged in the process, $\varepsilon_c - \varepsilon_t$, is defined as $n_c\hbar\omega - n_t\hbar\omega - E_0$ (being E_0 the energy difference between the minima of the two parabolas). The above equation is then approximated by considering a rather simple electron-lattice coupling term,

$$w = \frac{2\pi}{\hbar}|\left\langle t|\Delta V|c\right\rangle|^2 \left(\text{ave}_{n_c}\sum_{n_t} |\left\langle n_t|n_c\right\rangle|^2 \delta(\varepsilon_c - \varepsilon_t)\right). \tag{5.10}$$

The term in parenthesis was said to be identical to the line shape factor, $F(\nu)$, defined for radiative transitions with a zero-photon-frequency, $\nu = 0$, and it was then substituted by the Huang-Rhys derived expression. Taking the high temperature limit they wrote,

$$F(0) = (4\pi\hbar\omega kTS)^{-1/2}\exp\left(-E_B/kT\right), \tag{5.11}$$

with,

$$E_B = (E_0 - \hbar\omega S)^2/4\hbar\omega S \tag{5.12}$$

The capture cross section was then simply written as, $\sigma_c = AF(0)$, where the electronic matrix element, $A \propto |\left\langle t|\Delta V|c\right\rangle|^2$, was approximated as the one between a free and bound states subject to a spherical square potential of depth V_0. Their final, widely reproduced expression,

$$\sigma_c = \sigma_{\infty c}\, e^{-E_{\infty c}/kT}, \tag{5.13}$$

was then proposed, with $\sigma_{\infty c} = (\epsilon_1/S\hbar\omega)^{1/2}(\pi^2/2e)(\hbar^2/2m^*kT_R)$ and $E_{\infty c} = E_B - kT_R$, where ϵ_1 is a parameter of the model (energy position of the bound state with respect the continuum) and T_R is equal $T = 300$ K.

The theoretical work presented by Henry and Lang does therefore not present any further advance in the estimation of the non-radiative capture cross section, since their original contribution is merely to compute $\langle t|\Delta V|c\rangle$ within a rather simple model. Furthermore, one could argue against the approximation introduced between equations 5.9 and 5.10, where the electron-lattice coupling matrix element is only estimated for the electronic states,

taking the vibronic term as a simple overlap between the ionic wavefunctions, contradicting the Huang and Rhys theory for non-radiative transitions (equation 5.6). Even so, in the limit of high temperatures, they find the general expression for thermal-activated processes, characterized by the exponential factor, $\exp(-E_B/kT)$, defined by an energy barrier, E_B, retrieving the general expression discussed above. The merit of their early work is therefore justified by their phenomenological perspective, explicitly matching measured captures cross section curves to the Arrenhius plot defined by equation 5.13. It is thus important to keep in mind that the proposed expression for σ_∞ is merely an approximation of the general framework and deviations from the exponential law have to be treated with a higher level of theory.

To conclude, in the context of carrier recombination, non-radiative capture-cross sections are simply written in the form of Arrenhius laws, exclusively considering the classical or high-temperature limit. In particular, the Henry-Lang expression for the capture cross section, σ_∞ (equation 5.13) is still employed nowadays to *correct* DLTS activation energies or to model the temperature dependence of the measured σ_{na} (section 1.3.3). In the absence of a general framework describing all temperature regimes, one could then think of understanding the low temperature limit through the *accurate* description of the defect-induced phonon spectra within *ab initio* calculations, explicitly solving the matrix elements described in equation 5.6.

5.2.2 *Ab initio* modelling of non-radiative transitions

A full quantum-mechanical treatment of the electron-lattice system is of course beyond the possibilities of present *ab initio* methods, or more precisely, computational power. Even within the Born-Oppenheimer approximation or at frozen nuclei positions, the estimation of charged and neutral electronic excitations is still limited by computational resources. *Ab initio* calculations can therefore not address the *direct* estimation of transition probabilities, but they can estimate parameters of the early proposed theories (section 5.2.1), which previously relied on empirical values or rather simple theoretical models. It is the case of the recent estimation of Huang-Rhys factors for molecules (*e.g.* [156]) and defects (*e.g.* [157]) as part of the investigation of the light-absorption spectra.

Recent works have however tried to go one step further, reformulating the non-radiative transition rates, explicitely computing the electron-phonon coupling matrix element between electronic states [158, 159] (matrix element

denoted by A in Lang theory). In [158], the analytical expression for the electron transition rate between states s and l is adapted from the work of Freed and Jortner (1970) *for large molecules* [152],

$$W_{sl} = \sum_k |C_{sl}^k|^2 \, \mathcal{F}(\beta, \omega_k) \tag{5.14}$$

where C_{sl}^k is the so-called electron-phonon coupling constant for the phonon mode k, with frequency ω_k. The cumberstone function $\mathcal{F}$, corresponding to the vibronic term, is explictely given in [158]. Their work does therefore consist on developing a method to numerically estimate C_{sl}^k, or more precisely, $\langle \phi_s | \, \partial H / \partial R \, | \phi_l \rangle$, and to diagonalize the dynamic matrix for selected displacements for the defective cell to determine the phonon DOS and corresponding normal modes.

In [159], the capture rate is written in terms of the matrix element, $\Delta H_{im;fn}^{e-ph}$, including both the electronic, $|\phi_{i,f}\rangle$, and ionic, $|\chi_{im,fn}\rangle$, degrees of freedom,

$$\Delta H_{im;fn}^{e-ph} = \sum_k \langle \phi_i | \, \partial H / \partial Q_k \, | \phi_f \rangle \, \langle \chi_{im} | \, Q_k - Q_{0;k} \, | \chi_{fn} \rangle \tag{5.15}$$

where the sum runs over all phonon modes, Q_k. To numerically afford the estimation of the defined matrix elements, the many-frequency system is reduced to only one *special* phonon mode, circumventing the sum over all modes k. The highly dimensional problem is thus reduced to a one-dimensional model, where the configuration coordinate Q is defined as, $Q^2 = \sum_{\alpha,t} m_\alpha (R_{\alpha t} - R_{f;\alpha t})$, being $R_{\alpha t}$ and $R_{f;\alpha t}$ the atomic position of atom α at any configuration and at the final configuration respectively. Once all derived quantities for such effective mode of vibration are determined, matrix elements in equation 5.15 are computed numerically.

To summarize, in addition to the lack of a general and unified theory for non-radiative transitions, one needs to deal with the *ab initio* characterization of vibrational-related properties of a defective cell, which is still a rather unaffordable calculation, especially if one wants to guarantee the convergence of the DFT total energy second derivatives. Starting from the initial choice of an analytical expression for the matrix elements (equation 5.14 or the Freed-Jortner probability) to the important approximations when numerically estimating the vibrational modes or electron-phonon matrix elements, one might be tempted to criticize the transferability or reproducibility of the calculations.

As a more general conclusion, one might state that non-radiative transitions are ultimately conceived as either quantum or classical transitions between two intersected parabolas representing the energy surface of two different trap electronic occupations. In the high-temperature or classical limit, in which, in addition, the two parabolas are often described by the same curvature (Figure 5.4), the characteristic energy barrier is written in terms of a lattice relaxation energy or the Huang-Rhys factor. In recent DFT-based works [159], the quantum transition is described by estimating the relative displacement of both parabolas in normal coordinates and their respective curvature in an effective-vibrational-mode approximation. In such line of analysis, one might think of constructing a *simple model* based on the full theoretical pictures of the energy surfaces proposed in the present thesis, for which changes in the trap electronic occupations are characterized through relevant symmetry-determined modes of vibration.

Conclusions

On voit les qualités de loin et les défauts de près

V. Hugo

In a few lines, the main contribution of the present thesis to the long-established field of defects in silicon are the presented full-theoretical pictures for selected centers, unifying fundamental symmetry constraints and state-of-the-art *ab initio* calculations. A deep understanding of the basic features of the centers, and in particular the energy surface described by the trapped electron with respect to atomic distortions, have allows us to make a solid correspondence with experimental evidence, in opposition to previous first-principles simulations. Ultimately, the established quantitative theoretical frameworks were employed to link the presence of certain point-like defects to nowadays technologically relevant phenomena (*e.g.* photon-enhancing absorption in solar-cells, random burst noise in image sensors, or even more generally, the electronic activity of defects embedded in semiconductor wafers).

A *blind* DFT-based exploration of the potential energy surface has proven to give erroneous interpretations of the defect metastability or ground state geometry even in the simplest case of the silicon E-center, whose ground state properties are determined by an atomic trimer (constituted by the vacancy nearest silicon neighbours). In the present work, we have guided our *ab initio* calculations with the previously proposed Jahn-Teller model, developed from a simple molecular-orbital theory, which effectively describes how changes in the occupation of defect-induced levels (or charge state) trigger different atomic distortions. Within our DFT-based approach, we have established a one-to-one correspondence between the two theories, comparing the symmetry of the estimated localized wavefunctions and structural distortions. The Jahn-Teller model has been further confirmed by accurately determining the optical absorption bands with the inclusion of many-body effects. The hypothesized *Mexican hat* shape of the three-fold minima energy surface has also been supported by our extensive exploration of the PBE-

PES, matching the EPR-measured reorientation barriers between equivalent distortions with our calculations. The valuable insight into the defect basic features provided by EPR-spectroscopy (anticipated by G. D. Watkins), has been further enhanced by modelling the defect-axis reorientation process at high temperatures, matching the measured activation energies and confirming its role in the vacancy-mediated dopant diffusion mechanism.

The numerical investigation of the *Mexican hat* energy surface for the trimer has been generalized to different symmetry-breaking mechanisms in silicon, namely, the $D_{3d} \rightarrow C_{1h}$ (E-center), the $D_{2d} \rightarrow C_{2h}$ (the divacancy) and the $T_d \rightarrow D_{2d}$ (transition metals exhibiting vacancy-like distortions). Within such general framework, Jahn-Teller distortions lowering the symmetry of the precursor state with respect to different orientations of the symmetry axis (σ_h-reflection plane or C_2-rotation axis for the studied cases) might therefore co-exist, characterizing the finite-temperature reorientation between equivalent minima of the energy surface. Furthermore, in the considered cases of three-fold degenerate minima energy surfaces, we have shown that the reorientation process between the general axis $i \rightarrow j$ is defined by a saddle point corresponding to an opposite sense of the JT distortion with respect to the third axis k. A symmetry-restricted path does however force the system to pass through the highly symmetric precursor state. In the case of negative platinum, the complexity of the six-fold minima surface is explained by two consecutive Jahn-Teller distortions, $T_d \rightarrow D_{2d} \rightarrow C_{2v}$, required to lift completely the degeneracy of the precursor t_2-states. In such case, we have shown that minimization algorithms like the NEB method are incapable of finding accurate MEP between equivalent C_{2v} distortions, requiring symmetry considerations (or the description of the D_2-geometry of the same symmetry order) to describe the observed reorientation of Pt^- at cryogenic temperatures.

The PBE quantification of simple symmetry-based toy-models has generally proved to be in good agreement with EPR experimental evidence, especially for low trap occupations (*e.g.* neutral E-center, positive divacancy, the mono-vacancy at positive and neutral charge states). In the limit of large electronic localized densities (*e.g.* negative divacancy) we have however shown that DFT calculations are compromised by the approximations made in the exchange-correlation functional, resulting in a poor description of the occupied orbitals and the magnitude of the distortions. With such reliability of the PBE-accuracy in mind, we have questioned whether the non-measurable EPR signal for gold in silicon is effectively due to a C_{2v}-dynamical Jahn-Teller effect or whether it is a consequence of the *actual*

symmetry of the ground state geometry, here obtained as a D_2-distortion. For the employed approximation of the Coulomb electronic interaction, the existing controversy for certain centers in the *ab initio* community can not be dissipated, but we postulate the need of a higher level of theory. The here presented calculations are however fully consistent with fundamental symmetry restrictions.

In the limit of small Jahn-Teller distortions for which quantum effects might become relevant and the PBE accuracy might be questionable, we have considered the case of interstitial titanium in silicon. Even if such center has received a lot of recent attention due to its possible role as photon-absorption enhancing impurity, none of the previous theoretical studies have investigated the instability of the partially occupied 3d orbitals in the silicon crystal. Our proposed model is based on previous symmetry considerations of early transition metals subject to tetra- and octahedral crystal fields. For the precursor charge state, Ti^+, for which the triplet $t_2^{\uparrow\uparrow\uparrow}$ is stable against Jahn-Teller distortions, we have estimated the critical doping concentration to induce an intermediate band (in contrast with the localized defect orbital) and the relative position of the defect-states with respect to the bulk bands in the diluted regime.

Understanding Jahn-Teller effects for defects in silicon (*i.e.* the symmetry and magnitude of the distortions and the corresponding form and degeneracy of the defect-orbitals) allowed us to consequently compute the charge transition levels (CTLs) within the DFT+GW formalism, estimating the energy exchange at different atomic distortions at the PBE level of theory and the position of the partially occupied defect-levels with a many-body approach. Even if the DFT band gap problem is formally circumvented, we have provided numerical evidence supporting the few investigations claiming the lack of energy conservation in the electron capture-release cycle. Within such intrinsic error-bar, we have confirmed the electronic activity of selected defects in silicon within a full *ab initio* parameter-free approach, by comparing CTLs with DLTS activation energies.

A further characterization of the electronic activity of defects in semiconductors has finally been proposed with the estimation of the lattice-mediated electron-capture rate. By revisiting early established theoretical frameworks we have discussed the lack of a unified general theory to compute non-radiative transition probabilities, except for the high temperature limit, for which the capture rate is commonly defined as the one for a temperature-activated mechanism or a simple Arrhenius law. It is the case of the multi-

phonon emission theory proposed by Lang, which is still used nowadays to correct DLTS activation energies. On the *ab initio* front, we have commented on the rather big approximations required to estimate vibrational-related properties of localized atomic modes in the de-localized solid degrees of freedom.

To conclude, one should not undervalue the complexity of theoretically characterizing point defects in silicon, especially since atomistic modelling might be regarded as the key-asset in mitigation strategies for degraded Si-based electronic devices. From fundamental structural properties to the evaluation of electronic capture cross sections, sophisticated *ab initio* calculations should be guided by general symmetry-based models in order to establish a grounded comparison with experiments, allowing to determine the quality of the numerical approach. We hence propose to extrapolate the presented general theoretical frameworks to the study of any kind of defect in any given semiconductor and to determine the regime of accuracy of state-of-the-art calculations when computing certain defect properties (*i.e.* magnitude of Jahn-Teller distortions, variation of optical bands with the Fermi energy, etc.). Moreover, we aim to extend our *full* pictures of selected centers to address the static *versus* dynamical character of the Jahn-Teller effect in silicon and to consistently evaluate the electronic-capture non-radiative transition probability by accurately determining the symmetry of the promoting vibrational mode.

Publications

- G. Herrero-Saboya, L. Martin-Samos, A. Jay, A. Hemeryck, N. Richard, A comprehensive theoretical picture of E centers in silicon: From optical properties to vacancy-mediated dopant diffusion, *Journal of Applied Physics*, **127**, 085703 (2020)

- G. Herrero-Saboya, L. Martin-Samos, A. Hemeryck, D. Rideau, N. Richard, Electronic and structural properties of interstitial titanium in crystalline silicon from first-principles simulations, 2019 SISPAD *Conference Paper*, (2019)

Conferences

- International
  - APS March Meeting 2020 - Denver - Oral contribution (canceled due to sanitary crisis)
  - SISPAD 2019 - Udine - Poster contribution
- National
  - Toucam 2019 - Toulouse - Oral contribution

Formation

- Training School COST Action CA17126 - Rethymnos (Sept-Oct 2019)
- École d'été GDR MODMAT - Istres (Jul 2019)
- Abinit School - Bruyères-le-Châtel (Jan 2019)
- Total Energy and Force Methods Workshop - Trieste (Jan 2019)

Bibliography

[1] N. W. Ashcroft and N. D. Mermin. *Solid State Physics*. Harcout College, 1976.

[2] G. Grosso and G. P. Parravicini. *Solid State Physics*. Academic Press, 2003.

[3] P. Yu and M. Cardona. *Fundamentals of Semiconductors*. Springer-Verlag, 1990.

[4] K. Graff. *Metal Impurities in Silicon-Device Fabrication*. Springer, 2000.

[5] Christoph Freysoldt, Blazej Grabowski, Tilmann Hickel, Jörg Neugebauer, Georg Kresse, Anderson Janotti, and Chris G. Van de Walle. First-principles calculations for point defects in solids. *Rev. Mod. Phys.*, 86:253–305, Mar 2014.

[6] R W Pohl. Electron conductivity and photochemical processes in alkali-halide crystals. *Proceedings of the Physical Society*, 49(4S):3–31, aug 1937.

[7] A. Stoneham. *Theory of Defects in Solids*. Oxford University Press, 1975.

[8] Kun Huang and Avril Rhys. Theory of light absorption and non-radiative transitions inf-centres. *Proceedings of the Royal Society of London. Series A. Mathematical and Physical Sciences*, 204(1078):406–423, 1950.

[9] H. Y. Fan and A. K. Ramdas. Infrared absorption and photoconductivity in irradiated silicon. *Journal of Applied Physics*, 30(8):1127–1134, 1959.

[10] G. D. Watkins and J. W. Corbett. Defects in irradiated silicon. i. electron spin resonance of the si-*a* center. *Phys. Rev.*, 121:1001–1014, Feb 1961.

[11] J. W. Corbett, G. D. Watkins, R. M. Chrenko, and R. S. McDonald. Defects in irradiated silicon. ii. infrared absorption of the si-*a* center. *Phys. Rev.*, 121:1015–1022, Feb 1961.

[12] L. J. Cheng, J. C. Corelli, J. W. Corbett, and G. D. Watkins. 1.8-, 3.3-, and 3.9-μ bands in irradiated silicon: Correlations with the divacancy. *Phys. Rev.*, 152:761–774, Dec 1966.

[13] P. Pichler. *Intrinsinc Point Defcts, Impurities, and Their Diffusion in Silicon.* Springer-Verlag, 2004.

[14] Jr. & L. M. Slifkin (Eds.) J. H. Crawford. *Point Defects in Solids. Vol. 2 Semiconductors and Molecular Crystals.* Plenum Press, 1975.

[15] G. D. Watkins, J. W. Corbett, and R. M. Walker. Spin resonance in electron irradiated silicon. *Journal of Applied Physics*, 30(8):1198–1203, 1959.

[16] G.D. Watkins. An EPR study of the lattice vacancy in silicon. *J. Phys. Soc. Japan*, 18:Suppl. II, 22, 3 1963.

[17] G. D. Watkins and J. W. Corbett. Defects in irradiated silicon: Electron paramagnetic resonance and electron-nuclear double resonance of the Si-E center. *Phys. Rev.*, 134:A1359–A1377, Jun 1964.

[18] G. D. Watkins and J. W. Corbett. Defects in irradiated silicon: Electron paramagnetic resonance of the divacancy. *Phys. Rev.*, 138:A543–A555, Apr 1965.

[19] Edward L. Elkin and G. D. Watkins. Defects in irradiated silicon: Electron paramagnetic resonance and electron-nuclear double resonance of the arsenic- and antimony-vacancy pairs. *Phys. Rev.*, 174:881–897, Oct 1968.

[20] D. V. Lang. Deep level transient spectroscopy: A new method to characterize traps in semiconductors. *Journal of Applied Physics*, 45(7):3023–3032, 1974.

[21] W. Shockley and W. T. Read. Statistics of the recombinations of holes and electrons. *Phys. Rev.*, 87:835–842, Sep 1952.

[22] D. V. Lang and C. H. Henry. Nonradiative recombination at deep levels in gaas and gap by lattice-relaxation multiphonon emission. *Phys. Rev. Lett.*, 35:1525–1528, Dec 1975.

[23] C. H. Henry and D. V. Lang. Nonradiative capture and recombination by multiphonon emission in gaas and gap. *Phys. Rev. B*, 15:989–1016, Jan 1977.

[24] L. Scheffler, Vl. Kolkovsky, and J. Weber. Identification of titanium-hydrogen complexes with up to four hydrogen atoms in silicon. *Journal of Applied Physics*, 117(8):085707, 2015.

[25] H. Kortegaard Nielsen, A. Hallén, and B. G. Svensson. Capacitance transient study of the metastable m center in n-type $4h-$SiC. *Phys. Rev. B*, 72:085208, Aug 2005.

[26] D. Mathiot and S. Hocine. Titanium-related deep levels in silicon: A reexamination. *Journal of Applied Physics*, 66(12):5862–5867, 1989.

[27] L. Tilly, H. G. Grimmeiss, H. Pettersson, K. Schmalz, K. Tittelbach, and H. Kerkow. Electrical and optical properties of titanium-related centers in silicon. *Phys. Rev. B*, 43:9171–9177, Apr 1991.

[28] J.-W. Chen, A.G. Milnes, and A. Rohatgi. Titanium in silicon as a deep level impurity. *Solid-State Electronics*, 22(9):801 – 808, 1979.

[29] J.R. Morante, J.E. Carceller, P. Cartujo, and J. Barbolla. Thermal emission rates and capture cross-section of majority carriers at titanium levels in silicon. *Solid-State Electronics*, 26(1):1 – 6, 1983.

[30] Alex C. Wang and C. T. Sah. Complete electrical characterization of recombination properties of titanium in silicon. *Journal of Applied Physics*, 56(4):1021–1031, 1984.

[31] P. Hohenberg and W. Kohn. Inhomogeneous electron gas. *Phys. Rev.*, 136:B864–B871, Nov 1964.

[32] L. J. Sham and W. Kohn. One-particle properties of an inhomogeneous interacting electron gas. *Phys. Rev.*, 145:561–567, May 1966.

[33] W. Kohn. Density functional and density matrix method scaling linearly with the number of atoms. *Phys. Rev. Lett.*, 76:3168–3171, Apr 1996.

[34] D. M. Ceperley and B. J. Alder. Ground state of the electron gas by a stochastic method. *Phys. Rev. Lett.*, 45:566–569, Aug 1980.

[35] John P. Perdew and Yue Wang. Accurate and simple analytic representation of the electron-gas correlation energy. *Phys. Rev. B*, 45:13244–13249, Jun 1992.

[36] John P. Perdew, Kieron Burke, and Matthias Ernzerhof. Generalized gradient approximation made simple. *Phys. Rev. Lett.*, 77:3865–3868, Oct 1996.

[37] John P. Perdew and Karla Schmidt. Jacob's ladder of density functional approximations for the exchange-correlation energy. *AIP Conference Proceedings*, 577(1):1–20, 2001.

[38] Carlo Adamo and Vincenzo Barone. Toward reliable density functional methods without adjustable parameters: The PBE0 model. *The Journal of Chemical Physics*, 110(13):6158–6170, April 1999.

[39] J. F. Janak. Proof that $\frac{\partial e}{\partial n_i} = \epsilon$ in density-functional theory. *Phys. Rev. B*, 18:7165–7168, Dec 1978.

[40] R. Fletcher. A new approach to variable metric algorithms. *The Computer Journal*, 13(3):317–322, 01 1970.

[41] C. G. BROYDEN. The Convergence of a Class of Double-rank Minimization Algorithms 1. General Considerations. *IMA Journal of Applied Mathematics*, 6(1):76–90, 03 1970.

[42] HANNES JNSSON, GREG MILLS, and KARSTEN W. JACOBSEN. *Nudged elastic band method for finding minimum energy paths of transitions*, pages 385–404.

[43] Graeme Henkelman, Blas P. Uberuaga, and Hannes Jónsson. A climbing image nudged elastic band method for finding saddle points and minimum energy paths. *The Journal of Chemical Physics*, 113(22):9901–9904, 2000.

[44] X. Gonze, F. Jollet, F. Abreu Araujo, D. Adams, B. Amadon, T. Applencourt, C. Audouze, J.-M. Beuken, J. Bieder, A. Bokhanchuk, E. Bousquet, F. Bruneval, D. Caliste, M. Ct, F. Dahm, F. Da Pieve, M. Delaveau, M. Di Gennaro, B. Dorado, C. Espejo, G. Geneste, L. Genovese, A. Gerossier, M. Giantomassi, Y. Gillet, D.R. Hamann, L. He, G. Jomard, J. Laflamme Janssen, S. Le Roux, A. Levitt,

A. Lherbier, F. Liu, I. Lukaevi, A. Martin, C. Martins, M.J.T. Oliveira, S. Ponc, Y. Pouillon, T. Rangel, G.-M. Rignanese, A.H. Romero, B. Rousseau, O. Rubel, A.A. Shukri, M. Stankovski, M. Torrent, M.J. Van Setten, B. Van Troeye, M.J. Verstraete, D. Waroquiers, J. Wiktor, B. Xu, A. Zhou, and J.W. Zwanziger. Recent developments in the ABINIT software package. *Comput. Phys. Commun.*, 205:106–131, August 2016.

[45] F. Giustino. *Materials Modelling using Density Functional Theory. Properties & Predictions.* Oxford University Press, 2014.

[46] Richard M. Martin. *Electronic Structure. Basic Theory and Practical Methods.* Cambridge University Press, 2004.

[47] D. R. Hamann. Optimized norm-conserving Vanderbilt pseudopotentials. *Phys. Rev. B*, 88(8):085117, August 2013.

[48] `http://www.pseudo-dojo.org/`.

[49] M.J. [van Setten], M. Giantomassi, E. Bousquet, M.J. Verstraete, D.R. Hamann, X. Gonze, and G.-M. Rignanese. The pseudodojo: Training and grading a 85 element optimized norm-conserving pseudopotential table. *Computer Physics Communications*, 226:39 – 54, 2018.

[50] John P. Perdew, Robert G. Parr, Mel Levy, and Jose L. Balduz. Density-functional theory for fractional particle number: Derivative discontinuities of the energy. *Phys. Rev. Lett.*, 49:1691–1694, Dec 1982.

[51] Lars Hedin. New method for calculating the one-particle green's function with application to the electron-gas problem. *Phys. Rev.*, 139:A796–A823, Aug 1965.

[52] Fabien Bruneval and Xavier Gonze. Accurate *gw* self-energies in a plane-wave basis using only a few empty states: Towards large systems. *Phys. Rev. B*, 78:085125, Aug 2008.

[53] Mark S. Hybertsen and Steven G. Louie. Electron correlation in semiconductors and insulators: Band gaps and quasiparticle energies. *Phys. Rev. B*, 34:5390–5413, Oct 1986.

[54] R. W. Godby and R. J. Needs. Metal-insulator transition in kohn-sham theory and quasiparticle theory. *Phys. Rev. Lett.*, 62:1169–1172, Mar 1989.

[55] M. van Schilfgaarde, Takao Kotani, and S. Faleev. Quasiparticle self-consistent *gw* theory. *Phys. Rev. Lett.*, 96:226402, Jun 2006.

[56] Giovanni Onida, Lucia Reining, and Angel Rubio. Electronic excitations: density-functional versus many-body green's-function approaches. *Rev. Mod. Phys.*, 74:601–659, Jun 2002.

[57] E. E. Salpeter and H. A. Bethe. A relativistic equation for bound-state problems. *Phys. Rev.*, 84:1232–1242, Dec 1951.

[58] D. A. Drabold & S. K. Estreicher (Eds.). *Theory of Defects in Semiconductors*. Springer-Verlag, 2007.

[59] Hendrik J. Monkhorst and James D. Pack. Special points for brillouin-zone integrations. *Phys. Rev. B*, 13:5188–5192, Jun 1976.

[60] J S Smith, A Budi, M C Per, N Vogt, D W Drumm, L C L Hollenberg, J H Cole, and S P Russo. Ab initio calculation of energy levels for phosphorus donors in silicon. *Scientific Reports*, 7(1):6010, 2017.

[61] M. J. Puska, S. Pöykkö, M. Pesola, and R. M. Nieminen. Convergence of supercell calculations for point defects in semiconductors: Vacancy in silicon. *Phys. Rev. B*, 58:1318–1325, Jul 1998.

[62] M. I. J. Probert and M. C. Payne. Improving the convergence of defect calculations in supercells: An ab initio study of the neutral silicon vacancy. *Phys. Rev. B*, 67:075204, Feb 2003.

[63] A. F. Wright. Density-functional-theory calculations for the silicon vacancy. *Phys. Rev. B*, 74:165116, Oct 2006.

[64] Fabiano Corsetti and Arash A. Mostofi. System-size convergence of point defect properties: The case of the silicon vacancy. *Phys. Rev. B*, 84:035209, Jul 2011.

[65] M Leslie and N J Gillan. The energy and elastic dipole tensor of defects in ionic crystals calculated by the supercell method. *Journal of Physics C: Solid State Physics*, 18(5):973–982, feb 1985.

[66] C. Kittel. *Introduction to Solid State Physics*. John Wiley & Sons, 2005.

[67] G. Makov and M. C. Payne. Periodic boundary conditions in ab initio calculations. *Phys. Rev. B*, 51:4014–4022, Feb 1995.

[68] Christoph Freysoldt, Jörg Neugebauer, and Chris G. Van de Walle. Fully ab initio finite-size corrections for charged-defect supercell calculations. *Phys. Rev. Lett.*, 102:016402, Jan 2009.

[69] Samuel E. Taylor and Fabien Bruneval. Understanding and correcting the spurious interactions in charged supercells. *Phys. Rev. B*, 84:075155, Aug 2011.

[70] Patrick Rinke, Anderson Janotti, Matthias Scheffler, and Chris G. Van de Walle. Defect formation energies without the band-gap problem: Combining density-functional theory and the *gw* approach for the silicon self-interstitial. *Phys. Rev. Lett.*, 102:026402, Jan 2009.

[71] Wei Chen and Alfredo Pasquarello. Accuracy of *gw* for calculating defect energy levels in solids. *Phys. Rev. B*, 96:020101, Jul 2017.

[72] L. Martin-Samos, G. Roma, P. Rinke, and Y. Limoge. Charged oxygen defects in sio_2: Going beyond local and semilocal approximations to density functional theory. *Phys. Rev. Lett.*, 104:075502, Feb 2010.

[73] Fabien Bruneval and Guido Roma. Energetics and metastability of the silicon vacancy in cubic sic. *Phys. Rev. B*, 83:144116, Apr 2011.

[74] R.H. Hopkins, R.G. Seidensticker, J.R. Davis, P. Rai-Choudhury, P.D. Blais, and J.R. McCormick. Crystal growth considerations in the use of solar grade silicon. *Journal of Crystal Growth*, 42:493 – 498, 1977.

[75] A. Rohatgi, J.R. Davis, R.H. Hopkins, P. Rai-Choudhury, P.G. McMullin, and J.R. McCormick. Effect of titanium, copper and iron on silicon solar cells. *Solid-State Electronics*, 23(5):415 – 422, 1980.

[76] J. Olea, M. Toledano-Luque, D. Pastor, G. Gonzlez-Daz, and I. Mrtil. Titanium doped silicon layers with very high concentration. *Journal of Applied Physics*, 104(1):016105, 2008.

[77] Antonio Luque and Antonio Martí. Increasing the efficiency of ideal solar cells by photon induced transitions at intermediate levels. *Phys. Rev. Lett.*, 78:5014–5017, Jun 1997.

[78] Antonio Luque, Antonio Martí, and Colin Stanley. Understanding intermediate-band solar cells. *Nature Photonics*, 6(3):146–152, Mar 2012.

[79] Antonio Luque, Antonio Mart, Elisa Antoln, and Csar Tablero. Intermediate bands versus levels in non-radiative recombination. *Physica B: Condensed Matter*, 382(1):320 – 327, 2006.

[80] Jacob J. Krich, Bertrand I. Halperin, and Aln Aspuru-Guzik. Nonradiative lifetimes in intermediate band photovoltaicsabsence of lifetime recovery. *Journal of Applied Physics*, 112(1):013707, 2012.

[81] J Olea, G González-Díaz, D Pastor, and I Mártil. Electronic transport properties of ti-impurity band in si. *Journal of Physics D: Applied Physics*, 42(8):085110, mar 2009.

[82] E. Antoln, A. Mart, J. Olea, D. Pastor, G. Gonzlez-Daz, I. Mrtil, and A. Luque. Lifetime recovery in ultrahighly titanium-doped silicon for the implementation of an intermediate band material. *Applied Physics Letters*, 94(4):042115, 2009.

[83] J. Olea, A. del Prado, D. Pastor, I. Mrtil, and G. Gonzlez-Daz. Subbandgap absorption in ti implanted si over the mott limit. *Journal of Applied Physics*, 109(11):113541, 2011.

[84] Yi Zhang, R. Nelson, K.-M. Tam, W. Ku, U. Yu, N. S. Vidhyadhiraja, H. Terletska, J. Moreno, M. Jarrell, and T. Berlijn. Origin of localization in ti-doped si. *Phys. Rev. B*, 98:174204, Nov 2018.

[85] H. H. Woodbury and G. W. Ludwig. Spin resonance of transition metals in silicon. *Phys. Rev.*, 117:102–108, Jan 1960.

[86] G. W. Ludwig and H. H. Woodbury. Electronic structure of transition metal ions in a tetrahedral lattice. *Phys. Rev. Lett.*, 5:98–100, Aug 1960.

[87] D. A. van Wezep, R. van Kemp, E. G. Sieverts, and C. A. J. Ammerlaan. Electron-nuclear double resonance of titanium in silicon: ^{29}Si endor. *Phys. Rev. B*, 32:7129–7138, Dec 1985.

[88] F. Beeler, O. K. Andersen, and M. Scheffler. Theoretical evidence for low-spin ground states of early interstitial and late substitutional $3d$ transition-metal ions in silicon. *Phys. Rev. Lett.*, 55:1498–1501, Sep 1985.

[89] F. Beeler, O. K. Andersen, and M. Scheffler. Electronic and magnetic structure of 3d–transition-metal point defects in silicon calculated from first principles. *Phys. Rev. B*, 41:1603–1624, Jan 1990.

[90] D. J. Backlund and S. K. Estreicher. Ti, fe, and ni in si and their interactions with the vacancy and the a center: A theoretical study. *Phys. Rev. B*, 81:235213, Jun 2010.

[91] V. P. Markevich, S. Leonard, A. R. Peaker, B. Hamilton, A. G. Marinopoulos, and J. Coutinho. Titanium in silicon: Lattice positions and electronic properties. *Applied Physics Letters*, 104(15):152105, 2014.

[92] A. G. Marinopoulos, P. Santos, and J. Coutinho. Dft+u study of electrical levels and migration barriers of early 3d and 4d transition metals in silicon. *Phys. Rev. B*, 92:075124, Aug 2015.

[93] K. Sánchez, I. Aguilera, P. Palacios, and P. Wahnón. Assessment through first-principles calculations of an intermediate-band photovoltaic material based on ti-implanted silicon: Interstitial versus substitutional origin. *Phys. Rev. B*, 79:165203, Apr 2009.

[94] Edoardo G. Carnio, Nicholas D. M. Hine, and Rudolf A. Römer. Resolution of the exponent puzzle for the anderson transition in doped semiconductors. *Phys. Rev. B*, 99:081201, Feb 2019.

[95] J.D. Dunitz and L.E. Orgel. Electronic properties of transition-metal oxidesi: Distortions from cubic symmetry. *Journal of Physics and Chemistry of Solids*, 3(1):20 – 29, 1957.

[96] Dilyara Timerkaeva, Claudio Attaccalite, Gilles Brenet, Damien Caliste, and Pascal Pochet. Structural, electronic, and optical properties of the c-c complex in bulk silicon from first principles. *Journal of Applied Physics*, 123(16):161421, 2018.

[97] Michel Bockstedte, Andrea Marini, Oleg Pankratov, and Angel Rubio. Many-body effects in the excitation spectrum of a defect in sic. *Phys. Rev. Lett.*, 105:026401, Jul 2010.

[98] H. Lemke. Eigensehaften der dotierungsniveaus von mangan und vanadium in silizium. *physica status solidi (a)*, 64(2):549–556, 1981.

[99] Eicke R. Weber. 1983.

[100] T. Sadoh, H. Nakashima, and T. Tsurushima. Deep levels of vanadium and vanadiumhydrogen complex in silicon. *Journal of Applied Physics*, 72(2):520–524, 1992.

[101] A. Nylandsted Larsen, A. Mesli, K. Bonde Nielsen, H. Kortegaard Nielsen, L. Dobaczewski, J. Adey, R. Jones, D. W. Palmer, P. R. Briddon, and S. Öberg. *e* center in silicon has a donor level in the band gap. *Phys. Rev. Lett.*, 97:106402, Sep 2006.

[102] Ant Ural, Peter B. Griffin, and James D. Plummer. Fractional contributions of microscopic diffusion mechanisms for common dopants and self-diffusion in silicon. *Journal of Applied Physics*, 85(9):6440–6446, 1999.

[103] I. H. Hopkins and G. R. Hopkinson. Further measurements of random telegraph signals in proton irradiated CCDs. *IEEE Transactions on Nuclear Science*, 42(6):2074–2081, Dec 1995.

[104] D.R. Smith, A.D. Holland, and I.B. Hutchinson. Random telegraph signals in charge coupled devices. *Nuclear Instruments and Methods in Physics Research Section A: Accelerators, Spectrometers, Detectors and Associated Equipment*, 530(3):521 – 535, 2004.

[105] T. Nuns, G. Quadri, J. David, and O. Gilard. Annealing of proton-induced random telegraph signal in CCDs. *IEEE Transactions on Nuclear Science*, 54(4):1120–1128, Aug 2007.

[106] C. Virmontois, V. Goiffon, P. Magnan, O. Saint-Pe, S. Girard, S. Petit, G. Rolland, and A. Bardoux. Total ionizing dose versus displacement damage dose induced dark current random telegraph signals in cmos image sensors. *IEEE Transactions on Nuclear Science*, 58(6):3085–3094, Dec 2011.

[107] G. D. Watkins. Optical properties of group-V atom-vacancy pairs in silicon. *Radiation Effects and Defects in Solids*, 111-112(1-2):487–500, 1989.

[108] G.D. Watkins. Understanding the JahnTeller distortions for the divacancy and the vacancygroup-V-atom pair in silicon. *Physica B: Condensed Matter*, 376-377:50 – 53, 2006. Proceedings of the 23rd International Conference on Defects in Semiconductors.

[109] R. Virkkunen and R.M. Nieminen. First-principles study of the phosphorous-vacancy pair in silicon. *Computational Materials Science*, 1(4):351 – 357, 1993.

[110] Gernot Pfanner, Christoph Freysoldt, Jörg Neugebauer, and Uwe Gerstmann. Ab initio EPR parameters for dangling-bond defect complexes

in silicon: Effect of Jahn-Teller distortion. *Phys. Rev. B*, 85:195202, May 2012.

[111] M. G. Ganchenkova, A. Yu. Kuznetsov, and R. M. Nieminen. Electronic structure of the phosphorus-vacancy complex in silicon: A resonant-bond model. *Phys. Rev. B*, 70:115204, Sep 2004.

[112] M.G. Ganchenkova, L.E. Oikkonen, V.A. Borodin, S. Nicolaysen, and R.M. Nieminen. Vacancies and E-centers in silicon as multi-symmetry defects. *Materials Science and Engineering: B*, 159-160:107 – 111, 2009. EMRS 2008 Spring Conference Symposium K: Advanced Silicon Materials Research for Electronic and Photovoltaic Applications.

[113] Serdar Öğüt and James R. Chelikowsky. Charge state dependent Jahn-Teller distortions of the E-center defect in crystalline Si. *Phys. Rev. Lett.*, 91:235503, Dec 2003.

[114] U. R O. Madelung. *Semiconductors Impurities and Defects in Group IV Elements, IV-IV and III-V Compounds.*

[115] J. S. Nelson, P. A. Schultz, and A. F. Wright. Valence and atomic size dependent exchange barriers in vacancy-mediated dopant diffusion. *Applied Physics Letters*, 73(2):247–249, 1998.

[116] Xiang-Yang Liu, Wolfgang Windl, Keith M. Beardmore, and Michael P. Masquelier. First-principles study of phosphorus diffusion in silicon: Interstitial- and vacancy-mediated diffusion mechanisms. *Applied Physics Letters*, 82(12):1839–1841, 2003.

[117] A. Le Roch, C. Virmontois, P. Paillet, J. Belloir, S. Rizzolo, O. Marcelot, H. Dewitte, M. Van Uffelen, L. M. Casellas, P. Magnan, and V. Goiffon. Phosphorus versus arsenic: Role of the photodiode doping element in cmos image sensor radiation-induced dark current and random telegraph signal. *IEEE Transactions on Nuclear Science*, pages 1–1, 2020.

[118] Anton Kokalj. Xcrysdena new program for displaying crystalline structures and electron densities. *Journal of Molecular Graphics and Modelling*, 17(3):176 – 179, 1999.

[119] Osamu Sugino and Atsushi Oshiyama. Electronic structure of the silicon divacancy. *Phys. Rev. B*, 42:11869–11874, Dec 1990.

[120] Mineo Saito and Atsushi Oshiyama. Resonant bonds in symmetry-lowering distortion around a si divacancy. *Phys. Rev. Lett.*, 73:866–869, Aug 1994.

[121] George D. Watkins. Comment on "resonant bonds in symmetry-lowering distortion around a silicon divacancy". *Phys. Rev. Lett.*, 74:4353–4353, May 1995.

[122] Mineo Saito and Atsushi Oshiyama. Saito and oshiyama reply:. *Phys. Rev. Lett.*, 74:4354–4354, May 1995.

[123] Hyangsuk Seong and Laurent J. Lewis. First-principles study of the structure and energetics of neutral divacancies in silicon. *Phys. Rev. B*, 53:9791–9796, Apr 1996.

[124] M. Pesola, J. von Boehm, S. Pöykkö, and R. M. Nieminen. Spin-density study of the silicon divacancy. *Phys. Rev. B*, 58:1106–1109, Jul 1998.

[125] Serdar Öğüt and James R. Chelikowsky. Large pairing jahn-teller distortions around divacancies in crystalline silicon. *Phys. Rev. Lett.*, 83:3852–3855, Nov 1999.

[126] B.J Coomer, A Resende, J.P Goss, R Jones, S berg, and P.R Briddon. The divacancy in silicon and diamond. *Physica B: Condensed Matter*, 273-274:520 – 523, 1999.

[127] Serdar Öğüt and James R. Chelikowsky. Ab initio investigation of point defects in bulk si and ge using a cluster method. *Phys. Rev. B*, 64:245206, Dec 2001.

[128] D. V. Makhov and Laurent J. Lewis. Ab initio study of jahn-teller distortions for the divacancy in silicon. *Phys. Rev. B*, 72:073306, Aug 2005.

[129] R. R. Wixom and A. F. Wright. Formation energies, binding energies, structure, and electronic transitions of si divacancies studied by density functional calculations. *Phys. Rev. B*, 74:205208, Nov 2006.

[130] Jun-ichi Iwata, Kenji Shiraishi, and Atsushi Oshiyama. Large-scale density-functional calculations on silicon divacancies. *Phys. Rev. B*, 77:115208, Mar 2008.

[131] E. G. Sieverts, S. H. Muller, and C. A. J. Ammerlaan. Divacancy in silicon: Hyperfine interactions from electron-nuclear double-resonance measurements. ii. *Phys. Rev. B*, 18:6834–6848, Dec 1978.

[132] Paolo Giannozzi, Stefano Baroni, Nicola Bonini, Matteo Calandra, Roberto Car, Carlo Cavazzoni, Davide Ceresoli, Guido L Chiarotti, Matteo Cococcioni, Ismaila Dabo, Andrea Dal Corso, Stefano de Gironcoli, Stefano Fabris, Guido Fratesi, Ralph Gebauer, Uwe Gerstmann, Christos Gougoussis, Anton Kokalj, Michele Lazzeri, Layla Martin-Samos, Nicola Marzari, Francesco Mauri, Riccardo Mazzarello, Stefano Paolini, Alfredo Pasquarello, Lorenzo Paulatto, Carlo Sbraccia, Sandro Scandolo, Gabriele Sclauzero, Ari P Seitsonen, Alexander Smogunov, Paolo Umari, and Renata M Wentzcovitch. QUANTUM ESPRESSO: a modular and open-source software project for quantum simulations of materials. *Journal of Physics: Condensed Matter*, 21(39):395502, sep 2009.

[133] H. H. Woodbury and G. W. Ludwig. Spin resonance of pd and pt in silicon. *Phys. Rev.*, 126:466–470, Apr 1962.

[134] G. D. Watkins, M. Kleverman, A. Thilderkvist, and H. G. Grimmeiss. Structure of gold in silicon. *Phys. Rev. Lett.*, 67:1149–1152, Aug 1991.

[135] Frederick G. Anderson, Robert F. Milligan, and George D. Watkins. Epr investigation of pt^{-} in silicon. *Phys. Rev. B*, 45:3279–3286, Feb 1992.

[136] Frederick G. Anderson, Frank S. Ham, and George D. Watkins. Vacancy-model interpretation of epr spectrum of si:pt^{-}. *Phys. Rev. B*, 45:3287–3303, Feb 1992.

[137] G. D. Watkins and P. M. Williams. Vacancy model for substitutional ni^{-}, pd^{-}, pt^{-}, and au^{0} in silicon. *Phys. Rev. B*, 52:16575–16580, Dec 1995.

[138] A. Resende, R. Jones, S. Öberg, and P. R. Briddon. Calculations of electrical levels of deep centers: Application to au-h and ag-h defects in silicon. *Phys. Rev. Lett.*, 82:2111–2114, Mar 1999.

[139] Fabiano Corsetti and Arash A. Mostofi. Negative-u properties for substitutional au in si. *EPL (Europhysics Letters)*, 105(5):57006, mar 2014.

[140] F G Anderson. An explanation for the missing EPR from the isolated substitutional gold impurity in silicon. *Journal of Physics: Condensed Matter*, 3(24):4421–4432, jun 1991.

[141] S. T. Pantelides (Ed.). *Deep Centers in Semiconductors*. Gordon and Breach, 1992.

[142] G. A. Baraff, E. O. Kane, and M. Schlüter. Theory of the silicon vacancy: An anderson negative-*u* system. *Phys. Rev. B*, 21:5662–5686, Jun 1980.

[143] G. D. Watkins and J. R. Troxell. Negative-u properties for point defects in silicon. *Phys. Rev. Lett.*, 44:593–596, Mar 1980.

[144] Serdar Öğüt, Hanchul Kim, and James R. Chelikowsky. Ab initio cluster calculations for vacancies in bulk si. *Phys. Rev. B*, 56:R11353–R11356, Nov 1997.

[145] Fedwa El-Mellouhi, Normand Mousseau, and Pablo Ordejón. Sampling the diffusion paths of a neutral vacancy in silicon with quantum mechanical calculations. *Phys. Rev. B*, 70:205202, Nov 2004.

[146] Kurt Lejaeghere, Gustav Bihlmayer, Torbjörn Björkman, Peter Blaha, Stefan Blügel, Volker Blum, Damien Caliste, Ivano E. Castelli, Stewart J. Clark, Andrea Dal Corso, Stefano de Gironcoli, Thierry Deutsch, John Kay Dewhurst, Igor Di Marco, Claudia Draxl, Marcin Dułak, Olle Eriksson, José A. Flores-Livas, Kevin F. Garrity, Luigi Genovese, Paolo Giannozzi, Matteo Giantomassi, Stefan Goedecker, Xavier Gonze, Oscar Grånäs, E. K. U. Gross, Andris Gulans, François Gygi, D. R. Hamann, Phil J. Hasnip, N. A. W. Holzwarth, Diana Iuşan, Dominik B. Jochym, François Jollet, Daniel Jones, Georg Kresse, Klaus Koepernik, Emine Küçükbenli, Yaroslav O. Kvashnin, Inka L. M. Locht, Sven Lubeck, Martijn Marsman, Nicola Marzari, Ulrike Nitzsche, Lars Nordström, Taisuke Ozaki, Lorenzo Paulatto, Chris J. Pickard, Ward Poelmans, Matt I. J. Probert, Keith Refson, Manuel Richter, Gian-Marco Rignanese, Santanu Saha, Matthias Scheffler, Martin Schlipf, Karlheinz Schwarz, Sangeeta Sharma, Francesca Tavazza, Patrik Thunström, Alexandre Tkatchenko, Marc Torrent, David Vanderbilt, Michiel J. van Setten, Veronique Van Speybroeck, John M. Wills, Jonathan R. Yates, Guo-Xu Zhang, and Stefaan Cottenier. Reproducibility in density functional theory calculations of solids. *Science*, 351(6280), 2016.

[147] Fabien Bruneval. *gw* approximation of the many-body problem and changes in the particle number. *Phys. Rev. Lett.*, 103:176403, Oct 2009.

[148] Manish Jain, James R. Chelikowsky, and Steven G. Louie. Quasiparticle excitations and charge transition levels of oxygen vacancies in hafnia. *Phys. Rev. Lett.*, 107:216803, Nov 2011.

[149] G. D. Watkins and K. L. Brower. Epr observation of the isolated interstitial carbon atom in silicon. *Phys. Rev. Lett.*, 36:1329–1332, May 1976.

[150] Melvin Lax. The franckcondon principle and its application to crystals. *The Journal of Chemical Physics*, 20(11):1752–1760, 1952.

[151] Ryogo Kubo and Yutaka Toyozawa. Application of the Method of Generating Function to Radiative and Non-Radiative Transitions of a Trapped Electron in a Crystal. *Progress of Theoretical Physics*, 13(2):160–182, 02 1955.

[152] Karl F. Freed and Joshua Jortner. Multiphonon processes in the nonradiative decay of large molecules. *The Journal of Chemical Physics*, 52(12):6272–6291, 1970.

[153] A M Stoneham. Non-radiative transitions in semiconductors. *Reports on Progress in Physics*, 44(12):1251–1295, dec 1981.

[154] Melvin Lax. Giant traps. *Journal of Physics and Chemistry of Solids*, 8:66 – 73, 1959.

[155] R. A. Marcus. On the theory of oxidationreduction reactions involving electron transfer. i. *The Journal of Chemical Physics*, 24(5):966–978, 1956.

[156] Mi Kyung Lee and David F. Coker. Modeling electronic-nuclear interactions for excitation energy transfer processes in light-harvesting complexes. *The Journal of Physical Chemistry Letters*, 7(16):3171–3178, 2016. PMID: 27472379.

[157] Gerg ő Thiering and Adam Gali. Ab initio calculation of spin-orbit coupling for an nv center in diamond exhibiting dynamic jahn-teller effect. *Phys. Rev. B*, 96:081115, Aug 2017.

[158] Lin Shi and Lin-Wang Wang. Ab initio calculations of deep-level carrier nonradiative recombination rates in bulk semiconductors. *Phys. Rev. Lett.*, 109:245501, Dec 2012.

[159] Audrius Alkauskas, Qimin Yan, and Chris G. Van de Walle. First-principles theory of nonradiative carrier capture via multiphonon emission. *Phys. Rev. B*, 90:075202, Aug 2014.

Résumé

Dans cette thèse, nous décrivons l'effet des défauts localisés sur les propriétés électroniques du silicium. Après 60 ans de production industrielle de dispositifs à base de silicium, on pourrait s'attendre à ce que tous les caractéristiques de ce matériau soient parfaitement comprises, surtout si l'on considère que la fabrication des transistors actuels à l'échelle du nanomètre nécessite une précision quasi atomique. Cependant, en conséquence directe de cette miniaturisation extrême, la création accidentelle d'un seul défaut peut suffire à modifier les propriétés électroniques souhaitées de l'échantillon, devenant ainsi l'un des phénomnes les plus redoutés de lindustrie. Historiquement, l'identification de ces centres a été possible grâce au développement et à lamélioration des techniques de caractérisation, capables de cibler des propriétés de défaut spécifiques, par exemple, liées à la position des états induits par le centre dans la bande interdite du semi-conducteur (absorption optique infrarouge, spectroscopie DLTS) ou aux distorsions atomiques déclenchées par la forme de la densité électronique localisée (spectroscopie EPR). Une telle quantité de données expérimentales a motivé le développement de modèles simples basés sur la symétrie, reproduisant qualitativement les caractéristiques fondamentales des défauts. Plus récemment l'augmentation exponentielle de la puissance de calcul a fait des calculs *ab initio* le modèle théorique parfait pour fournir une representation quantitatif des défauts ponctuels dans les semi-conducteurs. Les simulations numériques léchelle atomique dans le silicium, basées sur la théorie de la fonctionnelle de la densité, ciblent cependant généralement des propriétés spécifiques des défauts, ne donnant pas une image théorique complète du système, et négligeant souvent les modèles précédents et les preuves expérimentales. Dans cette thèse, nous apportons une nouvelle vision sur les dfauts emblmatiques du silicium par la quantification de modles identifis de longue date, en tablissant un lien explicite avec les techniques de caractérisation. Notre exploration détaillée de la surface d'énergie potentielle du E-center du silicium, guidée par un modèle simple de Jahn-Teller, a confirm la dynamique des dfauts observe diffrents rgimes de temprature, nous permettant de relier la prsence d'un tel dfaut ponctuel un bruit lectronique dans les capteurs d'images. De plus, nous étudions l'hypothèse d'une amélioration de l'absorption des photons dans les cellules solaires en silicium dopé au titane en décrivant les effets à plusieurs corps à laide de lapproximation GW. De cette maniére, on attribue les excitations électroniques chargées aux transitions entre les états du titane, précédemment décrits par un modèle phénoménologique pour les métaux de transition dans le silicium. Nous proposons également une généralisation des toy-models préexistants pour aborder les centres complexes, pour lesquels une controverse notoire au sein de la communauté ab initio existe toujours, montrant explicitement les limites des approches de champ moyen lorsqu'elles ciblent des densités électroniques hautement localisées. Nous concluons par une brève revue critique de la caractérisation théorique de l'activité électronique des défauts, et en particulier de la section efficace de capture des transitions non radiatives.

Abstract

In this thesis, we describe the effect of localized defects on the electronic properties of silicon. After 60 years of silicon devices production, one might expect all details of this material to be fully understood, especially considering that the manufacture of nowadays nanometer-sized transistors requires quasi-atomic accuracy. However, as a direct result of such extreme miniaturization, the accidental creation of even one single trapping center can be sufficient to alter the desired electronic properties of the sample, becoming one of the most feared phenomena in the industry. Since the early years, the identification of these centers has been possible through the development of characterization techniques, capable of targeting specific defect properties, related to the position of the center-induced states within the semiconductor gap (infrared optical absorption, DLTS spectroscopy) or to the atomic distortions triggered by the form of the localized electronic density (EPR spectroscopy). Such collection of experimental data motivated the development of simple symmetry-based models, qualitatively reproducing the basic features of defects. The later exponential increase in computational power made ab-initio calculations the perfect candidate to give a quantitative theoretical model of point-defects in semiconductors. Atomistic numerical simulations in silicon, based on the Density Functional Theory, do however typically target specific defect-properties, not giving a complete theoretical picture of the system, often overlooking previous models and experimental evidence. In the present thesis, we provide new insight into iconic defects in silicon through the quantification of long-established atomistic models, making an explicit link with the characterization techniques. Our detailed exploration of the DFT energy surface of the silicon E-center, guided by a simple Jahn-Teller model, confirmed the observed defect-dynamics at different temperature regimes, allowing us to link the presence of such point-like defect to a burst noise in image sensors. Moreover, we investigate the hypothesis of enhancing photon-absorption in titanium-doped silicon solar cells by describing many-body effects in the form of the GW approximation, assigning the charged electronic excitations to transitions between Ti-related states, previously depicted by a phenomenological model for transition metals in silicon. We also propose a generalization of the preexisting toy-models to tackle complex centers, for which a notorious controversy within the ab-initio community still exists, showing explicitly the limitations of mean-field approaches when targeting highly localized electronic densities. We conclude with a brief critical review of the theoretical characterization of the defects electronic activity, and in particular the capture cross section of non-radiative transitions.